Etude et amélioration des performances et de la robustesse des lois de commande de procédés sidérurgiques Application à la régulation de niveau en coulée continue

Karim Jabri

N° D'ORDRE

THÈSE DE DOCTORAT

SPECIALITE : PHYSIQUE

Ecole Doctorale « Sciences et Technologies de l'Information des Télécommunications et des Systèmes »

Présentée par :

Karim JABRI

Sujet :

Etude et amélioration des performances et de la robustesse des lois de commande de procédés sidérurgiques Application à la régulation de niveau en coulée continue

Soutenue le 18 Juin 2010 devant les membres du jury :

M. Bertrand BELE	Invité
M. Didier DUMUR	Co-Directeur de Thèse
M. Emmanuel GODOY	Directeur de Thèse
M. Nicolas LANGLOIS	Rapporteur
Mme Xuefang LIN-SHI	Rapporteur
M. Alain MOUCHETTE	Invité
Mme Dorothée NORMAND-CYROT	Présidente
M. Eric OSTERTAG	Examinateur

A Mes Parents
Voyez ici le fruit de mon travail et de votre éducation !

''**Un peu de science éloigne de Dieu, beaucoup de science y ramène**''
Louis Pasteur

Remerciements

L'aboutissement d'une thèse de doctorat est le fruit de l'implication de nombreuses personnes. Je tiens ici à leur rendre un hommage appuyé. Merci à tous mes collègues et membres de mon entourage qui ont contribué directement ou indirectement à faire de ce travail une expérience très enrichissante et particulièrement agréable.

Je souhaite exprimer toute ma gratitude à Monsieur Didier DUMUR et Monsieur Emmanuel GODOY, Professeurs à SUPELEC, qui ont encadré ce travail de thèse. Par leurs qualités techniques et humaines, ils ont joué un rôle essentiel durant ces trois années. Leur patience et leur disponibilité ont permis à cette thèse de se dérouler dans de très bonnes conditions. Mines de savoir et d'expérience, ils ont su m'aider à bien diriger mes recherches et à aborder tous les aspects de la thèse. Merci Didier et Emmanuel et à bientôt dans d'autres collaborations.

J'adresse mes remerciements les plus chaleureux à Monsieur Alain MOUCHETTE, Chef adjoint du département Mesure et Contrôle d'ArcelorMittal Recherche et Développement de Maizières-Lès-Metz. Merci Alain pour le temps que tu as consacré à ce travail et d'avoir toujours été à l'écoute des problèmes que j'ai pu rencontrer. Ton efficacité et ta gentillesse m'ont été, à maintes reprises, d'un grand secours. J'espère que nous aurons à nouveau l'occasion de retravailler ensemble.

Je remercie Madame Dorothée NORMAND-CYROT, Directeur de Recherche au CNRS, de m'avoir fait l'honneur de présider mon jury de thèse. Mes remerciements les plus sincères s'adressent également à Madame Xuefang LIN-SHI, Professeur à l'INSA de Lyon, et à Monsieur Nicolas LANGLOIS, Chef du département Génie Electrique et Energie à l'ESIGELEC, d'avoir lu attentivement mon mémoire de thèse et d'avoir accepté d'en être les rapporteurs. J'associerai également à mes remerciements Monsieur Eric OSTERTAG, Professeur à l'ENSPS de Strasbourg, pour le temps précieux qu'il a consacré à la lecture de mon mémoire et d'avoir accepté de participer à mon jury de thèse.

Que soit remercié Monsieur Pierre-Jean Krauth, Chef du département Mesure et Contrôle d'ArcelorMittal Recherche et Développement, de m'avoir permis de réaliser mes travaux au sein de son département. Je remercie Monsieur Bertrand BELE de m'avoir proposé ce sujet de thèse. Je tiens à remercier également Monsieur Pascal GARDIN d'avoir assisté à toutes mes présentations lors des revues de projet et Monsieur Jean-François DOMGIN, Chef du service de la coulée continue pour ses conseils, ses explications et tous les documents qu'il m'a transmis. J'exprime mes remerciements à tous mes collègues d'ArcelorMittal Process Maizières qui, par un service ou un repas partagé, ont rendu conviviale cette expérience, en particulier, Marie, Jean-Marie, Laurence, Laura, Fayçal, Jérôme, Francis, Bernard, Nicolas, Edouard, Thomas, Florian, Sonia, Laurette, Jeannette, Daniel, Julien, Charles, Audrey, Martin, Didier, Sophie et Claude.
Je souhaite remercier également mes collègues du centre de Recherche et Développement d'ArcelorMittal Global R&D de Chicago aux Etats-Unis et notamment M. Hongbin YIN, M. William P. UMLAUF, M. Kai ZHENG et M. H. Thomas TSAI pour m'avoir accueilli au sein du centre, de m'avoir fait visiter plusieurs installations et de m'avoir fourni toutes les données dont j'avais besoin.
Ma collaboration avec mes collègues de l'usine de Dunkerque, en particulier, avec M. Laurent WULVERYCK, M. Antoine BLANCHARD, M. Thierry LECOESTER et M. Gregory MAES, a été un grand plaisir. Je les remercie pour leur confiance et d'avoir porté un grand intérêt aux différents outils que j'ai pu développer.

Un grand merci également à tous les membres, Professeurs et Thésards, du département Automatique de SUPELEC. Je remercie, en particulier, Monsieur Patrick BOUCHER, Professeur et Chef du département, pour m'avoir accueilli au sein du laboratoire et permis de présenter mes travaux dans de nombreuses conférences internationales. Je remercie très sincèrement les Professeurs du département : Mme Houria SIGUERDIDJANE, Mme Sihem TEBBANI, M. Gilles DUC, M. Dominique BEAUVOIS, M. Pedro RODRIGUEZ, M. Antoine CHAILLET, M. Sorin OLARU et Mlle Cristina STOICA. Je remercie Monsieur Sette DIOP, chargé de recherche CNRS, pour les discussions que nous avons eues à plusieurs reprises. Je remercie Madame Josiane DARTRON, secrétaire du département, pour son sourire communicatif et toute l'énergie qu'elle consacre aux tâches

administratives du laboratoire. Je remercie Monsieur Léon MARQUET, technicien du département, d'avoir apporté efficacement et rapidement des solutions à tous les problèmes liés au matériel informatique et aux logiciels qui se sont présentés à moi.
Je tiens par ailleurs à remercier tous les Thésards du département que j'ai côtoyés pendant ces trois années et qui ont permis de mettre un peu de ciel bleu dans la grisaille quotidienne. Je pense, en premier lieu, à Bastien qui m'a toujours apporté un soutien sans failles et qui m'a envoyé pour ma soutenance ses ondes positives depuis le Japon. Je voudrai évidemment remercier RF, Bogdan, Raluca, Cristina, Safta, Haitham, Ali, Henri, Guillermo, Hieu, Nam, Florin, Alaa, Anamaria, Warody, Ionela, Mara, Nicolas, Ju, Toon, Paula, Spilios, Ghizlane, Mariana et Bilal (que je rencontrais à chaque fois que je me rendais à un entretien de recrutement).

J'adresse mes remerciements également à Monsieur Adel RAZEK, mon conseiller aux thèses, à Madame Dominique MARTIN, secrétaire de l'école doctorale STITS et à Mademoiselle Marie-Christine MIGNIER du service scolarité de l'Université PARIS-SUD 11.

Mon étude sur l'architecture RMMAC a pu être menée grâce à la boîte à outils de la μ synthèse mixte développée par le Professeur Gary BALAS, Chef du département Aerospace Engineering and Mechanics à l'Université de Minnesota aux Etats-Unis. Je le remercie infiniment pour sa disponibilité et sa rigueur. J'espère que nous aurons l'occasion de retravailler et d'échanger sur d'autres sujets dans l'avenir.

Enfin et surtout, je réserve mes derniers remerciements à mes parents qui m'ont donné l'éducation nécessaire à la réalisation de ce travail. Qu'ils ne doutent pas de ma reconnaissance profonde et de mon inaltérable affection.

PUBLICATIONS

1. Journal Articles

Submitted:

"Particle swarm optimization based tuning of a modified Smith predictor for mould level control in continuous casting", K. Jabri, D. Dumur, E. Godoy, A. Mouchette, B. Bèle, Journal of Process Control.

"Cancellation of bulging effect on mould level in continuous casting: experimental validation", K. Jabri, E. Godoy, D. Dumur, A. Mouchette, B. Bèle, Journal of Process Control.

2. Conference Articles

K. Jabri, E. Godoy, D. Dumur, A. Mouchette, B. Bèle, "Robust adaptive control of the mold level in the continuous casting process using multiple models", *Proceedings of the American Control Conference*, Baltimore, Maryland, USA, June 30 – July 2, 2010.

K. Jabri, E. Godoy, D. Dumur, A. Mouchette, B. Bèle, "Cancellation of Bulging Effect on Mold Level in Continuous Casting: Experimental Validation", *IFAC workshop on Automation in Mining, Mineral and Metal Industry IFACMMM*, Vina del Mar, Chile, October 14-16, 2009.

K. Jabri, D. Dumur, E. Godoy, A. Mouchette, B. Bèle, "Particle Swarm Optimization Based Tuning of a Modified Smith Predictor for Mold Level Control in Continuous Casting", *IFAC workshop on Automation in Mining, Mineral and Metal Industry IFACMMM*, Vina del Mar, Chile, October 14-16, 2009.

K. Jabri, A. Mouchette, B. Bèle, E. Godoy, D. Dumur, "Periodic Disturbances Reduction in the Continuous Casting Process by Means of a Modified Smith Predictor", *6th International Conference on Informatics in Control, Automation and Robotics ICINCO*, Vol. 3, pp. 110-115, Milan, Italy, July 2-5, 2009.

K. Jabri, D. Dumur, E. Godoy, A. Mouchette, B. Bèle, "Modified Smith Predictor Scheme for Periodic Disturbances Reduction in the Continuous Casting Process", *7th Asian Control Conference ASCC*, pp. 1091-1096, Hong Kong, August 24-26, 2009.

K. Jabri, B. Bele, A. Mouchette, D. Dumur, E. Godoy, "Suppression of periodic disturbances in the continuous casting process", *IEEE Multiconference on Systems and Control MSC-CACSD 08*, pp. 91-96, San Antonio, Texas, USA, September 3-5, 2008.

K. Jabri, B. Bele, A. Mouchette, E. Godoy, D. Dumur, "Disturbances estimation for mold level control in the continuous casting process", *5th International Conference on Informatics in Control, Automation and Robotics ICINCO 08*, pp. 119-124, Funchal, Portugal, May 11-15, 2008.

Table of Contents

RÉSUMÉ DE THÈSE

Introduction générale

Contexte de l'étude

Le secteur de l'acier est une industrie moderne et bien établie qui fournit des produits à haute valeur ajoutée pour des clients de plus en plus exigeants, en particulier, dans des segments haut de gamme. Ses principaux points forts résident dans la qualité de ses produits grâce à ses moyens technologiques performants. Ses principales pistes à améliorer sont liées à la disponibilité des matières premières et aux contraintes économiques et de respect de l'environnement. En outre, la production ciblée sur de nouveaux produits à base d'aciers allégés et à haute résistance doit encore accentuer les contraintes sur l'ensemble de la filière de fabrication.
Le projet proposé par ArcelorMittal vise à faire bénéficier ses systèmes de production de solutions innovantes dans le domaine de l'automatisation des lignes, permettant de limiter les accès aux zones à risque et d'aboutir à un pilotage totalement automatique des outils. Le procédé adopté dans le cadre de cette thèse est celui de la coulée continue dont on souhaite améliorer la régulation de niveau afin de réduire les défauts du produit solidifié liés aux variations de niveau dans la lingotière.
La solution qui aura été développée dans le cadre de cette thèse devra présenter un caractère générique et être facilement généralisable à d'autres procédés sidérurgiques.
Ce travail de thèse résulte d'une collaboration entre le département Mesure et Contrôle d'ArcelorMittal Recherche et Développement à Maizières-Lès-Metz et le département Automatique de SUPELEC à Gif-sur-Yvette dans le cadre d'une Convention Industrielle de Formation par la Recherche (CIFRE) subventionnée par l'Association Nationale de la Recherche et de la Technologie (ANRT).

Description du procédé

Dans la filière de production de l'acier, la coulée continue occupe une place centrale et stratégique entre l'élaboration de l'acier liquide et le laminage. En effet, ce procédé a su remplacer la technique traditionnelle de coulée en lingots grâce à sa meilleure productivité permettant à la fois une économie d'énergie et de main d'œuvre.
Lors de sa solidification en coulée continue, l'acier liquide provenant du répartiteur s'écoule via une busette dans un moule en cuivre de section carrée ou rectangulaire sans fond appelé lingotière et se solidifie au contact de ses parois refroidies à l'eau (voir figure ci-après). Le débit entrant dans la lingotière est généralement contrôlé à l'aide d'une quenouille.

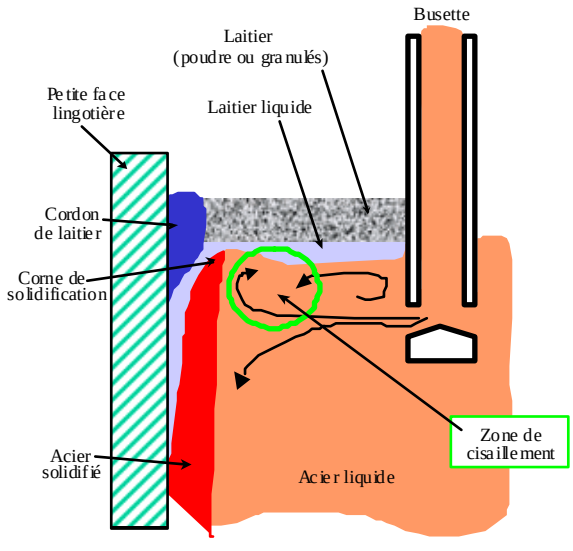

Interface busette - lingotière

Tiré vers le bas par un jeu de rouleaux extracteurs, la peau solidifiée entraîne l'acier en fusion qui achève de se solidifier. Arrivé à la sortie de la machine, l'acier est complètement solidifié et immédiatement découpé en tronçons aux longueurs désirées appelés brames. Le produit ainsi obtenu est réchauffé ensuite dans des fours avant d'accéder à l'étape de laminage. Il a été démontré qu'une partie importante des défauts de surface du produit solidifié est provoquée par les fluctuations importantes du niveau d'acier en lingotière qui entraînent dans leurs mouvements le laitier et les inclusions d'alumine au cœur de l'acier en fusion (voir figure précédente). De telles variations peuvent contraindre les opérateurs à déclasser systématiquement la brame solidifiée car ces défauts deviendraient visibles sur le produit final même après laminage.
De nombreux phénomènes sont à l'origine des variations du niveau d'acier dans la lingotière. Certains sont déclenchés par les opérateurs et sont donc prévisibles. En revanche, d'autres perturbations comme le débouchage peuvent survenir soudainement provoquant dans certains cas un débordement coûteux. On peut citer également :

- Les changements de points de fonctionnement comme la variation de largeur ou de vitesse de coulée qui ont pour effet d'imposer un mode d'écoulement particulier et de modifier en conséquence certains paramètres de la boucle de régulation. N'ayant pas été conçu pour fonctionner convenablement dans une large plage de variations des conditions de coulée, le régulateur ne parvient pas à garantir des performances satisfaisantes à ce nouveau point de fonctionnement. Les opérateurs ont généralement tendance à éliminer l'origine du problème en revenant au point de fonctionnement initial.
- Il est possible par ailleurs que le siège de la busette ainsi que ses parois internes se bouchent progressivement puis se débouchent brutalement. De l'argon est alors introduit à travers un circuit afin de ralentir ce phénomène dans le but d'allonger la durée de vie des busettes. Au niveau de la lingotière, le cycle bouchage/débouchage modifie particulièrement son débit entrant qui ne peut plus être déterminé à partir seulement de la position de la quenouille. Si ce problème est intrinsèquement lié à la composition de l'acier liquide, il n'en reste pas moins que son effet sur le niveau doit être confié à la boucle de régulation de niveau. De plus, il est fortement souhaitable de disposer d'un outil de diagnostic permettant de suivre l'évolution de ce phénomène dans le temps.
- Le volume d'acier liquide contenu dans la brame partiellement solidifiée évolue périodiquement. Ce phénomène appelé gonflement est directement lié à la vitesse de coulée et à la configuration des rouleaux extracteurs (diamètres et distances inter-rouleaux). Il a une influence directe sur le débit sortant de la lingotière qui varie alors de manière cyclique.
- D'autre part, la dynamique de niveau dans la lingotière est décrite par un modèle dont les paramètres sont incertains. En particulier, un retard existant entre le signal de commande (c'est-à-dire la consigne de position de la quenouille) et le débit d'acier entrant dans la lingotière n'est pas bien identifié à l'heure actuelle. Sachant qu'il peut remettre en cause la stabilité de la boucle de régulation, il convient de développer une méthode d'identification précise ou de concevoir une régulation qui tienne compte des incertitudes de cette boucle.

État de l'art

Depuis le début de l'exploitation industrielle du procédé de la coulée continue, de nombreuses solutions ont été proposées pour répondre au problème de la régulation de niveau. Dans une même usine, chaque ligne de production utilise un système de régulation adapté au produit coulé, à la configuration de la machine et au cahier des charges fixé par le client. On peut citer par exemple le PID qui est le régulateur le plus largement répandu, la commande Linéaire Quadratique Gaussienne LQG et la Commande Prédictive Fonctionnelle PFC. A partir des informations fournies par le capteur de la surface libre de l'acier, ces régulateurs sont capables de stabiliser le niveau en agissant sur le débit entrant dans la lingotière. Cependant, leurs performances sont étroitement liées aux conditions de coulée ainsi qu'à l'état des perturbations. Dans certains cas, les régulateurs parviendraient à maintenir les variations de niveau dans un intervalle d'un millimètre. Dans d'autres cas plus fréquents, les variations de niveau dépasseraient plusieurs millimètres et seul un changement de point de fonctionnement pourrait les amortir. C'est la raison pour laquelle les sidérurgistes ont introduit également des modules complémentaires à la boucle de régulation classique pour prendre en charge les variations engendrées par une perturbation donnée comme le débouchage, le gonflement ou les ondes stationnaires. D'autre part, des solutions

qui visent à estimer ces perturbations à partir des signaux disponibles dans le but d'alerter les opérateurs en cas de problèmes majeurs, ont également été déployées.
Au regard des performances des régulateurs actuels et de la réalité des problèmes rencontrés, il paraît primordial de développer une solution qui soit robuste face aux différentes évolutions du procédé durant la séquence de coulée afin de contrer les effets des perturbations internes et externes à la boucle de régulation.

Objectifs et organisation de la thèse

La régulation de niveau n'a cessé d'être une préoccupation majeure et constitue un élément clé pour la qualité du produit dans la chaîne d'élaboration de l'acier. La recherche sur ce sujet est fortement soutenue par un besoin constant de l'industrie sidérurgique. De plus, le chiffre d'affaires moyen généré par une machine de coulée étant de l'ordre d'un million d'euros par jour, la boucle de régulation doit être à même d'éviter les arrêts de production dus aux variations de niveau, d'où l'importance des enjeux qu'implique ce procédé.
Compte tenu de ce qui précède, l'étude devra porter sur la modélisation du procédé, la reconstruction des informations sur l'état des perturbations, l'application des lois de commande classiques adaptées à ce type de procédé, la conception et la validation d'une solution innovante de contrôle robuste de niveau en lingotière de coulée continue, qui devra être facilement généralisable à d'autres types de procédés sidérurgiques. Ceci amène à décomposer ce travail en différentes étapes faisant chacune l'objet d'un chapitre spécifique.

Le mémoire de thèse est organisé en cinq chapitres. Dans le chapitre 1, nous présenterons le procédé de la coulée continue et ses interfaces avec les autres procédés dans la chaîne de fabrication de l'acier. Nous rappellerons également quelques aspects clés de l'acier. Nous décrirons ensuite la tête de machine de coulée et les différentes perturbations à l'origine des variations de niveau. L'instrumentation associée à la boucle de régulation de niveau y sera notamment détaillée.

Dans le chapitre 2, nous présenterons deux modèles du niveau en lingotière. Le premier est basé sur la dynamique de l'acier et évoqué ici uniquement pour enrichir notre revue bibliographique. En revanche, le deuxième est un modèle linéarisé autour d'un point de fonctionnement à partir duquel seront synthétisées toutes les lois de commande. Nous veillerons à ce que ce modèle soit suffisamment représentatif de la dynamique du niveau en lingotière en le complétant notamment par les modèles des trois perturbations les plus courantes que sont le bouchage, le gonflement et les ondes stationnaires.

Dans le chapitre 3, le mémoire s'articule autour de trois axes principaux. Le premier point propose une méthode d'identification de la dynamique de l'actionneur et des paramètres du modèle de commande. Une grande partie de ce chapitre est ensuite consacrée à la mise en œuvre d'un outil de détection du bouchage et du gonflement par le biais d'un observateur d'état. Cet outil est également intégré dans une structure de compensation de l'effet du gonflement sur le niveau validée en simulation, à partir de signaux réels prélevés sur site et enfin sur maquette hydraulique.

Le chapitre 4 s'attache à présenter plusieurs lois de commande non-adaptatives dont certaines sont actuellement en service dans les usines d'ArcelorMittal. Ainsi, seront étudiées les lois de commande suivantes : PID, Commande Prédictive Fonctionnelle PFC, Commande Prédictive Généralisée GPC, prédicteur de Smith et ses versions modifiées et enfin la Commande par Modèle Interne IMC. Afin de faciliter le choix au sidérurgiste entre toutes ces lois de commande en vue d'une implémentation industrielle, une étude comparative a été réalisée pour évaluer les gains de la solution retenue en termes de rejet des perturbations et de marges de robustesse.

Enfin, le chapitre 5 sera consacré à l'application de la commande adaptative multi-modèles RMMAC à la régulation de niveau. Cette architecture est la seule à pouvoir garantir des performances satisfaisantes sur de larges intervalles de variation des paramètres. Après une brève introduction des architectures multi-modèles, de la procédure de μ synthèse et de ses deux variantes, nous appliquerons une approche formalisée afin de déterminer le nombre de modèles, les régulateurs robustes et les filtres de Kalman associés à chaque modèle. Pour illustrer l'intérêt de cette méthode, les résultats de simulation seront donnés et commentés.
Ce chapitre s'achève par la conclusion générale de ce mémoire de thèse.

Chapitre 1 : Présentation du procédé de la coulée continue

Coulée continue

L'acier liquide est élaboré selon deux filières de production. Dans la filière 'fonte', la fusion et la réduction des matières premières (essentiellement du minerai et du charbon) produisent de la fonte liquide qui est alors transformée en acier par insufflation d'oxygène et ajout d'additifs qui donnent au produit final les propriétés requises. Dans la filière 'ferrailles' qui représente 30% de la production mondiale, l'acier liquide est obtenu en faisant fondre les ferrailles dans un four à arcs électriques.
L'acier en fusion ainsi obtenu est ensuite coulé en utilisant l'un des deux procédés suivants : la coulée en lingots qui est en voie de régression ou la coulée continue largement répandue à travers le monde.
Dans le procédé de la coulée continue qui nous intéresse plus particulièrement dans le cadre de cette thèse, l'acier en fusion contenu dans une poche est coulé dans une lingotière sans fond. Au contact de ses parois maintenues à une température basse par un système de refroidissement, l'acier commence à se solidifier formant une peau solide. Des rouleaux extracteurs disposés sous la lingotière tirent le produit vers le bas de la machine. Dans le même temps, un système de refroidissement secondaire constitué de jets d'eau permet d'achever la solidification de l'acier liquide. En sortie de procédé, le produit complètement solidifié est découpé en tronçons de la longueur désirée (appelés brames) avant d'être envoyé vers un four (voir figure ci-après).

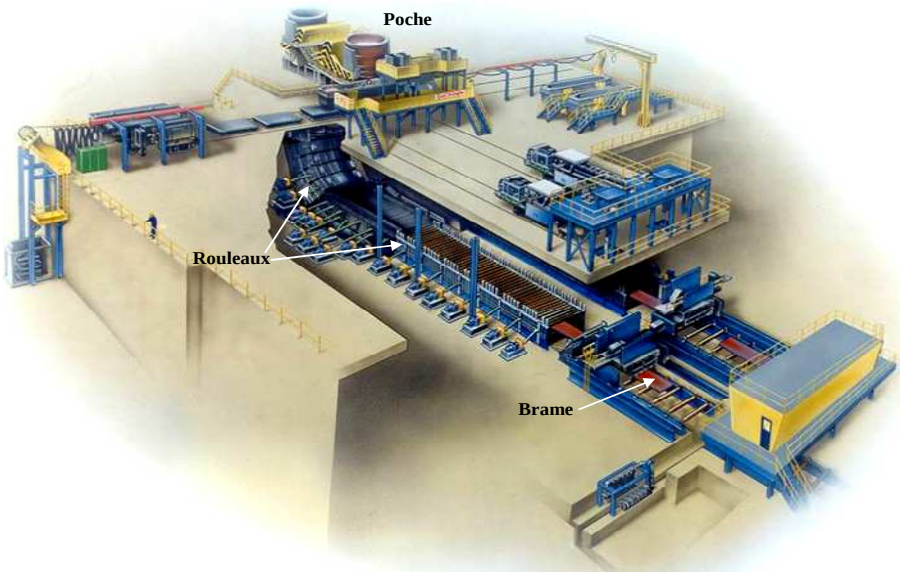

Machine de coulée continue

En se référant à cette figure, les éléments principaux d'une machine de coulée continue sont :

- **Le répartiteur** qui est un grand récipient d'une capacité moyenne de 20 tonnes, situé entre la poche et la lingotière. Son rôle est d'alimenter la lingotière en acier liquide avec un débit contrôlé par une quenouille ou par un système à tiroirs. Il permet d'alimenter simultanément plusieurs lingotières et de faire couler plusieurs poches consécutives sans arrêter la machine.

- **La lingotière**
  Le métal en provenance du répartiteur entre dans la lingotière par le biais des deux ports de la busette submergée. Grâce à une circulation intense d'eau froide, les parois de la lingotière sont refroidies, ce qui permettra de solidifier l'acier en fusion et de former une peau suffisamment épaisse et résistante pour contenir le métal liquide qui n'a pas été solidifié dans cette zone de refroidissement primaire. Afin de protéger l'acier de l'oxydation, la surface de l'acier liquide est souvent couverte d'une poudre appelée laitier. C'est au niveau de la lingotière que le métal est soumis à un brassage électromagnétique afin d'homogénéiser cette phase liquide. Enfin, la lingotière est animée d'un mouvement d'oscillation

verticale de faible amplitude destiné à empêcher avec l'aide d'un lubrifiant le collage de la peau solidifiée contre les parois en cuivre.

- **Le refroidissement secondaire** s'effectue grâce à deux systèmes. Le premier est un système mécanique composé de plusieurs rouleaux de soutien et de guidage dont certains sont motorisés pour faire avancer la brame. La vitesse est imprimée par les rouleaux moteurs extracteurs. Elle est choisie en fonction du format coulé, de la nuance d'acier et de l'intensité du refroidissement tout au long de la zone de refroidissement secondaire et de la lingotière. Le deuxième système assure la solidification de l'acier liquide et la maîtrise de la température de surface de la peau sous l'action de jets d'eau.
- **L'oxycoupage** permet de découper le produit solidifié à la longueur voulue et de l'identifier avant de l'envoyer vers le laminoir chaud.

Régulation de niveau en lingotière de coulée continue

Nous avons donné dans le paragraphe précédent une vue globale de la machine de coulée continue. Nous détaillerons dans ce paragraphe la tête de machine qui est le siège des variations de niveau d'acier liquide.
Comme le montre la figure suivante, la busette en matériau réfractaire plonge dans le bain de métal liquide dont on protège la surface contre l'oxydation grâce au laitier et à la poudre de couverture qui constituent ce que les aciéristes appellent le ménisque. Le métal coule du répartiteur jusqu'à la lingotière en passant par la busette dont les ouïes donnent, selon leurs formes, une direction au jet de métal.

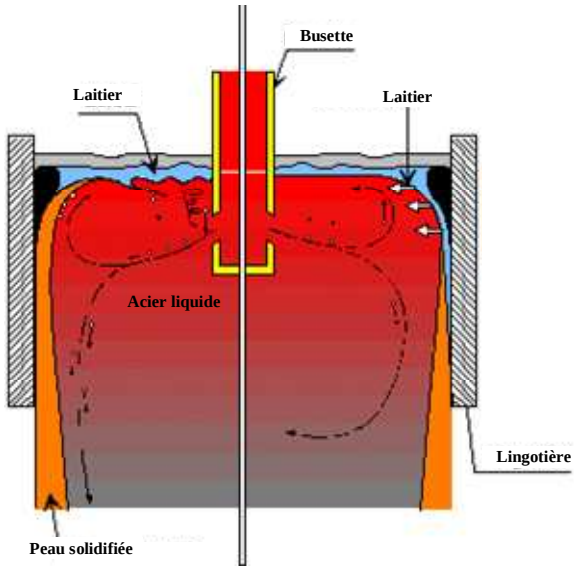

Vue en coupe de la tête de machine de coulée continue

En cours de coulée, il est d'usage d'injecter de l'argon au niveau de la busette submergée pour empêcher le bouchage de son siège et réduire les entrées d'air par aspiration à travers ses parois.
Le débit de métal est toujours contrôlé par un système à quenouille ou par un système à tiroirs afin de permettre aux opérateurs de faire couler l'acier à la vitesse fixée par la rotation des rouleaux extracteurs et de maintenir un niveau stable en lingotière pour une bonne qualité du produit final. Cette boucle de régulation peut être fortement perturbée par des évènements courants entraînant systématiquement des anomalies sur les brames. En effet, s'il apparaît des variations importantes et rapides autour de la consigne de niveau, il est probable que le laitier, initialement introduit pour conserver les propriétés de l'acier, se retrouve dans l'acier liquide. De plus, les particules présentes en surface et à proximité des parois sont également emprisonnées lors de variations brutales du niveau. Ceci se manifeste sur le produit final sous forme de fissures et de trous. Par ailleurs, il suffit de procéder à une analyse de quelques échantillons du produit défectueux pour mettre en évidence une solidification précoce liée à une forte variation de niveau ou détecter la présence d'inclusions d'alumine. C'est la raison pour laquelle les opérateurs déclassent de manière systématique les barres d'acier obtenues en présence de variations de niveau importantes.

Il est difficile de traiter de manière exhaustive les facteurs qui perturbent le niveau en lingotière. Ils peuvent provenir du procédé lui-même, de la composition du métal, des conditions de coulée et de la configuration choisies ou d'un appareillage spécifique. Ainsi, les perturbations peuvent être classifiées selon leurs origines :

- Perturbations liées à l'hydrodynamique en lingotière
  - ✓ Balancement de jets : ce phénomène se manifeste par un déséquilibre périodique des jets issus des ouïes de la busette qui fait apparaître une dépression de surface à proximité de la busette et qui se propage vers la petite face la plus proche. Cette perturbation est périodique de fréquence proche de 0,17Hz. Son amplitude est d'autant plus importante que le format du produit coulé est grand. Néanmoins, elle peut être atténuée en utilisant des busettes spéciales.
  - ✓ Ondes stationnaires : elles sont la conséquence d'une variation très importante de la vitesse de coulée mais dépendent du régime d'écoulement établi dans la lingotière. Leur bande de fréquence caractéristique semble être située entre 0,65 et 0,85Hz.
  - ✓ Perturbations dues à l'argon : l'injection de l'argon réduit considérablement le bouchage en coulée d'acier. Toutefois, les écoulements diphasiques dans la busette perturbent l'alimentation de la lingotière quand le débit de gaz excède une valeur critique au point de provoquer l'arrachement de laitier de couverture. Par ailleurs, les connexions du réseau d'alimentation en argon jusqu'à l'ensemble busette/quenouille ne sont pas toujours fiables et peuvent expliquer certaines périodes de bouchage.
- Perturbations liées aux organes de contrôle et d'amenée du métal
  - ✓ Bouchage/débouchage : ce phénomène bien connu par les sidérurgistes a été abondamment étudié et est souvent référencé dans la littérature. Il se présente sous la forme de particules qui s'accumulent sur les parois de la busette et se détachent soudainement provoquant un accroissement important du débit entrant dans la lingotière. A l'heure actuelle, plusieurs solutions sont adoptées pour limiter le bouchage comme l'injection de l'argon, la modification de la géométrie de la busette, de son matériau et de la composition chimique de l'acier.
  - ✓ Hauteur du métal dans le répartiteur : ce paramètre détermine la vitesse de coulée de l'acier du répartiteur à la busette. Il intervient dans la définition du gain statique de la boucle de régulation. Il serait judicieux de le maintenir constant, en dehors des phases transitoires, pour éviter que le système bascule vers un autre point de fonctionnement.
- Perturbations liées à l'extraction
  - ✓ Risques de percée : dans certains cas, la peau solidifiée risque de se déchirer, ce qui aura comme conséquence un arrêt complet de la machine. En sortie de la lingotière, les rouleaux sont équipés d'accéléromètres dont le rôle est de déceler un tel risque. La vitesse de coulée est alors ralentie entraînant une montée brutale du niveau en lingotière.
  - ✓ Gonflement : cette perturbation est liée aux défauts de géométrie des rouleaux extracteurs et se manifeste par un mouvement périodique de la peau entre les rouleaux et qui provoque des variations de niveau à la surface de la lingotière. Ainsi, ce phénomène perturbe à la fois l'asservissement de la vitesse des rouleaux extracteurs en bas de machine et la régulation de niveau en lingotière.

Une boucle de régulation efficace doit pouvoir maîtriser et minimiser l'effet de chaque perturbation identifiée dans le système. Les éléments intervenant dans cette boucle sont le régulateur, le capteur de niveau et l'actionneur du débit de métal (systèmes à quenouille ou à tiroirs). Il existe plusieurs types de capteurs à contact avec le métal en fusion (comme les capteurs flotteurs ou à contact électrique) et de capteurs sans contact (capteurs à courants de Foucault, gammamétrie, capteurs optiques ou thermométrie). Plusieurs aspects sont pris en compte dans le choix de la technologie à déployer dans les machines de coulée continue.

Chapitre 2 : Modélisation du procédé

Modèle de commande

Ce chapitre aborde la modélisation mathématique du procédé qui est une étape préliminaire à la synthèse des lois de commande. Nous avons étudié un premier modèle décrivant la dynamique du fluide dans la lingotière et qui est à même de mieux suivre l'évolution de la surface libre d'acier, en particulier, dans le cas d'un écoulement turbulent du métal liquide. Cependant, ce modèle nécessite des ressources en calcul considérables. Par conséquent, nous avons opté pour un modèle plus simple à mettre en œuvre et qui exprime la conservation de la matière à l'intérieur de la lingotière. En effet, dans ce deuxième modèle, le niveau d'acier théorique moyen est donné par l'équation suivante :

$$N = \frac{1}{S}\int (Q_{in} - Q_{out})dt \tag{1}$$

avec :

- Q_{in} : Débit d'acier entrant dans la lingotière ;
- Q_{out} : Débit d'acier sortant de la lingotière ;
- S : Section transversale de la lingotière.

Le débit sortant Q_{out} est fixé à partir de la vitesse d'extraction du produit solidifié v comme suit :

$$Q_{out} = S \cdot v \tag{2}$$

Le débit délivré par la vanne de contrôle Q_{in} est déterminé par la position de la quenouille P et est limité par la section transversale de la busette. La relation suivante est largement reprise par la littérature abordant les problématiques de modélisation :

$$Q_{in}(t) = G_n \cdot P(t - \tau_n) \tag{3}$$

G_n est le gain de la busette et τ_n est un retard introduit pour tenir compte de l'influence de la hauteur de la chute et des écoulements diphasiques dans la busette.
Une boucle de régulation interne, liée à la commande de l'actionneur, a pour rôle de maintenir la quenouille à une position fixée par la loi de commande principale, à l'aide d'un régulateur souvent choisi comme un gain proportionnel. Cette boucle ne sera pas étudiée dans le cadre de cette thèse et sera simplement modélisée par une dynamique du premier ordre :

$$TF_{actionneur} = \frac{1}{1 + \tau_a \cdot s} \tag{4}$$

Le capteur de niveau considéré ici est de type NKK qui mesure, sans contact, un niveau moyen en lingotière et dont la dynamique peut être modélisée par un système du premier ordre (d'après les données du constructeur).
En considérant ainsi tous les éléments de la boucle de régulation, la fonction de transfert du modèle de commande s'exprime de la manière suivante :

$$TF_{modèle}(s) = \frac{G_n e^{-\tau_n \cdot s}}{S \cdot s \cdot (1 + \tau_a \cdot s) \cdot (1 + \tau_s \cdot s)} \tag{5}$$

avec :

- s : Variable de Laplace ;
- τ_a : Constante de temps de l'actionneur ;
- G_n : Gain de la busette ;
- τ_n : Retard de la busette ;
- S : Section de la lingotière ;
- τ_s : Constante de temps du capteur de niveau.

Bouchage

En cours de coulée, il arrive fréquemment que des bouchons constitués principalement d'alumine se créent au niveau du siège de la quenouille, des parois et des ouïes de la busette. Ce bouchage progressif par des éléments non-métalliques peut modifier l'hydrodynamique dans la lingotière et ainsi perturber le niveau de la surface libre d'acier. Il peut même être dissymétrique, ce qui conduit à une différence des niveaux moyens de part et d'autre de la busette.
Au bout d'un certain temps, le système se débouche entraînant une augmentation brutale du débit entrant dans la lingotière et par conséquent une montée soudaine du niveau d'acier dans la lingotière. En cas d'importants débouchages, la boucle de régulation n'est plus en mesure de maintenir un niveau stable, ce qui nécessite de la part de l'opérateur une grande vigilance car le laitier, protégeant la surface libre de l'acier, peut se trouver piégé dans le puits liquide, ce qui peut être à l'origine de défauts de surface de la brame même après laminage.
En l'absence du bouchage, le débit entrant dans la lingotière est déterminé à partir de la position de la quenouille. En revanche, durant le cycle du bouchage/débouchage, le dépôt d'alumine restreint l'écoulement de l'acier liquide dans la busette. Par conséquent, le débit réel est inférieur à la valeur théorique. Cette diminution dans le débit entrant dans la lingotière sera modélisée par un signal exogène d_{clog} comme suit :

$$\begin{aligned} Q_{in} &= G_n \cdot P(t-\tau_n) - d_{clog} \\ \ddot{d}_{clog} &= 0 \end{aligned} \tag{6}$$

La dérivée seconde de d_{clog} est nulle car d'une part la position de la quenouille peut être décrite par une succession de rampes et d'autre part le niveau et la vitesse de coulée sont généralement constants.

Gonflement

Contrairement au cycle du bouchage/débouchage, le phénomène du gonflement se produit sous la lingotière en bas de la machine de coulée mais a une influence sur les variations de niveau en lingotière. La transmission des perturbations du bas de la machine jusqu'au ménisque est assurée par la peau solidifiée et le puits liquide. En effet, ce dernier exerce une pression sur la peau solidifiée dont le profil se voit imposer un mouvement sinusoïdal entre les rouleaux extracteurs, en particulier, lorsque son épaisseur est fine et irrégulière. Les désalignements et les faux ronds d'un ou de plusieurs rouleaux de soutien peuvent également être à l'origine de cette perturbation.
Les fréquences caractéristiques du gonflement appartiennent à la bande de fréquence entre 0,03 et 0,1Hz. Elles sont plus généralement données par les formules suivantes :

$$f_{i,1} = \frac{v}{\lambda_i} \tag{7}$$

$$f_{i,2} = \frac{v}{\pi \cdot D_r} \tag{8}$$

avec:

- v : Vitesse de coulée ;
- λ_i : Distance inter-rouleaux ;
- D_r : Diamètre du rouleau.

Enfin, il convient de signaler que, pour des nuances particulières (aciers ayant une certaine composition chimique), le gonflement peut être éliminé au moyen d'un durcissement du refroidissement secondaire.
En l'absence du gonflement, le débit sortant est fixé par la vitesse de coulée. En revanche, lorsqu'il a lieu durant une séquence de coulée, ce même débit n'est plus constant mais varie au cours du temps selon une loi périodique sinusoïdale.

Par conséquent, l'expression du débit sortant de la lingotière devient :

$$Q_{out} = S \cdot v + d_{bulge}$$

$$\begin{cases} d_{bulge} = d_{bulge1} + d_{bulge2} + \cdots \\ \ddot{d}_{bulge\,i} = -\omega^2_{bulge\,i} \cdot d_{bulge\,i} \\ \omega_{bulge\,i} = 2\pi f_{i,1} \end{cases} \quad (9)$$

où d_{bulge} est un signal exogène à la boucle de régulation modélisant ainsi l'effet du gonflement sur le débit de la machine.

Ondes stationnaires

Les ondes stationnaires sont une autre perturbation périodique qui se manifestent par des variations de niveau de faible amplitude, et qui se propagent à la surface de l'acier liquide dans la lingotière. Leurs fréquences dépendent de la géométrie et des dimensions de la lingotière et appartiennent à la bande de fréquence susceptible d'être amplifiée par la boucle de régulation. Elles sont données par la formule analytique suivante :

$$f_{waves,i} = \frac{1}{2\pi}\sqrt{\frac{g\pi \cdot i}{S_w}} \quad (10)$$

avec :

- S_w : Largeur de la lingotière ;
- g : Constante universelle de gravitation ;
- i : Nombre de nœuds.

L'effet des ondes stationnaires sur le niveau peut être modélisé par un signal exogène d_{waves} comme suit :

$$N = \frac{1}{S}\int (Q_{in} - Q_{out})dt + d_{waves}(t)$$

$$\begin{cases} d_{waves} = d_{waves1} + d_{waves2} + \cdots \\ \ddot{d}_{waves,i} = -\omega^2_{waves,i} \cdot d_{waves,i} \\ \omega_{waves,i} = 2\pi f_{waves,i} \end{cases} \quad (11)$$

La figure suivante donne le schéma bloc du modèle de commande en tenant compte des effets de ces trois perturbations.

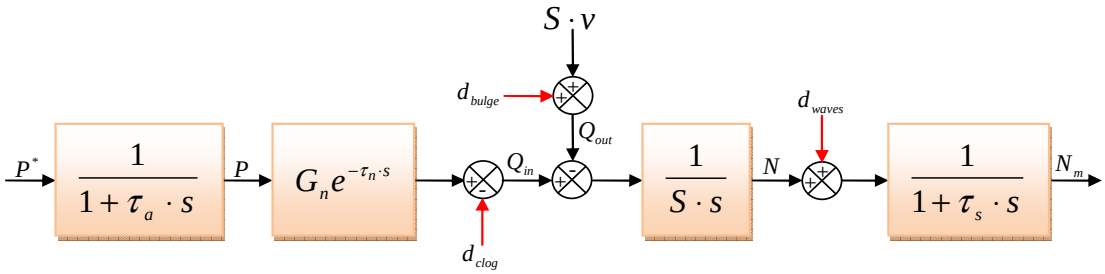

Modèle de commande

Chapitre 3 : Estimation et rejet de perturbations

En préalable à la synthèse des lois de commande abordées dans le chapitre suivant, nous allons présenter un module complémentaire à la boucle de régulation pour estimer et rejeter certaines perturbations. Dans ce qui suit, nous commencerons par identifier le modèle de commande pour permettre son utilisation à la fois par les techniques d'estimation de perturbations et dans la commande du procédé.
Le deuxième volet de ce chapitre concerne les essais sur la maquette hydraulique qui est un outil expérimental permettant de reproduire le procédé de la coulée continue en remplaçant l'acier en fusion par de l'eau. Elle sera utilisée dans ce chapitre à la fois pour valider la fonction de rejet du gonflement et pour déterminer les intervalles de variation des paramètres du modèle de commande en fonction des conditions de coulée.

Identification du modèle de commande

Les paramètres inconnus du modèle de commande dont la fonction de transfert est donnée par l'équation (5) sont le gain G_n et le retard τ_n de la busette d'une part et la constante de temps de l'actionneur τ_a d'autre part. Les autres paramètres de cette fonction sont soit donnés par le constructeur soit fixés par les opérateurs en début de séquence de coulée.
Classiquement la procédure d'identification peut se diviser en deux étapes : application du protocole d'essai et identification des paramètres en employant les algorithmes appropriés.
Aussi, sur site industriel, du fait des impératifs de production et de la nature du procédé, nous sommes contraints de réaliser une identification en boucle fermée. La boucle de régulation est ainsi excitée par des signaux superposés à la consigne de position de la quenouille. Les trois mesures nécessaires aux algorithmes d'identification sont le niveau N, la position de la quenouille P et le débit sortant de la lingotière Q_{out}.
Le signal d'excitation, appliqué autour d'un point de fonctionnement, est une Séquence Binaire Pseudo-Aléatoire SBPA dont les propriétés rappellent celles d'un bruit blanc. Il est réglé en tenant compte du point de fonctionnement et du temps de réponse de la boucle fermée.
La méthode des moindres carrés peut être appliquée directement pour identifier la constante de temps de l'actionneur en utilisant la consigne de position de la quenouille P^* comme entrée de la fonction de transfert à identifier et la position de la quenouille P comme sa sortie selon la formule suivante :

$$P(n) = a_1 \cdot P(n-1) + (1-a_1) \cdot P^*(n-1) \qquad \text{avec :} \qquad a_1 = e^{-\frac{T_s}{\tau_a}} \tag{12}$$

où T_s est la période d'échantillonnage.
Concernant la fonction de transfert de la busette, nous avons opté pour un algorithme basé sur l'erreur de prédiction et appliqué à une représentation d'état structurée où le retard a été approché par une fonction de Laguerre du premier ordre. Pour cela, nous avons besoin de développer un modèle linéaire du processus de la forme :

$$e^{-\tau_n s} \approx \left(\frac{1-\frac{\tau_n}{4}s}{1+\frac{\tau_n}{4}s} \right)^2 \qquad \begin{pmatrix} \dot{N} \\ \dot{x}_1 \\ \dot{x}_2 \end{pmatrix} = \begin{pmatrix} 0 & -1/S & 0 \\ 0 & -8/\tau_n & -16/\tau_n \\ 0 & 1/\tau_n & 0 \end{pmatrix} \begin{pmatrix} N \\ x_1 \\ x_2 \end{pmatrix} + \begin{pmatrix} G_n/S & -1 \\ 16G_n/\tau_n & 0 \\ 0 & 0 \end{pmatrix} \begin{pmatrix} P \\ v \end{pmatrix} \tag{13}$$

où x_1 et x_2 sont deux variables d'état internes à la fonction de Laguerre et n'ont aucune signification physique.

Estimation du bouchage et du gonflement

Le but de ce paragraphe est de présenter un nouvel outil de diagnostic de l'état des perturbations, en particulier, du bouchage et du gonflement, en se servant des signaux de mesures accessibles que sont la position de la quenouille, le niveau mesuré de l'acier liquide en lingotière et la vitesse d'extraction. En faisant référence aux résultats présentés dans le chapitre 2, il s'agit plus précisément d'estimer les allures des deux signaux d_{clog} et d_{bulge} modélisant respectivement l'effet du bouchage et du gonflement sur la boucle de régulation. Pour cela, nous avons développé un observateur global d'état qui admet pour entrées les signaux mesurés et dont deux composantes du vecteur d'état sont d_{clog} et d_{bulge}.

Dans le cas où le gonflement est décrit seulement par deux fréquences (le résultat pouvant se généraliser à un nombre plus grand de fréquences), le niveau d'acier est donné par l'équation suivante :

$$S\dot{N} = \underbrace{G_n\ P(t-\tau_n) - d_{clog}(t)}_{Q_{in}} - \underbrace{(S\cdot v + d_{bulge}(t))}_{Q_{out}} \quad \text{avec} \quad \begin{cases} \ddot{d}_{clog} = 0 \\ d_{bulge} = d_{bulge1} + d_{bulge2} \\ \ddot{d}_{bulge\ i} = -\omega^2_{bulge\ i}\cdot d_{bulge\ i} \end{cases} \tag{14}$$

Dans cette équation, la dynamique du capteur de niveau a été négligée car sa constante de temps est relativement faible comparée aux autres constantes de temps de la boucle de régulation.
Si l'analyse spectrale du niveau fait apparaître d'autres fréquences, il suffit de modifier le vecteur d'état en y incluant deux variables d'état par fréquence détectée (correspondant respectivement à $d_{bulge\ i}$ et à sa dérivée).
On obtient une représentation d'état mise sous sa forme usuelle :

$$\begin{cases} \dot{X} = A_{cb}\,X + B_{cb}\,U \\ Y = N = C_{cb}\,X \end{cases}$$

$$X^T = \begin{pmatrix} N & d_{clog} & \dot{d}_{clog} & d_{bulge1} & \dot{d}_{bulge1} & d_{bulge2} & \dot{d}_{bulge2} & q_p \end{pmatrix} \qquad q_p(t) = G_n P(t-\tau_n) + G_n P(t) \qquad U^T = \begin{pmatrix} P & v \end{pmatrix}$$

$$A_{cb} = \begin{pmatrix} 0 & -1/S & 0 & -1/S & 0 & -1/S & 0 & 1/S \\ 0 & 0 & 1 & 0 & 0 & 0 & 0 & 0 \\ 0 & 0 & 0 & 0 & 0 & 0 & 0 & 0 \\ 0 & 0 & 0 & 0 & 1 & 0 & 0 & 0 \\ 0 & 0 & 0 & -\omega^2_{bulge1} & 0 & 0 & 0 & 0 \\ 0 & 0 & 0 & 0 & 0 & 0 & 1 & 0 \\ 0 & 0 & 0 & 0 & 0 & -\omega^2_{bulge2} & 0 & 0 \\ 0 & 0 & 0 & 0 & 0 & 0 & 0 & -2/\tau_n \end{pmatrix} \quad B_{cb} = \begin{pmatrix} -G_n/S & -1 \\ 0 & 0 \\ 0 & 0 \\ 0 & 0 \\ 0 & 0 \\ 0 & 0 \\ 0 & 0 \\ 4G_n/\tau_n & 0 \end{pmatrix} \quad C_{cb}^T = \begin{pmatrix} 1 \\ 0 \\ 0 \\ 0 \\ 0 \\ 0 \\ 0 \\ 0 \end{pmatrix} \tag{15}$$

Ce système est complètement observable car sa matrice d'observabilité est de rang plein. La représentation d'état continue de l'observateur de Luenberger est alors de la forme :

$$\dot{\hat{X}} = (A_{cb} - K_{cb}\cdot C_{cb})\hat{X} + B_{cb}\,U + K_{cb}\,N \tag{16}$$

où K_{cb} est le gain de l'observateur.
Cette technique d'observation a été validée d'une part en simulation et d'autre part en vérifiant le bon comportement de l'observateur lorsqu'il est soumis à des signaux prélevés sur site.
Si l'un des deux phénomènes se résorbe complètement, le signal correspondant estimé sera toujours nul. Il serait alors possible de simplifier le vecteur d'état du système en supprimant les composantes de la perturbation inexistante.

Rejet du gonflement

Etant donné l'estimation de l'effet du gonflement, modélisé par d_{bulge}, et de sa dérivée, l'objectif de cette section est de proposer un module complémentaire à la boucle principale de régulation à même d'annuler cet effet sur le niveau. Il comporte, en plus de l'observateur, deux autres éléments pour prédire l'estimation à l'instant $t+\tau_n$ et calculer la correction de la commande à appliquer.
Nous commençons d'abord par réécrire la représentation continue de l'observateur comme suit :

$$\dot{\hat{X}} = (A_{cb} - K_{cb}\cdot C_{cb})\hat{X} + B^a_{cb}\,U^a$$

$$B^a_{cb} = \begin{pmatrix} B_{cb} & K_{cb} \end{pmatrix} \qquad U^a = \begin{pmatrix} P \\ v \\ N \end{pmatrix} \tag{17}$$

En résolvant cette équation différentielle, la prédiction du vecteur d'état à l'instant $t+\tau_n$ peut être obtenue par :

$$\hat{X}(t+\tau_n) = M_{cb} \cdot \hat{X}(t) + \hat{X}_0(t)$$
$$M_{cb} = e^{(A_{cb}-K_{cb}\cdot C_{cb})\cdot\tau_n} \qquad \hat{X}_0(t) = \int_t^{t+\tau_n} e^{(A_{cb}-K_{cb}\cdot C_{cb})(t+\tau_n-\tau)} B_{cb}^a U^a(\tau) d\tau \tag{18}$$

Finalement, les prédictions de $\hat{d}_{bulge}(t)$ à l'instant $t+\tau_n$ et de sa dérivée sont données par :

$$\hat{d}_{bulge}(t+\tau_n) = C_{\hat{d}} \cdot \hat{X}(t+\tau_n) \qquad \dot{\hat{d}}_{bulge}(t+\tau_n) = C_{\dot{\hat{d}}} \cdot \hat{X}(t+\tau_n)$$
$$C_{\hat{d}} = \begin{pmatrix} 0 & 0 & 0 & 1 & 0 & 1 & 0 & 0 \end{pmatrix} \qquad C_{\dot{\hat{d}}} = \begin{pmatrix} 0 & 0 & 0 & 0 & 1 & 0 & 1 & 0 \end{pmatrix} \tag{19}$$

Ces prédictions sont indispensables pour calculer la correction de la commande qui, lorsqu'elle sera appliquée au procédé, sera probablement retardée à travers le bloc représentant la busette.
Comme l'actionneur a été modélisé par une fonction de transfert du premier ordre, la correction de la commande $u_{bulge}(t)$ peut être calculée en inversant cette fonction de transfert de la façon suivante :

$$TF_{actionneur} = \frac{1}{1+\tau_a \cdot s} \qquad u_{bulge}(t) = \frac{\hat{d}_{bulge}(t+\tau_n)}{G_n} + \frac{\tau_a}{G_n}\dot{\hat{d}}_{bulge}(t+\tau_n) \tag{20}$$

Les trois composants de la structure de compensation du gonflement étant désormais décrits, sa validation expérimentale sur maquette hydraulique fait l'objet du prochain paragraphe.
Il est important de noter, en fin de ce paragraphe, que ce module complémentaire ne nécessite aucune modification de la structure de commande actuellement en service et peut, dès lors, être facilement intégré dans les automates de contrôle des machines de coulée.

Maquette hydraulique

Même si les propriétés de l'eau sont très différentes de celles de l'acier, la maquette hydraulique est un outil expérimental installé généralement dans les centres de recherche de la sidérurgie et fréquemment utilisé d'une part par les aciéristes pour mieux comprendre l'hydrodynamique du fluide dans la lingotière et d'autre part par les automaticiens afin de tester les nouvelles stratégies de régulation de niveau ainsi que l'instrumentation associée avant de les déployer dans les usines.
La figure suivante représente la maquette hydraulique et sa lingotière.

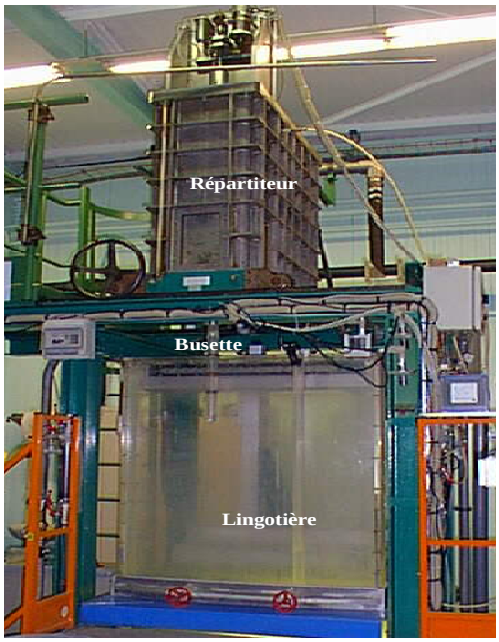

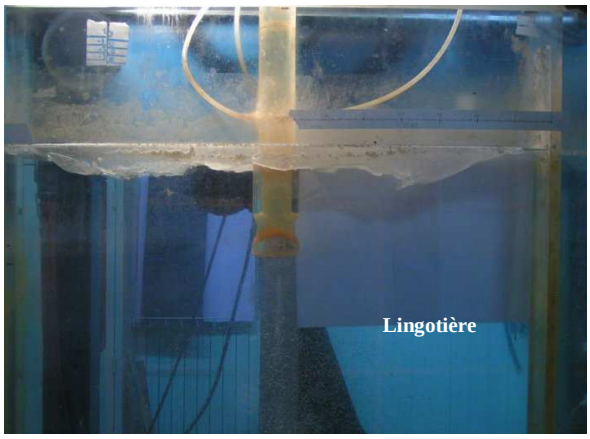

Maquette hydraulique

Après remplissage du répartiteur et de la lingotière, la circulation de l'eau dans la maquette hydraulique est assurée par une pompe qui injecte l'eau accumulée au fond de la lingotière dans le répartiteur. Le débit sortant de la lingotière est ainsi fixé à partir de la vitesse de la pompe.
La maquette est équipée d'un capteur à ultrasons pour mesurer le niveau en lingotière et d'un capteur LVDT pour mesurer la position de la quenouille. Enfin, la maquette permet également aux utilisateurs de modifier la position du répartiteur, la largeur de la lingotière et la position du capteur de niveau.
Dans le cadre de cette thèse, la maquette hydraulique a été utilisée d'une part pour valider la structure de compensation de l'effet du gonflement sur le niveau et d'autre part pour déterminer les intervalles de variation du gain et du retard du modèle de commande en fonction de la configuration et du point de fonctionnement choisis. Ce dernier point est indispensable pour montrer la nécessité de développer des lois de commande robustes pour ce type de procédé.

Validation de la structure de compensation du gonflement sur maquette

La structure de compensation de l'effet du gonflement sur le niveau, décrite dans ce chapitre, a été validée expérimentalement sur la maquette hydraulique.
Le phénomène du gonflement a été simulé en faisant varier le débit sortant de la lingotière suivant une fonction sinusoïdale de fréquence 0,05Hz injectée à partir de l'instant 200s. La structure de compensation a été activée pendant les intervalles de temps entre 400 et 600s et entre 800 et 1000s. La figure suivante présente les résultats obtenus :

- La première courbe représente le niveau ;
- La deuxième est la correction de la commande qui provient de la structure de compensation et qui se rajoute à la commande fournie par le régulateur principal ;
- La troisième courbe représente l'effet du gonflement sur le débit sortant ;
- La dernière est la position de la quenouille.

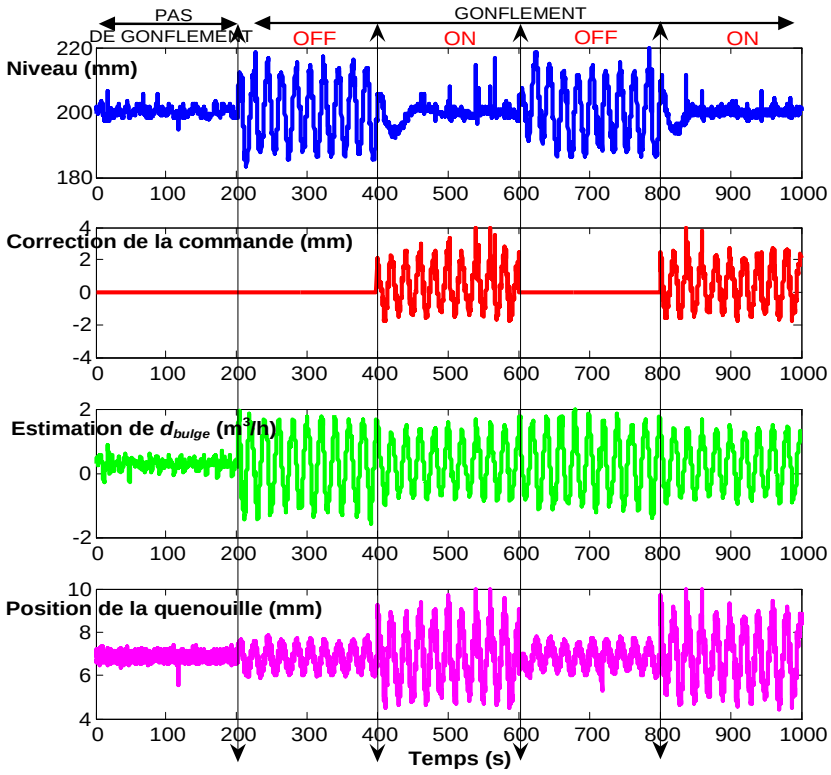

Signaux enregistrés durant la séquence de validation

On observe que lorsque la compensation est activée, les variations de niveau générées par le gonflement ont été réduites de ±18mm à moins de ±1mm. L'observateur fonctionne correctement puisqu'il reproduit avec une bonne précision le comportement de la perturbation sinusoïdale injectée. On peut donc conclure que cette structure permet de supprimer l'effet du gonflement sur le niveau tout en fournissant une estimation de son effet sur le débit sortant de la lingotière qui permettra de surveiller l'évolution de ce phénomène en ligne.

Intervalles de variation du gain et du retard en fonction des conditions de coulée

La maquette hydraulique a été également utilisée pour comprendre comment évoluent les valeurs du gain et du retard du modèle de commande en fonction de la configuration et du point de fonctionnement choisis. Plusieurs enregistrements ont été réalisés avec une busette propre ou légèrement bouchée et en faisant varier le débit d'eau (c'est-à-dire la vitesse de la pompe), le débit d'air, la position du capteur de niveau, la profondeur d'immersion de la busette et le niveau d'eau dans le répartiteur. Le gain et le retard ont été identifiés à chaque fois par un algorithme basé sur l'erreur de prédiction en utilisant une représentation d'état structurée où le retard a été approché par une fonction de Laguerre du premier ordre.
Nous avons démontré que le gain peut varier entre 0,15 et 0,2L$\cdot s^{-1} \cdot mm^{-1}$ et le retard peut varier entre 0,28 et 0,89s mais peut cependant atteindre une valeur élevée de 2,16s en cas de bouchage.
Ces essais ont permis également de mettre en évidence les liens suivants entre les paramètres identifiés et les conditions de coulée :

- ✓ Le gain est indépendant de la position du capteur de niveau, du débit d'air et de la profondeur d'immersion de la busette ;
- ✓ Le gain augmente avec le débit d'eau et le niveau d'eau dans le répartiteur ;
- ✓ Le retard est indépendant du niveau d'eau dans le répartiteur et de la profondeur d'immersion de la busette ;
- ✓ Le retard diminue en augmentant le débit d'eau ou d'air.

Chapitre 4 : Étude comparative des lois de commande non-adaptatives

Contrairement aux techniques de rejet de perturbations développées dans le chapitre 3 et qui opèrent comme un module complémentaire à la boucle de régulation, cette section vise à mettre en avant l'apport de certaines lois de commande utilisées comme unique régulateur principal de niveau en lingotière de coulée continue. Pour cela, nous présenterons, dans un premier temps, la commande PID telle qu'elle est implantée dans une usine et qui servira de référence par rapport à laquelle seront comparées toutes les autres lois de commande à savoir les deux commandes prédictives PFC et GPC, le prédicteur de Smith et ses versions modifiées et enfin la commande par modèle interne IMC.
Le régulateur PID possède une action proportionnelle, intégrale et dérivée comme le montre sa fonction de transfert continue :

$$TF_{PID}(s) = K_{PID}\left(1+\frac{1}{T_i s}+\frac{T_d s}{1+\frac{T_d}{\beta}s}\right) \qquad (21)$$

avec : $K_{PID}=0{,}38 \quad T_i=9\text{s} \quad T_d=0{,}2\text{s} \quad \beta=10$

La simplicité d'implantation du PID fait que cette technique est très largement utilisée pour la régulation de niveau mais aussi dans les schémas de contrôle des autres procédés sidérurgiques. Néanmoins, plusieurs simulations ont révélé qu'elle ne permet pas de satisfaire les spécifications contraignantes en termes de rejet de perturbations, en particulier, du gonflement et du bouchage à des vitesses de coulée et des largeurs de lingotière variées. Il convient à présent de déterminer quel serait le niveau de performances que l'on peut raisonnablement atteindre avec d'autres lois de commande non-adaptatives.

Commande Prédictive Fonctionnelle PFC

La commande prédictive PFC, introduite vers la fin des années 80 et faisant partie des commandes à base de modèle, connaît depuis de nombreuses années un réel essor dans de nombreuses applications et notamment lorsque la trajectoire à suivre dans le futur est connue à l'avance. Avant d'expliquer les principes élémentaires de la commande prédictive fonctionnelle, il serait utile de rappeler les concepts généraux communs à toutes les formes de la commande prédictive :

- Obtention d'un modèle numérique de procédé capable de prédire le comportement futur du système sur un horizon de prédiction en fonction d'un scénario de commande ;
- Minimisation d'un critère quadratique à horizon fini portant sur les erreurs de prédiction futures ;
- Elaboration d'une séquence de commandes futures dont seule la première valeur est appliquée sur le modèle et sur le procédé ;
- Réitération des étapes précédentes à la période d'échantillonnage suivante selon le principe de l'horizon fuyant.

Le principe de la commande prédictive fonctionnelle PFC se structure autour de quatre notions essentielles que sont le modèle de prédiction, la trajectoire de référence, la structure de la commande et la compensation de l'erreur processus-modèle.
Dans le cas de la régulation de niveau, l'idée de base de la commande prédictive fonctionnelle PFC est de développer un modèle numérique de prédiction afin d'être en mesure de prédire le comportement futur du niveau en lingotière. Comme ce processus est intégrateur et comprend une dynamique du premier ordre, il convient de décomposer le terme intégrateur en deux processus du premier ordre en parallèle.

La sortie du modèle décomposée N_{PFC} est donnée par :

$$N_{PFC} = N_{PFC1} + N_{PFC2} + N_{PFC3}$$

$$\begin{cases} N_{PFC1}(n) = a_1 \cdot N_{PFC1}(n-1) + (1-a_1) \cdot K_1 \cdot P^*(n-1) \\ N_{PFC2}(n) = a_2 \cdot N_{PFC2}(n-1) + (1-a_2) \cdot K_2 \cdot P^*(n-1) \\ N_{PFC3}(n) = a_2 \cdot N_{PFC3}(n-1) + (1-a_2) \cdot N_a(n-1) \\ \\ N_a(n) = N(n+r) \end{cases} \quad \text{avec:} \quad \begin{cases} a_1 = e^{-\frac{T_s}{\tau_a}} \\ a_2 = e^{-\frac{T_s}{\tau}} \\ \tau = \dfrac{TRBF}{3} \\ K_2 = \dfrac{\tau^2}{\tau - \tau_a} \dfrac{G_n}{S} \\ K_1 = \tau \cdot \dfrac{G_n}{S} - K_2 \\ r = \left\lfloor \dfrac{\tau_n}{T_s} \right\rfloor \end{cases} \tag{22}$$

où τ_a est la constante de temps de l'actionneur, G_n et τ_n sont le gain et le retard du processus, S est la section de la lingotière, T_s est la période d'échantillonnage et $TRBF$ est le temps de réponse en boucle fermée.
La deuxième étape est de spécifier la trajectoire que l'on souhaite voir la sortie du processus suivre jusqu'à atteindre la valeur de la consigne N^*. Pour les processus comprenant un retard pur, la trajectoire de référence S_{ref} est souvent présentée sous la forme suivante :

$$\begin{cases} N^* - S_{ref}(n+h) = (N^* - N_a(n)) \cdot \mu^h \\ \mu = e^{\frac{-3T_s}{TRBF}} \end{cases} \tag{23}$$

La commande est ensuite calculée en recherchant une coïncidence en un certain nombre de points entre la trajectoire de référence et la sortie prédite que nous avons estimée en faisant une prédiction plate de la différence objet-modèle. La commande est exprimée à l'aide d'un seul échelon utilisé comme une fonction de base. L'équation de la commande obtenue à l'issue de ce calcul dont certaines étapes ont été omises par souci de concision et pour un seul point de coïncidence, est alors :

$$P^*(n) = \theta_w \cdot N^* - \theta_N \cdot N(n) + \theta_1 \cdot N_{PFC1}(n) + \theta_2 \cdot N_{PFC2}(n) + \theta_2 \cdot N_{PFC3}(n) + \theta_a \cdot N_a(n)$$

$$\begin{cases} \theta_w = \dfrac{1-\mu^h}{\alpha} \qquad \theta_1 = \dfrac{1-a_1^h}{\alpha} \qquad \theta_2 = \dfrac{1-a_2^h}{\alpha} \qquad \theta_N = \dfrac{1}{\alpha} \qquad \theta_a = \dfrac{a_2^h + \mu^h - 1}{\alpha} \\ \alpha = K_1 \cdot (1-a_1^h) + K_2 \cdot (1-a_2^h) \end{cases} \tag{24}$$

Finalement, les paramètres de cette équation ont été réglés afin d'obtenir la même fréquence de coupure qu'avec le PID c'est-à-dire $1{,}06 \text{rad} \cdot \text{s}^{-1}$. Nous avons constaté au travers de plusieurs simulations que la loi de commande PFC est plus performante surtout pour rejeter les basses fréquences du gonflement. Toutefois, cette bonne performance conduit à une dégradation des marges de phase et de retard.

Commande Prédictive Généralisée GPC

La commande prédictive généralisée GPC repose sur les mêmes points fondamentaux que la commande prédictive fonctionnelle PFC.
Afin de prédire le comportement de la sortie du processus sur un horizon de prédiction fini, le niveau en lingotière $N_{GPC}(n+j)$ est décomposé en réponse libre et réponse forcée comme suit :

$$N_{GPC}(n+j) = \underbrace{F_j(q^{-1}) \cdot N(n) + H_j(q^{-1}) \cdot \Delta P^*(n-1)}_{\text{réponse libre}} + \underbrace{G_j(q^{-1}) \cdot \Delta P^*(n+j-1) + J_j(q^{-1}) \cdot \xi(n+j)}_{\text{réponse forcée}} \tag{25}$$

avec : $\Delta(q^{-1}) = 1 - q^{-1}$
où ξ est un bruit blanc centré.

Les polynômes inconnus F_j, G_j, H_j et J_j sont les solutions uniques des équations de Diophante :

$$\begin{cases} \Delta(q^{-1}) \cdot A_{GPC}(q^{-1}) \cdot J_j(q^{-1}) + q^{-j} \cdot F_j(q^{-1}) = 1 \\ G_j(q^{-1}) + q^{-j} \cdot H_j(q^{-1}) = B_{GPC}(q^{-1}) \cdot J_j(q^{-1}) \end{cases} \quad (26)$$

Le prédicteur optimal est obtenu en considérant que la meilleure prédiction du bruit est sa moyenne supposée nulle ici :

$$N_{GPC}(n+j) = F_j(q^{-1}) \cdot N(n) + H_j(q^{-1}) \cdot \Delta P^*(n-1) + G_j(q^{-1}) \cdot \Delta P^*(n+j-1) \quad (27)$$

La loi de commande GPC est enfin calculée en minimisant le critère quadratique suivant qui prend en compte les erreurs de modélisation futures et les carrés des incréments de commande futurs :

$$\begin{cases} J_{GPC}(n) = \sum_{j=N_1}^{N_2} (N_{GPC}(n+j) - N^*)^2 + \eta \cdot \sum_{j=1}^{N_u} (\Delta P^*(n+j-1))^2 \\ \Delta P^*(n+j) = 0 \quad \text{for} \quad j \geq N_u \end{cases} \quad (28)$$

avec :

- N_1 : Horizon de prédiction minimal ;
- N_2 : Horizon de prédiction maximal ;
- N_u : Horizon de prédiction sur la commande ;
- η : Coefficient de pondération sur la commande.

Ces quatre paramètres de réglage ont été ensuite ajustés afin d'obtenir une fréquence de coupure de la boucle ouverte voisine de $1{,}06 \text{rad} \cdot \text{s}^{-1}$ qui est celle obtenue avec le PID ou la commande prédictive PFC. Nous avons voulu rendre ce critère de performance commun à toutes les lois de commande dans le but de réaliser des comparaisons significatives. Nous avons constaté que la commande GPC est encore plus performante que la commande PFC en termes de rejet du gonflement mais avec une légère dégradation des marges de robustesse.

Prédicteur de Smith

Dans le cas des systèmes comprenant un retard comme celui de la régulation de niveau, l'effet néfaste du retard sur la stabilité peut être contré par le prédicteur de Smith qui rejette le retard hors de la boucle de régulation. Classiquement la fonction de transfert du modèle de commande est représentée par le produit d'une fraction rationnelle propre et d'un opérateur à retard :

$$TF_{modèle}(s) = H_0(s) \cdot e^{-\tau_n \cdot s} \quad (29)$$

Le prédicteur de Smith consiste à introduire un deuxième retour comprenant le bloc $H_0(s) \cdot (1 - e^{-\tau_n \cdot s})$ non pas à partir du niveau mesuré mais de la consigne de position de la quenouille.
L'équation caractéristique du système bouclé est donnée par :

$$\frac{N}{N^*} = \frac{C(s) \cdot H_0(s)}{1 + C(s) \cdot H_0(s)} e^{-\tau_n \cdot s} \quad (30)$$

où $C(s)$ est le régulateur principal.
Le correcteur équivalent intervenant dans la structure réelle prend la forme suivante :

$$TF_{SP}(s) = \frac{C(s)}{1 + C(s) \cdot H_0(s) \cdot (1 - e^{-\tau_n \cdot s})} \quad (31)$$

D'autre part, la fonction de rejet du gonflement devient :

$$\frac{N}{Q_{out}} = \frac{C(s) \cdot H_0(s) \cdot (e^{-\tau_n \cdot s} - 1) - 1}{S \cdot s \cdot (1 + C(s) \cdot H_0(s))} \quad (32)$$

On peut vérifier que l'erreur statique en réponse à un échelon de consigne est nulle car le système est de classe 1. Cependant, l'erreur statique en réponse à un échelon de perturbation ne peut pas l'être quelle que soit la nature du régulateur $C(s)$. D'autres versions modifiées du prédicteur de Smith sont citées dans la littérature pour surmonter cette difficulté. L'objet du paragraphe suivant est d'examiner celle proposée par Aström.

Version modifiée du prédicteur de Smith

Le problème de l'erreur statique qui résulte de la version initiale du prédicteur de Smith, fait que cette structure est plutôt utilisée pour les systèmes stables.
Pour les autres systèmes, en particulier, ceux comportant une intégration comme le nôtre, il est cependant recommandé d'envisager d'autres versions modifiées du prédicteur de Smith.
La structure proposée par Aström permet de piloter la réponse temporelle indépendamment du rejet de la perturbation. Ceci est rendu possible au moyen de deux correcteurs $C(s)$ et $M(s)$. Plus précisément, la réalisation d'Aström consiste en la mise en œuvre d'un prédicteur de Smith classique avec une modification sur la différence processus-modèle en vue de la compenser.
Dans le cas où nous disposons d'une bonne connaissance de la valeur du retard pur, l'équation caractéristique du système bouclé est toujours donnée par la relation (30) montrant que le retard pur n'interfère pas avec la régulation même s'il est toujours présent sur la sortie.
Cette structure induit une fonction de rejet de perturbation du type :

$$\frac{N}{Q_{out}} = \frac{-1}{S \cdot s \cdot (1 + M \cdot H_0 \cdot e^{-\tau_n \cdot s})} \tag{33}$$

L'intérêt qui se dégage de cette version modifiée du prédicteur de Smith est que le rejet du gonflement peut être réglé indépendamment du suivi de consigne. En effet, l'introduction d'un deuxième correcteur $M(s)$ permet de disposer de plus de degrés de liberté.
Dans le cadre de cette thèse, cette version modifiée du prédicteur de Smith a été utilisée pour améliorer la fonction de rejet du gonflement et garantir une marge de retard fixée à l'avance.
Pour résoudre ce problème et fournir aux utilisateurs non-spécialistes des règles simples, les spécifications ont été reformulées comme un problème de synthèse H_∞ où deux fonctions de pondération ont été introduites. Le premier filtre a été choisi pour imposer un gabarit à la fonction de rejet du gonflement comme suit :

$$W_1^{-1} = K_{w1} \frac{1 + T_{w1} \cdot s}{1 + a_{w1} T_{w1} \cdot s} \qquad \text{avec :} \qquad a_{w1} < 1 \tag{34}$$

Le deuxième filtre a été réglé à l'aide du théorème du petit gain qui a conduit à l'expression suivante :

$$W_2(s) = K_{w2} \frac{2\Delta\tau_n \cdot s}{1 + \Delta\tau_n \cdot s} \qquad \text{avec :} \qquad K_{w2} > 1 \tag{35}$$

où $\Delta\tau_n$ est la marge de retard souhaitée.

L'optimisation de ces deux pondérations par la méthode des essaims particulaires a permis d'améliorer le rejet du gonflement sur toute sa bande de fréquence, par rapport aux performances des autres lois de commande étudiées, tout en garantissant des marges de robustesse tout à fait satisfaisantes.
Le correcteur $M(s)$, ainsi obtenu, peut également se mettre sous la forme PID, ce qui facilitera son implantation dans les automates industriels.

Commande par Modèle Interne IMC

Dans un schéma de commande par modèle interne, le correcteur est mis en cascade avec le modèle interne. Son réglage dans le cas de la régulation de niveau ne peut se faire de la façon classique qui consiste à choisir le correcteur comme étant le produit des composantes inversibles du modèle interne et d'un filtre passe-bas sous peine de générer une erreur statique. Quelques modifications de ce schéma initial, rapportées dans la littérature, ont été appliquées sans pour autant atteindre le niveau de performance escompté.

Chapitre 5 : Contrôle robuste adaptatif – Architecture RMMAC

Au chapitre 3, nous avons démontré, à l'aide de la maquette hydraulique, que le gain et le retard du modèle de commande changent de valeurs en fonction de la configuration de la machine et des conditions de coulée. Nous avons déjà souligné que les correcteurs classiques comme ceux étudiés dans le chapitre 4 ne sont pas capables de garantir de bonnes performances notamment en termes de rejet de perturbations sur de larges domaines d'incertitudes sur les paramètres. Par ailleurs, il serait impossible d'atteindre certains points de fonctionnement avec de telles stratégies de régulation. Dans ce chapitre, nous allons présenter une approche efficace basée sur une architecture robuste adaptative multi-modèles baptisée RMMAC (Robust Multiple-Model Adaptive Control) permettant de maximiser les performances en cas de fortes incertitudes sur les paramètres en découpant l'intervalle d'incertitude initial en sous-intervalles et en synthétisant les régulateurs locaux associés qui assurent un niveau de performance minimal fixé à l'avance. De plus, cette structure contribue également à suivre les variations des paramètres incertains grâce à son dispositif d'identification en temps réel.

Architectures multi-modèles d'estimation MMAE

La structure multi-modèles d'estimation MMAE (Multiple-Model Adaptive Estimation) a été proposée pour estimer l'état d'un système non-linéaire quelconque ou pour tenir compte des incertitudes paramétriques. Elle est constituée d'une part d'un ensemble de filtres de Kalman qui estiment l'état du système en différents points de fonctionnement $\hat{x}_k(t)$ (k étant l'indice du modèle) et d'autre part d'un module baptisé PPE (Posterior Probability Evaluator) qui donne la possibilité de calculer la probabilité $P_k(t)$ que le système appartienne à un des modèles. Ces deux grandeurs sont ensuite liées par la relation suivante afin de calculer une estimation globale de l'état du système :

$$\hat{x}(t) = \sum_{k=1}^{n} P_k(t) \cdot \hat{x}_k(t) \tag{36}$$

où n est le nombre de modèles de la structure MMAE et t est le temps discret.

Chaque modèle k est représenté classiquement par le système d'équations :

$$\begin{cases} x_k(t+1) = A_k x_k(t) + B_k u(t) + L_k w_{WN}(t) \\ y_k(t) = C_k x_k(t) + v_{WN}(t) \end{cases} \tag{37}$$

avec :

- w_{WN} : Bruit blanc gaussien d'état ;
- v_{WN} : Bruit blanc gaussien de mesure.

A partir de ce modèle, un filtre de Kalman discret sera développé pour calculer à la fois une estimation locale de l'état du système $\hat{x}_k(t)$ et un résidu $r_k(t)$ qui sera utilisé par la fonction PPE. Le résidu (ou l'innovation) est la différence entre la sortie mesurée et celle prédite par le filtre de Kalman.
Ainsi, soit H_k une variable aléatoire modélisant le fait que c'est le modèle k qui génère la sortie du processus $N(t)$:

$$H_k \in \{H_1, H_2, \cdots, H_n\} \tag{38}$$

Les probabilités $P_k(t)$ sont définies de façon à satisfaire l'égalité suivante :

$$P_k(t) \geq 0, \quad \sum_{k=1}^{n} P_k(t) = 1$$

$$\begin{cases} P_k(0) = \text{Prob}(H = H_k) \\ P_k(t) = \text{Prob}(H = H_k \,|\, u(0) \cdots u(t-1), y(1) \cdots y(t)) \end{cases} \tag{39}$$

Elles sont calculées en ligne grâce à la formule récursive générale suivante implantée dans la fonction PPE :

$$\begin{cases} P_k(t+1) = \dfrac{\dfrac{1}{\sqrt{2\pi \det(S_k)}} e^{-\frac{1}{2} r_k(t+1)\cdot S_k^{-1}\cdot r_k(t+1)}}{\sum_{i=1}^{n} \dfrac{P_i(t)}{\sqrt{2\pi \det(S_i)}} e^{-\frac{1}{2} r_i(t+1)\cdot S_i^{-1}\cdot r_i(t+1)}} P_k(t) \\ P_k(0) = \dfrac{1}{n} \end{cases} \quad (40)$$

où S_k est la covariance du résidu $r_k(t)$.

Nous avons considéré dans cette équation que les probabilités initiales $P_k(0)$ sont toutes égales pour ne privilégier aucun modèle au départ.
Cette formule est valide uniquement si la vraie valeur du paramètre incertain est celle d'un des points de fonctionnement initialement fixés. Si tel n'est pas le cas, les probabilités doivent converger vers le modèle le plus proche. Dans la méthodologie RMMAC, que nous allons décrire dans ce chapitre et appliquer à la régulation de niveau, cette convergence est assurée si ces points nominaux ont été choisis en utilisant la notion de distance BPM (Baram Proximity Measure).

Architecture RMMAC pour une incertitude sur le retard

La commande adaptative multi-modèles robuste RMMAC est une technique qui a été introduite au début des années 2000 par M. Athans et S. Fekri. Dans la littérature, nous pouvons dénombrer de nombreux types de structures multi-modèles dont on peut distinguer deux classes principales. L'une est dédiée à la commande des systèmes tandis que l'autre est destinée à l'estimation de ses états. L'approche RMMAC fait partie des commandes multi-modèles mais présente l'avantage d'être aussi une extension de l'architecture multi-modèles d'estimation MMAE (voir figure suivante).

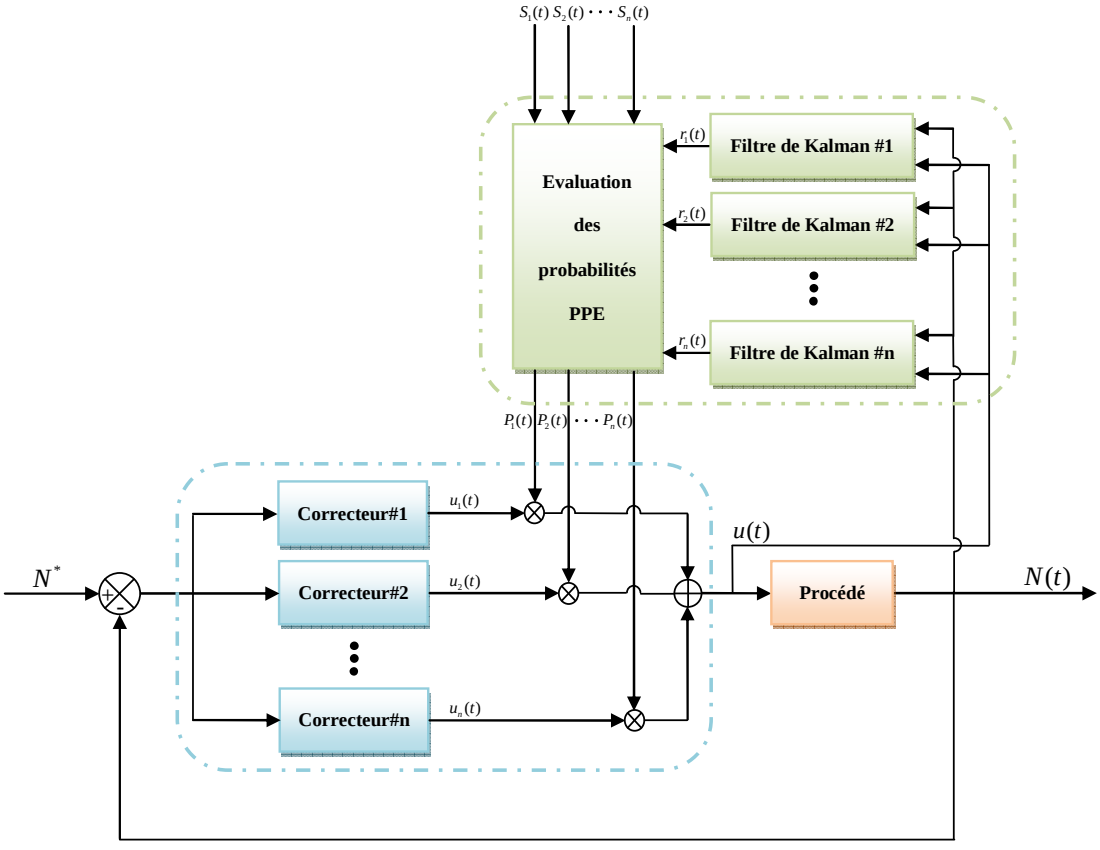

Architecture RMMAC

L'architecture RMMAC est basée sur de multiples modèles autour de différents points de fonctionnement. L'interpolation de ces modèles locaux est réalisée à l'aide de la fonction PPE déjà présentée dans ce chapitre.
Comme dans le problème de la régulation de niveau, des incertitudes affectent les valeurs de plusieurs paramètres réels, il serait particulièrement souhaitable d'implanter RMMAC pour permettre aux opérateurs de changer de conditions opératoires sans avoir de modifications à apporter aux réglages initiaux.
Considérons à présent le modèle du processus représenté par le système d'équations :

$$\begin{cases} \dot{x} = Ax + Bu \\ y = N = Cx + v_{WN} \end{cases}$$

$$x^T = \begin{pmatrix} N & P & q_p \end{pmatrix} \qquad u^T = \begin{pmatrix} Q_{out} & P^* \end{pmatrix} \qquad q_p(t) = G_n P(t-\tau_n) + G_n P(t) \tag{41}$$

$$A = \begin{pmatrix} 0 & -G_n/S & 1/S \\ 0 & -1/\tau_a & 0 \\ 0 & 4G_n/\tau_n & -2/\tau_n \end{pmatrix} \qquad B = \begin{pmatrix} -1/S & 0 \\ 0 & 1/\tau_a \\ 0 & 0 \end{pmatrix} \qquad C^T = \begin{pmatrix} 1 \\ 0 \\ 0 \end{pmatrix}$$

La mesure du niveau N est entachée d'un bruit blanc additif v_{WN} dont l'intensité est définie par :

$$\mathrm{E}\left(v_{WN}(t) \cdot v_{WN}(t-\tau)\right) = V_{WN} \cdot \delta(\tau) \tag{42}$$

Dans ce qui suit, nous allons appliquer la méthodologie RMMAC en considérant que le retard τ_n et la constante de temps de l'actionneur τ_a sont incertains d'une part et que le gain G_n est constant et connu. Cette dernière hypothèse a été adoptée pour n'avoir à traiter qu'un problème à une seule dimension.
Les paramètres suivants sont fixes :

$$G_n = 1\mathrm{L} \cdot \mathrm{s}^{-1} \cdot \mathrm{mm}^{-1} \qquad S = 0{,}3648\mathrm{m}^2 \qquad V_{WN} = 0{,}01\mathrm{mm}^2 \tag{43}$$

Quant aux paramètres incertains, seules les bornes supérieures et inférieures peuvent être déterminées comme suit :

$$\begin{cases} \tau_n \in [0{,}1\mathrm{s} \;\; 2\mathrm{s}] \\ \tau_a \in [0{,}001\mathrm{s} \;\; 0{,}1\mathrm{s}] \end{cases} \tag{44}$$

Dans un premier temps, nous commençons par définir le critère de performance suivant qui n'est autre que la moyenne du gain de la fonction de rejet du gonflement sur sa bande de fréquence caractéristique :

$$C_{perf} = \frac{\left(\max\limits_{\omega \in [0.03\ 0.1\mathrm{Hz}]} \left| TF_{bulge}(j\omega) \right| + \min\limits_{\omega \in [0.03\ 0.1\mathrm{Hz}]} \left| TF_{bulge}(j\omega) \right| \right)}{2} \tag{45}$$

La première étape consiste à déterminer une borne appelée GNARC (Global Non-Adaptive Robust Compensator) qui représente la performance maximale que l'on peut atteindre en tenant compte des incertitudes des paramètres. L'idée de base est d'utiliser la μ synthèse mixte pour synthétiser un correcteur avec une borne supérieure de μ telle que :

$$\forall \omega \quad \mu_{ub}(\omega) < 1 \tag{46}$$

Par conséquent, le processus est stable en boucle fermée et satisfait les performances imposées. La borne GNARC est ensuite calculée en minimisant le critère (45) jusqu'à ce que la borne supérieure de μ vérifie les inégalités suivantes :

$$\forall \omega \quad 0 < 1 - \mu_{ub}(\omega) < 0{,}01 \tag{47}$$

Les deux filtres suivants ont été utilisés pour la μ synthèse :

$$\begin{cases} W_b(s) = \dfrac{10{,}4 \cdot (s + 0{,}314) \cdot (s + 3{,}14)}{(s + 0{,}0209) \cdot (s + 314)} \\ W_n(s) = 0{,}01 \end{cases} \tag{48}$$

$W_b(s)$ a été introduit pour déterminer les performances sur la bande de fréquence du gonflement tandis que le niveau est pondéré par le filtre $W_n(s)$ afin de générer un bruit blanc de mesure avec une intensité de 0,01.
On peut aussi reformuler le critère de performance comme suit :

$$A_p = \frac{1}{10^{C_{perf}/20}} \tag{49}$$

A_p doit être le plus grand possible pour un meilleur rejet du gonflement.
La deuxième étape consiste à calculer la deuxième borne appelée FNARC (Fixed Non-Adaptive Robust Compensator) qui représente la performance maximale que l'on peut atteindre si le paramètre incertain, ici le retard, prend une valeur fixe.
En comparant les deux bornes GNARC et FNARC, nous avons constaté que les performances peuvent être améliorées d'une façon importante, notamment pour les faibles valeurs du retard, en mettant en œuvre une commande adaptative, en particulier, l'architecture RMMAC.

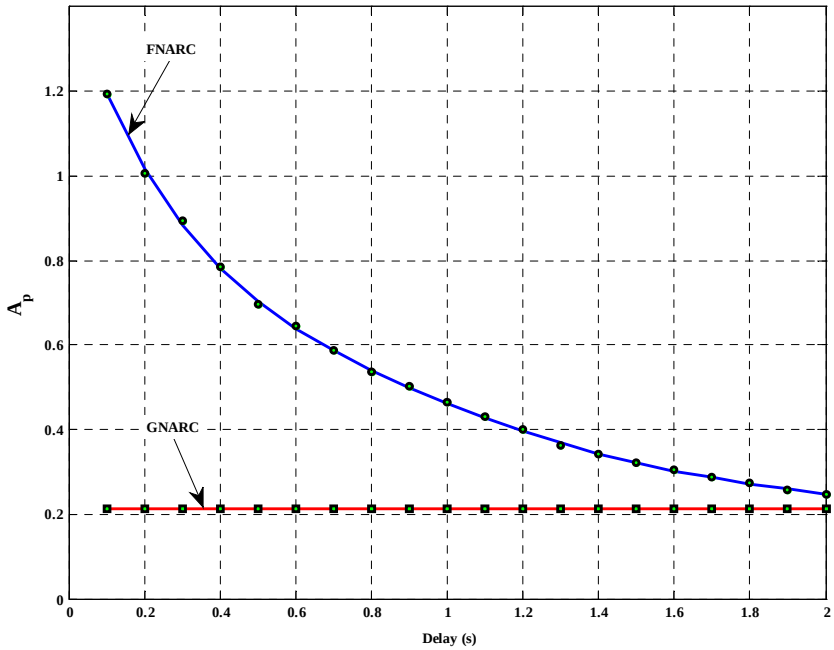

Performances GNARC et FNARC

L'objectif est maintenant de calculer le nombre minimum de modèles et les régulateurs locaux associés. Ce nombre est obtenu de telle sorte que le critère de performance soit supérieur ou égal à une limite fixée choisie comme étant une fraction de la borne maximale FNARC. A partir de la plus petite valeur du retard, on augmente progressivement l'incertitude du premier modèle tout en calculant avec la μ synthèse mixte la performance maximale que l'on peut espérer atteindre ainsi que le correcteur robuste associé. On réitère ce calcul jusqu'à ce que la performance calculée coïncide avec la limite fixée, ce qui détermine le premier modèle. Cet algorithme itératif est ainsi répété jusqu'à atteindre la valeur maximale du retard à savoir 2s. Nous avons identifié par ce moyen cinq modèles pour obtenir une performance globale supérieure ou égale à 60% de la borne FNARC comme le montre la figure suivante. Une performance plus élevée nécessitera probablement plus de modèles.

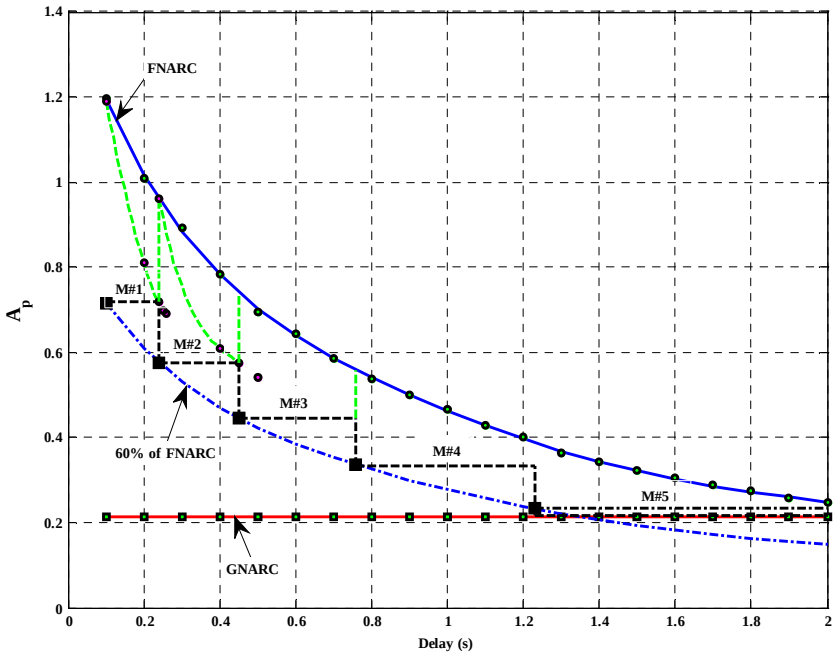

Détermination des modèles de l'architecture RMMAC

Reste à voir comment déterminer les points nominaux dans chaque modèle pour pouvoir développer le filtre de Kalman associé. En pratique, on les choisit à l'aide de la distance BPM (Baram Proximity Measure) définie par :

$$L_j^i = \log|S_j| + \text{trace}(S_j^{-1}\Gamma_j^i) \tag{50}$$

où la covariance Γ_j^i est donnée par :

$$\Gamma_j^i = E\left\{(y(t)-\hat{y}_j(t))(y(t)-\hat{y}_j(t))^T / H_i \neq H_j\right\} \tag{51}$$

Plus précisément, L_j^i mesure la distance entre un modèle j quelconque de l'ensemble et chacun des autres modèles i.
On définit également la quantité suivante qui représente l'information contenue dans la sortie y favorisant le modèle k au détriment du modèle j :

$$I_n(k,j) = \mathrm{E}\left\{\log\frac{p(y(t)/H_k, Y(t-1))}{p(y(t)/H_j, Y(t-1))}\right\} \tag{52}$$

avec : $Y(t) = (u(0)\cdots u(t-1), y(1)\cdots y(t))$

Nous pouvons démontrer que :

$$I_n(k,j) = \frac{1}{2}(L_j^* - L_k^*) \tag{53}$$

où le symbole * désigne la valeur réelle du retard.

Par conséquent, les deux inégalités suivantes sont équivalentes :

$$I_n(k,j) \geq 0 \qquad\qquad L_j^* \geq L_k^* \tag{54}$$

Si l'une des deux inégalités est vérifiée, alors la convergence des probabilités est mathématiquement assurée.
L'ultime étape consiste à déterminer les valeurs nominales du retard pour chaque modèle en utilisant un algorithme d'optimisation itératif de façon à faire coïncider les distances BPMs avec les frontières des modèles adjacents. Avec ce choix, la probabilité du modèle le plus proche de la vraie valeur du retard convergera vers 1.

L'architecture RMMAC a été finalement testée au travers de nombreuses simulations où ses performances ont été comparées au meilleur régulateur non-adaptatif (GNARC) qui est le seul à pouvoir stabiliser la boucle de régulation de niveau sur les intervalles d'incertitudes considérés. Dans le cas où le retard est constant comme dans le cas où il varie, RMMAC nous a permis d'améliorer significativement la fonction de rejet du gonflement en présence d'incertitudes sur le retard. Ce niveau de performance, que les autres commandes classiques ne peuvent atteindre, se traduit naturellement par une complexité accrue de la structure de commande.

Il importe de noter en fin de ce chapitre que l'extension de cette méthodologie au cas où le gain est un paramètre incertain est bien sûr possible au prix de quelques ajustements.

Conclusions et Perspectives

La coulée continue est une étape cruciale lors de l'élaboration de l'acier. Chaque année, plus de 500 millions de tonnes d'acier sont produites au moyen de ce procédé qui opère comme un échangeur thermique où se forme l'acier solide à partir d'une fonte liquide. Une coulée réussie est la conjugaison de nombreux facteurs. En effet, il faut s'assurer en amont de la bonne composition chimique de l'acier et dans la machine des bonnes conditions thermiques et mécaniques. Dans le cadre de cette thèse, nous nous sommes intéressés aux variations de niveau en lingotière qui sont liées à l'hydrodynamique du fluide mais aussi à de nombreuses perturbations internes et externes à la lingotière. Notre intérêt pour ces variations de niveau est principalement parce qu'elles sont à l'origine de plusieurs défauts sur le produit final. Ces irrégularités sont dues à la capture d'impuretés, à la thermique interne de l'acier comme aux pressions exercées sur le produit en cours de coulée. Afin de limiter leurs apparitions, il convient de contrôler les facteurs inhérents à leurs formations dont les variations de niveau en lingotière. C'est la raison pour laquelle toutes les machines de coulée sont équipées d'un système de régulation de niveau afin de maintenir une surface d'acier stable en lingotière et contrer toutes les perturbations.

Nous avons classifié les perturbations à l'origine des variations de niveau en trois catégories. La première (celle des perturbations lentes) contient toutes les perturbations qui ne se produisent pas fréquemment et dans ce cas, la loi de commande devrait conserver ses performances même si ces perturbations font évoluer le procédé vers un autre point de fonctionnement. La deuxième (celle des perturbations périodiques) est constituée de toutes les perturbations qui donnent lieu à des variations périodiques de niveau et dans ce cas la loi de commande devrait permettre de réduire l'effet de ces perturbations sur le niveau (et en aucun cas de l'amplifier). Enfin la troisième catégorie est celle des perturbations brutales qui entraînent une variation de niveau d'amplitude importante. Le correcteur devrait minimiser l'écart de niveau engendré.

Dans cette thèse, après la phase de modélisation du procédé, nous avons d'abord étudié les techniques d'estimation des perturbations. Puis nous avons mis en place un estimateur global pour mesurer les effets de certaines perturbations sur le niveau. Après l'avoir validé en simulation et expérimentalement sur des signaux prélevés sur site, nous l'avons intégré dans une structure de compensation de l'effet du gonflement sur le niveau. La maquette hydraulique nous a permis ensuite de valider l'ensemble de cette structure mais aussi d'établir des liens entre les paramètres de la boucle de régulation et les conditions de coulée.

Les lois de commande étudiées dans le chapitre 4 comme le PID, les commandes prédictives PFC et GPC, le prédicteur de Smith et la commande par modèle interne IMC ont fait l'objet de plusieurs analyses comparatives pour mettre en évidence les avantages et les inconvénients des structures de contrôle actuellement en service dans les usines. Ce qui nous a permis de définir un référentiel de performances que nous avons amélioré par la suite en appliquant la version modifiée du prédicteur de Smith proposée par Aström à notre problème. Cette extension du prédicteur de Smith présente l'avantage de découpler le réglage de la réponse temporelle de la fonction de rejet des perturbations à l'aide de deux correcteurs dont un a été conçu par une synthèse H_∞ standard. Ainsi, nous avons pu développer une méthode de réglage du prédicteur d'Aström afin de satisfaire les spécifications en termes de rejet des perturbations sinusoïdales tout en garantissant la marge de retard voulue et donc sans avoir à se soucier de l'identification exacte du retard pur. Le correcteur ainsi obtenu est généralement d'ordre élevé mais peut heureusement se mettre sous la forme conventionnelle PID comme ce fut le cas ici.

Enfin, le cinquième chapitre a été consacré à la mise en œuvre de la commande adaptative multi-modèles RMMAC qui constitue l'aboutissement de ce travail de thèse. S'il est vrai que cette architecture est plus complexe requérant une certaine technicité en matière de régulation, elle est la seule structure à pouvoir stabiliser le système, maximiser les performances et suivre les variations des paramètres incertains sur de larges domaines de fonctionnement de la machine de coulée continue.

Les approches, développées dans le cadre de cette thèse, présentent de nombreux prolongements possibles. Concernant la structure d'estimation des perturbations, il importe de la rendre plus robuste face aux incertitudes sur le modèle et aux variations des fréquences du gonflement. Dans un deuxième temps, la conception du prédicteur d'Aström pourrait être complétée pour tenir compte des autres perturbations comme le bouchage et les ondes stationnaires. Enfin, la phase ultime consistant à implanter la commande RMMAC sur une machine réelle reste une étape à franchir dans un avenir proche.

List of Figures

List of Tables

Notations and Acronyms

i. Notations

Symbol	Parameter	Unit
D_r	Roll diameter	mm
D_n	Nozzle diameter	mm
d_{clog}	Clogging effect model	$L \cdot s^{-1}$
d_{bulge}	Bulging effect model	$L \cdot s^{-1}$
d_{waves}	Standing waves effect model	mm
$\vec{F}_w$	Wall friction	$m \cdot s^{-2}$
$\vec{g}$	Gravitational acceleration	$m \cdot s^{-2}$
G_n	Nozzle gain	$L \cdot s^{-1} \cdot mm^{-1}$
N	Theoretical mould level	mm
N_m	Measured mould level	mm
N^*	Mould level setpoint	mm
N_{tun}	Tundish level setpoint	mm
P_r	Ferrostatic pressure	$N \cdot m^{-2}$
P^*	Stopper position setpoint	mm
P	Measured stopper position	mm
Q_{in}	Flow into the mould	$L \cdot s^{-1}$
Q_{out}	Flow out of the mould	$L \cdot s^{-1}$
s	Laplace variable	
S	Mould section	mm^2
S_t	Slab thickness	mm
S_w	Slab width	mm
T	Strand temperature	^oC
T_s	Sampling time	s
TF_{model}	Plant model transfer function	
τ_a	Actuator time constant	s
τ_s	Level sensor time constant	s
τ_n	Nozzle delay	s
$\vec{u}$	Fluid velocity	$m \cdot s^{-1}$
v	Casting speed	$m \cdot min^{-1}$
λ	Roll pitch	mm
ρ	Liquid steel density	$kg \cdot m^{-3}$
ν_e	Effective kinematic viscosity	$m^2 \cdot s^{-1}$
Δ	Uncertainty matrix	
$\mu_{\underline{\Delta}}$	Structured singular value	
$\overline{\sigma}$	Largest singular value of a matrix	
ε	Level error	mm

ii. Acronyms

BPM	Baram Proximity Measure
CC	Continuous Casting
CIS	Commonwealth of Independent States
CLRT	Closed Loop Response Time
CMMAC	Classical Multiple-Model Adaptive Control
EU	European Union
FNARC	Fixed Non-Adaptive Robust Compensator
GNARC	Global Non-Adaptive Robust Compensator
GPC	Generalized Predictive Control
IMC	Internal Model Control
LES	Large Eddy Simulation
LNARC	Local Non-Adaptive Robust Compensator
LS	Least Squares
MLC	Mould Level Control
MMAC	Multiple-Model Adaptive Control
MMAE	Multiple-Model Adaptive Estimation
NAFTA	North American Free Trade Agreement
NKK	Nippon Kaiji Kyokai
PEM	Prediction Error Method
PFC	Predictive Functional Control
PID	Proportional Integral Derivative
PIV	Particle Image Velocimetry
PRBS	Pseudo-Random Binary Sequence
PSO	Particle Swarm Optimization
RMMAC	Robust Multiple-Model Adaptive Control
SEN	Submerged Entry Nozzle
SMMAC	Supervisory Switching Multiple-Model Adaptive Control
SW	Standing Waves
ULC	Ultra Low Carbon
VOF	Volume Of Fluid
WM	Water Model

General Introduction

Motivation for Research

The steel sector is an advanced industry which involves several complex processes that need to meet international standards in terms of product quality, equipment performance, safety, environment and energy efficiency. Nowadays, the vast majority of steelmakers are continually looking at ways to improve the industrial machinery related to iron making, Electric Arc Furnace EAF steel making and continuous casting with the aim of achieving:

- Lower capital and operating costs,
- Availability and flexibility of raw materials,
- High level of innovative capacity,
- Value creation,
- Energy savings.

As the demand for steel grows hopefully at a constant rate, steel companies are facing a large number of challenges in providing solutions to demanding customers. In particular, this presents an opportunity for steelmakers to implement new technologies in order to measure and control the processes at existing facilities. Indeed, the need to improve control systems is becoming more urgent and necessary to maintain a high level of productivity and to cope with internal and external disturbances. Research in this area is as vital as ever.

Within the project general scope aiming at developing advanced control techniques for its factories, the work proposed by ArcelorMittal is mainly focused on the mould level control in the continuous casting process. The thesis is concerned with ensuring the stability of the mould level and improving the disturbances rejection to achieve a high product quality with the final objective to generalize such strategies to other processes such as the electric arc furnace or the rolling mill.
The thesis work results from a collaboration between the Measurement and Control Department of ArcelorMittal Global Research and Development, Maizières-Lès-Metz and the Control Department of SUPELEC Systems Sciences (E3S), Gif-sur-Yvette, France.

In the continuous casting process, molten steel flows from a ladle, through a tundish and then a nozzle into the mould where it freezes against water-cooled mould walls to form a solid shell as illustrated in the following figure.

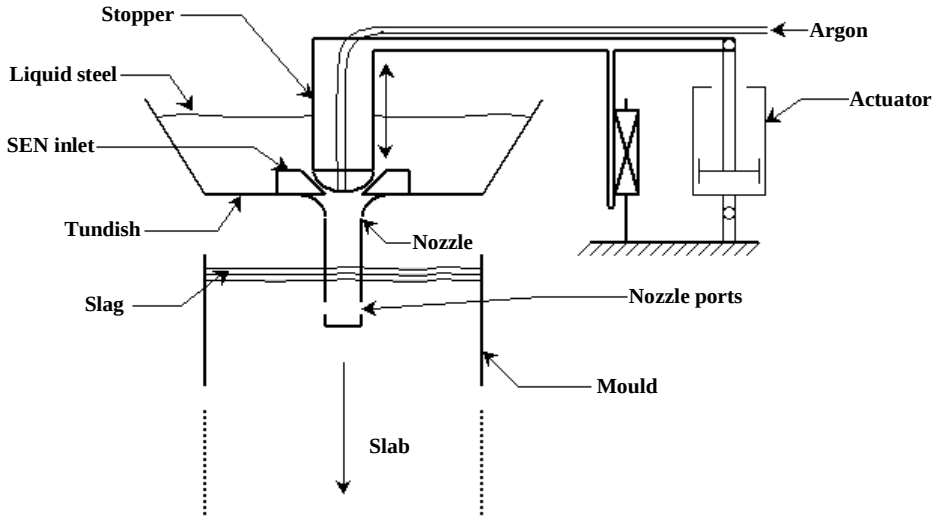

Upper part of the continuous casting process

Mould level fluctuations generated by undesired disturbances such as the clogging/unclogging and the bulging, cause refractory material, alumina inclusions and slag to be captured in the surface of the solidified shell leading to many defects in the semi-finished product so-called the slab. The role of the control system is to control the stopper position based on mould level measurements in order to keep the free surface variations to a minimum.

Contributions of the thesis

In the continuous casting process, the challenges faced by the operators are numerous. Amongst them, one should list:

- Casting conditions changes such as the variations of the mould format or the casting speed. In most practical situations, there are difficulties in maintaining the mould level stable because the controllers currently in use have not been designed to work over a large range of casting conditions. This requires a human intervention in a dangerous environment. The casting is, most of the time, slowed down to have an effective mould level control.
- Uncertain time-delay in the control feedback attributed to the argon flow inside the nozzle and to the distance between the stopper rod and the mould level.
- The clogging is a chronic disturbance in every casting operation causing a variety of problems. Although much work has been done to improve the controller's response to this type of disturbance, huge level variations occur and are proportional to the clogs leaving the nozzle walls.
- The bulging is another disruptive phenomenon which takes place in the lower part of the caster but has a major effect on the mould level. It is strengthened by an uneven and thin solidified shell but can be weakened by changing the roll pitch configuration with a strong cooling at the secondary cooling zone.

Since we wish to come up with a global solution intended to handle all the above obstacles, a work program has been established to pursue the following objectives:

- Understanding of mould level dynamics and the disturbances affecting the meniscus region.
- Development of online estimators to track the effects of the clogging/unclogging and the bulging on the mould level control system.
- Incorporation of these estimates into a compensation structure which would cancel the disturbances effects on the mould level.
- Analysis of the relationships between the process parameters (i.e. the gain and the delay) and the casting machine configuration (such as the flow rate out of the mould or the level sensor position). Particular attention will be paid to the effect of clogging on these relationships.
- Assessment of classical control laws performances in terms of robustness stability and disturbances rejection.
- Development of a robust solution which adapts automatically to the process parameters changes. Our proposal is to implement the Robust Multiple-Model Adaptive Control RMMAC which has been proven to be effective in case of slowly-varying uncertain parameters. Furthermore, its identification subsystem provides useful signals to detect the process parameters variations. The RMMAC architecture is already in use in the aerospace industry and has demonstrated satisfactory performance.

Organization of the thesis

The dissertation begins with an introduction to the continuous casting process which remains a vital stage of the global steel manufacturing chain. Are considered respectively some key aspects of the steel, the other processes which in turn interact with the continuous casting and a full description of the caster including the feeding zone, the solidification zone and the conditioning zone. Since our thesis is dedicated to the improvement of the flow control system in order to lower the mould level variations, we will describe extensively the mould level region as well as the instrumentation used for mould level control.

The first step in any control design is to carefully model the process dynamics with the disturbances effects. To accomplish this, we can describe exactly the fluid behavior by mathematical models. Nevertheless, it is much convenient for the designer to only consider the moving average level in the mould from the difference between the flow rate entering the mould and the flow rate leaving it. One reason for this is that the controller and the actuator are not able to maintain the entire free surface at a constant level. Additionally, the current sensors measure only the average level and never the local fluctuations. Therefore, during casting operations, only this measurement is available for the controller and this is what should be taken into account in the process modeling.
Thus, the two models are presented in chapter 2 but only the second one is adopted for control laws design. We also discuss the effect of different kind of disturbances in particular the clogging/unclogging cycle, the unsteady bulging and the standing waves that will be integrated in the global plant model.

The study of the disturbances will be continued in chapter 3. Emphasis will be on the clogging/unclogging cycle and the bulging. The use of observers to estimate these two disturbances is presented leading to a global observer that addresses simultaneously the clogging/unclogging and the bulging but could be applied also to the standing waves. The estimate of the bulging effect and its derivative are then used in a compensation structure whose role is to cancel the mould level variations generated by the bulging.
Chapter 3 is also devoted to the plant model identification procedure. First, we describe the experimental protocol for collecting data. Then, we explain how to identify the unknown parameters by means of offline algorithms. More precisely, the least squares method will be proposed to identify the actuator dynamics and a prediction error estimation method will be employed to identify the two key parameters of the plant model namely the gain and the delay.
The last part of chapter 3 is dedicated to validating the bulging compensation structure experimentally and determining the variation ranges of the gain and the delay in function of the casting conditions. Our experimental tool is the water model designed to simulate different types of flow and many phenomena in the mould region.

Chapter 4 is concerned with the non-adaptive control laws currently in use in real plants or which should be considered for the mould level control problem. Throughout this chapter, an important focus is placed on the PID control law, the predictive strategies PFC (Predictive Functional Control) and GPC (Generalized Predictive Control), the Smith predictor and its modified version initially proposed by Aström and finally the Internal Model Control IMC. All these control laws are compared in terms of disturbances rejection and robustness stability. More precisely, this comparison is carried out on the basis of several performance criteria including the gain margin, the delay margin, the modulus margin, the maximum gain of the bulging rejection transfer function over the bulging frequency range, the maximum level amplitude generated by the unclogging and other factors. This comparative analysis provides thus the operator with the means to choose an appropriate controller for the mould level.

In chapter 5, we consider the development of the RMMAC architecture adopted with a view to enhancing the bulging rejection. After introducing the multiple-model structures and the necessary knowledge about mixed-μ synthesis, we apply a stringent methodology to determine the number of models, the local controllers and the nominal values for Kalman filters design. In order to evaluate the performance improvement, some simulation examples are presented with the analysis and synthesis results.

Finally, we conclude the dissertation with some suggestions regarding future directions for this research.

CHAPTER 1
Continuous casting in the steel industry

1.1 Introduction

This chapter describes the continuous casting process which is an important stage of the steel production chain but is unfortunately at the origin of many quality problems in the semi-finished product. This is the reason why our thesis work is dedicated to the improvement of the steel flow control loop performances in the continuous casting machine in order to lower mould level variations responsible for several defects of the semi-finished product.

Prior to the introduction of the control problem in chapter 2, it appears particularly relevant to recall some aspects of steel, the main processing stages of the steel production and the basic principles and units of continuous casting. This is the purpose of this chapter which is structured in this way. In addition, it includes a section on the instrumentation universally used for mould level control.

1.2 General aspects of steel

This section presents the steel which is the material at the heart of all the developments in this dissertation. Here, our objective is to discuss briefly the reasons behind the leading role played by this essential element in some of the greatest technological achievements.

1.2.1 History

From a historical standpoint, the production of iron began probably from 2000 BC in south west or south central Asia. It replaced gradually bronze particularly in implements and weapons thanks to its mechanical properties. Produced by large quantities for over three thousand years, iron was the material basis in the development of human civilizations in Europe, Asia and Africa.

Alloyed with a bit of carbon, iron was made harder and more durable. The range of carbon contents involved was from 0.02 to 0.08% to make wrought iron and from 3 to 4.5% to obtain cast iron which makes the metal harder but non-malleable. In between these two proportions, there is steel with 0.2 to 1.2% carbon. Compared to the old wrought iron, steel is harder and at the same time malleable and flexible unlike cast iron [68].

Prior to 1856, there was no easy and cheap way to manufacture the steel. But after the introduction of Bessemer process, the carbon level in iron could be efficiently controlled enabling the production of large volumes of steel in liquid state. The Bessemer converter heralded thus the birth of modern steel industry. This growth has been accelerated by the emergence of huge markets for steel like railroads.

By 1930, the electric steelmaking was introduced. It represented a different approach to the steel production since it involves the direct recycling of scrap. However, the industrial production has been undertaken only after 1960 at the same time as the basic oxygen process for the production of steel from iron ore. Today, its importance is growing constantly. In the European Union, the volume of steel produced in that way rose from 19% in 1973 to reach 45% in 2005.

1.2.2 Composition

The focus of this paragraph is to explore the elements of steel composition. Carbon is undoubtedly the most important element in steel because it allows a large range of tensile properties. Fig. 1.1 lists the major families of steel classified according to carbon content.

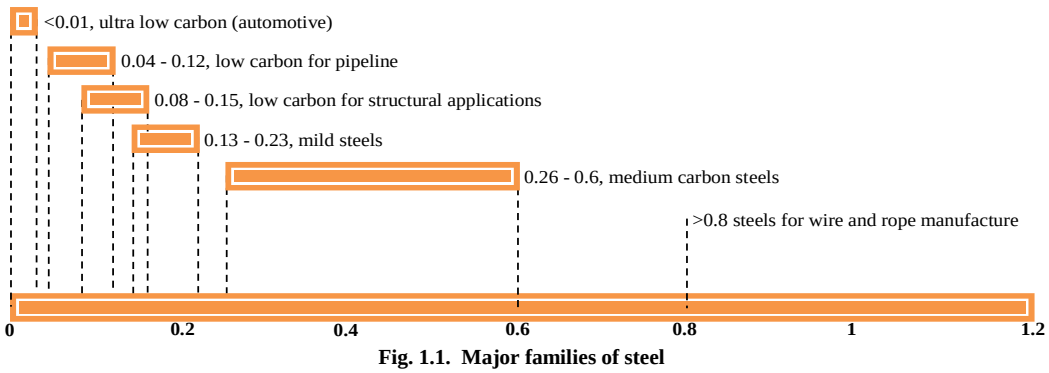

Fig. 1.1. Major families of steel

In addition to carbon, most steels contain several other elements such as manganese, phosphorus, sulfur, nickel, chromium, cobalt, silicon, vanadium, copper and more others. For instance, chromium is added to increase hardness, tensile strength and resistance to corrosion. Silicon improves yield strength and deoxidizes to remove oxygen from molten steel. Besides alloying elements, the composition of steel includes impurities derived from scrap but without any influence on steel properties.

1.2.3 Properties

Steel is the common name for a large family of iron alloys. Their properties depend on the carbon and other elements they contain. In fact, the chemical composition as well as the cooling system used in the solidification process determines the final microstructure of steel, responsible for the mechanical properties. Each application has its own standard usually agreed by a group representing users and steelmakers. For instance, steels used in the automotive are strong, though, corrosion resistant and recyclable. They contain less than 0.01% carbon and there are many standards which specify a range of composition of steel that will guarantee the properties required for this market. The properties of the major families of steel are listed in Table 1.1.
In this paragraph, only some of these concepts are introduced due to space limitations. For a precise development, the reader is referred to e.g. [65] [66].

- **Tensile properties**

They indicate how the steel will react to forces being applied on it. They include the modulus of elasticity, tensile strength, elastic limit, elongation, yield point and other parameters.
To determine these mechanical properties, a tensile test is performed. It consists of imposing a gradually increasing elongation on a thin specimen of the material until the breaking point is reached. This type of experiment is widely practiced to characterize the elastic and plastic deformation of steel.

- **Corrosion**

It designates electrochemical oxidation of steel (or any other metal) in reaction with an oxidant such as oxygen. It induces damages to the steel which tends sometimes to return to its natural state in the form of iron oxides. To prevent this deterioration, the steel is usually protected against corrosion by metallic coatings in particular zinc, aluminum and their alloys.

- **Hardness**

It measures the resistance of steel to deformation. This property gives an indirect indication of tensile properties but it can never replace the guaranteed values measured by the aforementioned test. The different hardness testing techniques can be classified in four categories which are indentation, scratch, rebound tests and non-destructive methods. The first one is by far the most employed test to measure the machinability, weldability and formability of steel, which tends to decrease as the hardness is raised.

- **Creep strength**

This is an important issue to investigate when considering elevated temperature applications such as plates, seamless tubes and forgings. The standard procedure is to apply a constant tensile on a cylindrical specimen placed in a furnace and to measure its elongation as a function of time. This property depends essentially on carbon, manganese and nitrogen contents.

Table 1.1. Properties of major families of steel

	Ultra low carbon	Low carbon	Medium carbon	High carbon
Carbon content (%)	<0.01	<0.25	0.25 - 0.6	0.8 - 1.2
Properties	High strength High toughness Formability	Less strong Cheap Easy to shape, high ductility Weldability	Ductility High toughness	Hardness Less formable Low toughness
Uses	Sheet materials for car structures Offshore and onshore structural applications	Structural steels Sheet materials for automotive	Rails Rods Forging Automotive components: gears...	Springs Cutting tools Gardening equipment Wires

1.2.4 Applications

This paragraph lists some of the many uses of steel. Considered as a versatile material, the steelmakers use to say that nothing is manufactured, processed or transported without steel. Little by little, the position occupied by steel has grown to cover a huge number of products designed for low and high tech industry as well as those found in our everyday life.
The steel has diverse applications which can be divided into the following categories also known as steel end-markets.

1.2.4.1 Automotive

The automotive industry is the single most important market for steel strip. In a car, the steel accounts for over than 50% of the whole weight. Thanks to its strength and ductility, it is used for car bodies, doors, bonnet, boot, gearbox, springs, suspension, wheels, axles…
The steel producers are increasingly involved in the full automotive product cycle. In the EU, they sell the equivalent of more than two Eiffel towers to automobile manufacturers.

Fig. 1.2. Car body

1.2.4.2 Construction

The steel industry feeds the most of its production to the construction industry (buildings, housings, stadiums, bridges, tunnels, suspension cables, piers, pipes and tubes, harbors…). In this regard, it is very sensitive to the growth of this sector. The steel used in construction is usually integrated into buildings and therefore has a long life cycle contrary to those designed for other markets.
Furthermore, it is appreciated also for its strength, its ability to work with other materials and its resistance to the most aggressive corrosive environments.

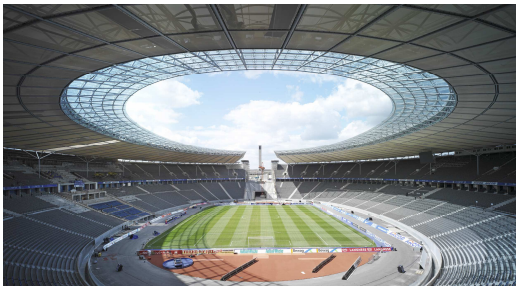

Fig. 1.3. Roof of Berlin's Olympic stadium

1.2.4.3 Packaging

Steel is also widely used as a packaging material for food and beverages in order to protect them from water, air and light (cans, aerosols, paint and chemical containers, bottle caps…). Contrary to automotive and building applications, strips used for packaging are much thinner (0.13 to 0.5mm). Steel packaging is 100% recyclable without loss of quality and contains up to 25% recycled steel. In France, steel is used for more than 80% of beverage cans because they do not alter the taste of the drink and constitute a cheap support for advertising messages. Moreover, it is also used to transport dangerous substances in drums including chemical and radioactive products.

Fig. 1.4. Cans to pack food, sprays and cosmetic articles

1.2.4.4 Domestic equipments

Steel uses cover also numerous domestic appliances such as fridges, sinks, ovens interiors and microwaves, work surfaces, radiators, cutlery, razors, pins, dishwashers, doors and drums of washing machines, tumble driers and many others. In 2008, domestic equipments represented 4% of the world finished steel consumption.

Fig. 1.5. Cutlery made of stainless steel

Fig. 1.6. Kitchen sink made of stainless steel

1.2.5 Steel in figures

Steel is essential to economic growth. The aim of this paragraph is to present some figures which provide indications of the level of the steel industry. Abundant data is available concerning steel. Here, the figures are limited to steel production and consumption. Fig. 1.7 and Fig. 1.8 display the production of crude steel by regions over a half century and in the last decade respectively (Source: World Steel Association). CIS is Commonwealth of Independent States including notably former Soviet Republics and NAFTA designates North American Free Trade Agreement which includes United-States, Canada and Mexico.

Particularly noticeable is the high growth between 1950 and 2008 where the production reaches more than 1300 million tonnes. China is principally responsible and represents today almost 38% of the world steel production. The last decade has seen an unprecedented increase in production taking place essentially in emerging countries.

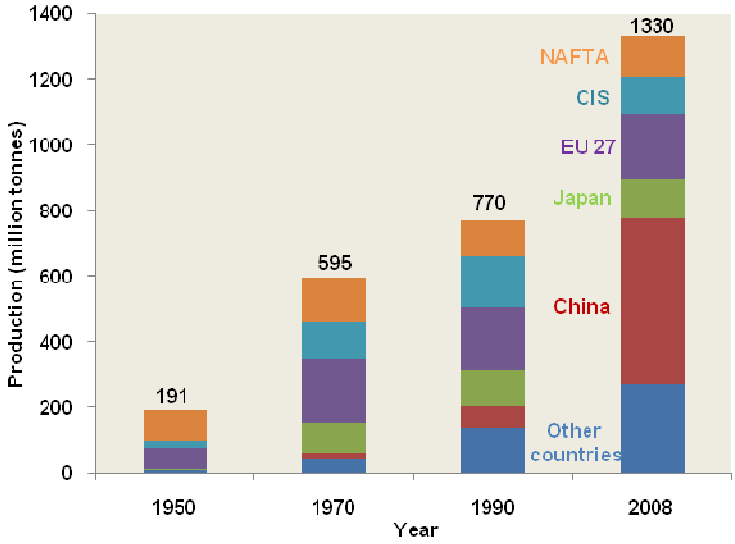

Fig. 1.7. World crude steel production evolution over a half century

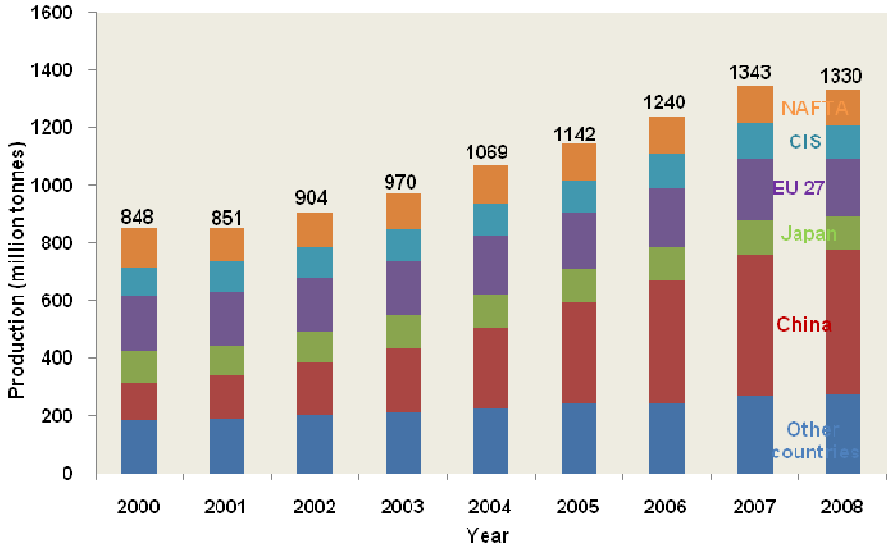

Fig. 1.8. World crude steel production over last decade

Fig. 1.9 lists the top fifteen produces in the world (Source: International Iron and Steel Institute). Large companies have been created especially in the 1990s and 2000s through privatizations, acquisitions and mergers. For instance, ArcelorMittal, the world's largest steel producer, was created in 2006 through the merger of Arcelor (created in 2001) and Mittal (created in 2004).

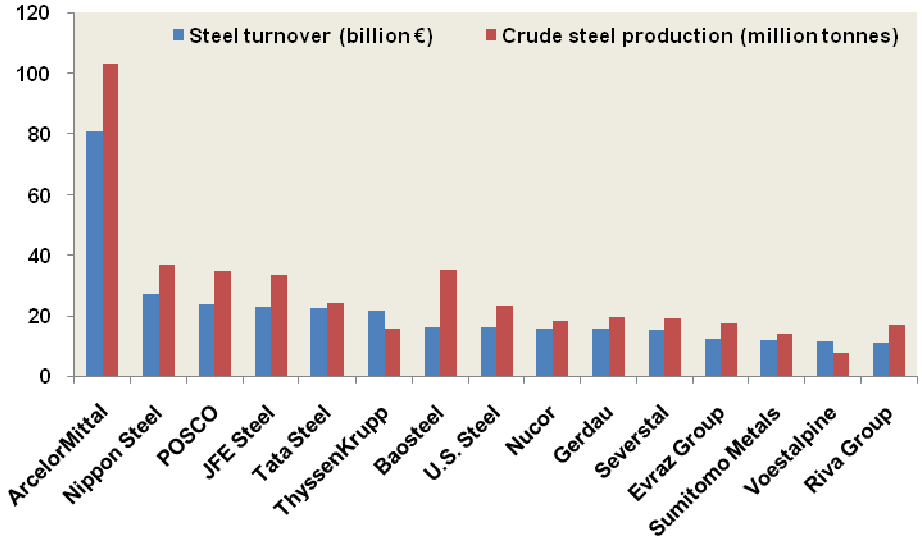

Fig. 1.9. List of biggest steel companies by turnover

Fig. 1.10 and Fig. 1.11 show the current global consumption by regions and sectors based on the steel statistical yearbook. Once more, China is the largest consuming region in the world with 36% followed by the European Union and North America. In terms of sectors, construction is by far the most important consuming sector accounting for 27% followed by the automotive industry.

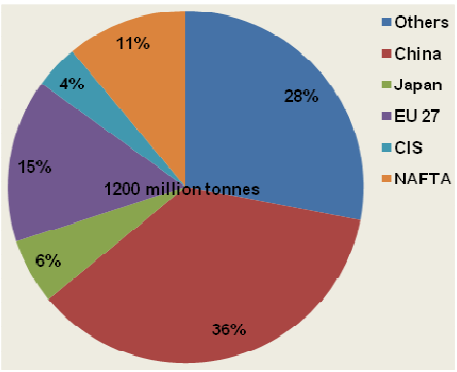

Fig. 1.10. World finished steel consumption in 2008 by region

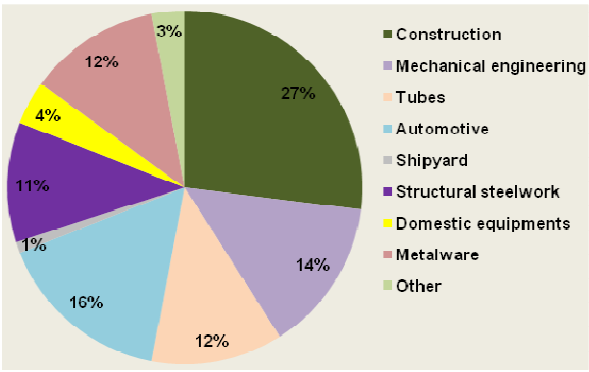

Fig. 1.11. World finished steel consumption in 2008 by sector

1.3 Steel manufacturing

The manufacture of steel is a complex industry which involves many processes. This section describes, process by process, the principles of steelmaking. For the sake of simplification, we do not intend to describe in detail its various stages but only the general aspects of each step in order to understand the role played by the continuous casting machine in the integrated steelworks.

A steel plant includes a hot section and a cold section. The objective of the hot part is to produce the steel products with the required dimensions from the iron ore. This product serves as the starting material of the cold section which includes pickling, rolling to improve the geometry and coating to protect the surface. Fig. 1.12 shows a simplified flow diagram of the hot section as designed for modern steelworks.

In short, the iron is first produced from raw materials with initial carbon content between 4 and 4.5%. Next, the steelmaking process reduces this content to the proportion required to produce steel i.e. less than 1.2% carbon. Thereafter, other adjustments are carried out during secondary steelmaking in order to achieve the final composition and the suitable temperature. The steel is then cast by continuous casting machine into slabs, blooms or billets. Once in the primary forming zone, these castings are rolled to the target dimensions. The achieved steel product leaves thus the hot section and enters the cold one where there is a variety of fabrication processes that intend to give it its final dimensions and properties.

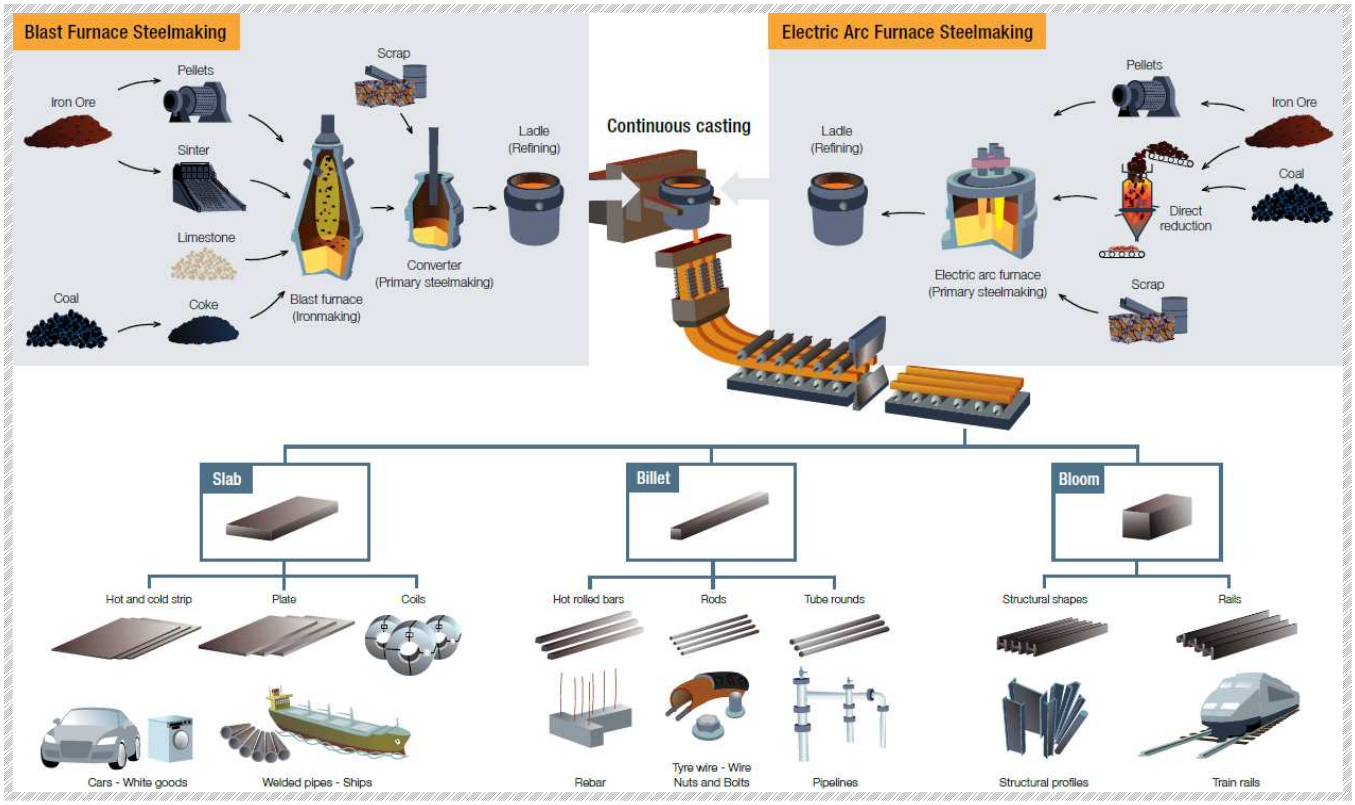

Fig. 1.12. Overview of the steel manufacturing process (Source: World Steel Association)

1.3.1 Ironmaking and steelmaking

The ironmaking is the first stage in the manufacture of steel, in which raw materials such as iron ore and coke are used to produce liquid iron. The separation of iron from iron ore is achieved through one of the three following methods: blast furnace method, direct reduction or iron smelting. At this first step, the carbon content of the produced iron lies between 4 and 4.5%. For this reason, the Basic Oxygen Steelmaking BOS is applied to remove the excess of carbon by blowing the oxygen in the converter which contains the liquid iron for about 15 minutes. The main reaction of this process is the oxidation of the carbon by oxygen gas. This production route represents 70% of the steel crude production.

Having said this, an alternative way to produce special quality steels is the Electric Arc Furnace EAF used to remelt scrap iron and steel. It represents 30% of the crude steel production. In comparison to the first production

route which is the most costly and energy intensive process in the whole production chain, the EAF has low energy costs and a profuse supply of recycled scrap.
Next, the molten steel emerging from both BOS and EAF is placed in a ladle where a range of processes is applied which includes powder injection, electromagnetic stirring and vacuum degassing. Typical ladle dimensions are 3m in diameter and 4m in depth. The objective of the so-called secondary steelmaking can be summarized as follows:

- Adjustment of chemical composition, alloys addition and control of carbon, phosphorus, nitrogen, hydrogen and oxygen contents which mainly determine the mechanical properties of the steel.
- Removal of hydrogen, deoxidation products (SiO_2, Al_2O_3) and other impurities.
- Homogenization of steel composition and temperature accomplished by argon stirring or injection of reagents such as CaSi.

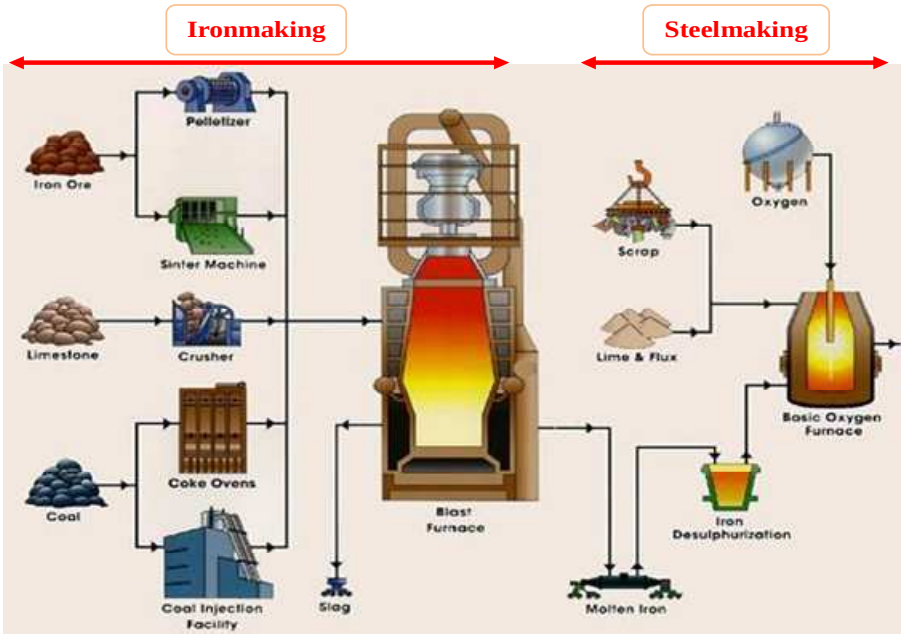

Fig. 1.13. Ironmaking and steelmaking processes (Source: sales brochure, Bethlehem Steel Corporation, Chesterton)

After ensuring that the steel temperature is suitable for casting, the ladle of liquid steel at the required composition is immediately transported to the continuous casting process.

1.3.2 Casting

After the steel has been refined, it is then continuously cast into various shapes by the casting process depicted in Fig. 1.14. Being at the heart of this dissertation, the caster machine will be deeply explored in the next chapter.

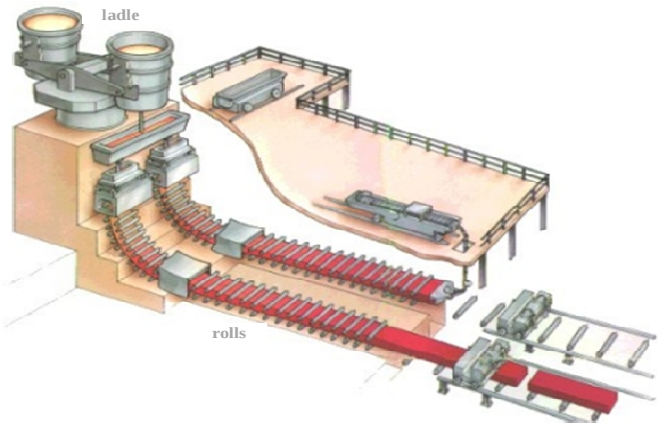

Fig. 1.14. Casting operations (Source: Corus)

1.3.3 Hot rolling and fabrication processes

After being cast, the steel undergoes a further stage of manufacturing called hot rolling which is the most used process to form steel into finished products. First, the semi-finished product is reheated to reach a temperature between 1200 and 1300°C. Next, it is passed backwards and forwards through the same rolls in order to reduce its thickness. The rolls are cylinder-shaped with a radius of 350mm. They can turn in both directions with a velocity that would reach $600 m \cdot min^{-1}$ [68].

Special emphasis must be placed on the rolling control system in particular to determine the number of passes and the reduction rate at each pass in order to avoid excessive deformation. The number of passes can reach 70 and depends on the rolled product and the target size of the finished product.

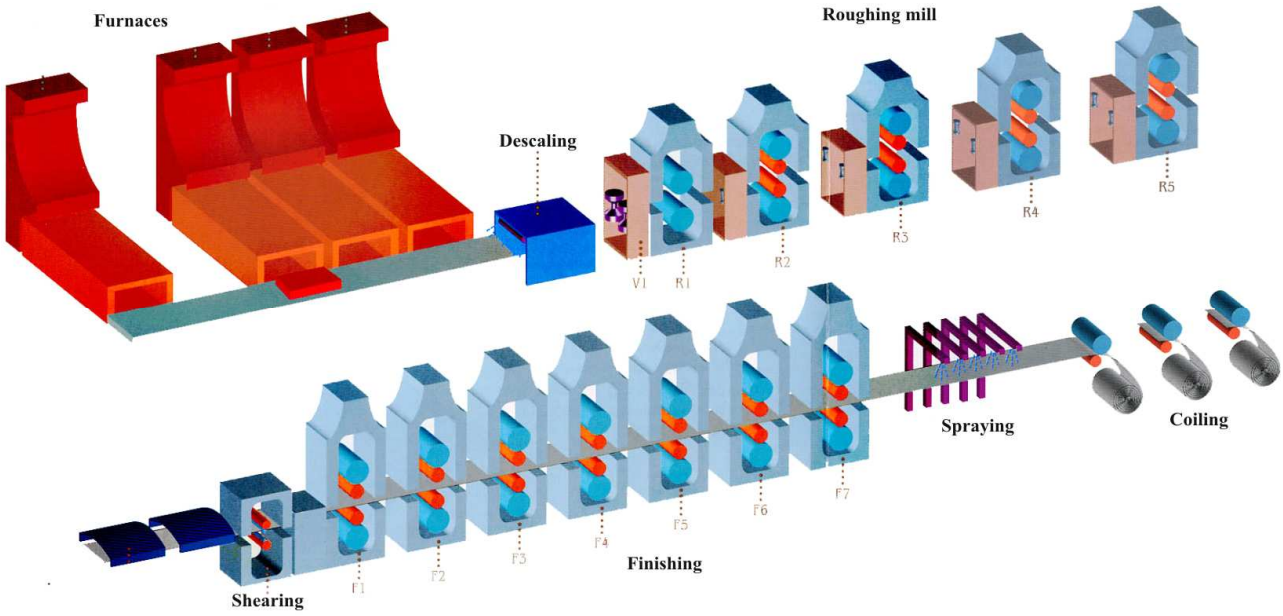

Fig. 1.15. Forming and finishing processes

In addition to its function of shaping the steel, hot rolling improves the mechanical properties and eliminates the structure defects.

Later, hot rolled products move to the cold section before becoming end products. The cold processing affords steel with the required final thickness and the final surface appearance and properties. It includes the following steps:

- **Pickling:** it is used to clean the surface of hot rolled products by means of a mildly acidic bath.
- **Cold rolling:** by applying a pressure on the strip, the cold rolling does not intend to alter the shape of the steel product but simply to reduce its thickness down to 0.15mm without preheating. It improves also the surface quality and the characteristics of the strip.
- **Annealing:** the steel is heated in a furnace between 800 and 1200°C to become more formable.
- **Coating:** these processes can be classified as hot-dip metallic coatings, electrocoating or non-metallic coatings. For instance, galvanizing belongs to the first category. It consists of applying zinc coating by dipping the steel in a bath of molten zinc. This is intended to extend the steel product life and to enhance its resistance to rust.

After the coating has been applied, the product goes through other post-treatments.

1.4 Continuous casting machine

The continuous casting is a very important stage of the manufacturing of steel. Since it is a way of reaching higher productivity with lower costs, the entire production of the most efficient steel plants is continuously cast today. The main purpose of continuous casting is the solidification of the molten steel provided by the primary and the secondary refining steps in order to produce cross sections of different shapes and sizes, i.e. a round section for tubes, a square section for bars and a rectangular section for sheet products. The following paragraphs of this section describe in detail all needed knowledge about this technology (Fig. 1.16).

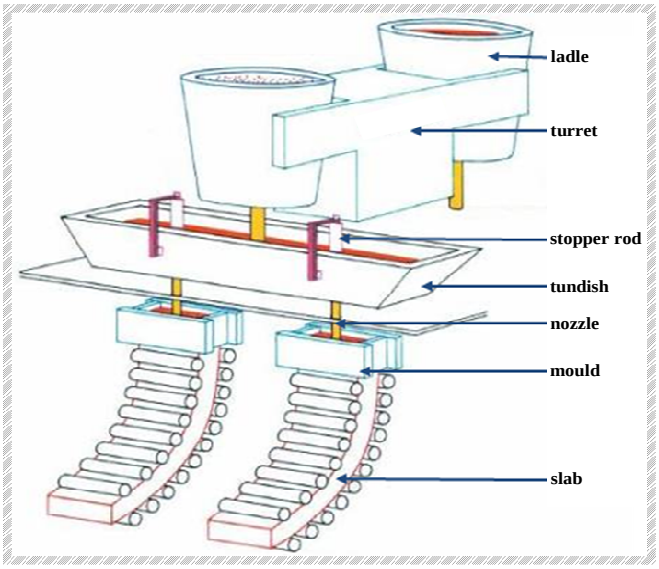

Fig. 1.16. Continuous casting machine

1.4.1 Historical development

It is somewhat difficult to say with certainty who developed first traditional continuous casting machines. Historians reveal that it was conceived initially in the 19th century by G.E. Sellars (1840), J. Laing (1843) and H. Bessemer (1846) [1] [68]. Since it has developed only in 1960's and reached a high degree of maturity by the 1980's, the continuous casting is relatively a new technology in historical terms.

Prior to the introduction of the continuous casting, steel was solidified by means of ingot moulds (Fig. 1.17). After solidification, the ingot is charged for later processing into semi-finished or finished products.

Although the continuous casting becomes the worldwide standard of the industry currently used to produce over 90% of steel throughout the world, ingot casting continues to be preferred to produce steel for large bar applications (e.g. power transmission) and tubing applications (e.g. bearings and gears).

Fig. 1.17. Ingots solidification in progress

The history of continuous casting goes back probably to the 19th century when the American technician G.E. Sellars has applied continuous casting to non-ferrous materials for the production of lead tubing and glass.

The high temperatures and the low conductivity of steel were the major technical problems which impeded the emergence of the continuous casting of steel. In 1855, Henry Bessemer received a patent for his industrial process which produces the steel from molten pig iron (an intermediate product of smelting iron ore with coke). In 1857, he received a second patent for casting metal between two contra-rotating rollers. In 1933, the first plant for continuous casting of brass was built by Junghans in Germany whereas those dedicated to steel were built at Babcock (USA), Low Moor (Great Britain) and Amagasaki (Japan) in 1946 and 1947. The early machines were totally vertical. Suffering from a considerable height, they evolve to the curved type which appears by the 1965's. This geometry is widely used nowadays.
The technological advances of continuous casting and their corresponding dates are sumed up in Table 1.2.

Table 1.2. Key dates in continuous casting history

Year	Developer/*Site*	Technological advances
1840	G.E. Sellars	First tests of the casting machine but details are not clear
1843	J. Laing	American patent N° 3023: design of the first equipment for continuous casting
1857	H. Bessemer	Patent for casting molten metal between contra-rotating rollers
1887	R.M. Daelen	Patent for solidifying the steel using a water cooled mould open at the top and the bottom
1890	B. Atha	Casting of high alloy steel but many troubles occurred such as surface cracks
1914	J.T. Rowley	Casting using vertical and fixed mould
1944-1949	*USSR*	• Establishment of the continuous casting conditions • Introduction of various control techniques, self control system • Conclusive experiments
1946-1947		First plants for continuous casting of steel built at Babcock and Wilcocks (USA), Low Moor (Great Britain) and Amagasaki (Japan)
1952	O. Schaeber *Germany*	German patent describing the casting of a bent vertical machine instead of a straight vertical strand
	O. Schaeber and Junghans *Germany*	Design of the first electromagnetic stirrer for continuous casting at Mannesmann
1956	*Great Britain*	Vertical cutting of the billet strand is replaced by horizontal cutting at Barrow
1963	*Germany*	Design of the first vertical slab caster with a horizontal discharge at Dillinger steelworks
1970-1983		• Rapid changing of the ladle and the tundish • Adjustment of the mould width • Control of the whole casting process • Protection of the molten steel during the flow from the ladle to the mould in order to avoid exposure to air which leads to reactions with oxygen

1.4.2 Principle and technologies

Although the continuous casting has a higher capital cost, it is the most efficient way to solidify large volumes of liquid steel into a variety of sizes and shapes. Developed as an alternative to ingot casting, the continuous casting has however a lower operating cost. Many different types of continuous casting processes exist. Fig. 1.18 pictures the curved one used in the majority of steel plants. The slab is bent with a radius of about 10 to 15m. It is then straightened as soon as the steel is completely solidified.
Other types exist and are distinguished by their geometries. Vertical machines, in which the mould, the rolls and the cutoff system are aligned, are used to cast aluminum and other metals but they are relatively rare nowadays. Horizontal casting did not gain widespread use and is occasionally employed for non-ferrous alloys. Finally, thin strip machines are used as well to cast steel and other metals for special markets. They do not require an important investment in rolling system.

Fig. 1.18. Global view of the pilot caster (Corus)

The continuous casting machine adopted in this dissertation is the curved one. Fig. 1.19 shows its diagram as found in the plants.

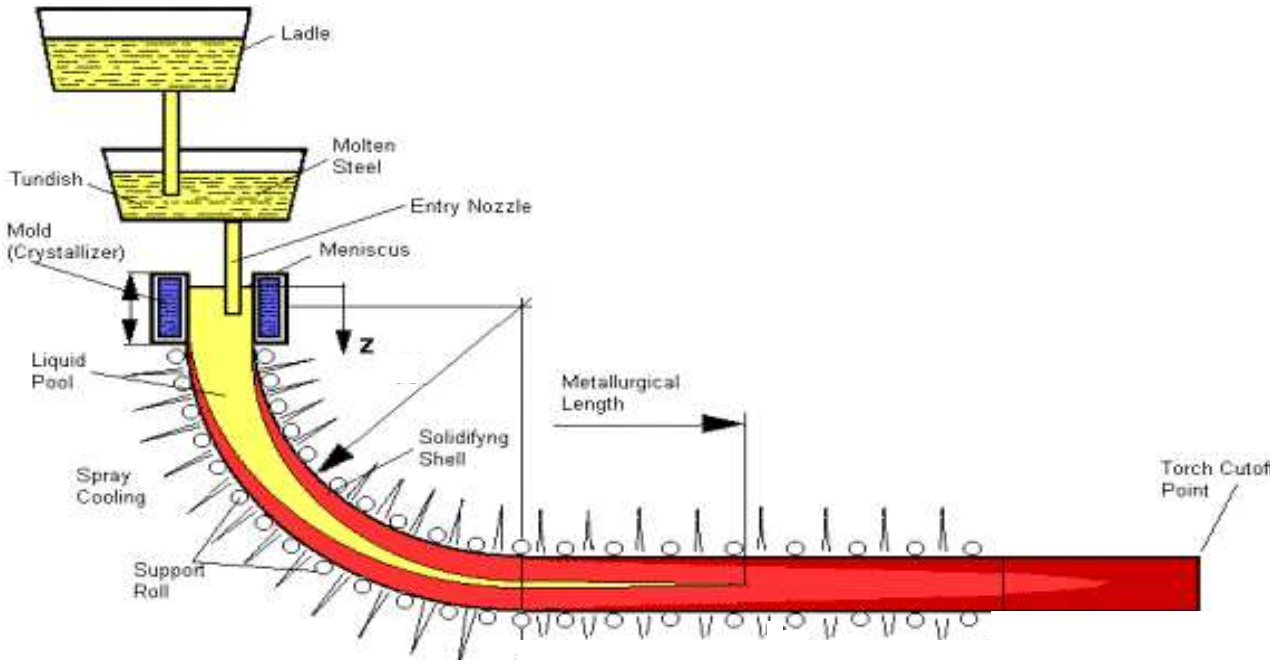

Fig. 1.19. Side view of the continuous casting machine

To understand the basic principles of continuous casting, one should split the caster into three zones which are the feeding zone, the solidification zone and the conditioning zone.

- **Feeding zone**

The steel is first introduced in the caster by means of the ladle from which it is poured into a tundish initially used as a reservoir to sustain casting while changing ladle (Fig. 1.20). When the ladle supplying the molten steel to the caster is empty, it is evacuated by the turret which brings in a full one. The liquid is covered with a thin layer of furnace slag because it is essential to maintain its temperature and homogeneity. Sources of heat losses are numerous inside the ladle where the liquid temperature must be sufficiently high.

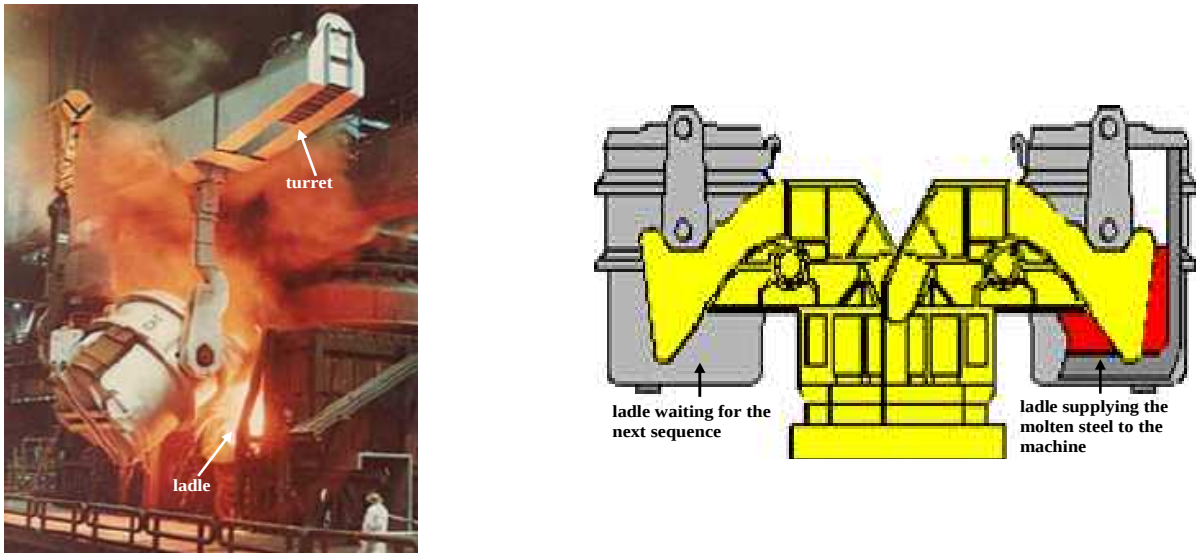

Fig. 1.20. Supply of molten steel to the continuous casting machine

From the tundish, the steel flows into the water cooled mould through the nozzle which plays a major role in the casting process. There are various reasons why the steel is not poured directly from the ladle into the mould. The tundish serves indeed as a metallurgical reaction vessel where quality can be improved. It encourages also uniformity and avoids surface turbulence and vortexing.

In multi-strand machines as pictured in Fig. 1.21, steel flows from the ladle into one or more tundishes and from these to the moulds from one or more nozzles. The flow rate is determined from stopper rod or sliding gate opening and the nozzle cross section.

The nozzle used is of various compositions. Its geometry has an important influence on the liquid flow pattern and the characteristics of jets entering the mould.

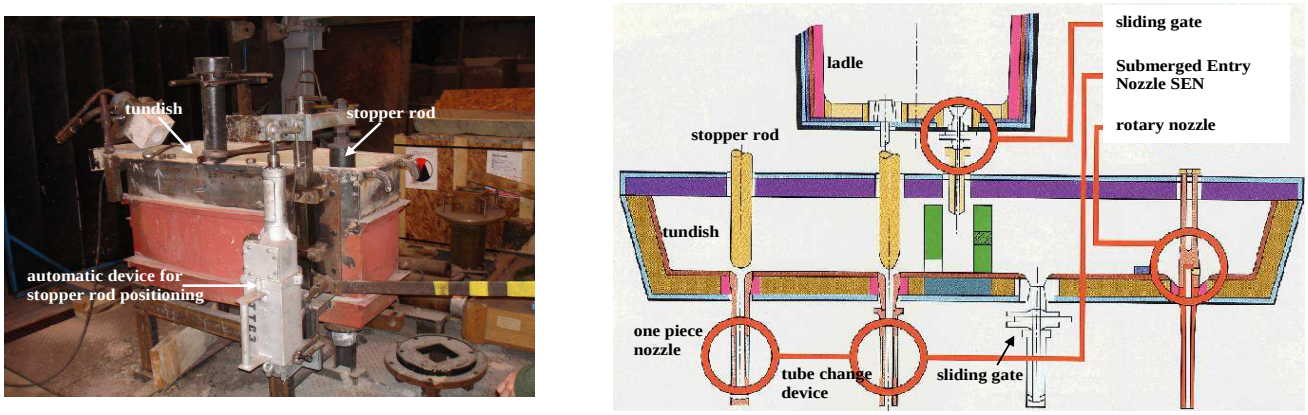

Fig. 1.21. Feeding zone of the continuous casting machine

- **Solidification zone**

The key element of the caster is the mould depicted in Fig. 1.22. This open-ended unit is less than one meter long. Its section is that of the product to be cast. In this regard, the role of mould is to give the suitable geometry to the solidified product.

The walls made from copper are cooled by a high speed water flow. The purpose is to remove just enough heat from steel to form a solid outer skin which will contain the liquid until solidification is completed. The primary cooling of the steel takes place thereby in the mould where about 10% of the heat should be abstracted.

The mould sides are carefully lubricated to decrease the friction with solid shell aided by sinusoidal or triangular oscillations in order to ensure a continuous release of the shell. At commercial withdrawal speeds, this implies to supply a film of about 0.001 inches over mould surfaces [67]. As for sinusoidal oscillations, it is necessary to use long stroke (e.g. 80mm) with low frequency (e.g. 2Hz) for sticker grades and short stroke with high frequency for the others.

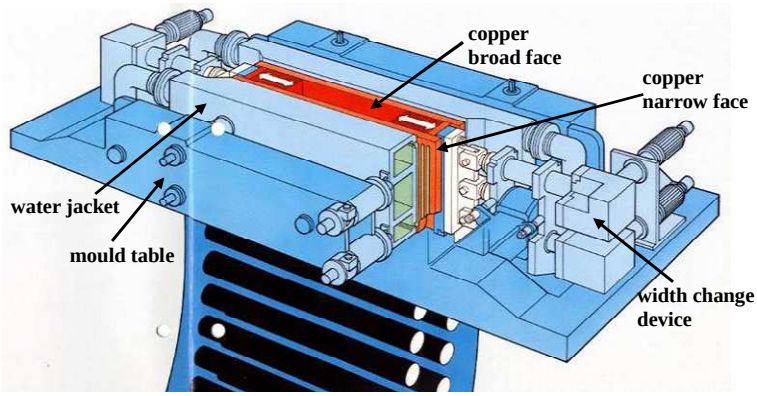

Fig. 1.22. Mould: upper part of the solidification zone

Control of the flow into the mould is achieved by a nozzle and a stopper rod or a slide gate. More precisely, the standard instrumentation of process control includes a sensor to detect level fluctuations, an actuator to adjust the valve opening and a software program implemented in a PLC to deliver the opening setpoint. This controller should perform well over the entire range of operating conditions. This is the most common and serious deficiency of all those currently used in the plants. **The improvement of the control strategies, implemented in this software, is the main object of this doctoral dissertation**.

The secondary cooling starts immediately at the bottom of the mould (Fig. 1.23). In contrast with the primary cooling, here steel is cooled directly by the water jets. They reach all faces of steel allowing thus a heat extraction of about 90%. Cooling conditions depend basically upon several parameters which include the size of the product, the poured grade, the steel quality and degree of cooling already achieved at each point. Prior to being cut by a torch device, the solidified product leaves the cooling system and travels downwards with the help of several pairs of rolls. Their purpose is twofold. The first aspect is to grip the fully solidified bar without deforming it. The second is to control the casting speed at which the bar will emerge for cutting at the exit of the machine.

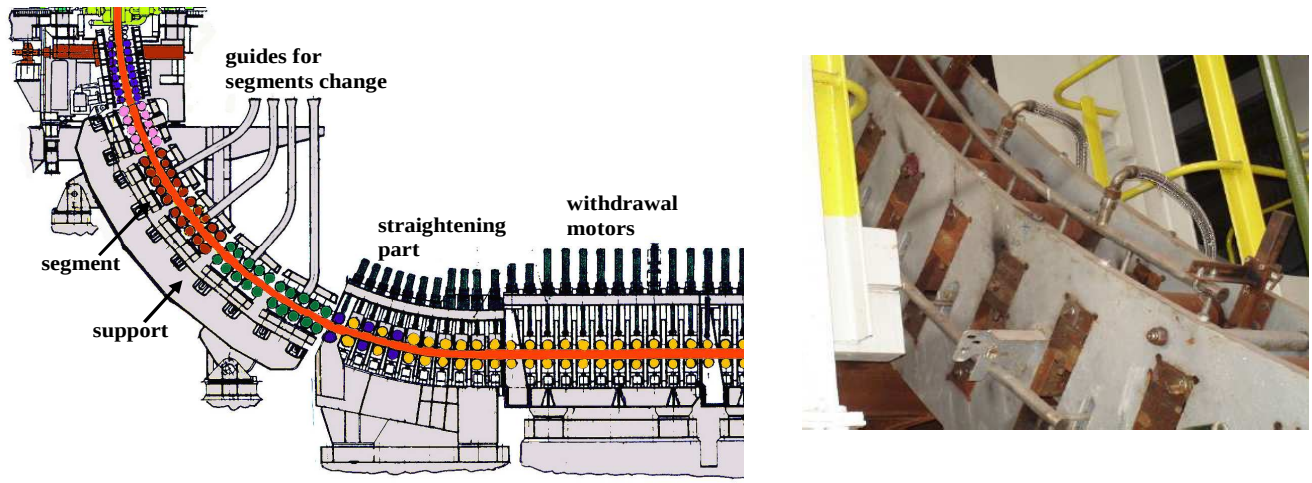

Fig. 1.23. Solidification zone of the continuous casting machine

- **Conditioning zone**

After the product has left the solidification zone and the withdrawal rolls, it will emerge for cutting in a horizontal plane. Fig. 1.24 illustrates the cutoff of a slab by a cutting torch. The appropriate cut section is derived from the customer specifications. Of importance also is the cutting speed which determines the productivity of the machine. Important precautions must be incorporated against cutting system failures.

After cutting is completed, the bar is marked for identification purposes. Then, it is collected on banks or removed directly from the machine as shown in Fig. 1.24. Various arrangements exist to discharge the bars.

Thereafter, the product is stacked up for spray cooling and inspection or loaded for further processing to the hot rolling mill.

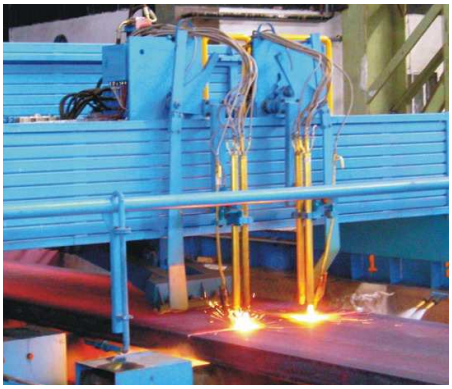


Fig. 1.24. Conditioning zone showing the cutoff and the discharge of the product

1.4.3 Types of products

Different configurations of casting machines exist to produce various shapes and sizes of the semi-finished product. Table 1.3 gives a list of cast products. More specifically, the billet has a square section up to 200mm^2 and is rolled into long products such as bars, springs and axles. The bloom has the same square geometry up to 450mm^2 and is most suitable for bars and rails. Belonging to the same products family, other shapes are commonly produced such as round billets used in seamless pipe manufacturing.

The slabs belong to the second family so-called flat products, and are characterized by a rectangular section from 150 to 300mm thick and from 900 to 2700mm wide. They are designed for plates and sheets. **This doctoral dissertation is devoted to this type of product.**

Table 1.3. Types of products cast in continuous casting machines

	FLAT PRODUCTS	**LONG PRODUCTS**				
Type	**SLAB**	**BLOOM**	**BILLET**	**ROUND**	**HEXAGON**	**BEAM BLANK**
Shape						
Picture						
Dimensions (mm²)	900-2700 × 150-300	200-450 × 200-450	100-200 × 100-200	∅ = 90-240mm		
Applications	Heavy plates Thin sheets Strips	Bars Beams Rails Piles	Wires Springs Axles	Tubes without welding		(I - H) beams

1.4.4 Defects from level variations

The surfaces of semi-finished products suffer from a variety of defects. Problem sources include: the entrapment of argon bubbles and solid inclusions, entrainment of mould slag due to level fluctuations and breakouts. All these problems are ascribed to fluid flow in the continuous casting process. Because it is the last liquid processing step, the caster is always equipped with a monitoring system to detect abnormal operating conditions which may lead to defects that cannot be eliminated after the casting stage. Each of these defects will be discussed in turn.

1.4.4.1 Longitudinal cracks

This type of cracks is generally located within 100mm from the slab axis at the bottom of a surface depression, through a thinner shell. Its length varies from a few centimeters to some meters. Fig. 1.25 shows an example where a longitudinal crack was caused by a variation of mould level larger than 10mm. Rapid changes in casting speed can also lead to the formation of longitudinal cracks. On the other hand, the influence of mould powder has also been demonstrated.
The crystallization of mould powder is necessary to avoid the production of such defects.

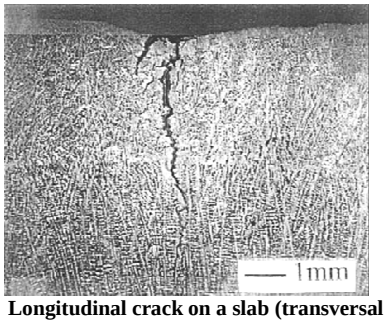

Fig. 1.25. Longitudinal crack on a slab (transversal section)

1.4.4.2 Transverse corner cracks

Transverse cracks are mainly met on medium carbon steels. They are located at the bottom of oscillation marks. An example is shown in Fig. 1.26. Once more, variations of the mould level appear to be the major cause responsible for these defects.

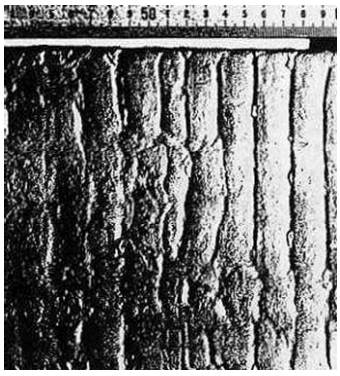

Fig. 1.26. Transverse cracks on a slab (longitudinal section)

Minimizing the sulphur content as well as the maintenance of the caster (rolls alignment, water amount distribution in secondary zone…) tends to reduce these defects.

1.4.4.3 Internal segregated cracks

They have an important impact on the quality of final product since they reduce its toughness properties. Fig. 1.27 displays an example of internal defects.
Internal cracks are formed as a result of too intense or uneven cooling by water sprays. The geometry of withdrawal rolls as well as the high sulphur proportion in the steel also contributes to internal defects formation [65].

Furthermore, these defects are directly related to the entrapment of the inclusions and the gas bubbles in the solidifying strand, especially during nozzle clogging or transient operations.

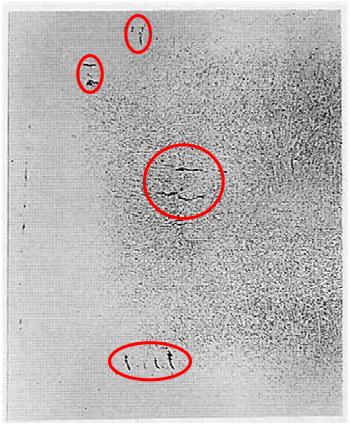

Fig. 1.27. Sulphur print on transverse section near slab small face

1.4.4.4 Axial segregated defects

They take the form of a central porosity probably caused by an incorrect secondary cooling and difficulties to maintain a liquid central core which is too long especially in curved mould machines (Fig. 1.28). Normally, these defects may disappear during rolling.

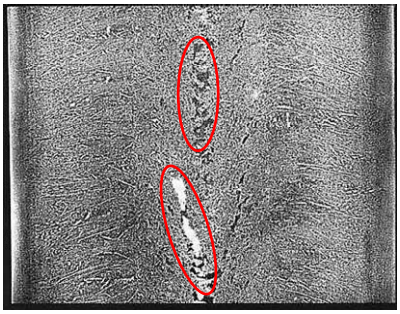

Fig. 1.28. Axial segregated defects on slab longitudinal section

1.4.5 Mould level disturbances

As it has been mentioned in the caster description, one of the most critical parts of this process is the initial solidification in the mould because this is where the surface of the final product is formed as illustrated below in Fig. 1.29. A slag layer is added to the liquid free surface in order to protect it against air and to lubricate the junction between the mould and the solidified shell. Unfortunately, mould level fluctuations are high in this region, so slag entrainment leading to surface defects is likely.

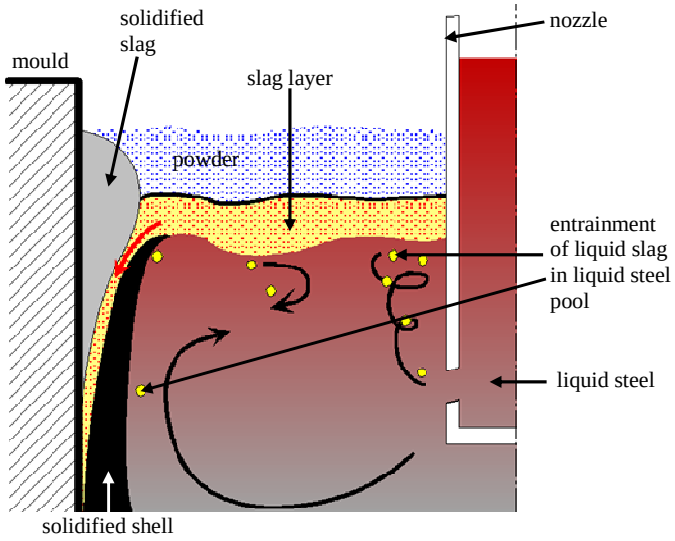

Fig. 1.29. Schematic of the mould region showing nozzle and meniscus

Level variations have many causes. Table 1.4 lists the important disturbances which contribute to local level fluctuations. First of all, there are the periodic events such as the bulging which takes place in the secondary cooling zone but has a detrimental effect on the mould level. Their frequency ranges are given in Fig. 1.30.
On the other hand, the turbulent nature of the flow in the meniscus region increases also level fluctuations. Additionally, other phenomena disturb the hydrodynamics inside the mould especially the biased flows and the standing waves generated by electromagnetic stirring. The second category regroups the slow disturbances which develop progressively with time. Amongst them, the most disruptive one is the clogging.
The third category includes the sudden problems such as the unclogging which is likely to happen after clogging, causing thereby significant changes in the flow into the mould. Because the control loop has always difficulties to compensate for these changes, an abrupt increase in the level occurs leading sometimes to overflows.

Table 1.4. Types of mould level disturbances

Periodic disturbances	Slow disturbances	Sudden disturbances
Biased flows	Clogging	Unclogging
Bulging	Argon bubbles	Sudden changes of casting speed
Standing waves	Change of liquid height in tundish	
Mould oscillations	Breakouts	
Actuator backlash	Nonlinear characteristics of the control valve	
Containment rolls eccentricity	Problems with level control feedback	

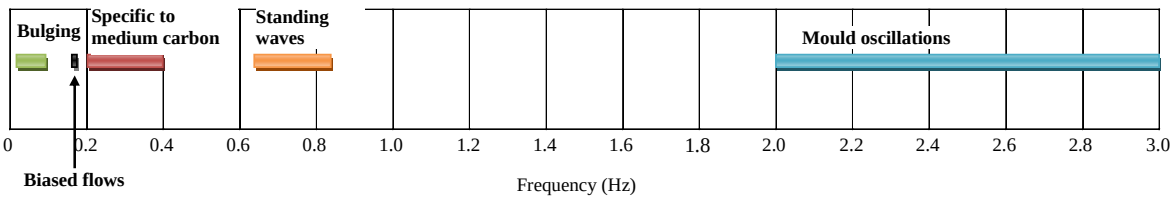

Fig. 1.30. Frequency ranges of periodic disturbances

1.4.6 Online measurements and control systems

The continuous casting is a complex heat exchanger which must be monitored to detect abnormal conditions leading to defects on semi-finished product or to casting incidents. A complete process control is based on the use of a large number of sensors and actuators. The appropriate sensors are located along the caster including the ladle-tundish area, the mould, the secondary cooling and the conditioning zone.

- **Ladle-tundish**

In this part of the caster, two parameters have to be controlled [70]:

- The steel level inside the tundish, that must be kept constant apart from transient periods such as the beginning or the end of the sequence.
- The liquid slag poured from the ladle into the tundish.

- **Mould**

Several useful measurements are collected to ensure the mould monitoring activities. They are used as part of control systems or as indices for quality prediction schemes. Amongst these signals, one should list:

- Mould steel level,
- Mould vertical displacement and acceleration (measured by LVDTs and accelerometers),
- Stopper rod position,
- Strand casting speed,
- Mould cooling water temperature, water temperature increase in the mould,
- Copper plates temperature (measured by thermocouples),
- Tundish weight and temperature,
- Electrical current intensity of the mould oscillator motor,
- Friction force between the solidified shell and the mould,
- Electrical current intensity of the withdrawal rolls motors.

In this research work, the idea is to develop a robust control structure able to stabilize the mould level and to lower the disturbances effect for all possible casting conditions.

- **Secondary cooling**

In this region, it is important to control the thermal state of steel from the mould exit until the solidification is completed. Thus, it is a common practice to control the pressure and the flow rate characteristics of the different spray zones.
Additionally, three measurements are performed [70]:

- The slab surface temperature using two-color pyrometers associated with optical fibers.
- The solidified shell thickness from the difference in ultrasonic velocity between liquid and solid steel.
- Solidified shell bulging.

- **Conditioning zone**

In this section of the machine, the geometry of the withdrawal and straightening rolls is of great importance. It impacts directly the product emerging from the caster as well as the solidification process.
The following parameters can be measured [70]:

- Rolls position and displacement (measured by ultrasonic sensors),
- Rolls eccentricities,
- Efforts applied on the rolls (measured by load cells),
- Spray water distribution in the gaps between rolls.

As a matter of fact, it is somewhat difficult to monitor the entire zone due to the large number of rolls. In the plants, the monitoring is focused on the region at the end of liquid pool.

1.4.7 Emerging developments

The above elements illustrate the technical development achieved hitherto in the continuous casting process. A revolutionary technology is likely to emerge in the short or mid-term, backed up by many advanced research studies and industrial experiments.

This technology so-called Hollow Jet Nozzle (HJN) is shown in Fig. 1.31. A special nozzle is installed between the tundish and the mould. The objective is to create and maintain a 'hollow jet' inside. A thin layer of molten steel coming from the tundish, flows over a refractory dome. Once in the nozzle, two sources extract the heat without any risk of clogging. The first one is the copper tubes cooled by the water jacket. The second one is the iron powder fed by means of a screw conveyor through the refractory dome. Its injection in the centre of the HJN nozzle whereupon the liquid free surface takes place, is ensured by the hollow jet created.

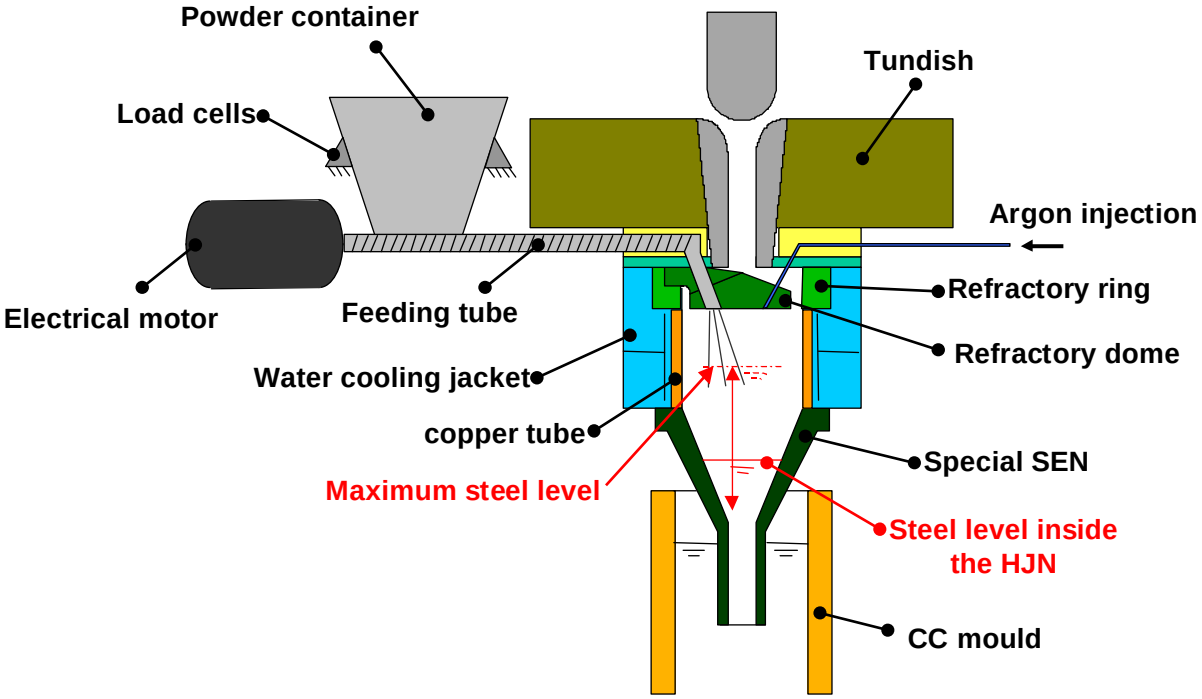

Fig. 1.31. Hollow Jet Nozzle (HJN) principle

As a first advantage, this technique aims to obtain pasty steel in the nozzle before its entry to the mould. This is accomplished by increasing the area of thermal exchange thanks to the dome which trickles down the molten steel in a thin layer along the nozzle walls. The excess of heat is thus removed in the nozzle contrary to what happens in the case of a conventional Submerged Entry Nozzle (SEN). Therefore, such a technique can be used to reduce the superheat of steel entering the mould. This will reduce probably the axial segregated defects of high carbon steels and alloys.

Another advantage that should be mentioned concerns the possibility to obtain fine and homogenous structures by creating new solidification seeds.

1.5 Instrumentation for mould level control

In the continuous casting process, the instrumentation used for mould level control is made up of two components as it is usually the case for all control issues. The first device has to control the flow from the tundish into the mould. This task is performed by means of a mobile valve and a nozzle. The second component is the monitoring system used to detect level variations in the mould. The purpose of this section is to summarize the different technologies employed in the steelworks.

1.5.1 Flow control devices

1.5.1.1 Valve

At present, there appear to be at least two schools of thought concerning the nature of the control valve. In fact, the flow rate is controlled by restricting the narrow passage between the tundish and the nozzle with either a stopper rod widely used in Europe or a slide gate whose use is almost universal in North America. The two systems are illustrated in Fig. 1.32. Control using a stopper rod is more difficult since the valve is submerged in the molten steel inside the tundish. Moreover, the effective flow area is highly sensitive to its displacement. However, it is installed in a huge number of plants and is found to be of much advantage compared to slide gate especially in preventing vortex formation above the tundish well and in distributing uniformly the flow to both ports of nozzle [67].

Another type is reported in literature [7] and shown in Fig. 1.32. The principle of the Vaterlaus valve is to produce vortexing in the nozzle in order to weaken the liquid movement inside the mould. No further published information is available at the time of writing this dissertation.

Stopper rod (Vesuvius) ***Sliding gate (Vesuvius)*** ***Vaterlaus valve***

Fig. 1.32. Types of flow control valves

1.5.1.2 Submerged Entry Nozzle (SEN)

Associated with the flow control valve, the nozzle has other complementary functions:

- Control of the delivery of steel into the mould,
- Protection of molten steel from reoxidation and heat losses,
- Control of the liquid flow pattern inside the mould.

The nozzles in use in the plants are of various compositions and have for the most part simple geometries as illustrated at first glance in Fig. 1.33 or with greater detail in Fig. 1.34.

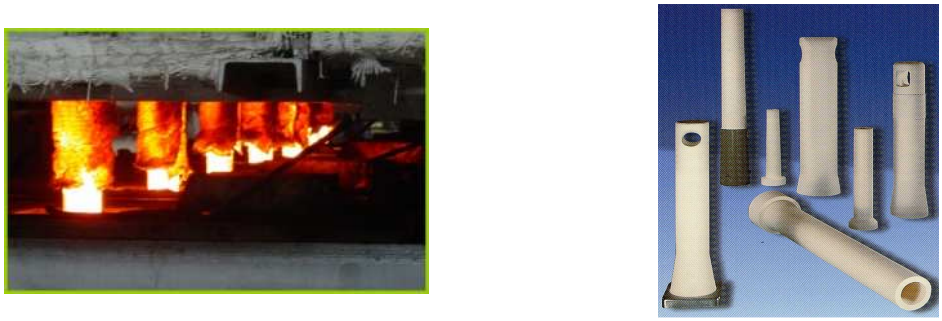

Fig. 1.33. Different types of nozzles

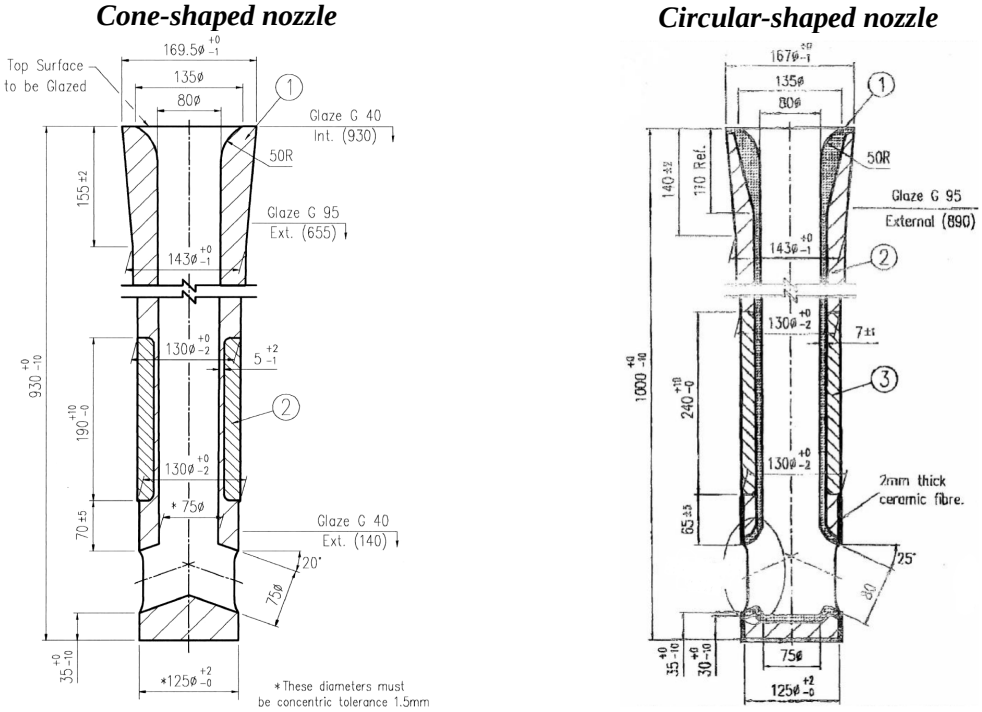

Fig. 1.34. General design of typical nozzles

The nozzles are relatively inexpensive to change and it is thus possible to test different configurations in order to obtain an optimum SEN design (using FLUENT's package for example).

The nozzles have two ports each discharging the molten steel in opposite directions along the large faces of the mould. Their most suitable length has been established to lie between 0.6 and 1.3m.

Two general procedures of nozzle submergence are practiced. The first consists of imposing a sine-type variation less than 200mm with a period of about a half an hour. In the latter case, the nozzle is maintained at a certain submergence depth that the operator proceeds to change by a few millimeters at the end of each casting sequence.

1.5.2 Mould level sensor

A wide variety of methods are used to measure the metal level. Firstly, it is important to notice that this measurement should not be confused with the measurement of level fluctuations. Moreover, the control of the flow rate into the mould requires the knowledge of only the average liquid level measured directly in different ways, which include the NKK sensor, radioactive systems and electromagnetic methods. As for local level variations, they can be examined by combining information from level sensor, thermocouples signals and semi-finished product defects.

All the methods used to measure the average level have limitations in accuracy and reliability as summarized in Table 1.5. The most common systems are the following:

- **Eddy current system (NKK):** It is based on the effect of induced eddy currents on the electromagnetic field generated by sensor coils. Using this technique which operates above the steel meniscus, it is possible to reach a high accuracy and avoid the slag layer effect.
- **VUHZ [36]:** These electromagnetic devices have immunity to mould powder and are widely used in slab casting. They rely on primary coils which induce magnetic fields whose effect on molten steel is measured by secondary coils.
- **Radioactive sensors (Berthold) [71]:** Installed outside the mould, radioactive sources such as the Cobalt-60 ^{60}Co or the Caesium-137 ^{137}Cs emit γ-rays which are attenuated as they pass through the mould level. These sensors have a long response time and are sensitive to slag layer. They measure indeed a combination of steel and powder levels. Furthermore, the measurement is corrupted by significant noise.
- **Thermocouples:** The level difference near the small faces is derived from the temperature profile in the copper plates of the mould.
- Other methods such as infrared analysis of the free surface, Fakir carpet or external electrodes.

Sensor	Technical characteristics					Advantages	Drawbacks
	Accuracy (mm)	Response time (ms)	Measurement range (mm)	Temperature working range (°C)	Cooling system		
NKK	1	500	0 - 200	20 - 50	Air	Contactless sensor Adjustable location	Sensitive to temperature variations
VUHZ	0.2	< 100	0 - 120	< 50	Water	Low cost (5 times less than NKK) Wide-reaching measure	Narrow bandwidth Sensitive to variations of mould walls temperature Intrusion around the mould area
Berthold	NA	> VUHZ	0 - 100	30	Water	Contactless sensor Small size	Precaution of use Location non-adjustable High noise Slag effect
EMLI	2	NA	20 - 160	NA	NA	Transparent to powder, smoke, slag and dust radiation	Sensitive to external magnetic fields Duration: 2000 hours
Poncet	0.5 - 20	NA	50 - 2000	NA	NA	NA	Slag effect
Ladar	1 - 5	NA	0 - 400	NA	NA	NA	Slag effect Reliability

Table 1.5. Main characteristics of mould level sensors

1.6 Concluding remarks

The continuous casting machine has been described with greater detail in this chapter. Likewise, its peremptory role in the manufacture of steel has been developed extensively. Summarizing the advantages of continuous casting, it can be said that it allows lower cost production, higher productivity with better quality. Nonetheless, the improvement of instrumentation and automation existing in the machine still remains a major concern for steelmakers. Sometimes, the casting of certain grades is delicate because a significant number of parameters has to be controlled in order to guarantee a satisfactory quality of the product that emerges from the caster. Among them, those connected to the meniscus region where both liquid and solid steel coexist, are critical since they offer a direct way to monitor casting operations.

In this chapter, special attention was given to solidified product defects caused by level variations within this region. Hence, it is of utmost importance to prevent the occurrence of such variations. Thankfully, there are two techniques in common use for stabilizing the mould level which are the flow into the mould control and casting speed control. Flow control using a stopper rod, a sliding gate or occasionally Vaterlaus valve is the norm in the vast majority of plants, albeit the speed control is still in use in billet casting. For this reason, the scope of this dissertation is dedicated to the first technique.

As for mould level measurement systems, there are two basic types: electromagnetic and radiometric. In spite of its high cost, the first devices are preferred because the measured signal is less noisy and not affected by mould powder.

In the next chapter, we shall examine first the different plant models used to design the mould level control laws with particular emphasis on the centralized model. Next, the most disruptive disturbances will be discussed with particular regard to their effects on the mould level control loop.

CHAPTER 2
Continuous casting process modeling

2.1 Introduction

The previous chapter has shown the necessity for mould level control to ensure a good quality of the solidified steel. In general, it can be stated that both stability and performance robustness are needed to have a stable level in the mould whatever the casting conditions. The purpose of this chapter is to develop an accurate model of all important elements involved in the control loop including the disturbances. This model, identified in chapter 3, will be further used to synthesize a robust control law in chapters 4 and 5. The adjective 'robust' means that the control loop should remain stable and meet the required specifications for all configurations.
The structure of this chapter is as follows. In section 2, a review of the most frequent models is presented. Section 3 describes the three disruptive disturbances and discusses their effects on the control loop. In the chapter summary, the behavioral integral model is given taking into consideration only the static balance between the flow into and the flow out of the mould.

2.2 Process modeling

Fig. 2.1 depicts the parts of the casting machine that are involved in the mould level control.

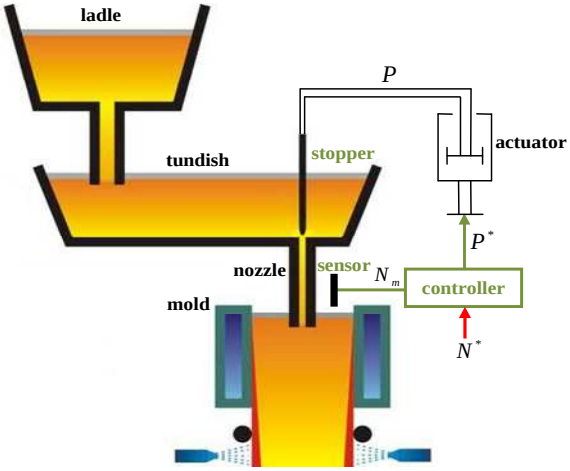

Fig. 2.1. Mould level control structure

Let us first establish some notation:

- P^*: Stopper position setpoint,
- P: Measured stopper position,
- Q_{in}: Flow into the mould,
- Q_{out}: Flow out of the mould,
- N: Theoretical mould level,
- N_m: Measured mould level,
- N^*: Level setpoint,
- S: Mould section,
- s: Laplace variable.

The local measurement provided by level sensor N_m is fed into a control computer which compares it to a setpoint N^* (set by the operator) and calculates a control signal P^* able to compensate the difference. This signal which is in reality the stopper position setpoint, is sent to the actuator in order to move the stopper vertically to adjust the ingoing flow into the mould Q_{in}. As for the flow out of the mould Q_{out}, it is set by the operator from the angular speed of the driven rolls.
The idea is to develop the plant model between the stopper position setpoint P^* and the measured level N_m. This section presents a couple of models. The first one is based on an analysis of liquid steel dynamics. The physical phenomena taking place in the mould are thereby taken into account in the control problem. This model so-called 'distributed model' captures more details as the free surface motion with time, in contrast to the second model so called 'centralized model', which considers the free surface static and completely determined from the balance

between the flow into the mould and the casting speed. From the outset, this is the model adopted by the vast majority of steelmakers to develop a controller for mould level, unlike the first technology whose effectiveness has been evaluated only recently during high speed casting operations in Japan.

2.2.1 Distributed model (numerical fluid dynamics method)

Most of the research undertaken to investigate the fluid dynamics in the nozzle and in the mould was performed by steelmakers in order to better understand and improve the solidification process. In recent years, process control technologists are making it possible to apply mathematical models of turbulent fluid flow as an additional tool to stabilize the mould level.

The purpose of this paragraph is to provide some insight into the mould level control using the numerical fluid dynamics method which consists in tracking the meniscus movement and maintaining the free surface at a constant level by means of a PI controller in the most cases [4] [28]. Fig. 2.2 shows the block diagram of the control loop based on numerical fluid dynamics method. The Large Eddy Simulation (LES) method is used as turbulence model [29] and the Volume Of Fluid method (VOF) is used to track the free surface [30]. From a practical point of view, the distributed model is especially useful in higher speed casting where the flow is more turbulent and the free surface is more fluctuant.

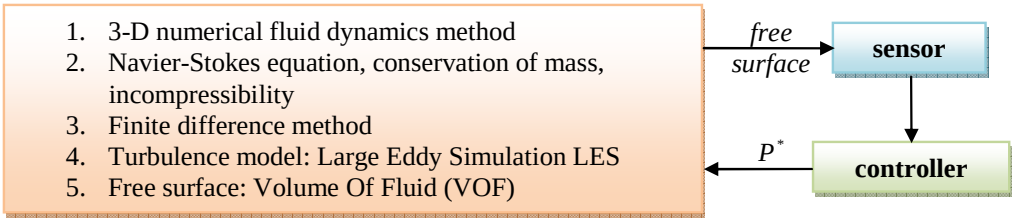

Fig. 2.2. Mould level control loop based on numerical fluid dynamics method

In the mould, the steel is regarded as a non-compressible liquid whose flow is governed by the following partial differential equations [35]:

$$\nabla \vec{u} = 0 \text{ (mass conservation equation)} \tag{2.1}$$

$$\frac{\partial \vec{u}}{\partial t} + \vec{u} \cdot \nabla \vec{u} = -\frac{1}{\rho} \nabla P_r + \nu_e \cdot \nabla^2 \vec{u} + \vec{g} + \vec{F}_w \text{ (momentum conservation equation)} \tag{2.2}$$

where:

$$\vec{u} \cdot \nabla \vec{u} = u_x \cdot \frac{\partial \vec{u}}{\partial x} + u_y \cdot \frac{\partial \vec{u}}{\partial y} + u_z \cdot \frac{\partial \vec{u}}{\partial z}$$

- $\nabla \cdot$: Gradient operator,
- $\nabla^2 \cdot$: Laplace operator,
- $\vec{u}$: Fluid velocity,
- u_x, u_y and u_z: $\vec{u}$ components along x, y and z axis respectively,
- ρ: Liquid steel density,
- P_r: Ferrostatic pressure,
- ν_e: Effective kinematic viscosity,
- $\vec{g}$: Gravitational acceleration,
- $\vec{F}_w$: Wall friction.

The wall friction is proportional to the second power of fluid velocity as follows:

$$\vec{F}_w = -\frac{0.3164}{8\delta} Re^{-1/4} \|\vec{u}\| \vec{u} \tag{2.3}$$

where:

- δ: Distance from the wall in the cell,
- Re: Reynolds number.

In the VOF method, a function f whose value is unity at any point occupied by fluid and zero otherwise is introduced. The value of f represents a fractional volume of the cell occupied by the fluid and satisfies:

$$\frac{\partial f}{\partial t} + \nabla(\vec{u} \cdot f) = 0 \tag{2.4}$$

First, the equations above are discretized. Then, they are solved using the Finite Difference Method (FDM) and the Successive Over Relaxation method (SOR) as a pressure iteration solver [4].
In order to evaluate the free surface velocity, the eddy value is defined as follows:

$$\omega_z = \left| \frac{\partial u_x}{\partial y} - \frac{\partial u_y}{\partial x} \right| \tag{2.5}$$

where u_x and u_y are the velocity components along x-axis and y-axis respectively.
It measures the intensity of the vortex to entrap the powder into the molten steel. When the eddy value is large, free surface velocity has large variation that encourages the formation of vortices [28].
Fig. 2.3 illustrates an example of results achieved with the distributed model. It can be seen that the level is well controlled in the white area where a sensor is provided in contrast to other zones especially near the narrow faces of the mould or around the Submerged Entry Nozzle where the flow is more turbulent (Fig. 2.4). Moreover, the free surface is asymmetric with fewer variations in the controlled side and more fluctuations in the opposite side. This tendency is more obvious in high speed casting.

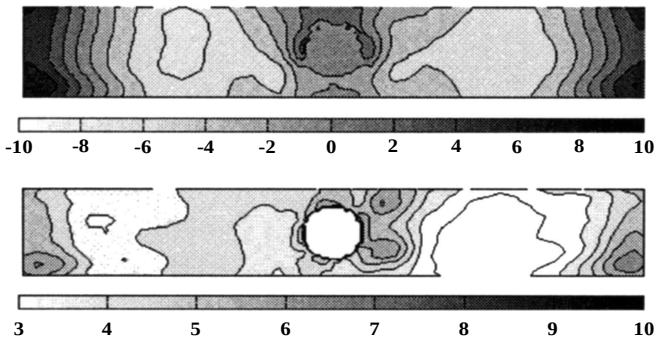

Fig. 2.3. Average and standard deviation of mould level (mm)

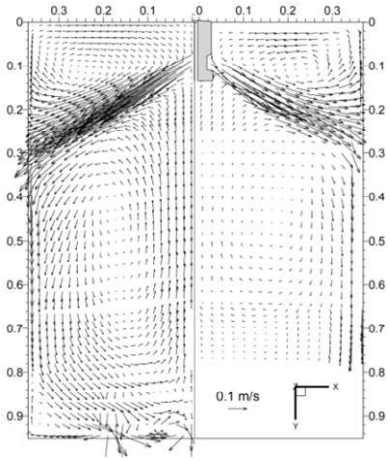

Fig. 2.4. Distribution of velocity vector time average

These observations only revealed by the distributed model are important for practical mould level control. They give a clear indication on the physical phenomena to be controlled and are very useful for evaluation of the controller performances as well as for an optimal positioning of the level sensor. However, this model appears to be too complex for control law design purposes.

2.2.2 Centralized model

Based on the previous remark, a simple model used afterwards for control law design is detailed below.
Fig. 2.5 shows a basic block diagram for the centralized plant model. It will be extended subsequently to include in particular some disturbances.

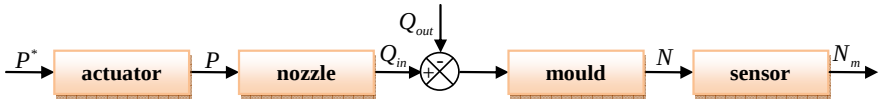

Fig. 2.5. Plant model

The development hereafter is focused on the transfer functions of the actuator, the nozzle, the outgoing flow, the mould and the level sensor in order to determine the plant dynamics. The flow into the mould Q_{in} cannot be measured contrary to the flow out of the mould Q_{out} directly related to the casting speed.

2.2.2.1 Mould

Contrary to the numerical fluid dynamics method, in the centralized model, the turbulence of molten steel flow is ignored. The mould is regarded as a tank with one input Q_{in} and one output Q_{out}. The equation governing the level N is merely given by:

$$\frac{dN}{dt} = \frac{Q_{in} - Q_{out}}{S} \tag{2.6}$$

where S is the mould section.
The resulting transfer function from the difference between Q_{in} and Q_{out} to N is:

$$TF_{mould} = \frac{1}{S \cdot s} \tag{2.7}$$

The mould section S is variable particularly during start-up stages. For instance, its width may vary from 850 to 2050mm. The current controllers are fixed and not designed to run with this parameter variation leading usually to low performances and at times to instability problems.
Sometimes, the section used in this transfer function is the cross section area of the free surface which differs from the mould section.

2.2.2.2 Level sensor

In the previous chapter, the sensors used to measure mould level have been presented. Mould level can indeed be measured directly in several ways, which include NKK eddy-current sensor, radioactive sources or electromagnetic methods. Contrary to the distributed model, control flow loop of the centralized model requires only the measurement of the moving average level in the mould. In practice, operators use to position the sensor in the most stable regions in order to avoid transient fluctuations. Additionally, the sensors listed above are known to be influenced by noise. Therefore, it is of benefit for control loop if the measurement is filtered to reject noise as well as local fluctuations which are not directly related to the mean level. Nevertheless, it is noteworthy to mention that quality detection systems should monitor the unfiltered signal because these local fluctuations are important to surface quality.
In the sequel, the level sensor is of NKK type. Its dynamic response is modeled by a simple first order transfer function:

$$TF_{sensor} = \frac{1}{1 + \tau_s \cdot s} \tag{2.8}$$

where τ_s is the sensor time constant.

2.2.2.3 Inflow/Nozzle

To derive a model for the flow rate into the mould, one should use the basic laws of physics. Then, the flow dynamics through the nozzle should be taken into consideration.
Whatever the control valve (stopper rod or sliding gate), Q_{in} is governed by the following equation widely adopted in literature [6] [35] and derived from Bernoulli's equation:

$$Q_{in} = \beta \cdot A_v \cdot \sqrt{2gN_{tun}} \tag{2.9}$$

with:

- β : Coefficient of discharge,
- A_v : Effective flow area,
- g : Gravitational acceleration,
- N_{tun} : Height of liquid steel in the tundish.

The coefficient of discharge is related to the liquid viscosity which decreases the pouring velocity exiting the flow control zone. The effective flow area A_v is determined from the control valve position and the cross section of the nozzle.
In respect to the flow dynamics through the nozzle, it is important to include a delay in the transfer function, assumed to be linked to the argon injection into many locations. Furthermore, its presence is profitable, all the

more so since it may be at the origin of many stability problems of the control loop often encountered in the plants. In addition, one can detect it experimentally with the help of some identification trials by comparing the mould level signal to the control valve position signal.
A first approximation may be obtained from the Newton's laws:

$$\tau_n = \sqrt{\frac{2(N_{tun} + N_{SEN})}{g}} - \sqrt{\frac{2N_{tun}}{g}} \tag{2.10}$$

where N_{SEN} is the height of the liquid steel from to the nozzle upper well to the mould free surface in contact with the slag (Fig. 2.6).
Nevertheless, the actual value should be identified from measurement signals.
All that remains is to give an explicit expression of the effective flow area A_v. To achieve this, one should consider the distinctive features of each control valve.

2.2.2.3.1 Stopper rod

Fig. 2.6 shows the geometry of the flow control zone between the stopper and the nozzle. Starting from an initial position which closes entirely the liquid flow passage, the actuator moves the stopper vertically to adjust the flow rate into the mould according to the casting speed. The actual stopper position is subsequently multiplied by a proportional gain resulting in the effective flow area. Beyond a certain position P_0, the nozzle cross section limits the ingoing flow and the effective flow area is equal to the cross section of the nozzle. This leads to the characteristic curve illustrated in Fig. 2.7.

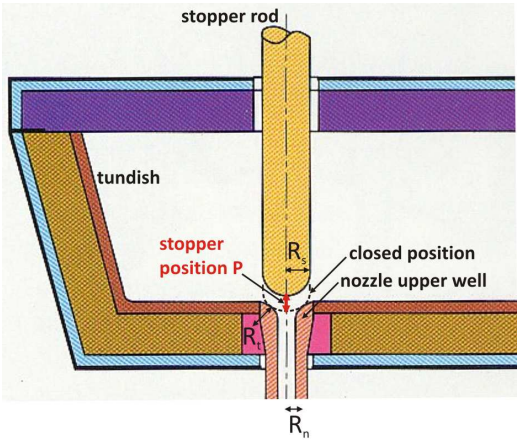

Fig. 2.6. Control zone geometry

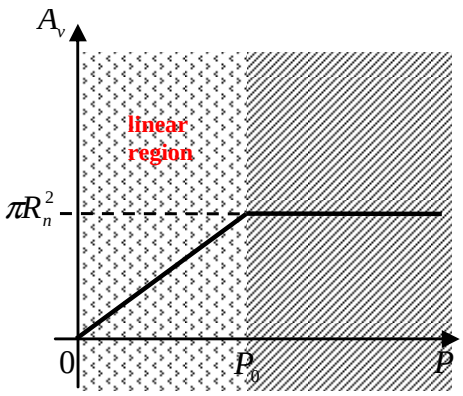

Fig. 2.7. Effective flow area depending on the stopper position

Assuming that the stopper position is small compared to the three radii denoted R_s, R_n and R_t in Fig. 2.6, the actual flow area is given by the following equations:

$$\begin{aligned} P \prec P_0 \qquad & A_v \approx \frac{2\pi \cdot (R_t + R_n) \cdot R_s}{(R_s + R_t)^2} \sqrt{(R_s + R_t)^2 - (R_t + R_n)^2} \cdot P \\ P \geq P_0 \qquad & A_v = \pi R_n^2 \end{aligned} \tag{2.11}$$

where:

- R_s: Stopper radius,
- R_n: Nozzle radius,
- R_t: Radius of nozzle upper well.

P_0 can be determined by calculating the limit of the first equation (2.11) when the stopper position approaches P_0.

$$P_0 = \frac{\pi R_n^2}{\frac{2\pi \cdot (R_t + R_n) \cdot R_s}{(R_s + R_t)^2} \sqrt{(R_s + R_t)^2 - (R_t + R_n)^2}} \tag{2.12}$$

In practice, normal casting conditions ensure that the stopper position does not exceed P_0. Hence, the stopper displacement holds in the linear region leading to the following ingoing flow equation:

$$Q_{in}(t) = G_n P(t-\tau_n)$$

$$G_n = \beta\sqrt{2gN_{tun}}\left(\frac{2\pi\cdot(R_t+R_n)\cdot R_s}{(R_s+R_t)^2}\sqrt{(R_s+R_t)^2-(R_t+R_n)^2}\right) \qquad \tau_n = \sqrt{\frac{2(N_{tun}+N_{SEN})}{g}}-\sqrt{\frac{2N_{tun}}{g}} \tag{2.13}$$

2.2.2.3.2 Sliding gate

Although the control valve adopted in this dissertation is the stopper rod, the objective of this paragraph, is to explain how another control valve (here the sliding gate) impacts the effective flow rate.
In this system pictured in Fig. 2.8, there are three plates. The central one is moved by means of a hydraulic actuator to adjust the opening between the upper and lower stationary plates. The Submerged Entry Nozzle (SEN) is attached to the moving plate and travels to control the flow into the mould cavity.

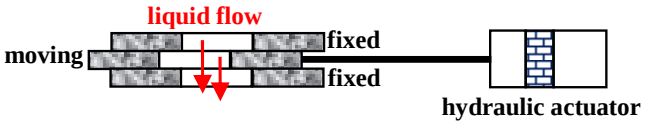

Fig. 2.8. Sliding gate (side view)

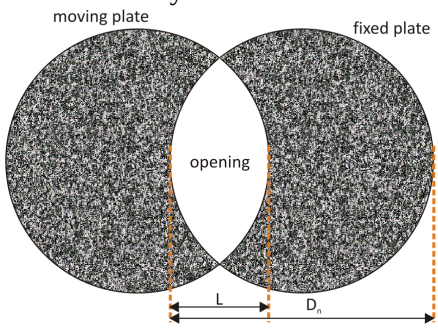

Fig. 2.9. Sliding gate (plan view)

Elementary trigonometric considerations show that the effective flow area is governed by the length of opening as follows:

$$A_v = 2R_n^2\left(\cos^{-1}\left(1-\frac{L}{2R_n}\right)-\left(1-\frac{L}{2R_n}\right)\sqrt{1-\left(1-\frac{L}{2R_n}\right)^2}\right) \tag{2.14}$$

where:

- L : Length of opening,
- R_n : Nozzle radius (equal to $D_n/2$).

The steel flow rate is thus mainly influenced by the length of opening and the nozzle bore size. Under ideal conditions, it may be quantified by:

$$Q_{in}(t) = G_n(t)\cdot L(t-\tau_n)$$

$$G_n(t) = 2\beta R_n^2\sqrt{2gN_{tun}}\left(\cos^{-1}\left(1-\frac{L(t)}{2R_n}\right)-\left(1-\frac{L(t)}{2R_n}\right)\sqrt{1-\left(1-\frac{L(t)}{2R_n}\right)^2}\right) \qquad \tau_n = \sqrt{\frac{2(N_{tun}+N_{SEN})}{g}}-\sqrt{\frac{2N_{tun}}{g}} \tag{2.15}$$

Clearly, this exact model is non linear due to the geometry of the circular orifices. It could be linearized by a static characteristic curve.

2.2.2.4 Outflow

In the absence of any disturbance, the flow out of the mould Q_{out} is determined from the casting speed v (set by the operator) and the mould section S. It is calculated as follows:

$$Q_{out} = S\cdot v \tag{2.16}$$

These two parameters change during casting. v should be considered as a setpoint and not a measurement. This equation should be completed by disturbances acting on the outflow, especially the bulging.

2.2.2.5 Actuator

The actuator designates the transfer between the control signal P^* and the stopper position P which is controlled by means of its velocity v_p through a proportional gain in the vast majority of cases (Fig. 2.10).

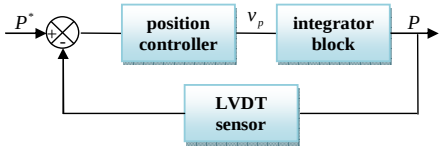

Fig. 2.10. Actuator block diagram

The objective of this first inner loop is to maintain the stopper position measured by a LVDT (Linear Variable Displacement Transducer) sensor at the stopper position setpoint delivered by the main controller. Without loss of generality, the position sensor dynamics has been neglected. As a result, the actuator will be considered as a first order function:

$$TF_{actuator} = \frac{1}{1+\tau_a \cdot s} \tag{2.17}$$

where τ_a is the actuator time constant.
In other configurations, the actuator is modeled by a second order transfer function as follows:

$$TF_{actuator} = \frac{1}{1+\frac{1}{G_a}s+\frac{\tau_a}{G_a}s^2} \tag{2.18}$$

All these parameters appearing in the actuator transfer function are fixed and given by the manufacturer.

2.2.2.6 Block diagram

By considering the different blocks, Fig. 2.11 depicts the global plant model.

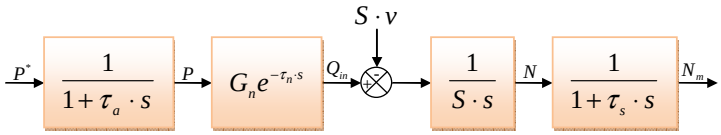

Fig. 2.11. Plant model transfer function

Therefore, as a conclusion of this section, the transfer function of the global plant model is given by:

$$TF_{model} = \frac{G_n e^{-\tau_n \cdot s}}{S \cdot s \cdot (1+\tau_a \cdot s) \cdot (1+\tau_s \cdot s)} \tag{2.19}$$

where:

- G_n : Nozzle gain ($l \cdot s^{-1} \cdot mm^{-1}$),
- τ_n : Nozzle delay (s),
- S : Mould section (mm^2),
- τ_a : Actuator time constant (s),
- τ_s : Level sensor time constant (s).

The identification of this transfer function will be addressed in the next chapter. Meanwhile, Table 2.1 provides some typical values coming from a real plant. They will be considered in all the developments below.

Table 2.1. Typical numerical values of model parameters

Parameter	Value
τ_a	0.05s
τ_n	0.5s
τ_s	0.01s
G_n	$10^6 mm^3/s/mm$
S	$1600 \times 228 mm^2$
v	$1.5 m \cdot min^{-1}$

2.3 Disturbances

2.3.1 Introduction

In the continuous casting process, several disturbances take place at different parts of the machine. They have been introduced in the first chapter. In this section, the three important ones which cause considerable troubles are described. Another aspect being investigated is their effects on the level control loop performances. A model for each disturbance is thereby derived and added to the plant model of Fig. 2.11, which will be used to design different control strategies presented in the next chapters.

2.3.2 Clogging/unclogging cycle

2.3.2.1 Description

Nozzle clogging in continuous casting is a serious problem for aluminum killed steels since it increases operating costs and decreases caster productivity. During the steel flow from the tundish into the mould, some clogs appear as a result of alumina and other solid inclusions deposition (Fig. 2.12). They take place essentially at the nozzle wall but can occur anywhere inside the nozzle. In practice, there are many forms of nozzle clogging. The first one is the deposition of solid inclusions already present in the steel. The second one is attributed to reactions between aluminum present in the steel and the oxygen coming from inside the nozzle (i.e. refractory) or outside through cracks. Finally, the steel could also be solidified in the nozzle as a result of heat losses [2]. Therefore, these forms prove that there are many factors behind the clogging, in particular, the steel cleanness and its aluminum content, the geometry and the material of the nozzle. In addition, the heat transfer inside the nozzle might strengthen the clog and help it to grow further.

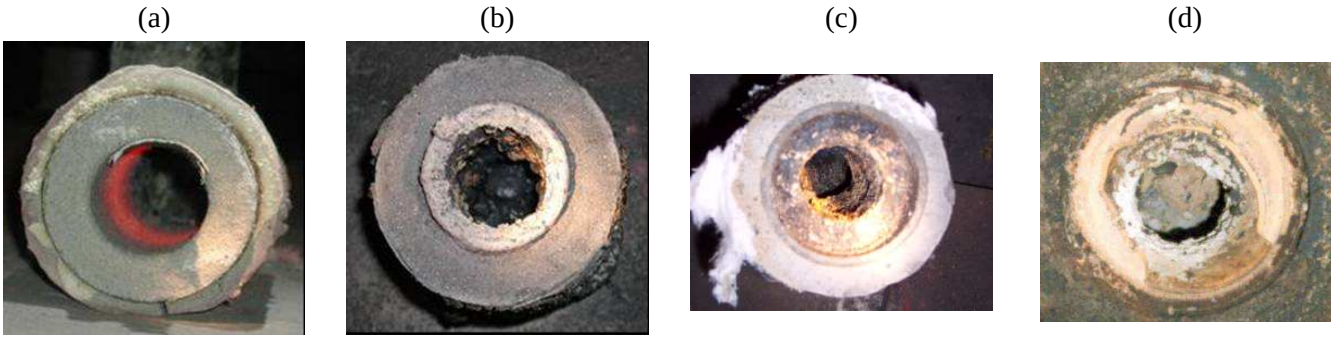

Fig. 2.12. (a): New nozzle, (b), (c) and (d): Clogged nozzles

In the plants, the clogging/unclogging follows the cycle displayed in Fig. 2.13. It is not an instantaneous phenomenon but it develops slowly with time. After an initial clog layer of some millimeters, other clogs appear and take the form of a uniform film generated by chemical reactions. The unclogging occurs after a random period generally between 10 seconds and 2 hours. The amount of the clogs leaving the nozzle walls cannot be predicted in advance.

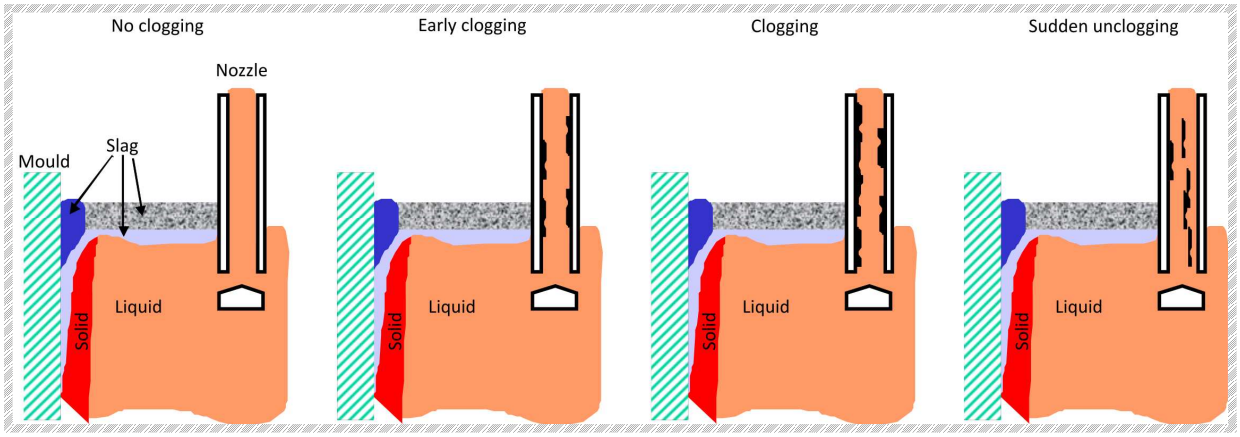

Fig. 2.13. Clogging/unclogging cycle

In order to develop an accurate model of the clogging effect on the mould level, it is necessary to identify how this cycle disturbs the control loop. It is noteworthy to mention that, initially, the clogging increases the flow before restricting it [2].
The caster has a control zone located between the nose of the stopper and the entry portion of the nozzle. As shown in Fig. 2.14, the steel liquid pressure across the control zone drops from a value greater than the atmospheric pressure in the tundish to reach a smaller value in the nozzle.

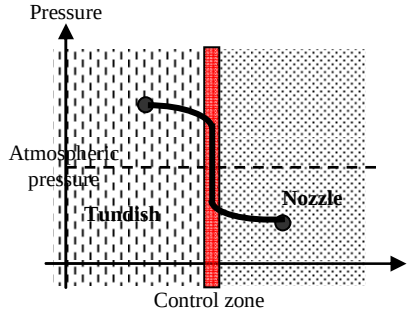

Fig. 2.14. Steel liquid pressure around the control zone

The clogging affects the pressure profile across the nozzle. The stopper must move to compensate these variations. Unfortunately, the controller does not respond appropriately. The resulting changes of the flow rate generate level variations in the mould. In addition, the clogging affects also the jet exiting the ports. In [2], the authors report that, in some cases, the clogging may modify the flow dynamics in the mould from two symmetric swirls to a single large one. This leads to transient changes in the flow which are accompanied by level fluctuations in the mould.

2.3.2.2 Detection

To develop an accurate clogging/unclogging index, it could be advantageous to monitor several measurements in real time. To achieve this, [2] lists the following four parameters:

- **Argon back pressure**: may indicate the clogging caused by air aspiration. Drops in back pressure indicate that there are cracks in the refractory allowing air aspiration. Increases in back pressure can be related to high resistance applied by the clogs formed in the nozzle against argon.

- **Nitrogen**: its content in the steel between the tundish and the mould gives a reliable indication of the exposure to air and may be used thus to quantify the extent of reoxidation problems in the nozzle.

- **Mould level**: the effect on mould level is more visible when the unclogging occurs suddenly. The level rises then considerably. There is also an increase in level fluctuations during the clogging. Fig. 2.15 compares the mould level measured in normal conditions and during the clogging or the bulging (this disturbance will be described with greater detail in the sequel). The changes affecting the flow passage shape as well as the pressure drop generate indeed many difficulties for the control loop to maintain a constant flow rate into the mould. However, the severity of clogging cannot be measured only from the mould level signal since it is disturbed by other phenomena even if Fig. 2.15 reveals that variations generated by clogging/unclogging do not have the same properties as those generated by the bulging.

- **Stopper position**: compared to the casting speed, it shows the discrepancy between the theoretical flow rate in the absence of clogging and the measured one. During the clogging, alumina clogs restrict the steel flow inside the nozzle. The control loop must increase the stopper position progressively to maintain the same casting speed. When the unclogging occurs, the flow passage becomes larger and the control loop brings back the stopper to an initial position which depends on the amount of the clogs leaving the nozzle wall. Therefore, during the clogging/unclogging cycle, the stopper position signal is a succession of ramps whose periods are random whereas the casting speed does not vary. On the contrary, in the case of a clean nozzle, each significant movement of the stopper is related to a casting speed variation. This analysis is in good agreement with the measurements recorded during an experimental sequence characterized by multiple cycles of clogging/unclogging (Fig. 2.16). This conclusion can be exploited to model the clogging effect on the mould level control loop.

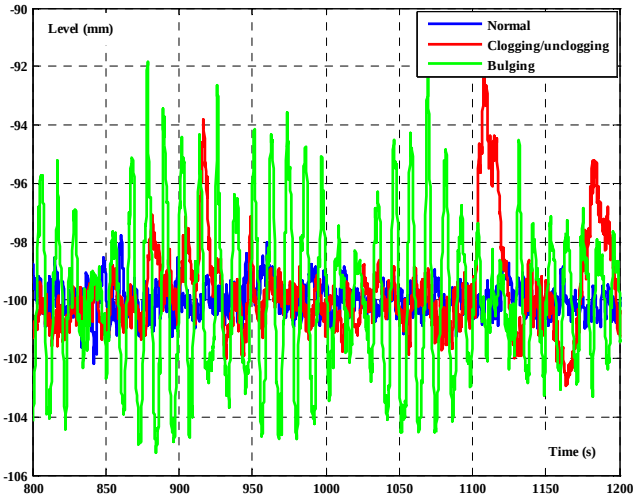

Fig. 2.15. Example of mould level variations caused by the clogging

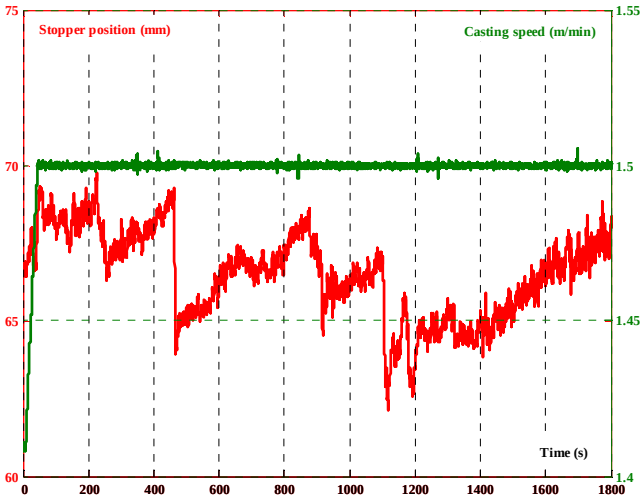

Fig. 2.16. Stopper position relative to casting speed during clogging/unclogging phenomenon

Hence, a clogging ratio can be derived and used to measure the clogging intensity inside the nozzle. It can also include other factors as the tundish weight and the slab width.

The method widely used to prevent clogging is the argon injection into many locations inside the nozzle. The argon gas may prevent indeed inclusion contact with the wall. In addition, it reduces air aspiration and retards chemical reactions between the steel and the refractory. Similarly, other efforts have also been dedicated to improve nozzle material and design as well as steel cleanness in order to provide other solutions to the clogging problem.

2.3.2.3 Modeling

In the absence of clogging, the flow rate into the mould is determined from the stopper position regardless of casting speed. During the clogging, deposition impedes the flow. Therefore, the actual rate, measured from the casting speed, is less than the theoretical value. The reduction of the flow rate will be modeled by an additional exogenous signal d_{clog} to the theoretical rate (Fig. 2.17). d_{clog} models thereby the effect on the flow and subsequently on the mould level variations. Since the stopper position is described by a succession of ramps, d_{clog} will have the same behavior because the casting speed and the level are generally kept constant. From a mathematical point of view, the plant dynamics equations will consider d_{clog} as a state variable whose second derivative is zero ($\ddot{d}_{clog} = 0$) as developed in the next chapter.

Otherwise, an alternative way to model the clogging effect is to consider the nozzle gain G_n as variable. Since this gain is influenced by several other factors, the first model will be adopted.

To complete this model, one should take into account other considerations. More precisely, the deposit mainly made of aluminum oxide Al_2O_3 takes place at many sites inside the nozzle but with different proportions leading to an asymmetry of the flow between the both ports of the nozzle. Instead of monitoring one level measurement, an accurate plant model should consider the two sides of the nozzle and two level measurements on both sides of the mould. In this new model, the block 'mould' of the initial linear model is substituted by two blocks 'half mould'. The same operation is performed for the block 'nozzle'. Furthermore, connection between the two half mould is modeled by an additional flow (determined from the difference between the two levels) into each half mould. For the sake of simplicity, this feature will not be incorporated in the plant model.

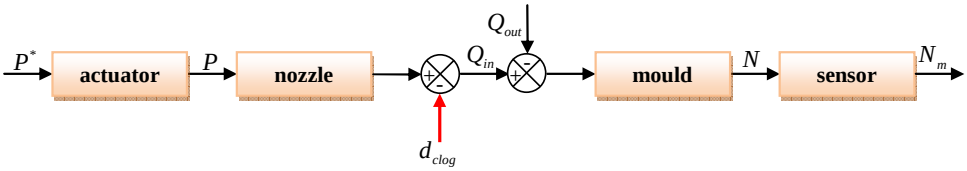

Fig. 2.17. Clogging effect integrated in the plant model

2.3.3 Bulging

2.3.3.1 Description

Contrary to the clogging/unclogging cycle, the bulging occurs at the lower part of the caster, in the secondary cooling section. Due to increasing pressure inside the strand carried out by the liquid steel height, the volume of liquid steel inside the solidified shell varies and so its profile varies too (Fig. 2.18).
The bulging increases in severity when the shell is thin and its formation is uneven especially in the upper levels just below the mould. In the worst case, it makes the casting operations impossible to manage. The structure of the casting machine has thus an important prevention role. Overall, the bulging can be divided into static or dynamic and steady or unsteady (Fig. 2.19) as follows, where P_r is the ferrostatic pressure, T the strand temperature, λ the roll pitch and v the casting speed [28]:

- **Static**: the maximum of bulging is located at the center of the roll pitch.
- **Dynamic**: the maximum of bulging moves from the center of the roll pitch according to the movement of the solidified shell.
- **Steady**: neither the shell profile nor the liquid steel volume inside varies with time.
- **Unsteady**: this is the most disruptive type since it affects other parts of the caster. In this case, the shell profile varies with time and so the mould level varies too.

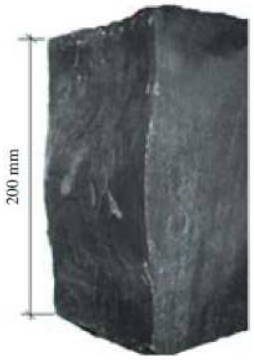

Fig. 2.18. Example of bulging defect on slab face

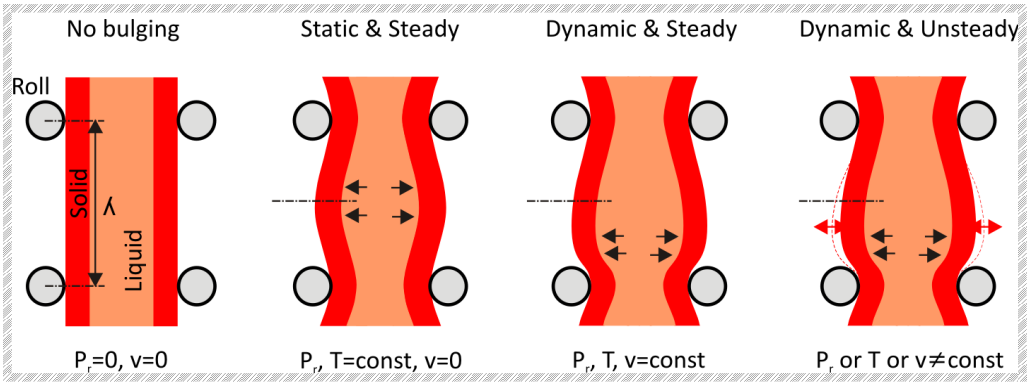

Fig. 2.19. Types of bulging

2.3.3.2 Unsteady bulging effect

During unsteady bulging phenomenon, mould level fluctuations increase all the time with a magnitude depending on the movement of the solidified shell. Its mechanical interaction with the rolls impacts directly the flow out of the mould. Because of its complexity, no model can include all of the considerations at once. Many researchers have proposed different models based on high temperature creep and elastic bending behavior analysis [33]. For control purposes, it is assumed that the shell profile is described by a sine function at each site. All the initial phases are supposed to be the same. The effect of unsteady bulging depends then on how the phases change with time. If they follow the same trajectory, a large fluctuation of the mould level occurs. In fact, when the convex part of the shell profile is located between the two rolls, the mould level falls. On the contrary, if it is the concave part which is located between the rolls, the mould level rises (Fig. 2.20). On the other hand, it should be mentioned that if the sine waves are in antiphase, the change in the liquid volume at each site is compensated by another one from another site resulting in small fluctuations of the mould level.
A spectral analysis of shell profile displacement has revealed that there are two kinds of frequencies. The first one depends on the roll pitch λ_i (2.20) whereas the second one is related to the roll rotation (2.21).

$$f_{i,1} = \frac{v}{\lambda_i} \tag{2.20}$$

$$f_{i,2} = \frac{v}{\pi \cdot D_r} \tag{2.21}$$

where D_r is the roll diameter.

However, only the first kind affects really the mould level. The effect of the second kind is negligible because its associated phases are random [32]. The disruptive frequencies $f_{i,1}$ depend thus on the configuration of the caster and the casting speed but they are generally between 0.03 and 0.1Hz.

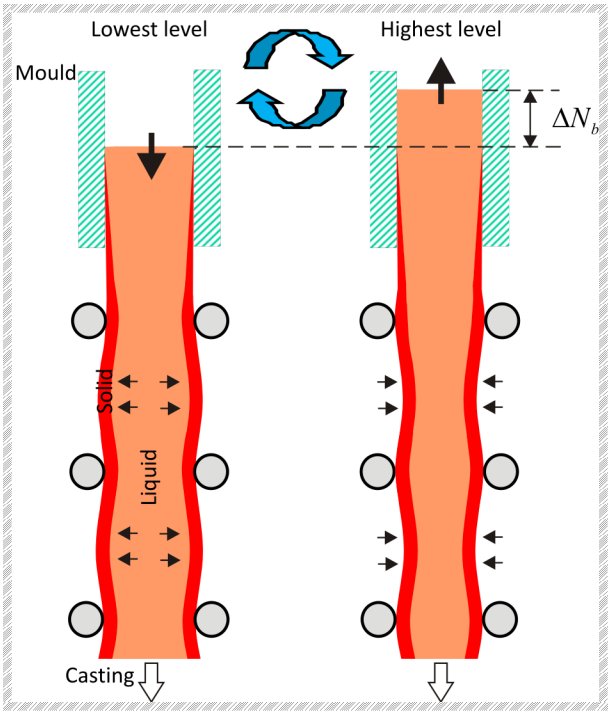

Fig. 2.20. Unsteady bulging effect on mould level

To simplify calculations, we assume that the area change of shell profile is a triangle. Under this assumption, the amount of mould level variations generated ΔN_b can be expressed using the following equation:

$$\Delta N_b \cdot S_t = -2 \cdot \sum_i \frac{\lambda_i}{2} \cdot \frac{(B_i^{\max} - B_i^{\min})}{2} \cdot \sin(2\pi f_{i,1} \cdot t) \qquad (2.22)$$

with:

- ΔN_b : Mould level variations caused by bulging,
- S_t : Slab thickness,
- λ_i : Roll pitch of site i,
- B_i : Shell movement magnitude at site i,
- $f_{i,1}$: Shell movement frequency at site i (first kind),
- t : Time.

The shell profile magnitude B_i can be measured using special equipment (described in the following paragraph) or determined by the model of a two dimensional continuous beam structure with multi-roll supports as proposed in [33].

In order to weaken the bulging, the methods generally used are the strong cooling at the secondary cooling zone and the enhancement of roll pitch configuration.

2.3.3.3 Measurement

In some plants, the equipment used to measure the shell profile or the bulging displacement is shown in Fig. 2.21. More concretely, the change in bulging magnitude brings the guide rod to move vertically. This displacement is measured by a LVDT sensor. Sometimes, the driven rolls stir because of unsteady bulging and this may corrupt the measurement.

The bulging magnitude is a function of casting speed, ferrostatic pressure, roll pitch, shell thickness, strand temperature and time. It is steady when all these variables remain constant in time but it is rarely the case during real casting conditions. Using this equipment, it has been verified that the bulging is strongly affected by the roll pitch and slightly by the cooling system. The bulging magnitude is particularly high at segments where the roll

pitch is large. Moreover, it increases with the casting speed. For instance, in the case of a roll pitch equal to 340mm, the maximum of bulging displacement is around 0.2mm at $1.4\text{m}\cdot\text{min}^{-1}$ and 0.7mm at $2\text{m}\cdot\text{min}^{-1}$ [34].

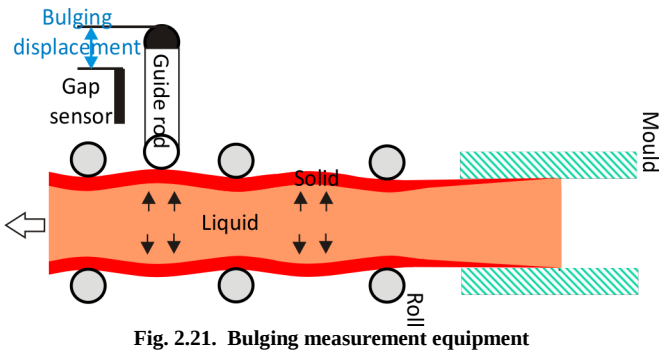

Fig. 2.21. Bulging measurement equipment

2.3.3.4 Modeling

In the absence of bulging, the flow rate out of the mould is calculated from the casting speed. During unsteady bulging, it is assumed that the shell movement is described by a sine wave at each site between two rolls. This displacement induces changes in the theoretical outflow rate, which must be included in the plant model. Similarly to the model adopted in the case of clogging/unclogging phenomenon, this alteration of the outflow rate will be modeled by an additional exogenous signal d_{bulge} to the theoretical rate. d_{bulge} is a sum of several sine waves (Fig. 2.22). The frequencies can be determined by selecting the most significant magnitudes in the level signal spectrum belonging to the bulging frequency range ([0.03 0.1Hz]). In the state space formalism, each sine wave of d_{bulge} and its derivative are state variables. In the sequel, without loss of generality, only two frequencies are considered but the conclusions remain valid whatever the number of frequencies.

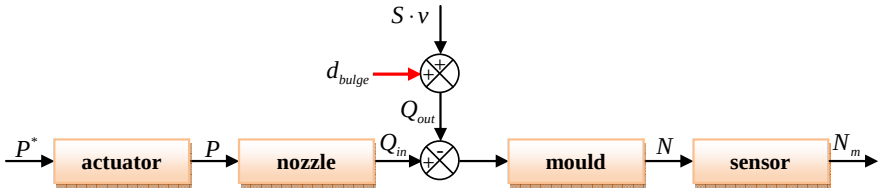

Fig. 2.22. Bulging effect integrated in the plant model

According to Fig. 2.22, it comes:

$$Q_{out} = S\cdot v + d_{bulge}$$
$$\begin{cases} d_{bulge} = d_{bulge\,1} + d_{bulge\,2} + \cdots \\ \ddot{d}_{bulge\,i} = -\omega_{bulge\,i}^2 \cdot d_{bulge\,i} \\ \omega_{bulge\,i} = 2\pi f_{i,1} \end{cases} \tag{2.23}$$

2.3.4 Standing waves

The standing waves are another periodic disturbance but it acts directly on the meniscus surface contrary to the previous ones which disturb the flows into and out of the mould. Its effect can be integrated in the plant model by means of an exogenous signal d_{waves} as depicted in Fig. 2.23.

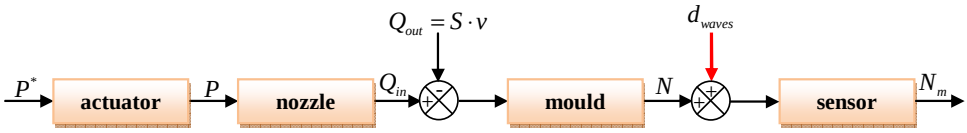

Fig. 2.23. Standing waves effect integrated in the plant model

The causes are various. For instance, it appears as a consequence of the very high variations of the casting speed and depends on the prevalent flow regime in the mould. Its frequencies depend on the mould geometry and belong to the frequency range (between 0.65 and 0.85Hz) which may be amplified by the control loop (Fig. 2.24).

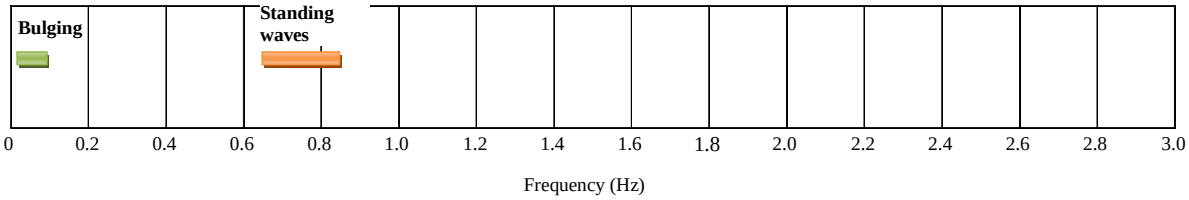

Fig. 2.24. Frequency ranges of bulging and standing waves

In the case of a mould format equal to 1500×190mm², the frequency is around 0.7Hz. More generally, these frequencies are well known and described by the equation (2.24).

$$f_{wavesi} = \frac{1}{2\pi}\sqrt{\frac{g\pi \cdot i}{S_w}} \tag{2.24}$$

with:

- g : Gravitational acceleration,
- i : Number of nodes (typically about 5 to 6 nodes),
- S_w : Slab width.

The surface waves can be generated experimentally using a specific experimental set-up. For instance, Fig. 2.25 shows 2-nodes and 4-nodes symmetric waves on the free surface of the Siemens VAI water model test facility. The asymmetric waves (1-node, 3-nodes …) cannot be excited.

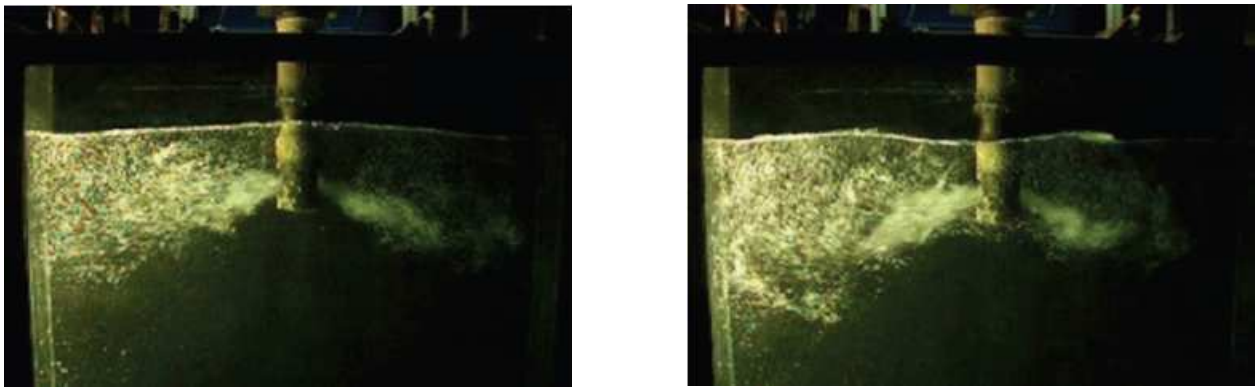

Fig. 2.25. Standing waves in the water model (Siemens VAI)

Other studies about the standing waves are reported in the literature. In [5], a mathematical model based on theoretical considerations is presented. First, an equation between the pressure on the surface and the velocity at the surface is established. Then, the formation of surface waves is expressed from the pressure distribution.

2.4 Chapter summary

This chapter has attempted to summarize the different models currently used by steelmakers to design mould level controller. Since the distributed model is not well documented and still requires further development, this work has focused on the centralized model in use from the outset.

With regard to all the considerations discussed above, the following block diagram of the global plant model can be drawn:

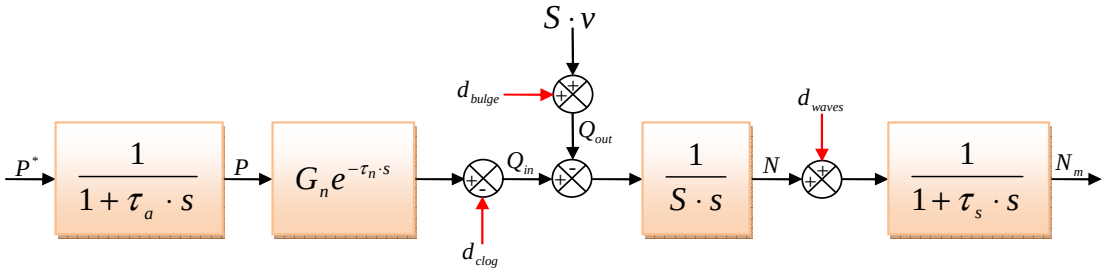

Fig. 2.26. Global plant model

where:

- s : Laplace variable,
- τ_a : Actuator time constant,
- G_n : Nozzle gain,
- τ_n : Nozzle delay,
- S : Mould section,
- v : Casting speed,
- τ_s : Level sensor time constant.

The disturbances which have huge effect on the meniscus region are included by means of three exogenous signals such as:

$$\ddot{d}_{clog} = 0 \qquad \begin{cases} d_{bulge} = d_{bulge1} + d_{bulge2} + \cdots \\ \ddot{d}_{bulge\,i} = -\omega_{bulge\,i}^2 \cdot d_{bulge\,i} \\ \omega_{bulge\,i} = 2\pi f_{i,1} \end{cases} \qquad \begin{cases} d_{waves} = d_{waves1} + d_{waves2} + \cdots \\ \ddot{d}_{waves\,i} = -\omega_{waves\,i}^2 \cdot d_{waves\,i} \\ \omega_{waves\,i} = 2\pi f_{waves\,i} \end{cases} \tag{2.25}$$

where:

- d_{clog} : Clogging effect model,
- d_{bulge} : Bulging effect model,
- d_{waves} : Standing waves effect model.

Therefore, as a conclusion of this chapter, the centralized model, as illustrated in Fig. 2.26, will be the starting point for the development of control strategies. Special care has to be taken to cope with the variations of the plant parameters, in particular G_n and τ_n, which are highly correlated with casting conditions.

CHAPTER 3
Estimation and rejection of disturbances

3.1 Introduction

As discussed in chapters 1 and 2, various disturbances take place in the casting machine and impact the mould level stability. One common strategy widely adopted nowadays is to tune the control system in order to handle the worst case conditions. Based upon operators experience, the process may vary over a large range of casting conditions. Therefore, this approach cannot guarantee the best performances in terms of disturbances rejection. Effective control systems should accommodate indeed the process changes as well as different classes of disturbances. This is the main goal of the thesis that will be achieved by using RMMAC architecture developed in chapter 5.

In this chapter, we plan to explore other techniques based on observer design that allow the operator to estimate the disturbances and to reject them through a complementary module to the main feedback control. The first step is to identify the plant model that will be used both in disturbances rejection and in control laws design. Furthermore, this chapter provides a range of variations of key parameters depending on casting conditions. This will convince the reader of the necessity to implement robust control techniques and will introduce the next chapters.

This chapter is organized into four sections. The first one describes step by step the complete procedure classically undertaken to collect data that will be used to derive the unknown values of the plant model. Also examined are the offline identification algorithms. Then, we move to the estimation and rejection of disturbances which are the heart of this chapter. The disturbances considered here are the clogging/unclogging cycle, the bulging but these strategies could be also transposed to the standing waves. This result will be validated experimentally by means of the water model in the last section. Using this experimental tool, we also demonstrate that the values of the gain and the delay appearing in the centralized model change when the casting parameters vary greatly.

3.2 Plant model identification

Let us consider the transfer function of the global plant model developed in the previous chapter:

$$TF_{model} = \frac{G_n e^{-\tau_n \cdot s}}{S \cdot s \cdot (1 + \tau_a \cdot s) \cdot (1 + \tau_s \cdot s)} \tag{3.1}$$

On the one hand, the mould section S and the sensor time constant τ_s are known. The first one depends on the desired product geometry and is set by the operator. The second value however is a product specification data provided by the manufacturer.

On the other hand, the gain G_n, the delay τ_n and the actuator time constant τ_a are unknown and should be identified before designing controllers. This section presents all needed steps to do this. First, we start by collecting data delivered by the available sensors according to an experimental protocol. Based on these measurements, the identification algorithm is then applied to determine the unknown values.

3.2.1 Data acquisition protocol

3.2.1.1 Identification scheme

In this subsection, we suggest an identification method able to extract a mathematical model of the actuator and the nozzle dynamics from measurements of inputs and outputs of the mould level control loop.

First of all, it is worthwhile to mention that the identification trials may be conducted in open loop or closed loop. We know, however, that the stopper position is never set manually in real plants and the level control loop is consequently always turned on. For this reason, we shall focus only on the second setup because it is the only configuration which can actually be deployed in real plants.

The mould level control loop is thus excited by a computer generating excitation signals which are added to either stopper position setpoint or level setpoint (Fig. 3.1). The dynamic responses measured by the dedicated sensors, are then recorded for processing at a later time [72].

After turning on the level control loop, it is necessary to wait until the stationary regime is established i.e. the level fluctuations are damped enough. Of course the introduction of the excitation signal will cause the free surface to move periodically what cannot be easily accomplished during casting operations. Such variations will degrade indeed the quality of the cast product even if this process is not supposed to generate local fluctuations but only to disturb the liquid level average.
To reduce the costs of the identification trials, one should limit their number and duration.

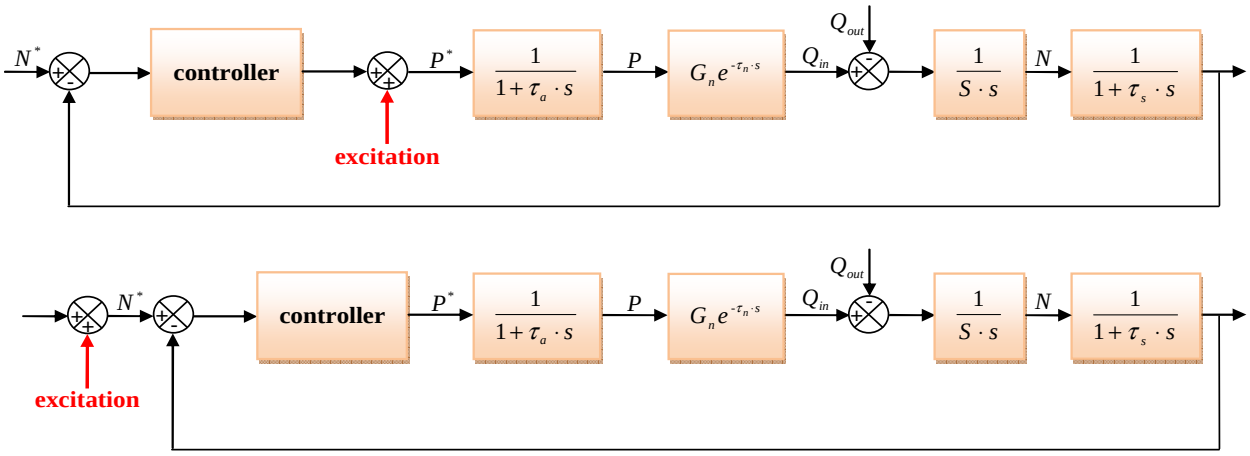

Fig. 3.1. General structure of offline identification scheme

Without loss of generality, the excitation is assumed to be applied, from now on, on the stopper position setpoint.
Several kinds of system excitations may be used: a step movement of the stopper, a harmonic excitation or a Pseudo-Random Binary Sequence (PRBS).
For the step excitation, the stopper position setpoint is suddenly lifted to a lower or higher level depending on the flow rate out of the mould. The controller is then engaged to keep the free surface at the target setpoint. For the harmonic excitation, a sinusoidal stopper movement with constant amplitude and frequency is required.
Because it covers a broad frequency range, the PRBS signal will be preferred. In addition, the measurements data base collected in this way can be handled by various identification algorithms contrary to measurements achieved by means of the two first methods which need specific algorithms. As a consequence, they will be disregarded thereafter.
During each recording, the plant configuration and the casting conditions should not change. As we shall see in the last section of this chapter, the identification results depend on them. So, if they are modified, new trials are needed.

3.2.1.2 Pseudo-Random Binary Sequence (PRBS)

The PRBS signal is a sequence of several bits, commonly used for identification problems as an approximation of a discrete white noise. The generation of such sequences is well known and is ensured through the Linear Feedback Shift Registers (LFSR) as described in [73] and illustrated in Fig. 2.5.

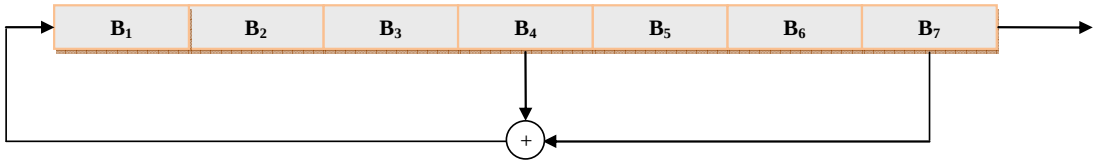

Fig. 3.2. Generation of a sequence of 127 bits

PRBS generator consists of multiple binary elements B_i so-called stages connected in series and one or more logic gates to compute the 'exclusive OR' of the outputs of at least two register stages. It is important to notice that at least one stage of the PRBS generator should have an initial value different from 0. In practice, all initial values are set to 1.
Table 3.1 lists the selected bits for the exclusive disjunction operation, associated to each sequence length.

Table 3.1. Pseudo-Random Binary Sequence generator

Number of stages N_{PRBS}	Sequence length $2^{N_{PRBS}}-1$	Bits addition
2	3	$B_1 \oplus B_2$
3	7	$B_1 \oplus B_3$
4	15	$B_3 \oplus B_4$
5	31	$B_3 \oplus B_5$
6	63	$B_5 \oplus B_6$
7	127	$B_4 \oplus B_7$
8	255	$B_2 \oplus B_3 \oplus B_4 \oplus B_8$
9	511	$B_5 \oplus B_9$
10	1023	$B_7 \oplus B_{10}$

The excitation signal is then generated from the PRBS sequence according to Fig. 3.3.

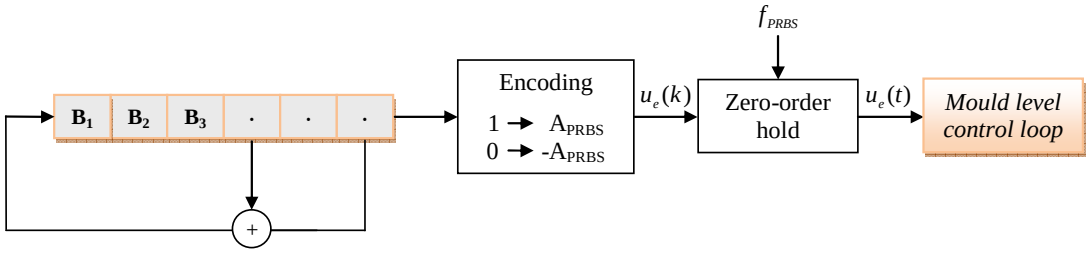

Fig. 3.3. Generation of the excitation signal

The spectral density of the excitation signal u_e is given by:

$$\Gamma_{u_e}(f) = \frac{A_{PRBS}^2}{N_{PRBS}^2}\delta(f) + \frac{A_{PRBS}^2 (N_{PRBS}+1)}{N_{PRBS}^2}\sum_{i\neq 0}\left(\frac{\sin(i\cdot\pi/N_{PRBS})}{i\cdot\pi/N_{PRBS}}\right)^2 \delta(f - \frac{i\cdot f_{PRBS}}{N_{PRBS}}) \tag{3.2}$$

with:

- $\delta(\cdot)$: Dirac impulse,
- N_{PRBS} : Number of stages,
- A_{PRBS} : Amplitude of u_e ,
- f_{PRBS} : Sampling frequency of the zero-order hold block, classically tuned according to both time response of the control loop and operating point.

Small values of A_{PRBS} should be chosen to minimize disruptions to casting process. However, they must be sufficiently greater than the instrumentation noise.

3.2.2 Offline algorithms

A significant number of identification algorithms have been reported in the literature for both discrete and continuous systems [37] [38] [39] [72] [74]. Of all these methods, we shall present two identification algorithms in this paragraph. We recommend using the least squares method to identify the actuator transfer function and the iterative prediction error minimization method to identify the gain and the delay. For both methods, only the measurements of the level, the stopper position and the flow rate out of the mould are used by the algorithm. After eliminating the instrumentation biases and scale factors, the parameters to be identified have to be chosen so that the predictions generated by the model are in good agreement with the experimental measurements.
We stress that neither the controller nor the excitation signal is explicitly involved and that is clearly another major advantage of our identification approach.

3.2.2.1 Least squares

3.2.2.1.1 Principle

For the sake of simplicity, we consider a quite basic process completely unknown. We denote the input by $u(t)$ and the output by $y(t)$ as shown in Fig. 3.4.

Fig. 3.4. Process to identify

Assume that this process is represented by:

$$\begin{cases} A(q^{-1})y(k) = q^{-r}B(q^{-1})u(k) + \omega(k) \\ A(q^{-1}) = 1 + a_1 q^{-1} + \cdots + a_{n_a} q^{-n_a} \\ B(q^{-1}) = b_1 q^{-1} + \cdots + b_{n_b} q^{-n_b} \end{cases} \tag{3.3}$$

where q^{-1} is the backward shift operator and ω is a white noise. This can be rewritten as:

$$y(k) = -\sum_{i=1}^{n_a} a_i y(k-i) + \sum_{i=1}^{n_b} b_i u(k-r-i) + \omega(k) \tag{3.4}$$

Some notation will be as follows. Let φ contain all the unknown coefficients of the process transfer function and $\phi(t)$ regroup many past samples of the input and the output up to time $k-1$. Their numbers depend on the degrees of the two polynomials $A(z^{-1})$ and $B(z^{-1})$. Given these notations, we can write:

$$\begin{cases} y(k) = \varphi^T \phi(k-1) + \omega(k) \\ \varphi^T = (a_1 \quad \cdots \quad a_{n_a} \quad b_1 \quad \cdots \quad b_{n_b}) \\ \phi^T(k-1) = \big(-y(k-1) \quad \cdots \quad -y(k-n_a) \quad u(k-r-1) \quad \cdots \quad u(k-r-n_b)\big) \end{cases} \tag{3.5}$$

Let us further suppose that n samples are available. The unknown vector φ is then determined by minimizing the following global error criterion:

$$\varphi^* = \underset{\varphi}{argmin}\, J_{LS}(n) \qquad \begin{cases} J_{LS}(n) = \dfrac{1}{n}\displaystyle\sum_{k=1}^{n} \varepsilon^2(k) \\ \begin{cases} \varepsilon(k) = y(k) - \hat{y}(k) & \text{(prediction error)} \\ \hat{y}(k) = \varphi^T \phi(k-1) & \text{(predicted output)} \end{cases} \end{cases} \tag{3.6}$$

φ^* is also the solution of the following equation:

$$\frac{\partial J_{LS}(n)}{\partial \varphi} = \frac{2}{n}\left\{\sum_{k=1}^{n}(y(k)-\varphi^T\phi(k-1))\right\}\phi(k-1)=0 \tag{3.7}$$

Then, it is easy to show that:

$$\varphi^T\cdot\phi(k-1)\phi(k-1)=\phi(k-1)\phi^T(k-1)\cdot\varphi \tag{3.8}$$

Substituting (3.8) into (3.7) yields:

$$\left[\sum_{k=1}^{n}\phi(k-1)\phi^T(k-1)\right]\cdot\varphi^*=\sum_{k=1}^{n}\phi(k-1)y(k) \tag{3.9}$$

On the other hand, one can readily see that the matrix $\phi\phi^T$ is non-singular because its columns are independent. As a result, an estimate of φ may be obtained by:

$$\varphi^*=\left[\sum_{k=1}^{n}\phi(k-1)\phi^T(k-1)\right]^{-1}\sum_{k=1}^{n}\phi(k-1)y(k) \tag{3.10}$$

3.2.2.1.2 Application

The least squares method can be directly applied to identify the actuator transfer function using the position setpoint as the input and the measured position as the output based on the following finite difference equation:

$$P(n)=a_1\cdot P(n-1)+(1-a_1)\cdot P^*(n-1) \qquad \text{with:} \quad a_1=e^{-\frac{T_s}{\tau_a}} \tag{3.11}$$

where τ_a is the actuator time constant and T_s is the sampling time.
As for the nozzle transfer function, attempts to apply the least squares algorithm considering the flow rate into the mould as an output and the stopper position as an input were not successful in particular because the estimate of the flow rate from the level measurement, according to equation (3.12), was cumbersome.

$$S\dot{N}(t)=Q_{in}(t)-Q_{out}(t) \tag{3.12}$$

In fact, we had to find the derivative of the level and this operation is extremely sensitive to noise. The differentiation is not consistent indeed when there is measurement noise.
To overcome this difficulty, two solutions may be quite effective:

- Use of the autocorrelation of the position as the input and the cross-correlation between the position and the flow into the mould as the output.
- Instead of calculating the derivative of the level, we propose to integrate equation (3.12) in order to calculate the integral of the flow rate into the mould $\int Q_{in}(t)dt$ according to equation (3.13). Then, the least squares method may be applied considering this integral as the output and the integral of the position as the input.

$$\int Q_{in}(t)dt = SN(t)+\int Q_{out}(t)dt \tag{3.13}$$

Nevertheless, we shall use the least squares method only to identify the actuator dynamics.

3.2.2.2 Structured state space formalism

3.2.2.2.1 Principle

This approach is based on Prediction Error Methods (PEM) applied on a structured state space representation [75]. It uses the same algorithm as other parameter estimation methods but differs in the computation of prediction errors and gradients.

Let the input and output of the system be denoted, one again, by $u(t)$ and $y(t)$ respectively. They have been sampled at discrete time points and $y(k)$ is assumed to be generated according to:

$$y(k) = G(q^{-1})u(k) + H(q^{-1})\omega(k) \tag{3.14}$$

The PEM method uses optimization to minimize the following cost function where $\varepsilon(k)$ represents the difference between the measured output $y(k)$ and the predicted output $G(q^{-1})u(k)$:

$$\begin{aligned} J_{PEM}(n) &= \sum_{k=1}^{n} \varepsilon^2(k) \\ \varepsilon(k) &= H^{-1}(z^{-1}) \cdot (y(k) - G(z^{-1})u(k)) \end{aligned} \tag{3.15}$$

with n the number of data samples.

The optimization is carried out using the damped Gauss-Newton method.

As with any identification algorithm, we should now describe the plant dynamics. In the sequel, it will willfully be expressed by means of a structured continuous-time state space equation. With that choice, we need to formulate, once more, an approximation of the time-delay in order to develop a linear model.

3.2.2.2.2 Time-delay approximations

Time-delay systems are present in a wide range of industrial processes [72]. Communication systems, chemical processing, heavy machinery, aircraft and transportation systems are typical examples that exhibit time-delays. In such dead-time systems, the control input takes a certain time before it affects the measured outputs. Moreover, the time-delay is a source of instability which may degrade drastically the performances of control systems [77]. In the continuous casting process, the delay introduced in the plant model is a function of time which has been a source of difficulty to many control engineers, all the more so because its cause is not well known. Nevertheless, most of them believe that it is related to the fluid flow through the nozzle before entering the mould, coupled with the argon injection.

Because the plant model is not linear in the time-delay parameter, we shall use a rational approximation to derive a linear model. A number of such approximations are proposed in literature [8].

Using the Taylor series expansion of the exponential function, the Laplace transform $e^{-\tau_n s}$ can be written as:

$$e^{-\tau_n s} = \sum_{k=0}^{\infty} \frac{(-s\tau_n)^k}{k!} = 1 - s\tau_n + \frac{(s\tau_n)^2}{2} + \frac{(-s\tau_n)^3}{3!} + \frac{(s\tau_n)^4}{4!} + \cdots \tag{3.16}$$

Therefore, many equivalent frequency domain transfer functions may be formulated. A first simple approach consists of regarding $e^{-\tau_n s}$ as $1/e^{\tau_n s}$ and then using equation (3.16). This leads to the first order and second order functions defined in Table 3.2.

Initially proposed by Padé, another approximation is likewise widely used and provides a better fit than a Taylor series [40]:

$$e^{-\tau_n s} \approx \frac{1 - \frac{\tau_n}{2}s + \left(\frac{\tau_n}{2}\right)^2 s - \cdots}{1 + \frac{\tau_n}{2}s + \left(\frac{\tau_n}{2}\right)^2 s + \cdots} \tag{3.17}$$

Yet, another approximation based on the following Laguerre Formula is ubiquitous in literature [41]:

$$L_k(\tau_n s) = \left(\frac{1 - \frac{\tau_n}{2k} s}{1 + \frac{\tau_n}{2k} s} \right)^k \tag{3.18}$$

where k is a positive number so-called the order.
Table 3.2 shows some of the rational approximations considered in this section to calculate a linear plant model for identification purposes.

Table 3.2. Time-delay rational approximations

Model	Transfer function
First order	$\frac{1}{1+\tau_n s}$
Padé first order	$\frac{1-\frac{\tau_n}{2}s}{1+\frac{\tau_n}{2}s}$
Second order	$\frac{1}{1+\tau_n s+\frac{\tau_n^2}{2}s^2}$
Laguerre second order	$\left(\frac{1-\frac{\tau_n}{4}s}{1+\frac{\tau_n}{4}s}\right)^2$

By examining the bode diagrams of these rational approximations in case of a time-delay equal to 1s (Fig. 3.5), it can be seen that the Laguerre function has the closest frequency response to the time-delay Laplace transform response. Similar conclusions were reached for other values of the delay.

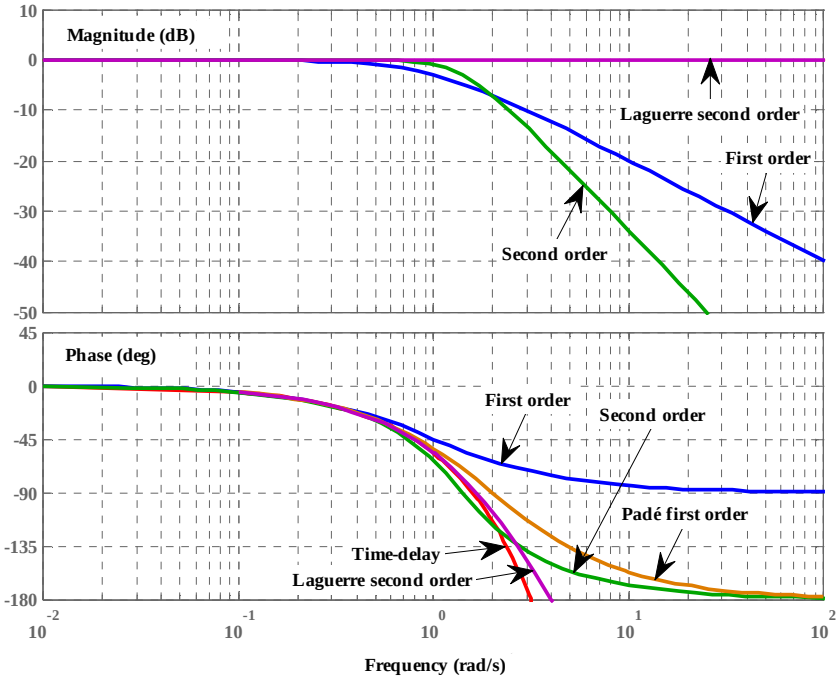

Fig. 3.5. Bode diagrams of rational approximations in case of τ_n=1s

3.2.2.2.3 State space representation of the plant model

Using a rational approximation of the time-delay, we can derive the following continuous-time state space representations where x_i are state variables without any physical meaning introduced to model the approximation and v is the casting speed:

$$e^{-\tau_n s} \approx \frac{1}{1+\tau_n s} \qquad \begin{pmatrix} \dot{N} \\ \dot{x}_1 \end{pmatrix} = \begin{pmatrix} 0 & 1/S \\ 0 & -1/\tau_n \end{pmatrix} \begin{pmatrix} N \\ x_1 \end{pmatrix} + \begin{pmatrix} 0 & -1 \\ G_n/\tau_n & 0 \end{pmatrix} \begin{pmatrix} P \\ v \end{pmatrix} \tag{3.19}$$

$$e^{-\tau_n s} \approx \frac{1-\frac{\tau_n}{2}s}{1+\frac{\tau_n}{2}s} \qquad \begin{pmatrix} \dot{N} \\ \dot{x}_1 \end{pmatrix} = \begin{pmatrix} 0 & 1/S \\ 0 & -2/\tau_n \end{pmatrix} \begin{pmatrix} N \\ x_1 \end{pmatrix} + \begin{pmatrix} -G_n/S & -1 \\ 4G_n/\tau_n & 0 \end{pmatrix} \begin{pmatrix} P \\ v \end{pmatrix} \tag{3.20}$$

$$e^{-\tau_n s} \approx \frac{1}{1+\tau_n s+\frac{\tau_n^2}{2}s^2} \qquad \begin{pmatrix} \dot{N} \\ \dot{x}_1 \\ \dot{x}_2 \end{pmatrix} = \begin{pmatrix} 0 & 1/S & 0 \\ 0 & 0 & 1 \\ 0 & -2/\tau_n^2 & -2/\tau_n \end{pmatrix} \begin{pmatrix} N \\ x_1 \\ x_2 \end{pmatrix} + \begin{pmatrix} 0 & -1 \\ 0 & 0 \\ 2G_n/\tau_n^2 & 0 \end{pmatrix} \begin{pmatrix} P \\ v \end{pmatrix} \tag{3.21}$$

$$e^{-\tau_n s} \approx \left(\frac{1-\frac{\tau_n}{4}s}{1+\frac{\tau_n}{4}s} \right)^2 \qquad \begin{pmatrix} \dot{N} \\ \dot{x}_1 \\ \dot{x}_2 \end{pmatrix} = \begin{pmatrix} 0 & -1/S & 0 \\ 0 & -8/\tau_n & -16/\tau_n \\ 0 & 1/\tau_n & 0 \end{pmatrix} \begin{pmatrix} N \\ x_1 \\ x_2 \end{pmatrix} + \begin{pmatrix} G_n/S & -1 \\ 16G_n/\tau_n & 0 \\ 0 & 0 \end{pmatrix} \begin{pmatrix} P \\ v \end{pmatrix} \tag{3.22}$$

For each representation, the two parameters G_n and τ_n appear both in state matrix and input matrix. The identification algorithm should take into account the relations between the coefficients of these two matrices. For example, it is made possible through the system identification toolbox of Matlab software by using Grey-Box models instead of Black-Box models.

3.2.2.3 Concluding remarks

In this section, two offline identification algorithms have been presented. The first one is based on the least squares method and will be utilized in the sequel to identify the dynamics of the actuator of the water model. The other one is based on the iterative prediction error estimation method applied to a linear structured state space formalism. The delay term will be thus approximated by a first order Laguerre function in order to develop a linear model of the process. The outcome of this second algorithm is to be used in synthesizing the observers as well as to establish a correlation between the variations of the plant model parameters and the water model configuration.

3.3 Disturbances estimation

During casting operations, it is important to monitor the different parts of the caster machine in order to detect, when it is possible, the disturbances which are detrimental to product quality. In this section, two of them are examined. The first one is the clogging/unclogging whose effect on the level control loop has been modeled by an additional exogenous signal d_{clog} in chapter 2. The second one is the bulging located beneath the mould. As discussed in the precedent chapter, its effect on the flow out of the mould may be modeled by an additional exogenous signal d_{bulge} to the theoretical rate imposed by the casting speed. This section explains how to estimate d_{clog} and d_{bulge} from the available measurements.

3.3.1 Clogging/unclogging

In this subsection, it is assumed that the only disturbance acting on the level control loop is the clogging/unclogging phenomenon.

3.3.1.1 Principle

All details about clogging/unclogging disturbance can be found in chapter 2. The important point to recall here is its effect on the flow into the mould. In the case of a clean nozzle, the flow rate is determined according to the curve plotted in Fig. 3.6. When the clogs appear inside the nozzle, the actual rate is then reduced. As a result, this curve is shifted down by an unknown function of time so-called $d_{clog}(t)$.

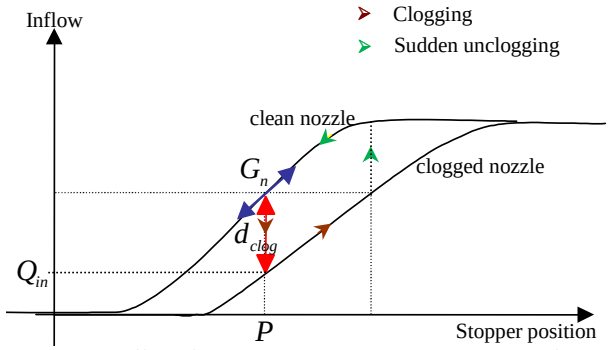

Fig. 3.6. Effect of the clogging/unclogging cycle on the inflow

Therefore, the online estimation of $d_{clog}(t)$ can help to monitor the clogging/unclogging evolution. Fortunately, this can be achieved using Kalman or Luenberger observers [72] [79]. Other recent estimation schemes are reported in the literature. Representative references are [9] [10]. Since they rely on the same basic principle as Luenberger observer, all the estimators developed in this chapter will be based on this technique.
The plant model with the $d_{clog}(t)$ signal is shown in Fig. 2.26.

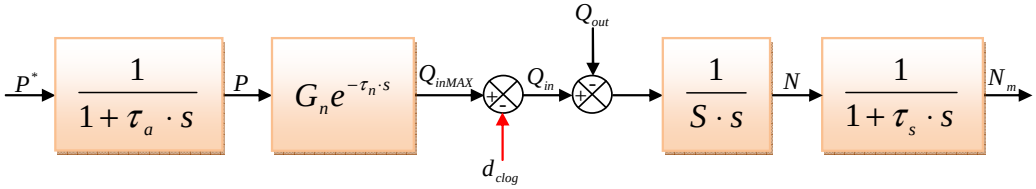

Fig. 3.7. Plant model with clogging effect

The flow rate out of the mould, as well as the level, is generally kept constant. $d_{clog}(t)$ will have thus the same behavior as the stopper position (i.e. in the form of ramps).
Without loss of generality, the level sensor dynamics has been overlooked in the following calculation. According to the previous figure, it comes:

$$S\,\dot{N}(t) = \underbrace{G_n\,P(t-\tau_n) - d_{clog}(t)}_{Q_{in}} - \underbrace{S \cdot v(t)}_{Q_{out}} \qquad (3.23)$$

$$\text{with} \quad \ddot{d}_{clog} = 0$$

To derive a linear model from this figure, the time-delay was approximated by a first order Padé function:

$$e^{-\tau_n s} \approx \frac{1-\frac{\tau_n}{2}s}{1+\frac{\tau_n}{2}s} \tag{3.24}$$

Therefore, the linearized continuous-time state space equation for the system can be written as:

$$\begin{cases} \dot{X}_{clog} = A_c X_{clog} + B_c U \\ Y = N = C_c X_{clog} \end{cases}$$

$$X_{clog}^T = \begin{pmatrix} N & d_{clog} & \dot{d}_{clog} & q_p \end{pmatrix} \qquad q_p(t) = G_n P(t-\tau_n) + G_n P(t) \qquad U^T = \begin{pmatrix} P & v \end{pmatrix}$$

$$A_c = \begin{pmatrix} 0 & -1/S & 0 & 1/S \\ 0 & 0 & 1 & 0 \\ 0 & 0 & 0 & 0 \\ 0 & 0 & 0 & -2/\tau_n \end{pmatrix} \qquad B_c = \begin{pmatrix} -G_n/S & -1 \\ 0 & 0 \\ 0 & 0 \\ 4G_n/\tau_n & 0 \end{pmatrix} \qquad C_c^T = \begin{pmatrix} 1 \\ 0 \\ 0 \\ 0 \end{pmatrix} \tag{3.25}$$

The flow rate $q_p(t)$ has been introduced to include the Padé approximation but it does not have any physical meaning.

Since the stopper position is measured, it is not necessary to include the actuator dynamics in the equation above. It will require indeed an additional state variable without providing any further information. It is noteworthy to mention that this approach can be implemented thus in various plants whatever the actuator could be.

To check the observability of the system, one should calculate the observability matrix O_c:

$$O_c = \begin{pmatrix} C_c \\ C_c \cdot A_c \\ C_c \cdot A_c^2 \\ C_c \cdot A_c^3 \end{pmatrix} = \begin{pmatrix} 1 & 0 & 0 & 0 \\ 0 & -1/S & 0 & 1/S \\ 0 & 0 & -1/S & -2/(S \cdot \tau_n) \\ 0 & 0 & 0 & 4/(S \cdot \tau_n^2) \end{pmatrix} \tag{3.26}$$

O_c has full rank 4 and the system is thereby completely observable.

The Luenberger observer is thus given by the following continuous-time equation [79]:

$$\dot{\hat{X}}_{clog} = (A_c - K_c \cdot C_c)\hat{X}_{clog} + B_c U + K_c N \tag{3.27}$$

where K_c is the observer gain chosen so that the eigenvalues of $A_c - K_c \cdot C_c$ are strictly negative and to achieve a desired dynamics. This choice is made possible because the system is completely observable.

The clogging observer delivers thus an estimation of $d_{clog}(t)$ from the three available measurements: the mould level, the stopper position and the casting speed.

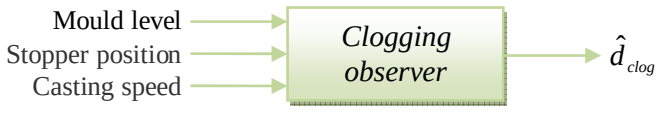

Fig. 3.8. Inputs and outputs of clogging observer

The equation (3.27) should be converted from continuous to discrete-time model to be implemented in an industrial PLC. For example, one can use zero-order hold on the inputs and a sampling time of 0.01s.

3.3.1.2 Simulation results

In the mould level control simulator developed using the typical values of Table 2.1, the flow into the mould has been disturbed by a succession of ramps in order to produce the clogging/unclogging cycle.
The level is maintained at -100mm from the top of the mould by means of a PID controller whose transfer function is the following:

$$TF_{PID}(s) = K_{PID}\left(1+\frac{1}{T_i s}+\frac{T_d s}{1+\frac{T_d}{\beta}s}\right) \tag{3.28}$$

The parameters of this transfer function are given in Table 2.1. Such PID controller is currently in use in a real plant.

Table 3.3. PID parameters

Parameter	Value
K_{PID}	0.38
T_i	9s
T_d	0.2s
β	10

The eigenvalues of the clogging observer have been tuned to –0.6, –0.63, –0.57 and –0.65.
Results are illustrated in Fig. 3.9. In the left-hand side, the inputs of the observer, which are the mould level and the stopper position, are represented. In the right-hand side, four signals are plotted:

- The disruptive signal $d_{clog}(t)$ and its estimation $\hat{d}_{clog}(t)$ (observer output),
- The maximal flow rate into the mould determined from the stopper position,
- The actual flow rate calculated by deducting $\hat{d}_{clog}(t)$ from the maximal rate.

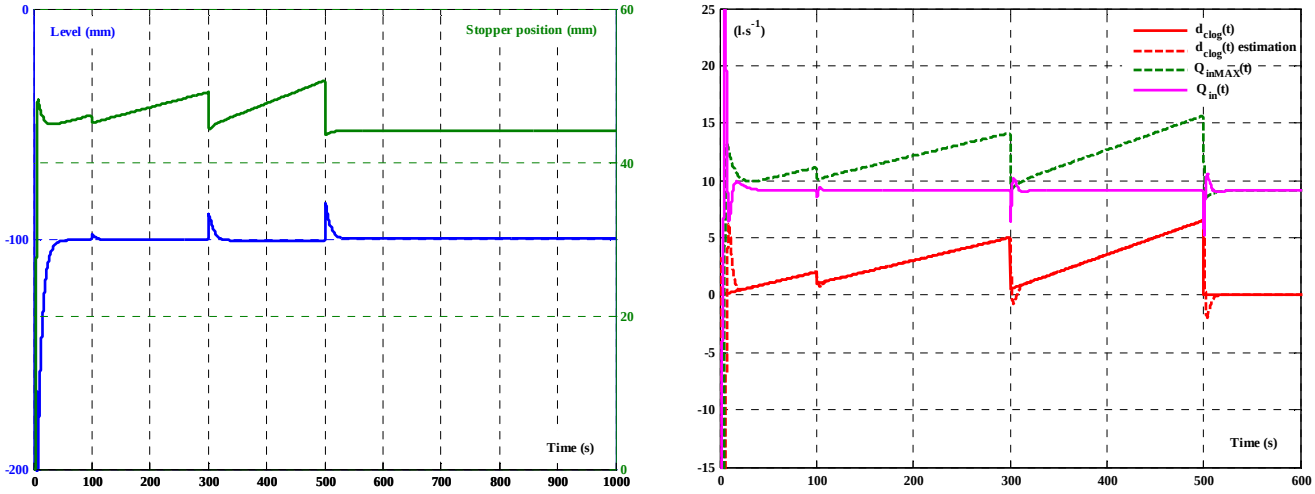

Fig. 3.9. Simulation results showing inputs and outputs of clogging observer compared to flow rate into the mould

The clogging observer performs well because it reproduces accurately the behavior of the disruptive signal $d_{clog}(t)$. It is also able to detect the unclogging instants. Furthermore, by comparing $Q_{in}(t)$ and $Q_{inMAX}(t)$, it can be seen clearly how the clogging restricts the flow through the nozzle.
Similarly, other simulations have been done for other plant parameters and disruptive signals with the same positive results.
Therefore, the clogging observer affords the operators with needed signals to monitor the clogging extent and the amount of clogs leaving nozzle walls at unclogging instants.

3.3.2 Bulging

In this subsection, the mould level is assumed to be affected only by the bulging.

3.3.2.1 Principle

In chapter 2, the bulging effect on the mould level control loop has been modeled by an additional exogenous signal d_{bulge} to the theoretical rate of the flow out of the mould (Fig. 3.10). Based on the same methodology as for the clogging estimation, this sinusoidal function of time will be estimated using a Luenberger observer.

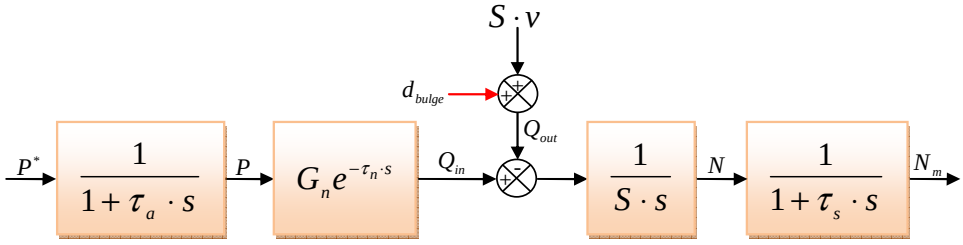

Fig. 3.10. Plant model with bulging effect

Neglecting the level sensor dynamics, the governing equation of the mould level is given by the following differential equation:

$$S\,\dot{N} = \underbrace{G_n\ P(t-\tau_n)}_{Q_{in}} - \underbrace{(S\cdot v + d_{bulge}(t))}_{Q_{out}}$$

$$\text{with}\quad \begin{cases} d_{bulge} = d_{bulge1} + d_{bulge2} + \cdots \\ \ddot{d}_{bulge\,i} = -\omega^2_{bulge\,i}\cdot d_{bulge\,i} \end{cases} \tag{3.29}$$

Once more, the time-delay was approximated by a first order Padé function (3.24) to calculate a linear model. As a consequence, the continuous-time state space equation for the system with bulging effect is:

$$\begin{cases} \dot{X}_{bulge} = A_b\ X_{bulge} + B_b\,U \\ Y = N = C_b\ X_{bulge} \end{cases}$$

$$X^T_{bulge} = \begin{pmatrix} N & d_{bulge1} & \dot{d}_{bulge1} & d_{bulge2} & \dot{d}_{bulge2} & q_p \end{pmatrix} \qquad q_p(t) = G_n P(t-\tau_n) + G_n P(t) \qquad U^T = \begin{pmatrix} P & v \end{pmatrix}$$

$$A_b = \begin{pmatrix} 0 & -1/S & 0 & -1/S & 0 & 1/S \\ 0 & 0 & 1 & 0 & 0 & 0 \\ 0 & -\omega^2_{bulge1} & 0 & 0 & 0 & 0 \\ 0 & 0 & 0 & 0 & 1 & 0 \\ 0 & 0 & 0 & -\omega^2_{bulge2} & 0 & 0 \\ 0 & 0 & 0 & 0 & 0 & -2/\tau_n \end{pmatrix} \qquad B_b = \begin{pmatrix} -G_n/S & -1 \\ 0 & 0 \\ 0 & 0 \\ 0 & 0 \\ 0 & 0 \\ 4G_n/\tau_n & 0 \end{pmatrix} \qquad C_b^T = \begin{pmatrix} 1 \\ 0 \\ 0 \\ 0 \\ 0 \\ 0 \end{pmatrix} \tag{3.30}$$

Recall that the actuator dynamics has not been considered in this representation for the same reasons listed previously.

Only two bulging frequencies have been introduced. If the level spectrum analysis reveals other frequencies, this structure remains valid. All the designer has to do is to add two additional state variables per frequency.

The observability matrix O_b is classically calculated as follows:

$$O_b = \begin{pmatrix} C_b \\ C_b\cdot A_b \\ C_b\cdot A_b^2 \\ C_b\cdot A_b^3 \\ C_b\cdot A_b^4 \\ C_b\cdot A_b^5 \end{pmatrix} = \begin{pmatrix} 1 & 0 & 0 & 0 & 0 & 0 \\ 0 & -1/S & 0 & -1/S & 0 & 1/S \\ 0 & 0 & -1/S & 0 & -1/S & -2/(S\cdot\tau_n) \\ 0 & \omega^2_{bulge1}/S & 0 & \omega^2_{bulge2}/S & 0 & 4/(S\cdot\tau_n^2) \\ 0 & 0 & \omega^2_{bulge1}/S & 0 & \omega^2_{bulge2}/S & -8/(S\cdot\tau_n^3) \\ 0 & -\omega^4_{bulge1}/S & 0 & -\omega^4_{bulge2}/S & 0 & 16/(S\cdot\tau_n^4) \end{pmatrix} \tag{3.31}$$

O_b has full rank 6 because the two frequencies ω_1 and ω_2 are different, and so the system is completely observable.
The Luenberger observer is designed considering the stopper position P and the casting speed v as inputs, and the mould level N as output according to the following continuous-time equation:

$$\dot{\hat{X}}_{bulge} = (A_b - K_b \cdot C_b)\hat{X}_{bulge} + B_b\, U + K_b\, N \tag{3.32}$$

where K_b is the observer gain chosen so that the eigenvalues of $A_b - K_b \cdot C_b$ are strictly negative. It is adjusted afterwards to achieve an appropriate dynamics knowing that its stability decreases with increasing dynamics.
The equation (3.32) should be converted from continuous to discrete-time model to be implemented in an industrial PLC. For example, one can use zero-order hold on the inputs and a sampling time of 0.01s.
The estimations of $d_{bulge1}(t)$ and $d_{bulge2}(t)$ are thus provided by the bulging observer from the three available measurements: the mould level, the stopper position and the casting speed.

Fig. 3.11. Inputs and outputs of bulging observer

Finally, an estimation of the global bulging effect $d_{bulge}(t)$ is expressed as the sum of $\hat{d}_{bulge1}(t)$ and $\hat{d}_{bulge2}(t)$.

3.3.2.2 Simulation results

Based on the same previous simulator with the same PID controller, the disruptive signal $d_{clog}(t)$ has been removed and the flow out of the mould has been disturbed by a sum of two sine waves $d_{bulge1}(t)$ and $d_{bulge2}(t)$ as shown in Table 3.4.

Table 3.4. Sine waves parameters

Sine wave	Frequency (Hz)	Peak to peak value ($L \cdot s^{-1}$)		
		First case	Second case	Third case
$d_{bulge1}(t)$	0.1	4	0	4
$d_{bulge2}(t)$	0.03	0	10	10

The eigenvalues of the bulging observer have been tuned to –0.6, –0.57, –0.54, –0.48, –0.45 and –0.66. Simulation results are graphed in Fig. 3.12, Fig. 3.13 and Fig. 3.14 where the six following signals are plotted for each case:

- The mould level and the stopper position (observer inputs),
- $d_{bulge1}(t)$ and $d_{bulge2}(t)$ estimations (observer outputs),
- The disruptive signal $d_{bulge}(t)$ and its estimation $\hat{d}_{bulge}(t)$.

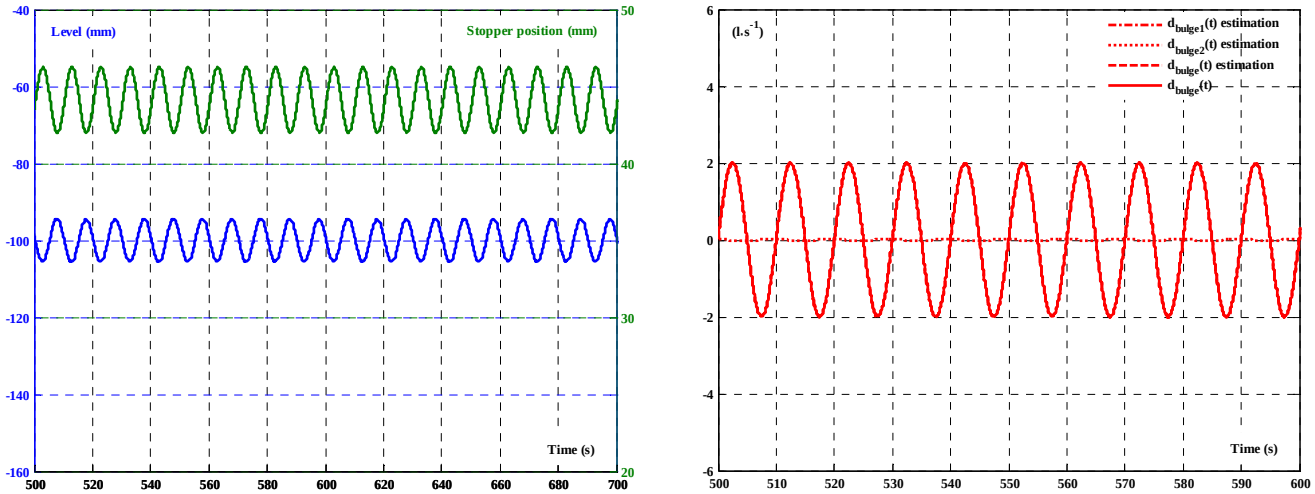

Fig. 3.12. Bulging observer results in the first case

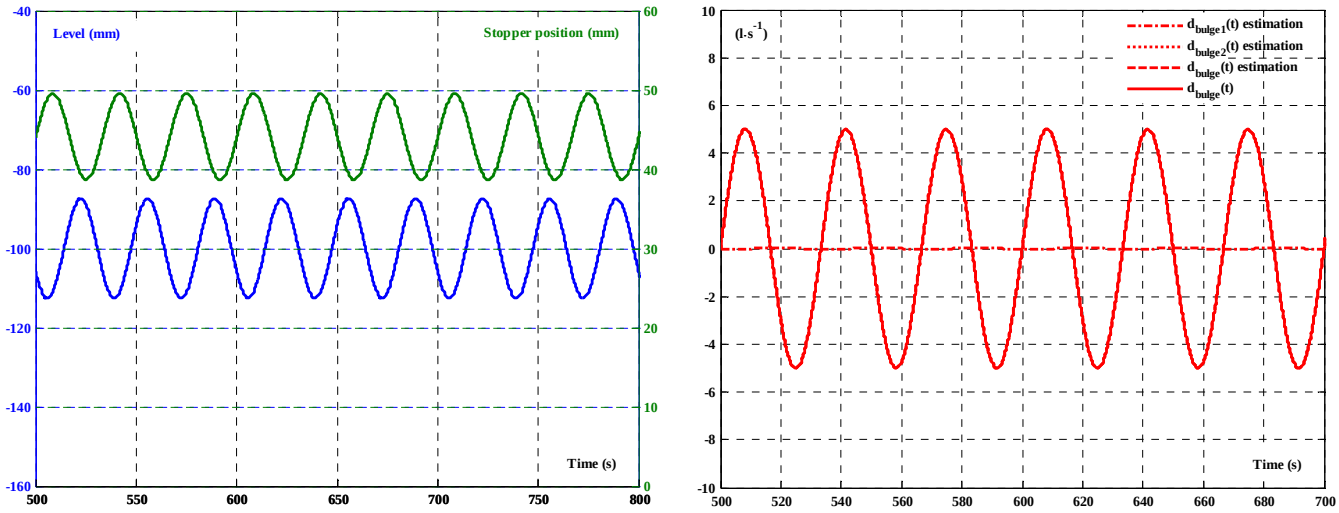

Fig. 3.13. Bulging observer results in the second case

In the first and second case, the flow rate out of the mould is disturbed by a unique sine wave. Clearly, the bulging observer is able to detect the disruptive frequency. In the third case (Fig. 3.14), the two disruptive frequencies with the correct amplitudes are detected separately as expected. Furthermore, $d_{bulge}(t)$ is confounded with its estimation calculated as the sum of $\hat{d}_{bulge1}(t)$ and $\hat{d}_{bulge2}(t)$.

These results, with some others not presented here, demonstrate the ability of the bulging observer to evaluate the bulging effect on the flow rate out of the mould.

Therefore, the operators may take advantage of this estimation scheme to pinpoint the sites between rolls wherein the bulging of the solidified shell takes place.

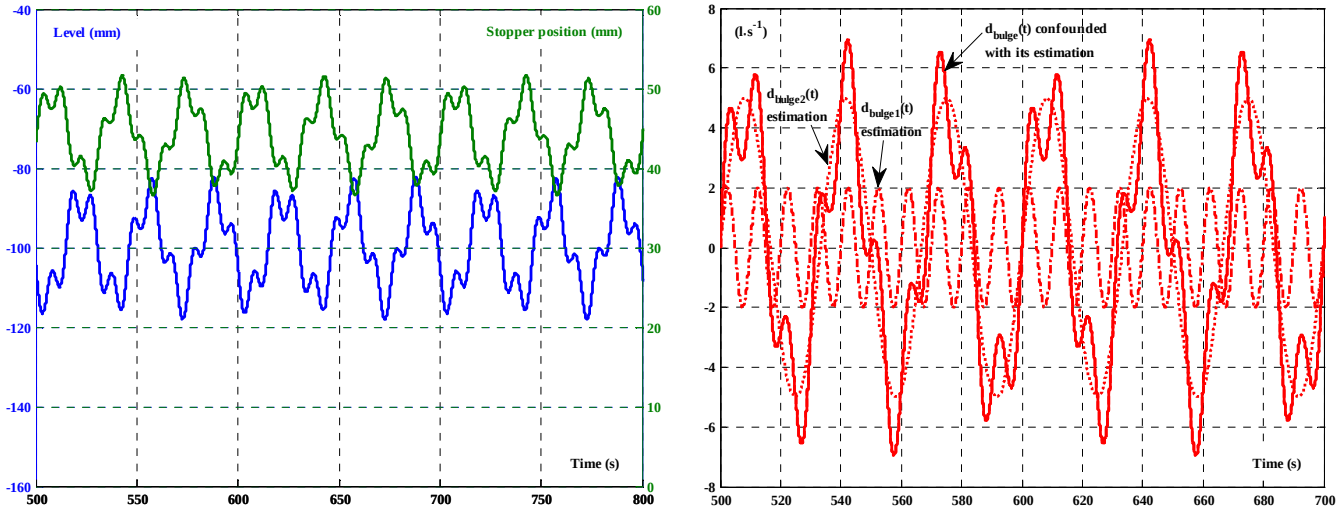

Fig. 3.14. Bulging observer results in the third case

3.3.3 Global estimation

The previous clogging and bulging observers were designed separately to estimate the clogging and the bulging respectively when only one disturbance takes place during casting. However, when the two disturbances occur simultaneously, the two observers should be merged into a single global one whose objective is to estimate $d_{clog}(t)$ and $d_{bulge}(t)$ individually.

3.3.3.1 Principle

As shown in Fig. 3.15, both $d_{clog}(t)$ and $d_{bulge}(t)$ are now taken into account in the plant model.

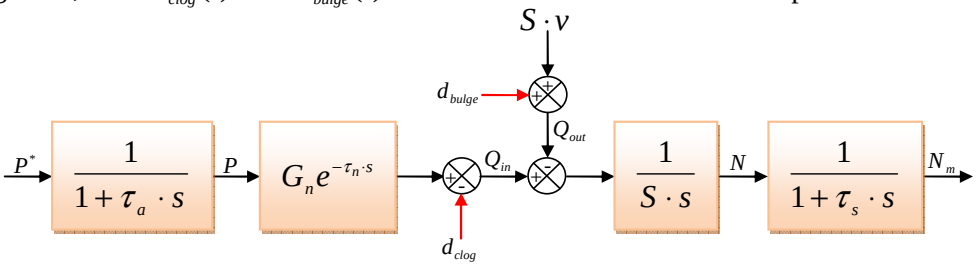

Fig. 3.15. Plant model with both clogging and bulging effects

Neglecting the level sensor dynamics, the new equation of level variation is given by:

$$S\dot{N} = \underbrace{G_n\ P(t-\tau_n) - d_{clog}(t)}_{Q_{in}} - \underbrace{(S\cdot v + d_{bulge}(t))}_{Q_{out}} \quad \text{with} \quad \begin{cases} \ddot{d}_{clog} = 0 \\ d_{bulge} = d_{bulge1} + d_{bulge2} + \cdots \\ \ddot{d}_{bulge\,i} = -\omega^2_{bulge\,i}\cdot d_{bulge\,i} \end{cases} \tag{3.33}$$

The overall continuous-time state-space representation, including both clogging and bulging effects, becomes:

$$\begin{cases} \dot{X} = A_{cb}\,X + B_{cb}\,U \\ Y = N = C_{cb}\,X \end{cases}$$

$$X^T = \begin{pmatrix} N & d_{clog} & \dot{d}_{clog} & d_{bulge1} & \dot{d}_{bulge1} & d_{bulge2} & \dot{d}_{bulge2} & q_p \end{pmatrix} \qquad q_p(t) = G_n P(t-\tau_n) + G_n P(t) \qquad U^T = \begin{pmatrix} P & v \end{pmatrix}$$

$$A_{cb} = \begin{pmatrix} 0 & -1/S & 0 & -1/S & 0 & -1/S & 0 & 1/S \\ 0 & 0 & 1 & 0 & 0 & 0 & 0 & 0 \\ 0 & 0 & 0 & 0 & 0 & 0 & 0 & 0 \\ 0 & 0 & 0 & 0 & 1 & 0 & 0 & 0 \\ 0 & 0 & 0 & -\omega^2_{bulge1} & 0 & 0 & 0 & 0 \\ 0 & 0 & 0 & 0 & 0 & 0 & 1 & 0 \\ 0 & 0 & 0 & 0 & 0 & -\omega^2_{bulge2} & 0 & 0 \\ 0 & 0 & 0 & 0 & 0 & 0 & 0 & -2/\tau_n \end{pmatrix} \quad B_{cb} = \begin{pmatrix} -G_n/S & -1 \\ 0 & 0 \\ 0 & 0 \\ 0 & 0 \\ 0 & 0 \\ 0 & 0 \\ 0 & 0 \\ 4G_n/\tau_n & 0 \end{pmatrix} \quad C_{cb}^T = \begin{pmatrix} 1 \\ 0 \\ 0 \\ 0 \\ 0 \\ 0 \\ 0 \\ 0 \end{pmatrix} \tag{3.34}$$

In this case, we obtain the observability matrix:

$$O_{cb} = \begin{pmatrix} 1 & 0 & 0 & 0 & 0 & 0 & 0 & 0 \\ 0 & -1/S & 0 & -1/S & 0 & -1/S & 0 & 1/S \\ 0 & 0 & -1/S & 0 & -1/S & 0 & -1/S & -2/(S\cdot\tau_n) \\ 0 & 0 & 0 & \omega^2_{bulge1}/S & 0 & \omega^2_{bulge2}/S & 0 & 4/(S\cdot\tau_n^2) \\ 0 & 0 & 0 & 0 & \omega^2_{bulge1}/S & 0 & \omega^2_{bulge2}/S & -8/(S\cdot\tau_n^3) \\ 0 & 0 & 0 & -\omega^4_{bulge1}/S & 0 & -\omega^4_{bulge2}/S & 0 & 16/(S\cdot\tau_n^4) \\ 0 & 0 & 0 & 0 & -\omega^4_{bulge1}/S & 0 & -\omega^4_{bulge2}/S & -32/(S\cdot\tau_n^5) \\ 0 & 0 & 0 & \omega^6_{bulge1}/S & 0 & \omega^6_{bulge2}/S & 0 & 64/(S\cdot\tau_n^6) \end{pmatrix} \tag{3.35}$$

O_{cb} has full rank 8, and so the system is completely observable. Based on equation (3.34), the global Luenberger observer, depicted in Fig. 3.16, is given by the following continuous-time equation:

$$\dot{\hat{X}} = (A_{cb} - K_{cb} \cdot C_{cb})\hat{X} + B_{cb}\, U + K_{cb}\, N \tag{3.36}$$

where K_{cb} is the observer gain.

Fig. 3.16. Inputs and outputs of global observer

3.3.3.2 Simulation results

Among the numerous simulations done, two representative results of global observer are presented in this paragraph. In the first case, the flow out of the mould has been disturbed by the sum of the two previous sine waves whose properties were given in Table 3.4. In addition to this disturbance, $d_{clog}(t)$ was reintroduced to model the clogging/unclogging cycle.

The eigenvalues of the global observer have been tuned to –0.6, –0.63, –0.51, –0.57, –0.54, –0.48, –0.45 and –0.66.

Simulation results, plotted in Fig. 3.17, indicate that both $d_{clog}(t)$ and $d_{bulge}(t)$ are confounded with their estimations. The global observer is thus capable of monitoring each disturbance without any interference effect between them.

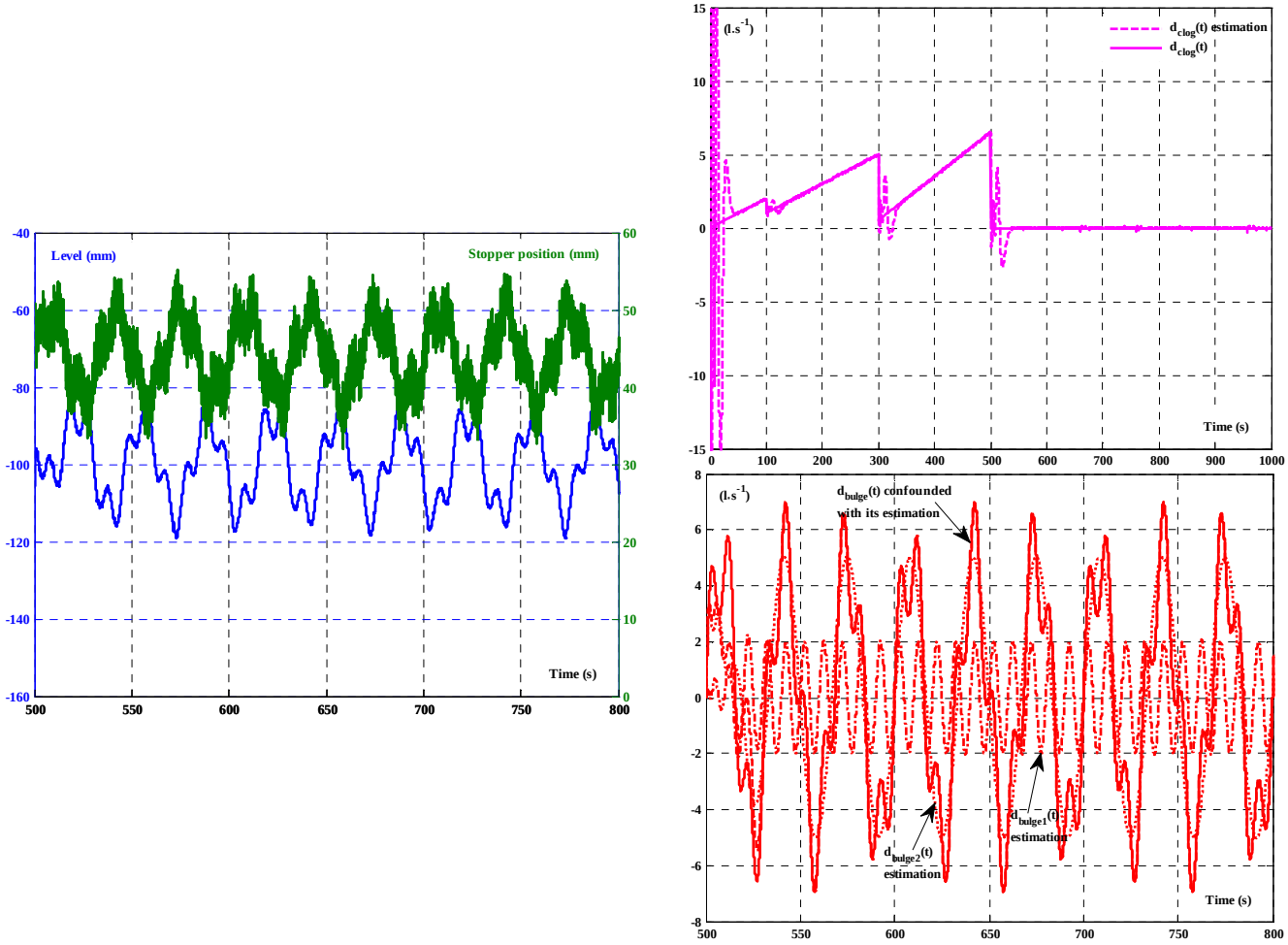

Fig. 3.17. Global observer results in the first case

In the second case, a new signal $d_{clog}(t)$ was generated to simulate another clogging/unclogging cycle. $\hat{d}_{bulge1}(t)$ has been removed and $\hat{d}_{bulge2}(t)$ was introduced only between 0 and 250s and between 500 and 750s. Once more, the global observer yields good estimations of disruptive frequencies, bulging effect intensity, unclogging instants and progress of clogging severity (Fig. 3.18).

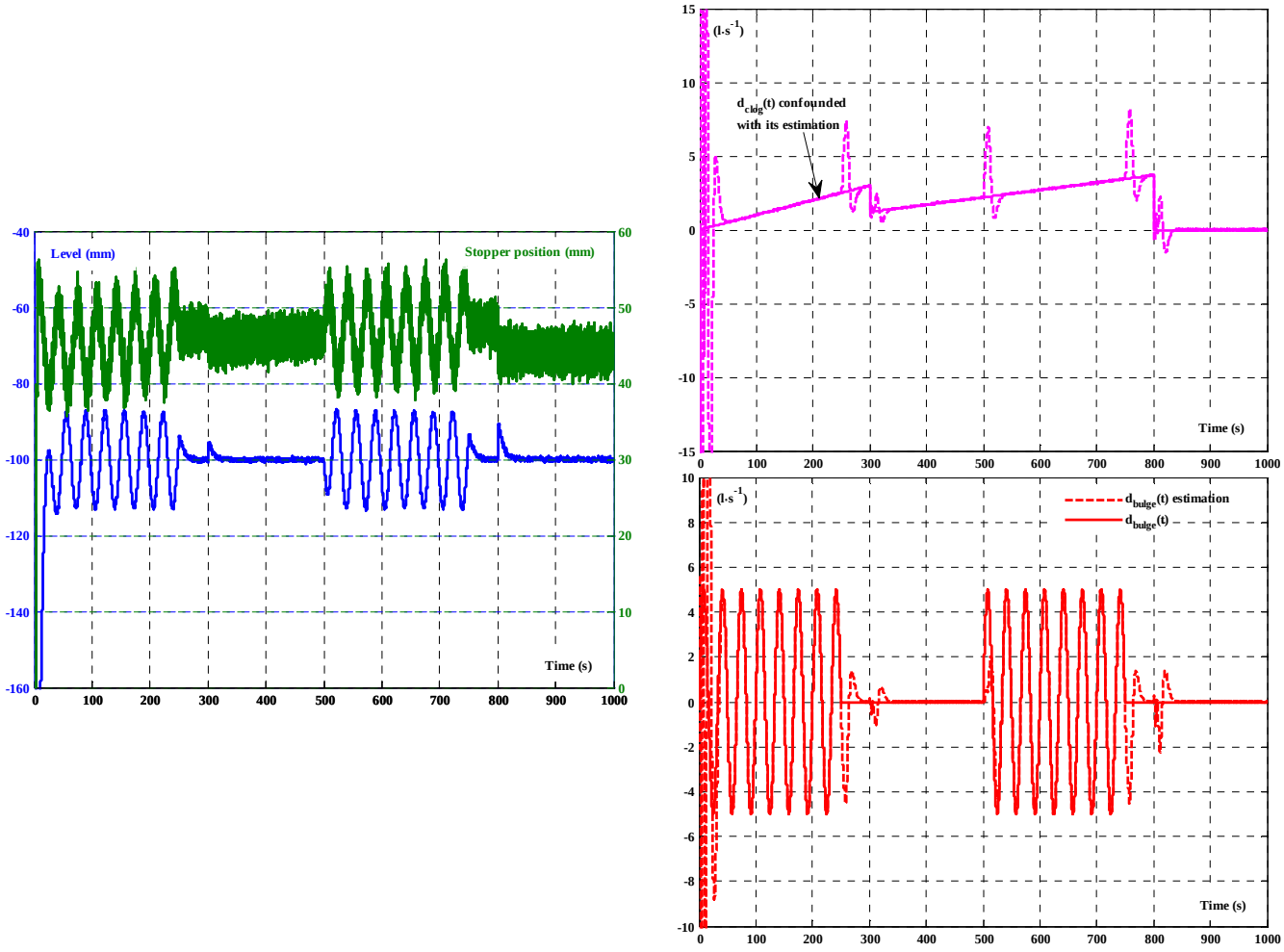

Fig. 3.18. Global observer results in the second case

3.3.3.3 Experimental validation

The previous global observer is now applied on experimental data collected during a casting sequence. A spectrum analysis of the level has identified three bulging frequencies 0.084, 0.095 and 0.082Hz ranked by decreasing intensity (Fig. 3.19).

The plant model is then described by the continuous-time state-space representation:

$$\begin{cases} \dot{X} = A_{cb}\, X + B_{cb}\, U \\ Y = N = C_{cb}\, X \end{cases}$$

$$X^T = \begin{pmatrix} N & d_{clog} & \dot{d}_{clog} & d_{bulge1} & \dot{d}_{bulge1} & d_{bulge2} & \dot{d}_{bulge2} & d_{bulge3} & \dot{d}_{bulge3} & q_p \end{pmatrix} \qquad U^T = \begin{pmatrix} P & v \end{pmatrix}$$

$$A_{cb} = \begin{pmatrix} 0 & -1/S & 0 & -1/S & 0 & -1/S & 0 & -1/S & 0 & 1/S \\ 0 & 0 & 1 & 0 & 0 & 0 & 0 & 0 & 0 & 0 \\ 0 & 0 & 0 & 0 & 0 & 0 & 0 & 0 & 0 & 0 \\ 0 & 0 & 0 & 0 & 1 & 0 & 0 & 0 & 0 & 0 \\ 0 & 0 & 0 & -\omega_{bulge1}^2 & 0 & 0 & 0 & 0 & 0 & 0 \\ 0 & 0 & 0 & 0 & 0 & 0 & 1 & 0 & 0 & 0 \\ 0 & 0 & 0 & 0 & 0 & -\omega_{bulge2}^2 & 0 & 0 & 0 & 0 \\ 0 & 0 & 0 & 0 & 0 & 0 & 0 & 0 & 1 & 0 \\ 0 & 0 & 0 & 0 & 0 & 0 & 0 & -\omega_{bulge3}^2 & 0 & 0 \\ 0 & 0 & 0 & 0 & 0 & 0 & 0 & 0 & 0 & -2/\tau_n \end{pmatrix} \quad B_{cb} = \begin{pmatrix} -G_n/S & -1 \\ 0 & 0 \\ 0 & 0 \\ 0 & 0 \\ 0 & 0 \\ 0 & 0 \\ 0 & 0 \\ 0 & 0 \\ 0 & 0 \\ 4G_n/\tau_n & 0 \end{pmatrix} \quad C_{cb}^T = \begin{pmatrix} 1 \\ 0 \\ 0 \\ 0 \\ 0 \\ 0 \\ 0 \\ 0 \\ 0 \\ 0 \end{pmatrix} \qquad (3.37)$$

This system is completely observable because its observability matrix has full rank 10. The chosen eigenvalues for the observer were –1.5, –1.57, –1.27, –1.42, –1.35, –1.2, –1.12, –1.15, –1.6 and –1.05.

In Fig. 3.19, we visualize the results of the global observer applied on a first data record. $\hat{d}_{clog}(t)$ is compared to the maximum flow rate into the mould $Q_{inMAX}(t)$ calculated from the stopper position. It appears that $\hat{d}_{clog}(t)$ does not possess ramp components and this means that no clogging phenomenon is detected in this record.

In reference to the same figure, $\hat{d}_{bulge}(t)$ is compared to the flow rate out of the mould calculated from the casting speed and the mould section. $\hat{d}_{clog}(t)$ should be added to $\hat{d}_{bulge}(t)$ to determine the actual bulging effect. From a control point of view, it is not critical to have the $\hat{d}_{bulge}(t)$ average included in $\hat{d}_{clog}(t)$. For instance, the control structure, developed in the next section, uses the sum of the two estimations to compensate the bulging and clogging effects.

In summary, we conclude that this casting sequence has been disturbed only by the bulging.

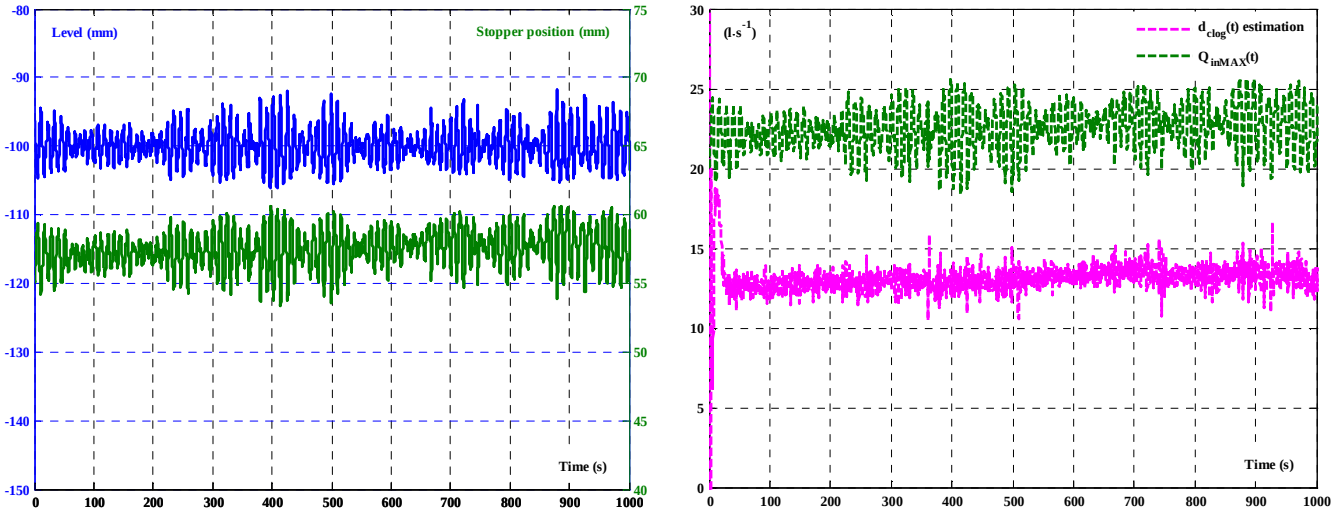

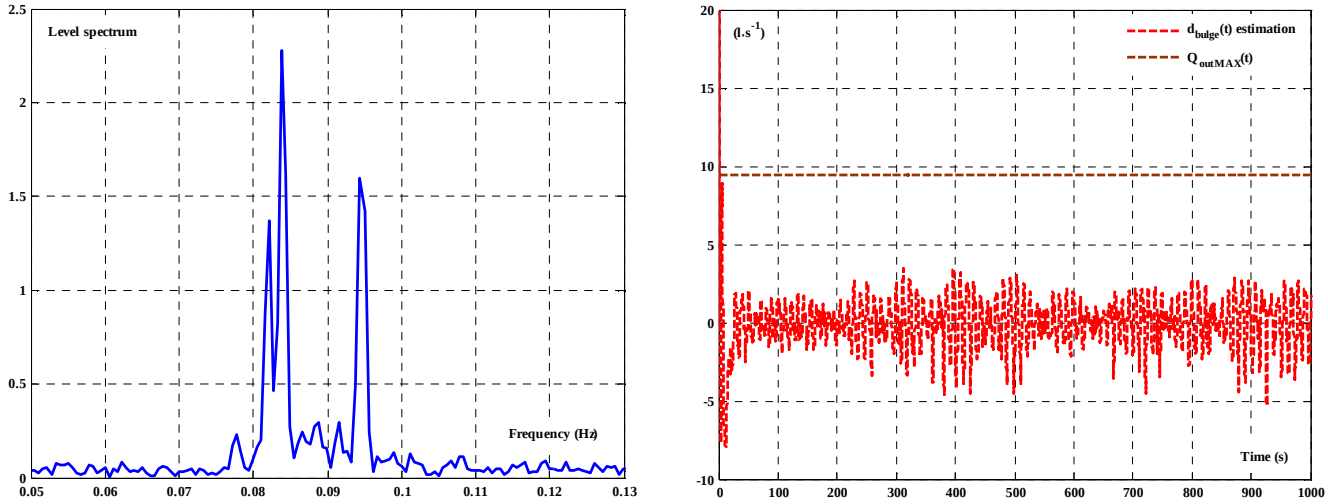

Fig. 3.19. Results of global observer applied on a first data record

The same global observer is now applied on a second data record coming from a real plant (Fig. 3.20). $\hat{d}_{clog}(t)$ clearly indicates multiple clogging/unclogging cycles, i.e. ramp variations during the clogging followed by sudden drops at the unclogging instants. The actual flow rate into the mould $Q_{in}(t)$ is then calculated from the difference of $Q_{inMAX}(t)$ and $d_{clog}(t)$. It is three times smaller than the maximum rate obtained in the absence of clogging. On the other hand, it seems that $Q_{outMAX}(t)$ is ten times greater than $\hat{d}_{bulge}(t)$ whose effect on the actual flow can thereby be neglected. In short, it may reasonably be inferred that this second casting sequence has certainly not been disturbed by the bulging phenomenon.

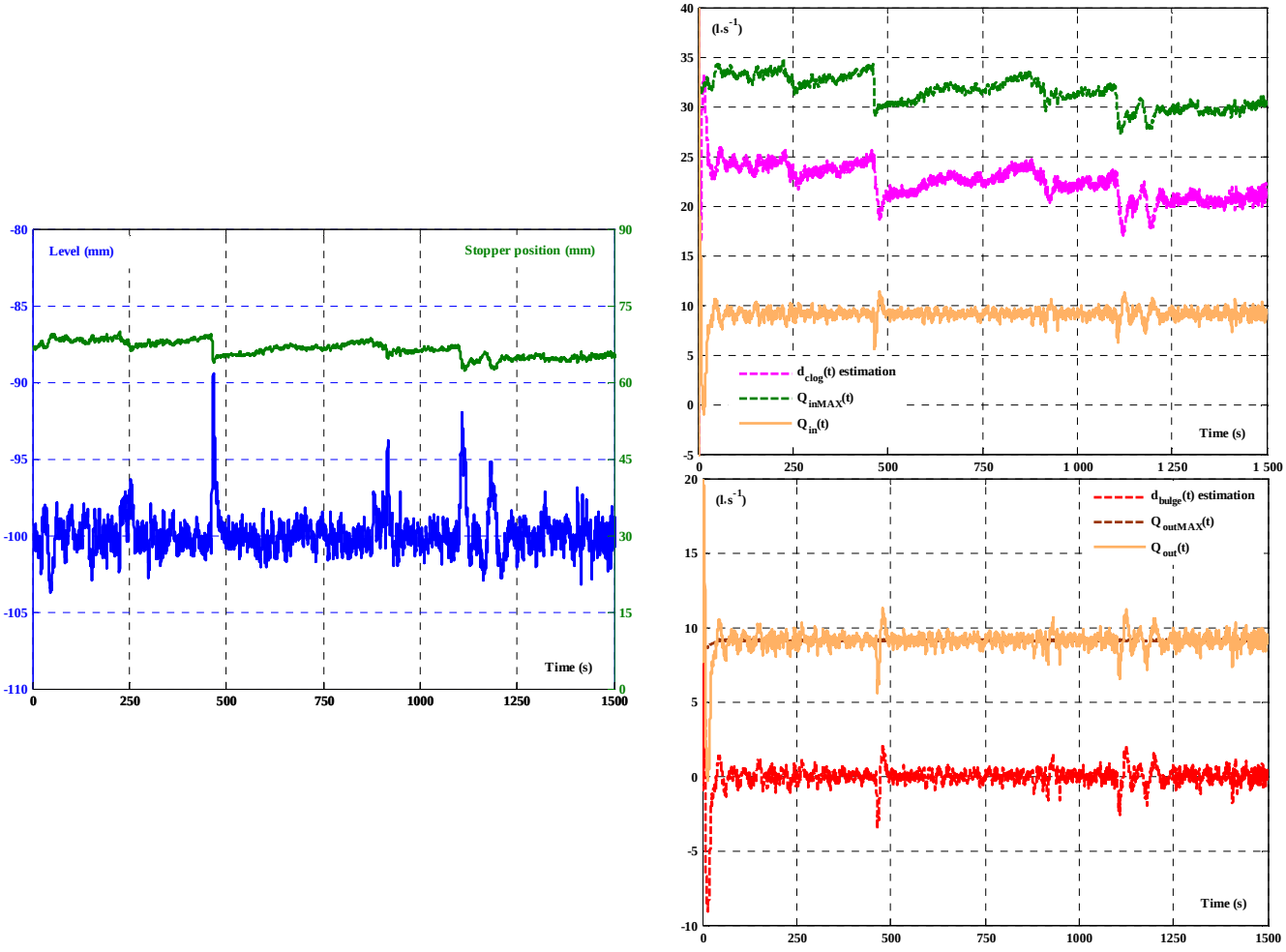

Fig. 3.20. Results of global observer applied on a second data record

As stated before, this experimental validation demonstrates, once again, that the global observer is able to provide valuable insights about the disturbances affecting the meniscus region.

3.4 Bulging rejection

The vast majority of control techniques implemented to keep mould level fluctuations to a minimum, have only a single controller which calculates the control signal from the difference between the average level and the target setpoint. Chapter 4 will be devoted to such strategies which are used currently on many plants with varying degrees of success.

The aim of this section is to develop ways of rejecting disturbances effect with a view to enhancing the mould level stability. The disturbance, used as an example in this section, is the bulging.

Knowing that controllers currently in use at best can control only the average level, bulging rejection should be addressed, in our view, through a complementary module to the main control loop with the help of bulging estimation techniques. Moreover, our proposed additional tool, fully presented hereinafter, can be easily integrated in the industrial casters since it does not require any change or tuning of the existing control scheme.

3.4.1 Bulging effect compensation principle

The idea behind the bulging compensation structure, described in this paragraph, is to include both bulging estimation techniques and feed-forward actions in the mould level control loop. It consists of three major components which are the global observer aforementioned, the prediction block and the actuator inversion as illustrated in Fig. 3.21, where $\hat{d}_{bulge}(t)$ is the estimation of the bulging effect, $\dot{d}_{bulge}(t)$ the estimation of its derivative, $\hat{d}_{bulge}(t+\tau_n)$ its prediction at $t+\tau_n$, $\dot{\hat{d}}_{bulge}(t+\tau_n)$ the prediction of $\dot{\hat{d}}_{bulge}(t)$ at $t+\tau_n$ and finally u_{bulge} is the feed-forward signal. This should result in a system which is capable to cancel the bulging effect on the level and to estimate its effect on the flow out of the mould.

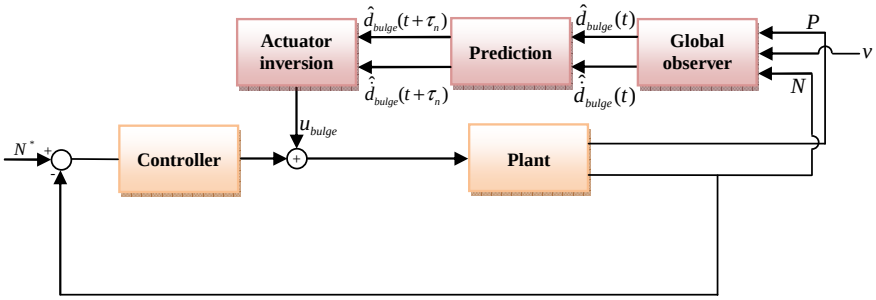

Fig. 3.21. Bulging effect compensation structure

The global observer has been presented with greater detail in the previous section. Due to the presence of a time-delay in the plant model, a prediction step of the bulging estimation is needed because the feed-forward signal calculated from the bulging estimation will be most probably delayed through the nozzle block. Finally, the prediction of bulging estimation cannot be immediately sent to the real process. An additional control input is calculated because the only input available in the real process is the stopper position setpoint. This calculation is performed by inverting the actuator transfer function that is made possible thanks to the observer and prediction blocks which estimate both the bulging effect and its derivative.

3.4.1.1 Prediction of the bulging effect estimation

The purpose of this step is to predict the bulging estimation at $t+\tau_n$ because the plant model incorporates a time-delay and the feed-forward signal u_{bulge} should be added to the main control signal which will be delayed afterwards through the nozzle block. To do so, the prediction block uses only the estimations delivered by the global Luenberger observer (Fig. 3.22).

Fig. 3.22. Inputs and outputs of prediction block

In [11] and [12], a simple prediction method is proposed taking advantage of the periodicity of $\hat{d}_{bulge}(t)$. Since the two periods $2\pi/\omega_{bulge1}$ and $2\pi/\omega_{bulge2}$ are greater than the time-delay τ_n, it is then easy to predict future values as follows:

$$\hat{d}_{bulge1}(t+\tau_n)=\hat{d}_{bulge1}(t+\tau_n-2\pi/\omega_{bulge1}) \qquad \hat{d}_{bulge2}(t+\tau_n)=\hat{d}_{bulge2}(t+\tau_n-2\pi/\omega_{bulge2})$$
$$\hat{d}_{bulge}(t+\tau_n)=\hat{d}_{bulge1}(t+\tau_n)+\hat{d}_{bulge2}(t+\tau_n)=\hat{d}_{bulge1}(t+\tau_n-2\pi/\omega_{bulge1})+\hat{d}_{bulge2}(t+\tau_n-2\pi/\omega_{bulge2}) \tag{3.38}$$

From our point of view, this attempt may succeed only if the amplitudes of the sine waves are constant which is not usually the case. For this reason, we propose, in the sequel, another approach based on the prediction of the state vector.

First of all, equation (3.36) should be rewritten as:

$$\dot{\hat{X}}=(A_{cb}-K_{cb}\cdot C_{cb})\hat{X}+B_{cb}^{a}U^{a}$$
$$B_{cb}^{a}=\begin{pmatrix}B_{cb} & K_{cb}\end{pmatrix} \qquad U^{a}=\begin{pmatrix}P\\ v\\ N\end{pmatrix} \tag{3.39}$$

Solving this linear differential equation, we obtain:

$$\hat{X}(t+\tau_n)=M_{cb}\cdot\hat{X}(t)+\hat{X}_0(t)$$
$$M_{cb}=e^{(A_{cb}-K_{cb}\cdot C_{cb})\cdot\tau_n} \qquad \hat{X}_0(t)=\int_{t}^{t+\tau_n}e^{(A_{cb}-K_{cb}\cdot C_{cb})(t+\tau_n-\tau)}B_{cb}^{a}U^{a}(\tau)d\tau \tag{3.40}$$

M_{cb} may be calculated using for instance Matlab software. Calculation of $\hat{X}_0(t)$ is however much more complicated. Fortunately, it is frequent that U^a remains constant over the integration interval. As a result, one can approximate the vector $\hat{X}_0(t)$ as:

$$\hat{X}_0(t)\approx\left(\int_{t}^{t+\tau_n}e^{(A_{cb}-K_{cb}\cdot C_{cb})\cdot(t+\tau_n-\tau)}d\tau\right)B_{cb}^{a}U^{a}(t) \tag{3.41}$$

Finally, using the Taylor series expansion of the exponential function, we can write:

$$\hat{X}_0(t)\approx\left(\int_{0}^{\tau_n}e^{(A_{cb}-K_{cb}\cdot C_{cb})\cdot\tau}d\tau\right)B_{cb}^{a}U^{a}(t)\approx\tau_n\cdot\left(\sum_{i=0}^{\infty}\frac{((A_{cb}-K_{cb}\cdot C_{cb})\cdot\tau_n)^{i}}{(i+1)!}\right)B_{cb}^{a}U^{a}(t) \tag{3.42}$$

This sum is calculated offline and truncated to a finite order for practical reasons.

Thus, the prediction of the state vector may be generated using equation (3.40). In particular, the prediction of the bulging estimation and its derivative can likewise be derived as follows:

$$\hat{d}_{bulge}(t+\tau_n)=C_{\hat{d}}\cdot\hat{X}(t+\tau_n) \qquad \dot{\hat{d}}_{bulge}(t+\tau_n)=C_{\dot{\hat{d}}}\cdot\hat{X}(t+\tau_n)$$
$$C_{\hat{d}}=\begin{pmatrix}0 & 0 & 0 & 1 & 0 & 1 & 0 & 0\end{pmatrix} \qquad C_{\dot{\hat{d}}}=\begin{pmatrix}0 & 0 & 0 & 0 & 1 & 0 & 1 & 0\end{pmatrix} \tag{3.43}$$

3.4.1.2 Inversion of the actuator dynamics

The final step is to obtain the additional control input u_{bulge} whose function is to cancel the bulging effect on the mould level.

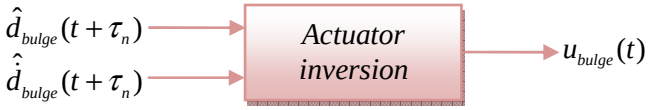

Fig. 3.23. Inputs and outputs of actuator inversion block

To do so, $u_{bulge}(t)$ can be considered as the input of the actuator block, which generates the output $\hat{d}_{bulge}(t+\tau_n)/G_n$ (Fig. 3.24).

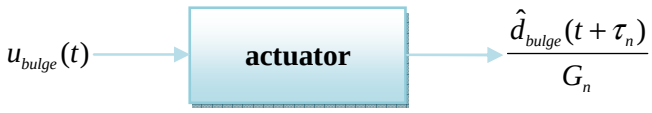

Fig. 3.24. Relationship between $u_{bulge}(t)$ and $\hat{d}_{bulge}(t+\tau_n)$

According to chapter 2, the actuator dynamics is systematically modeled using a first or second order function. In both cases, $u_{bulge}(t)$ may be computed only using $\hat{d}_{bulge}(t+\tau_n)$ and $\dot{\hat{d}}_{bulge}(t+\tau_n)$ with possibly $\hat{d}_{bulge1}(t+\tau_n)$ and $\hat{d}_{bulge2}(t+\tau_n)$ delivered by the prediction block, as:

$$TF_{actuator} = \frac{1}{1+\tau_a \cdot s} \qquad u_{bulge}(t) = \frac{\hat{d}_{bulge}(t+\tau_n)}{G_n} + \frac{\tau_a}{G_n}\dot{\hat{d}}_{bulge}(t+\tau_n)$$

$$TF_{actuator} = \frac{1}{1+\frac{1}{G_a}s+\frac{\tau_a}{G_a}s^2} \qquad \begin{cases} u_{bulge}(t) = \frac{\hat{d}_{bulge}(t+\tau_n)}{G_n} + \frac{1}{G_n G_a}\dot{\hat{d}}_{bulge}(t+\tau_n) + \frac{\tau_a}{G_n G_a}\ddot{\hat{d}}_{bulge}(t+\tau_n) \\ \ddot{\hat{d}}_{bulge}(t+\tau_n) = -\omega^2_{bulge1}\hat{d}_{bulge1}(t+\tau_n) - \omega^2_{bulge2}\hat{d}_{bulge2}(t+\tau_n) \end{cases} \tag{3.44}$$

3.4.2 Simulation validation

This paragraph reports the efforts to assess the performances of the proposed control structure.
In the mould level control simulator, the level is maintained at −100mm by means of PID controller (Table 2.1). The flow out of the mould has been disturbed by the sum of two sine waves whose parameters are given in Table 3.4. Because our purpose is to test the bulging rejection only, it is not necessary to take other phenomena into account. Another point to be tested was the influence of the prediction step on the compensation performances. In this respect, the compensation structure is activated at the instant 150s without including the prediction block. At the instant 250s, this restriction is lifted and so the entire structure is now operating.

Fig. 4.4 shows the results of this analysis. In particular, it can be seen the following:

- Thanks to the whole compensation structure, the mould level variations have been significantly reduced from ±15mm to less than ±1mm.
- The global observer performs quite well after a transient phase.
- If the prediction block is not active, this degrades the performances. Therefore, it is an indispensable component of the compensator.
- The time-shift between the bulging estimation and its prediction is equal to the time-delay of the plant model. This means that the prediction block provides thus the required signal to the actuator inversion block in order to calculate the feed-forward action.

Other aspect to be checked is that the input vector U^a of equation (3.39) should remain constant over the integration interval.

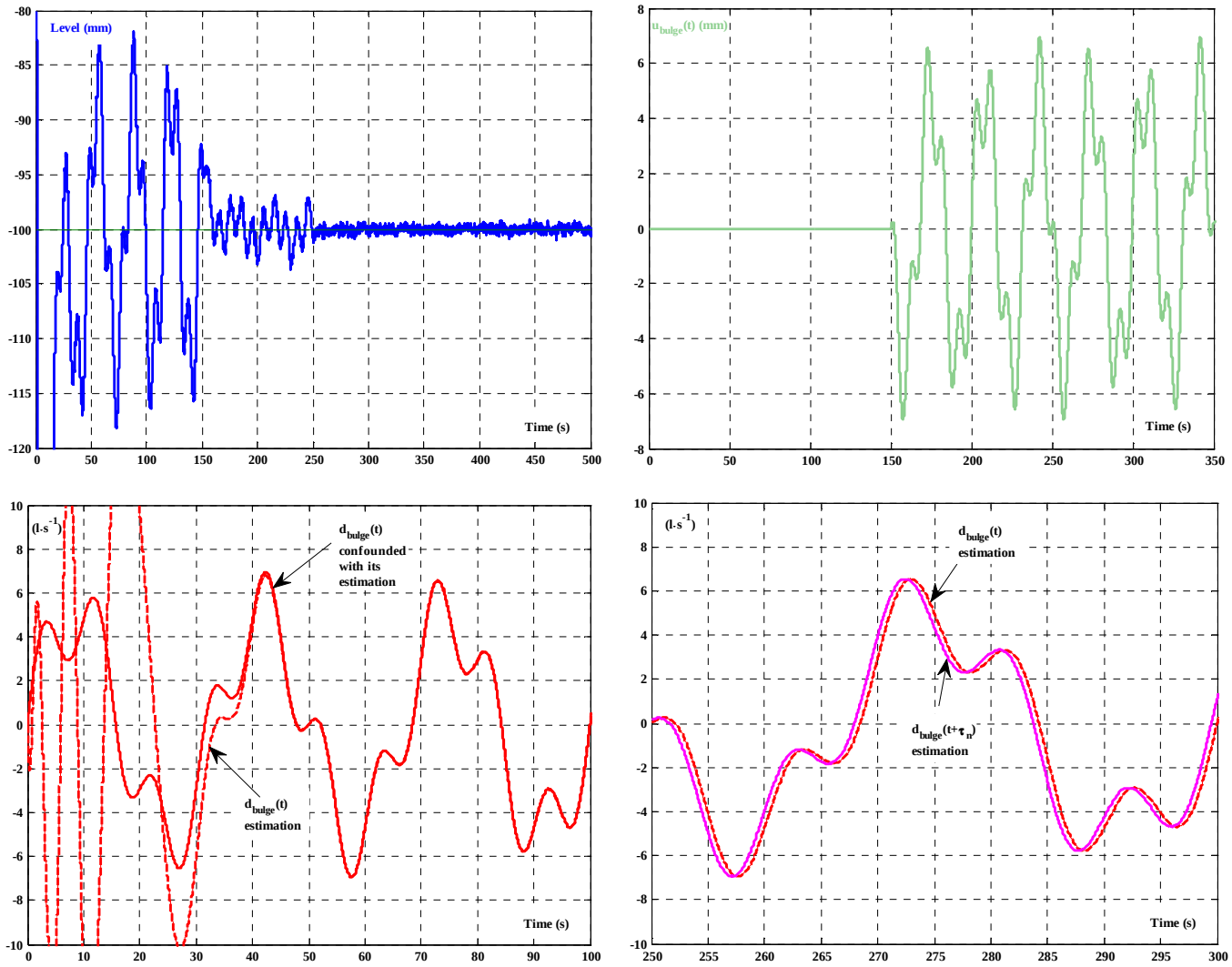

Fig. 3.25. Relevant signals of the bulging compensation structure during a simulation test

In summary, this compensation structure combining bulging effect estimation and feed-forward actions has proved to be effective for reducing unsteady bulging effect on the mould level. An experimental validation will be conducted in the next section confirming the same high performances.

3.5 Experiments

Even though the properties of water differ from those of the steel, the water model is a valuable experimental tool often used to understand the flow regimes inside the mould, as well as to test new instruments or equipment designs. In the framework of this thesis, the water model has been used to validate the bulging compensation structure described above and to determine the ranges of values reached by two key parameters in all possible configurations. As we shall see later, this second outcome is crucial for the mould level control problem.

3.5.1 Water model description

The schematic diagram of the 1:2 scaled water model used hereinafter for testing purposes is shown in Fig. 3.26. It includes a tundish, a transparent nozzle, a transparent mould made of Plexiglas and a suction pump. The dimensions are given in Table 1.1.

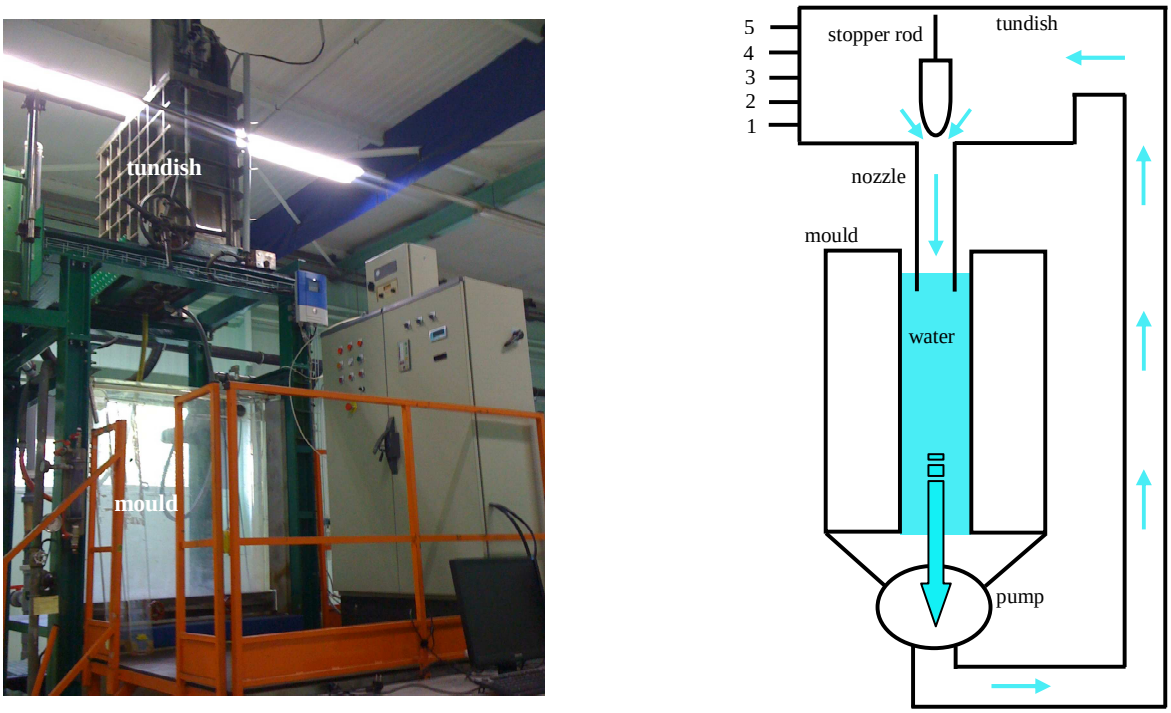

Fig. 3.26. Water model

The water used in lieu of steel flows from the tundish into the mould through the nozzle. The stopper position permits to vary the inflow to the mould. In order to enable the testing of various mould dimensions, this experimental rig is equipped with a mobile wall able to move horizontally to adjust the desired mould width. It allows also the testing of different Submerged Entry Nozzles (SEN) that we place in a support rigidly fixed to the sliding tundish. To model the slag layer effect, one should use silicone oil.

Water circulation is sustained by a pump which delivers water from the collector located at the bottom of the mould to the tundish. Thus, the flow rate out of the mould can be easily set from the pump speed.

To avoid water overflows in the mould, a pipe located at the top of the mould, is provided to drain off the excess of water. Finally, air can be injected at different rates through the SEN to mimic argons gas.

Table 3.5. Tundish and mould dimensions in the water model

Dimension	Tundish	Mould
Width (mm)	1000	1000
Thickness (mm)	360	100
Height (mm)	990	2000

The stopper position is measured by a LVDT sensor. The mould level can be measured either by an ultrasonic sensor or a pressure sensor submerged in the water. The first one is a contactless device which has an adjustable response time with limitations in accuracy whereas the second delivers a noisy signal and is able to reach a high

accuracy. The water model allows also the ultrasonic level sensor to move horizontally above the water free surface by means of a linear positioning unit.
Other measurements are available that include the air flow rate, the air pressure and the flow rate out of the mould. In addition, this system allows the setting of pump speed as well as air flow rate and stopper position when the mould level controller is turned off.
As mentioned earlier, the water model is also used to simulate different types of flow and many phenomena encountered in real situations (Fig. 3.27). The similarity with the real conditions will be addressed in the next paragraph.
Although it is not easy to model the clogging/unclogging cycle, its effect on the mould level or the jet leaving the nozzle could be simulated by acting on the nozzle ports for instance (Fig. 3.27 (b)). As for the bulging, it can be simulated merely by varying the pump speed according to an appropriate sinusoidal wave as we shall see later in this section.

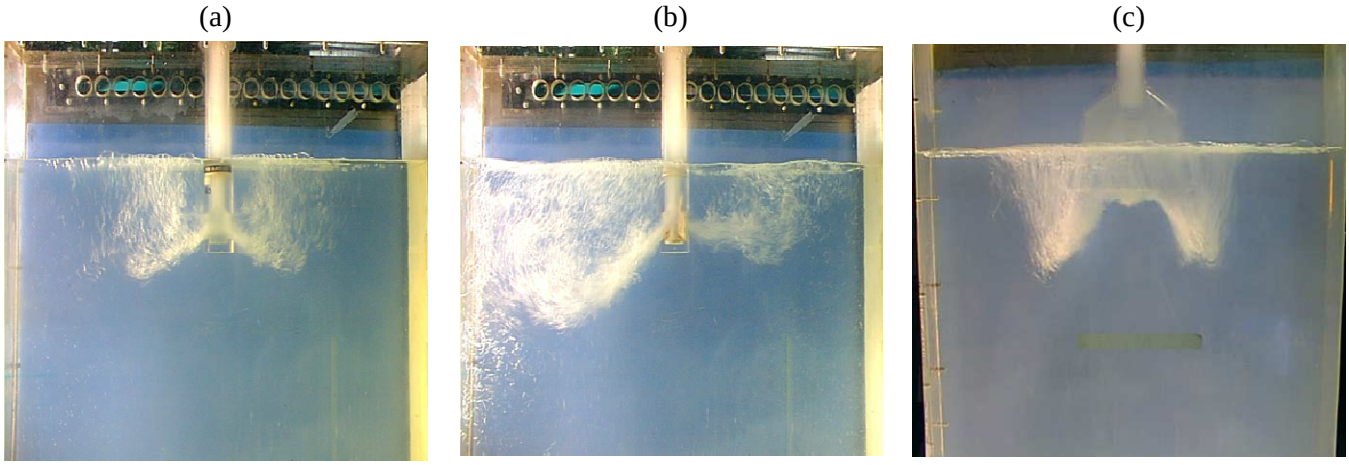

Fig. 3.27. Effect of nozzle geometry on the type of flow inside the mould

Fig. 3.28 shows the free surface interface at low and high flow rates with or without oil. This confirms that mould level is more fluctuant at high rates and these instabilities can be captured by the water model, whence the interest of this experimental setup.

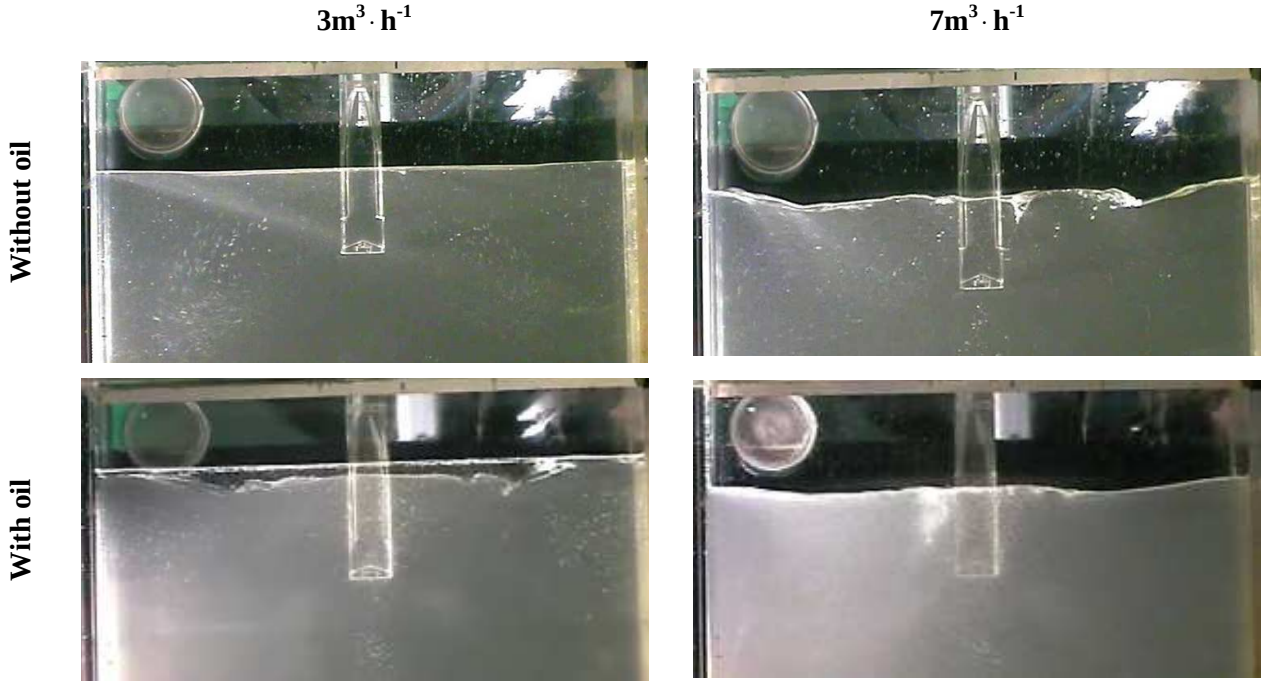

Fig. 3.28. Free surface shape at two different flow rates

3.5.2 Similarities with real situation

The water model should fulfill the Froude similarity with respect to the real flow situation on the caster [80]. The dimensionless Froude number is defined as:

$$Fr = \frac{v}{\left(g\, S_w/2\right)^{1/2}} \tag{3.45}$$

The similarity based on the conservation of the Froude number is the most appropriate to represent the hydrodynamics phenomena in the nozzle as well as in the mould. Additionally, this approach guarantees a similar viscosity, similar turbulence and similar free surface fluctuations.
Table 3.6 summarizes the rules of transposition with the real caster and the necessary formulas to determine the configuration of the water model.

Table 3.6. Similarity rules between the water model and the site

Parameter	Site	Water model
Thickness	S_t	S_t^{WM}
Proportional factor for length	S_t^{WM}/S_t	
Mould width	S_w	$\left(S_t^{WM}/S_t\right)\cdot S_w$
Nozzle diameter	D_n	$\left(S_t^{WM}/S_t\right)\cdot D_n$
Proportional factor for casting speed	v	$\left(S_t^{WM}/S_t\right)^{1/2}\cdot v$
Liquid flow rate	Q_{out}	$\left(S_t^{WM}/S_t\right)^{5/2}\cdot Q_{out}$
Temperature (^oC)	$T_{steel}=1550$	$T_{water}=20$
Gas flow rate	Q_{argon}	$\left(S_t^{WM}/S_t\right)^{5/2}\cdot Q_{argon}\cdot\frac{T_{steel}+173}{T_{water}+273}$

3.5.3 Mould level control loop

The part of the water model, which is under consideration during these real-time experiments, is the mould level control loop. It was designed to have the same structure as those encountered in real situations. It consists of the level sensor, the actuator, the controller, the nozzle and the mould.
The dynamics of the level sensor has been overlooked. On the other hand, the dynamics of the actuator has been identified using the least squares method based on equation (3.11). The actuator time constant was found to be too small and can fairly be neglected resulting in the use of a basic block diagram, as seen in Fig. 3.29, that should be extended to include the disruptive phenomena.
In our experimental setup, we decided to choose the top of the mould as the level measurement origin. The level increases consequently with increasing flow rate. Contrary to the plant models already presented in other sections, the level is calculated here from the difference of the outflow and the inflow. A few sign changes, in the matrices of the plant model equation, are necessary to deal with this chosen level origin.

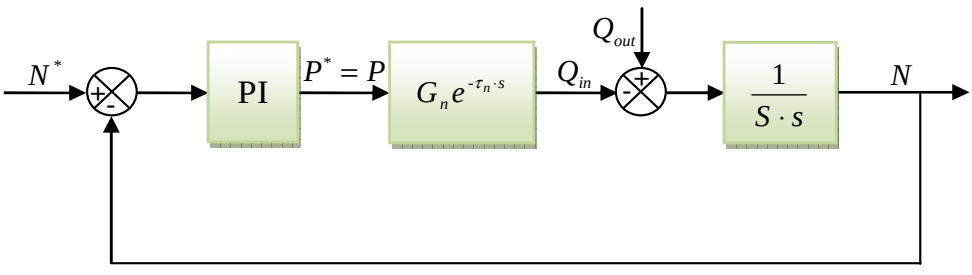

Fig. 3.29. Mould level control loop of the water model

Measurements of the mould level, the stopper position, the flow rates of water and air are fed into a control computer through the software environment dSPACE (Fig. 3.30) which contains the following real-time hardware:

- DS 1005 microprocessor,
- DS 2003 card provides 32 analog input channels,
- DS 2102 card provides 6 analog output channels.

Generated by three PI controllers, the setpoint signals are then sent out to actuators in order to adjust the stopper position, the pump speed and the air flow rate. The dSPACE is wired to the PC via Ethernet connection.

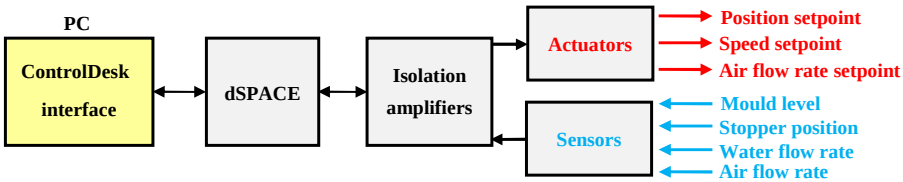

Fig. 3.30. Connections between the control interface and the water model

As the water model provides voltage signals in the range of ±10V or ±5V for each of the physical quantities, some proportional gains should be used, in the Simulink scheme, to convert these voltage signals into their associated values expressed in the appropriate units.

3.5.4 Water model identification

Using this setup, several experiments have been carried out to identify the gain and the delay of the plant model as a function of the flow rate out of the mould (var_1), the air flow rate (var_2), the level sensor position (var_3), the nozzle submergence depth (var_4) and the water level in the tundish (var_5) (Fig. 3.31 and Fig. 3.32). For each function, we vary only one parameter while keeping the rest at their default values.

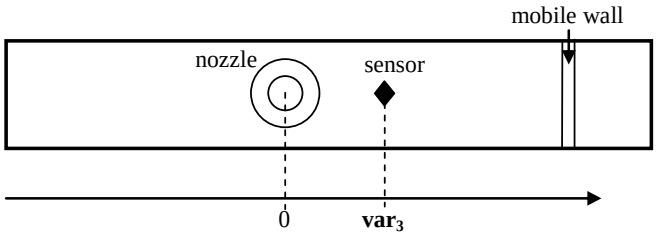

Fig. 3.31. Mould level top view showing the level sensor position

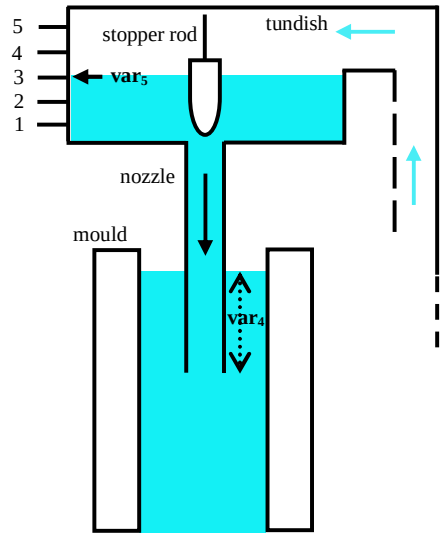

Fig. 3.32. Default mould level in the tundish

3.5.4.1 Experimental conditions

All the experiments have been carried out using a cone-shaped nozzle. The utilized configuration of the water model, outlined in Table 3.7, has been determined to fulfill the Froude similarity with respect to the real flow situation in the caster.

Table 3.7. General configuration of the water model

Parameter	Value	Real situation
Flow rate out of the mould var_1	$3.55m^3 \cdot h^{-1}$	$1.08m \cdot min^{-1}$
Air flow rate var_2 ($Nl \cdot min^{-1}$)	0	0
Level sensor position var_3 (mm)	91	200
Nozzle submergence depth var_4 (mm)	68	220
Water level in the tundish (var_5)	3	NA
Mould section (mm^2)	727×100	1600×220
Tundish position (mm)	333	NA

Level 3 in Table 3.7 corresponds to a half-full tundish.
To collect data, we followed the procedure described in the first section of this chapter. An external PRBS signal is added to the stopper position setpoint as shown in Fig. 3.33.

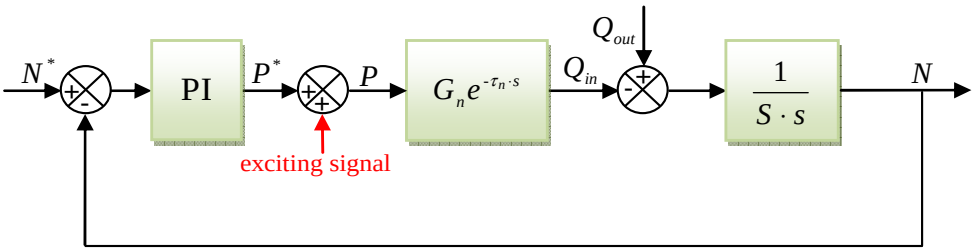

Fig. 3.33. Acquisition protocol for water model identification

The PRBS signal is classically tuned according to the operating point and the control loop response time. The chosen tuning parameters of the PRBS signal and the discrete PI controller are listed in Table 4.1.

Table 3.8. PI and PRBS parameters

	Parameter	Value
PI controller	K_{PI}	0.3
	T_{PI} (s)	12
	Sampling time (s)	0.01
PRBS	Register length	5
	Amplitude (mm)	0.5
	Sampling frequency (Hz)	0.5

The following signals are recorded at sampling frequency of 100Hz:

- Time t,
- Mould level N,
- Mould level setpoint N^*,
- Stopper position P,
- Stopper position setpoint P^*,
- PRBS signal,
- Flow rate out of the mould Q_{out},
- Casting speed setpoint v^*,
- Air flow rate Q_{air},
- Air flow rate setpoint Q_{air}^*.

Each recording lasts about two minutes (i.e. two consecutive sequences) and is repeated at least three times to compare identification results. Data were collected for different water and air flow rates. The water model configuration as well as the casting conditions should not be changed during recording because the identification results depend on them.

3.5.4.2 Results

3.5.4.2.1 The gain and the delay as a function of the flow rate out of the mould

In the real flow situation aforementioned, the casting speed lies between 0.9 and 1.4m · min^{-1}. In order to investigate the tendency of the gain and the delay in these conditions, the flow rate out of the mould should vary from 2.95 to 4.59m^3 · h^{-1} in the water model according to Froude similarity. It is made possible by changing the speed of the pump. Moreover, two high flow rates (5 and 6m^3 · h^{-1}) lying outside this variation interval have also been considered. Meanwhile, the other parameters were set to their default values.

We stress that the record must be repeated many times to compare the identification results. It should be cautioned that experience has shown that the measurements may lead sometimes to erroneous conclusions. The gain and the delay have been identified using the iterative prediction error estimation method applied to a structured state space formalism where the delay is approximated by a first order Laguerre function.

The results are summarized in Table 3.9 and plotted in Fig. 3.34.

Table 3.9. The gain (L · s^{-1} · mm^{-1}) and the delay (s) as a function of the flow rate out of the mould

Q_{out} (m^3 · h^{-1})	Record 1	Record 2	Record 3	Average	Q_{out} (m^3 · h^{-1})	Record 1	Record 2	Record 3	Average
2.95	0.16	0.159	0.16	**0.16**	**2.95**	0.746	0.854	0.814	**0.805**
3.1	0.163	0.163	0.162	**0.163**	**3.1**	0.764	0.72	0.756	**0.747**
3.3	0.167	0.167	0.164	**0.166**	**3.3**	0.551	0.536	0.536	**0.541**
3.55	0.168	0.168	0.168	**0.168**	**3.55**	0.611	0.67	0.662	**0.648**
3.8	0.172	0.173	0.172	**0.172**	**3.8**	0.447	0.452	0.43	**0.443**
4	0.176	0.175	0.175	**0.175**	**4**	0.615	0.63	0.591	**0.612**
4.2	0.179	0.179	0.179	**0.179**	**4.2**	0.618	0.585	0.573	**0.592**
4.4	0.183	0.183	0.183	**0.183**	**4.4**	0.446	0.485	0.407	**0.446**
4.59	0.186	0.186	0.185	**0.186**	**4.59**	0.319	0.427	0.318	**0.355**
5	0.191	0.191	0.192	**0.191**	**5**	0.461	0.419	0.403	**0.428**
6	0.205	0.205	0.205	**0.205**	**6**	0.241	0.392	0.378	**0.337**

The two following graphs clearly show that both the gain and the delay vary depending on the flow rate. The gain varies from 0.16 to 0.205l · s^{-1} · mm^{-1} and the delay from 0.805 to 0.337s. The higher is the flow rate, the smaller is the delay and the larger is the gain.

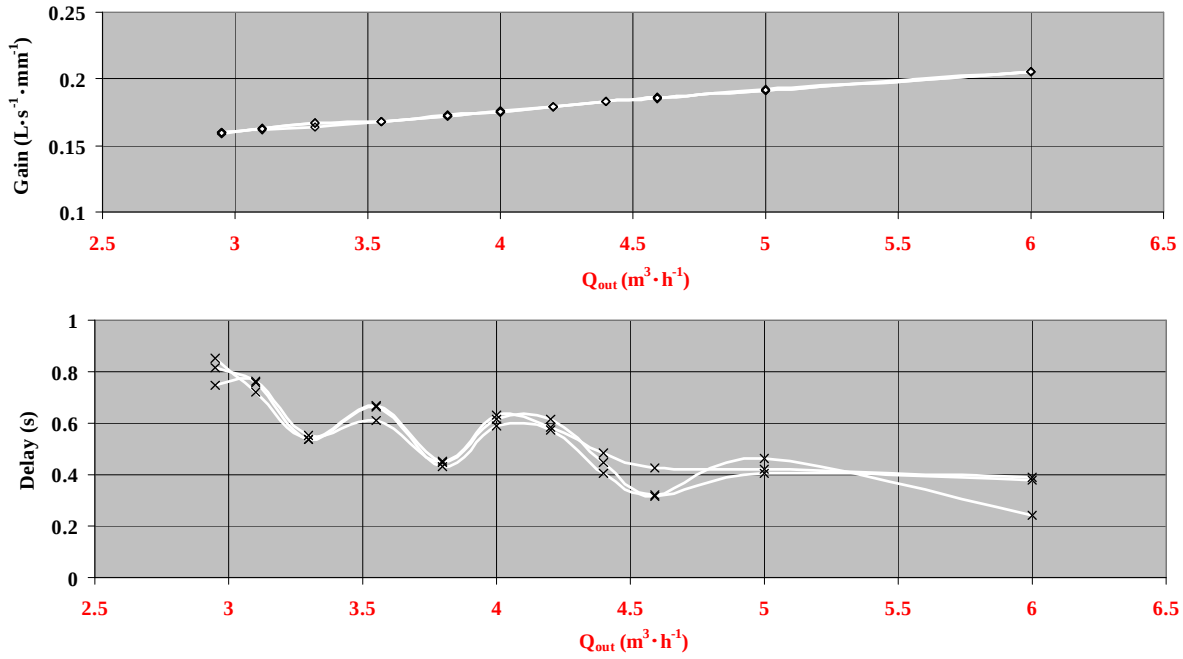

Fig. 3.34. Effect of flow rate on gain and delay

To understand this behavior, several PIV (Particle Image Velocimetry) measurements of water flow pattern inside the mould have been carried out. Unfortunately, there was no obvious relation between the flow regime established and the plant model parameters.
These identification results confirm that the flow rate out of the mould has a great influence on the gain and the delay. The next step would be undertaken to determine the controller performances over the gain and the delay variation intervals and to design, if necessary, another one leading to the required performances.

3.5.4.2.2 The gain and the delay as a function of the air flow rate

In the real plant, considered for this experimentation, the flow rate of argon ranges from 3 to 6Nl · min^{-1} and that of air should vary consequently from 2.79 to 5.59Nl · min^{-1} as determined using Froude similarity. It is made possible by means of an air flow rate control loop.
Here, the trials have been performed at the same water flow rate (3.55m^3 · h^{-1}).
The results, obtained using the same identification algorithm, are presented in Table 3.10 and plotted in Fig. 3.35.

Table 3.10. The gain (L · s^{-1} · mm^{-1}) and the delay (s) as a function of the air flow rate

Q_{air} (Nl · min^{-1})	Record 1	Record 2	Record 3	Average	Q_{air} (Nl · min^{-1})	Record 1	Record 2	Record 3	Average
0	0.168	0.168	0.168	**0.168**	**0**	0.611	0.67	0.662	**0.648**
1	0.165	0.165	0.165	**0.165**	**1**	0.573	0.575	0.575	**0.574**
2	0.164	0.164	0.164	**0.164**	**2**	0.467	0.492	0.473	**0.477**
2.79	0.166	0.167	0.166	**0.166**	**2.79**	0.468	0.416	0.421	**0.435**
3	0.167	0.167	0.167	**0.167**	**3**	0.372	0.329	0.344	**0.348**
3.5	0.167	0.166	0.167	**0.167**	**3.5**	0.264	0.207	0.259	**0.243**
4	0.166	0.166	0.166	**0.166**	**4**	0.247	0.263	0.254	**0.255**
4.5	0.166	0.165	0.166	**0.166**	**4.5**	0.275	0.216	0.256	**0.249**
5	0.165	0.165	0.166	**0.165**	**5**	0.231	0.228	0.224	**0.228**
5.59	0.166	0.166	0.166	**0.166**	**5.59**	0.282	0.281	0.283	**0.282**

The gain is approximately constant over the air flow range. This observation is different from the observation in the case of water flow change, where the gain increases with increasing flow rate.
As for the delay, two trends should be highlighted. Starting from usual conditions without air injection, the delay decreases from 0.648 to 0.243s with increasing air flow rate from 0 to 3.5Nl · min^{-1}. Then, it becomes stable.
Specific finding of this experimentation is that the flow rate of gas hardly affects the delay until a certain limit is reached. Here, the delay decreases by a factor of 3. As a result, this variation should be taken into account when designing controllers.

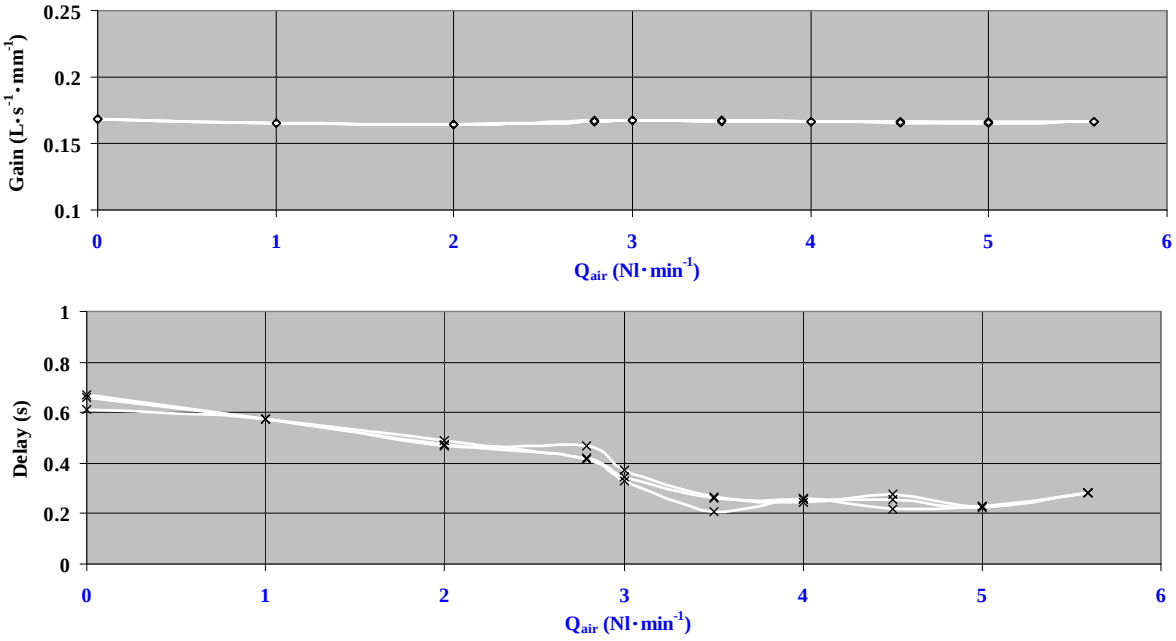

Fig. 3.35. Effect of air flow rate on gain and delay

3.5.4.2.3 The gain and the delay as a function of the level sensor position

In this paragraph, our objective is to relate the level sensor position to the gain and the delay values. Thereby, the sensor position is the variable subject to change. This is made possible by moving the sensor across both sides of the nozzle with the help of a positioning unit. The other variables are kept constant and equal to their default values. The results are listed in Table 3.11 and displayed in Fig. 3.36.

Table 3.11. The gain ($L \cdot s^{-1} \cdot mm^{-1}$) and the delay (s) as a function of the level sensor position

var_3 (mm)	Record 1	Record 2	Record 3	Average	var_3 (mm)	Record 1	Record 2	Record 3	Average
-250	0.168	0.169	0.169	**0.169**	**-250**	0.588	0.592	0.539	**0.573**
-200	0.168	0.168	0.168	**0.168**	**-200**	0.755	0.716	0.732	**0.734**
-150	0.169	0.169	0.168	**0.169**	**-150**	0.815	0.854	0.789	**0.819**
-90	0.168	0.168	0.168	**0.168**	**-90**	0.643	0.593	0.612	**0.616**
91	0.168	0.168	0.168	**0.168**	**91**	0.611	0.67	0.662	**0.648**
150	0.168	0.168	0.168	**0.168**	**150**	0.707	0.758	0.717	**0.727**
200	0.168	0.169	0.168	**0.168**	**200**	0.783	0.87	0.812	**0.822**
250	0.169	0.169	0.169	**0.169**	**250**	0.955	0.853	0.855	**0.888**

It appears that the gain is independent of level sensor position. On the other hand, the results in Fig. 3.36 quantify how changing sensor position tends to modify the delay. In the right side of the nozzle (positive sensor positions), the delay increases slightly as the sensor moves away from the nozzle axis. In the other side (negative sensor positions), the delay increases to reach a peak when the sensor is located at 150mm from the nozzle axis. Further increase in the sensor position causes the delay to decrease until it reaches its initial value. There is a discontinuity between the two sides because the level sensor cannot reach the zone close to the nozzle axis.

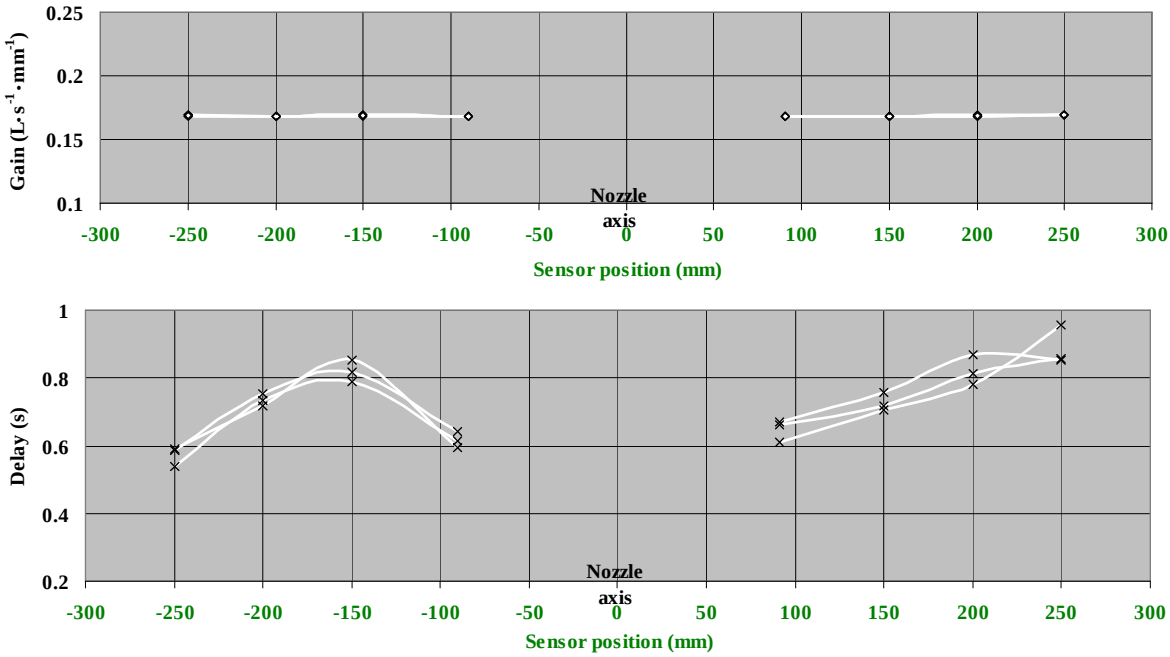

Fig. 3.36. Effect of level sensor position on gain and delay

3.5.4.2.4 The gain and the delay as a function of the nozzle submergence depth

In real plants, it is usual to impose a few variations to the Submerged Entry Nozzle. Therefore, it is worthwhile to study the relationship between the plant model parameters and the nozzle submergence depth. In practice, this variable can be modified in the water model by changing the mould level setpoint.

The identification results in Table 3.12 and Fig. 3.37 suggest that the nozzle submergence depth has a negligible effect on the gain as well as on the delay.

Table 3.12. The gain ($L \cdot s^{-1} \cdot mm^{-1}$) and the delay (s) as a function of the nozzle submergence depth

var_4 (mm)	Record 1	Record 2	Record 3	Average	var_4 (mm)	Record 1	Record 2	Record 3	Average
45	0.169	0.169	0.169	**0.169**	**45**	0.676	0.625	0.669	**0.657**
68	0.168	0.168	0.168	**0.168**	**68**	0.611	0.67	0.662	**0.648**
95	0.166	0.166	0.166	**0.166**	**95**	0.612	0.599	0.607	**0.606**

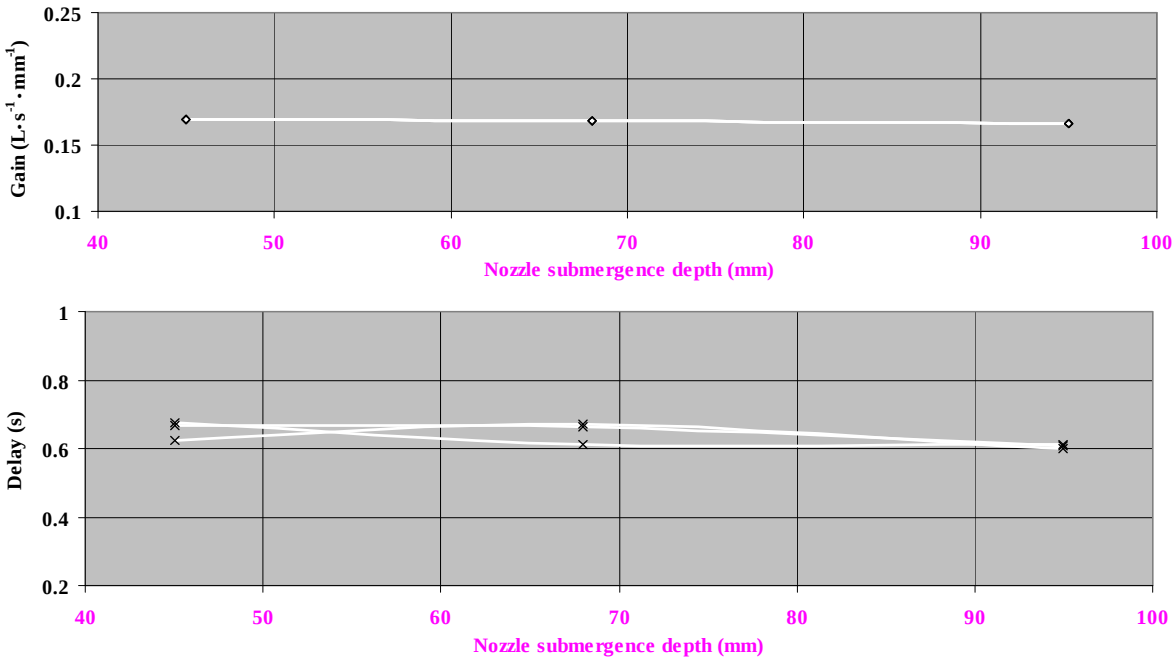

Fig. 3.37. Effect of nozzle submergence depth on gain and delay

3.5.4.2.5 The gain and the delay as a function of the water level in the tundish

The latter aspect to be investigated is the effect of the tundish level. During casting, it changes essentially at the beginning or at the end of the sequence. The water model allows the tundish bath depth to vary only from level 1 to level 4 (Fig. 3.32). The gain and the delay identified for each tundish level are given in Table 3.13 and plotted in Fig. 3.38.

Table 3.13. The gain ($L \cdot s^{-1} \cdot mm^{-1}$) and the delay (s) as a function of the water level in the tundish

var_5 (mm)	Record 1	Record 2	Record 3	Average	var_5 (mm)	Record 1	Record 2	Record 3	Average
1	0.151	0.151	0.151	**0.151**	**1**	0.499	0.527	0.543	**0.523**
2	0.16	0.161	0.16	**0.16**	**2**	0.527	0.557	0.583	**0.556**
3	0.168	0.168	0.168	**0.168**	**3**	0.611	0.67	0.662	**0.648**
4	0.177	0.177	0.176	**0.177**	**4**	0.744	0.653	0.727	**0.708**

Relatively small changes can be observed in both cases. This may be explained in part by the fact that the levels of the tundish are close to each other.

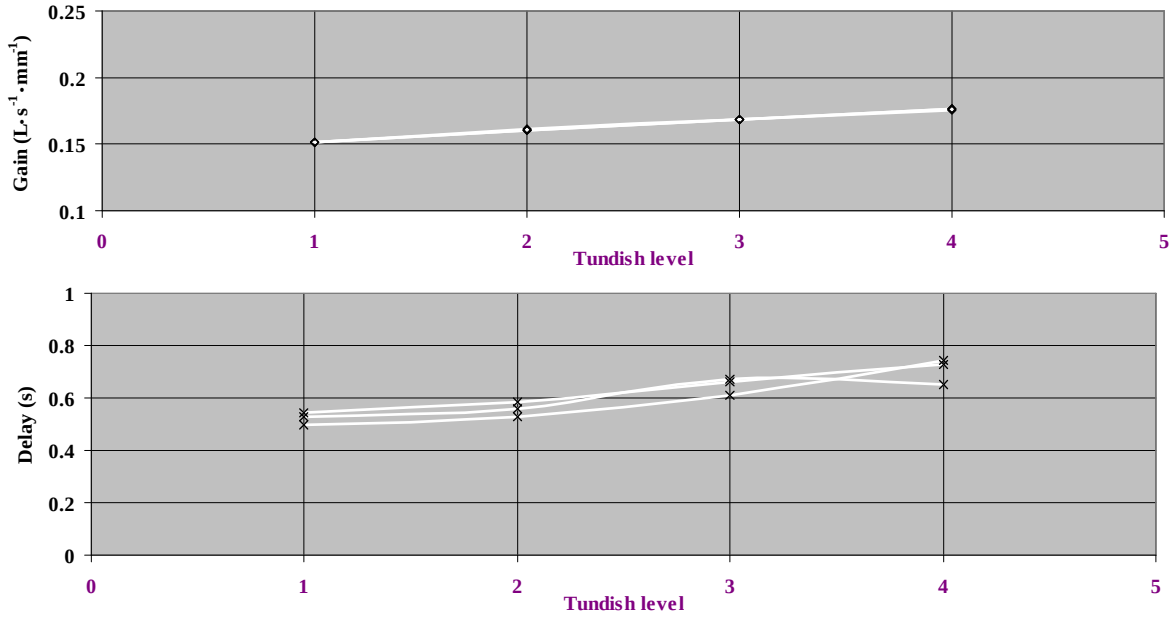

Fig. 3.38. Effect of tundish level on gain and delay

3.5.4.2.6 The gain and the delay as a function of the flow out of the mould in case of a clogged nozzle

Even though the clogging effect on the mould level control loop has been modeled by an additional exogenous signal to the theoretical flow rate into the mould, it seems particularly relevant to examine how the previous functions are modified in case of a clogged nozzle. From a practical point of view, the nozzle port near to the level sensor has been partially closed to produce the clogging phenomenon. We varied only the flow rate out of the mould from 2.95 to 6$m^3 \cdot h^{-1}$. The results are listed in Table 3.14 and compared with those of a clean nozzle in Fig. 3.39.

Table 3.14. The gain ($L \cdot s^{-1} \cdot mm^{-1}$) and the delay (s) as a function of the flow rate in case of a clogged nozzle

Q_{out} ($m^3 \cdot h^{-1}$)	Record 1	Record 2	Record 3	Average	Q_{out} ($m^3 \cdot h^{-1}$)	Record 1	Record 2	Record 3	Average
2.95	0.151	0.152	0.152	**0.152**	**2.95**	0.537	0.529	0.49	**0.519**
3.55	0.162	0.162	0.162	**0.162**	**3.55**	0.45	0.486	0.452	**0.463**
4	0.168	0.168	0.168	**0.168**	**4**	0.445	0.472	0.446	**0.454**
4.59	0.175	0.175	0.175	**0.175**	**4.59**	0.491	0.452	0.514	**0.486**
6	0.186	0.186	0.186	**0.186**	**6**	0.494	0.457	0.494	**0.482**

The gain is clearly lower than for a clean nozzle at each flow rate. This result agrees with the fact that the clogging reduces the flow rate entering the mould. Nevertheless, the same behavior is preserved, confirming that the gain increases with increasing flow rate. On the other hand, these experiments show, in contrast with the first observations, that the delay remains relatively constant even at high flow rates.

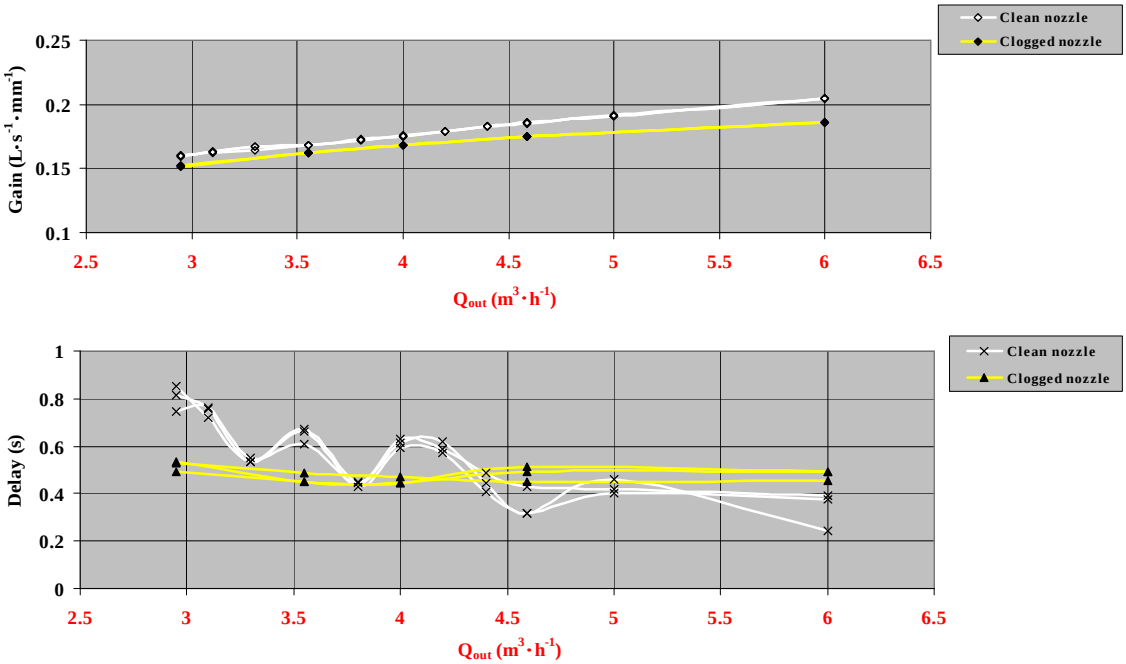

Fig. 3.39. Effect of flow rate on gain and delay in case of a clogged nozzle

3.5.4.2.7 The gain and the delay as a function of the air flow rate in case of a clogged nozzle

Within the same conditions as that of the previous paragraph, the air flow rate has been varied over the range 2.79 - 5.59$Nl \cdot min^{-1}$. Meanwhile, the flow rate out of the mould is kept constant at 3.55$m^3 \cdot h^{-1}$.
The identification results are given in Table 3.15 and graphed in Fig. 3.40.

Table 3.15. The gain ($L \cdot s^{-1} \cdot mm^{-1}$) and the delay (s) as a function of the air flow rate in case of a clogged nozzle

Q_{air} ($Nl \cdot min^{-1}$)	Record 1	Record 2	Record 3	Average	Q_{air} ($Nl \cdot min^{-1}$)	Record 1	Record 2	Record 3	Average
0	0.161	0.161	0.161	**0.161**	**0**	0.522	0.494	0.472	**0.496**
1	0.161	0.162	0.161	**0.161**	**1**	0.386	0.402	0.383	**0.39**
2.79	0.16	0.16	0.16	**0.16**	**2.79**	0.351	0.385	0.352	**0.363**
3.5	0.16	0.16	0.16	**0.16**	**3.5**	0.365	0.377	0.353	**0.365**
4.5	0.159	0.159	0.159	**0.159**	**4.5**	0.37	0.407	0.405	**0.394**
5.59	0.157	0.157	0.157	**0.157**	**5.59**	0.449	0.446	0.46	**0.452**

Similarly to the results achieved in case of a clean nozzle, the gain is approximately constant over the air flow range considered. As expected, its value has been reduced as an obvious consequence of the clogging phenomenon.
As for the delay, the experiments show that its value does not decrease beyond a certain air flow rate which is probably somewhere between 2.5 and 3Nl · min^{-1}. Furthermore, the delay reaches its initial value, when no air is injected, at high flow rates.

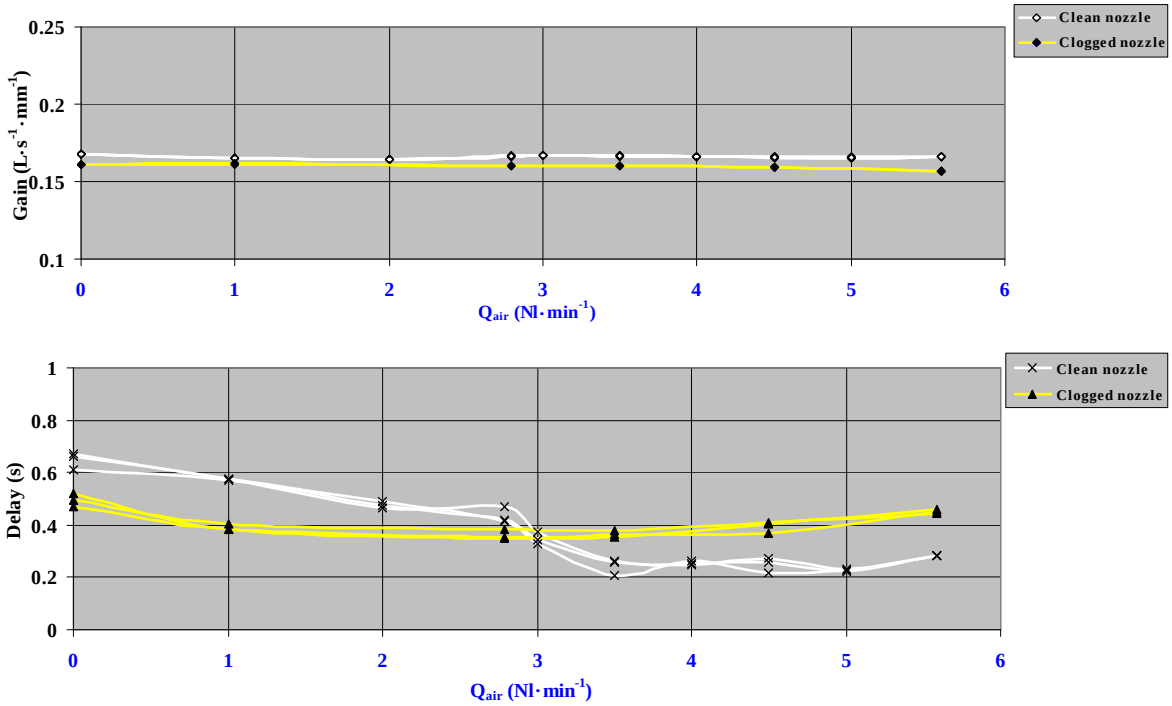

Fig. 3.40. Effect of air flow rate on gain and delay in case of a clogged nozzle

3.5.4.2.8 The gain and the delay as a function of the sensor position in case of a clogged nozzle

Another parameter that has been varied in case of a clogged nozzle is the level sensor position. The results, listed in Table 3.16, reveal that the gain is, once more, independent of sensor position.

Table 3.16. The gain (L · s^{-1} · mm^{-1}) and the delay (s) as a function of the level sensor position in case of a clogged nozzle

var$_3$ (mm)	Record 1	Record 2	Record 3	Average	var$_3$ (mm)	Record 1	Record 2	Record 3	Average
-250	0.162	0.161	0.161	**0.161**	**-250**	1.25	1.22	1.21	**1.23**
-150	0.161	0.161	0.16	**0.161**	**-150**	2.15	2.15	2.18	**2.16**
-90	0.161	0.161	0.162	**0.161**	**-90**	0.554	0.548	0.569	**0.557**
91	0.162	0.162	0.162	**0.162**	**91**	0.45	0.486	0.452	**0.463**
150	0.162	0.162	0.162	**0.162**	**150**	0.493	0.491	0.449	**0.478**
250	0.162	0.162	0.163	**0.162**	**250**	0.453	0.466	0.47	**0.463**

On the other hand, the sensor position greatly affects the delay in the left side of the nozzle where this parameter reaches its highest value of 2.16s as shown in Fig. 3.41. An explanation of such finding still needs further investigations.

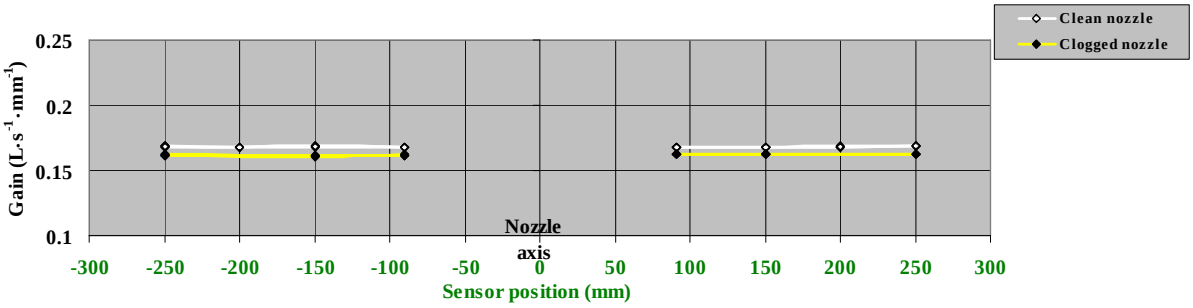

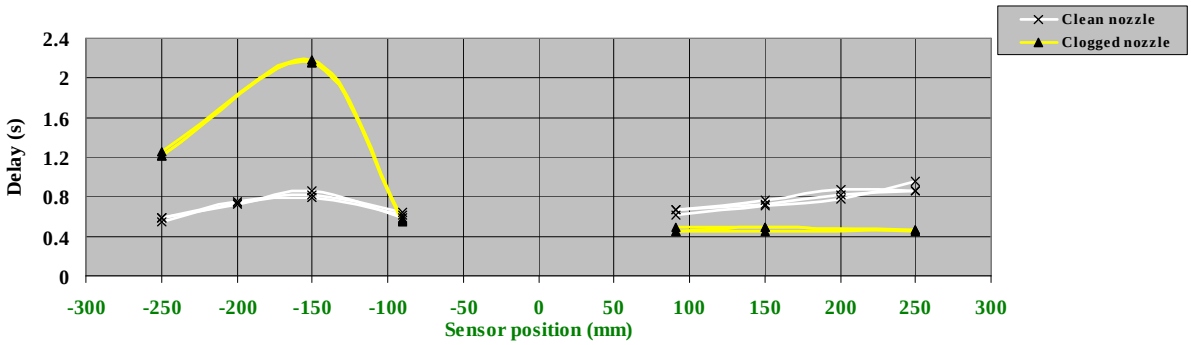

Fig. 3.41. Effect of level sensor position on gain and delay in case of a clogged nozzle

3.5.4.2.9 Conclusion

With regard to these experiments, the following conclusions were drawn in the presence or absence of the clogging:

- The gain is independent of sensor position, nozzle submergence depth and air flow rate.
- The gain increases with increasing flow rate out of the mould and with tundish level. Under normal process conditions, its value varies between $0.151\text{L}\cdot\text{s}^{-1}\cdot\text{mm}^{-1}$ and $0.205\text{L}\cdot\text{s}^{-1}\cdot\text{mm}^{-1}$.
- The delay is independent of tundish level and nozzle submergence depth.
- The higher the flow rate of water or air the lower the delay whose value varies between 0.888s and 0.282s. During the clogging, it may reach 2.16s.

3.5.5 Experimental validation of bulging effect cancellation

In this paragraph, the water model is used to evaluate the performances of the bulging effect compensation structure described in the previous section (Fig. 3.21). The utilized configuration of the water model is the default one summarized in Table 3.7.
The mould level is maintained at 200mm from the top of the mould by means of the same PI controller. The flow rate out of the mould is set to $3.55\text{m}^3\cdot\text{h}^{-1}$ and no air is injected.
In these conditions, the retained values for the gain and the delay are $0.168\text{L}\cdot\text{s}^{-1}\cdot\text{mm}^{-1}$ and 0.65s respectively.
In order to simulate the bulging effect on the mould level, the flow out of the mould has been purposely disturbed at the instant 200s by a sine wave $d_{bulge}(t)$ whose frequency is 0.05Hz (i.e. at the middle of the bulging frequency range) and magnitude is $2\text{m}^3\cdot\text{h}^{-1}$ leading to visible mould level variations (Fig. 3.42).

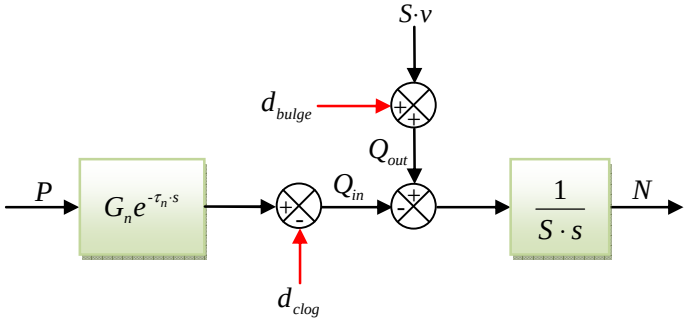

Fig. 3.42. Integral plant model of the water model

The mould level variation is governed by the linear differential equation:

$$S\,\dot{N} = \underbrace{(S\cdot v + d_{bulge}(t))}_{Q_{out}} - \underbrace{(G_n\ P(t-\tau_n) - d_{clog}(t))}_{Q_{in}} \tag{3.46}$$

Using (3.46), we can write the overall continuous-time state-space representation including both clogging and bulging effects:

$$\begin{cases} \dot{X} = A_{cb}\, X + B_{cb}\, U \\ Y = N = C_{cb}\, X \end{cases}$$

$$X^T = \begin{pmatrix} N & d_{clog} & \dot{d}_{clog} & d_{bulge} & \dot{d}_{bulge} & q_p \end{pmatrix} \qquad q_p(t) = G_n P(t-\tau_n) + G_n P(t)$$

$$U^T = \begin{pmatrix} P & v \end{pmatrix} \tag{3.47}$$

$$A_{cb} = \begin{pmatrix} 0 & 1/S & 0 & -1/S & 0 & 1/S \\ 0 & 0 & 0 & 0 & 0 & 0 \\ 0 & 0 & 0 & 0 & 0 & 0 \\ 0 & 0 & 0 & 0 & 1 & 0 \\ 0 & 0 & 0 & -\omega_{bulge}^2 & 0 & 0 \\ 0 & 0 & 0 & 0 & 0 & -2/\tau_n \end{pmatrix} \qquad B_{cb} = \begin{pmatrix} -G_n/S & -1 \\ 0 & 0 \\ 0 & 0 \\ 0 & 0 \\ 0 & 0 \\ 4G_n/\tau_n & 0 \end{pmatrix} \qquad C_{cb}^T = \begin{pmatrix} 1 \\ 0 \\ 0 \\ 0 \\ 0 \\ 0 \end{pmatrix}$$

The global observer and the prediction block have been developed following the methodology presented in the third and fourth section of this chapter. The observer gain K_{cb} has been chosen so that the eigenvalues of $A_{cb} - K_{cb} \cdot C_{cb}$ are –0.85, –0.95, –1.05, –0.9, –0.8 and –1.

Since the actuator dynamics has been neglected, no actuator inversion block is needed. $u_{bulge}(t)$ is thereby merely given by:

$$u_{bulge}(t) = \frac{\hat{d}_{bulge}(t+\tau_n)}{G_n} \tag{3.48}$$

The adopted scenario was the following. The compensation structure was activated only during the intervals between 400 and 600s and between 800 and 1000s. It does not operate otherwise. The most useful signals from the water model have been monitored and analyzed. Amongst them, the mould level N, the feed-forward signal $u_{bulge}(t)$, the bulging effect estimation $\hat{d}_{bulge}(t)$ and the stopper position P are depicted in Fig. 3.43.

During the periods where the compensation structure is active, it can be seen clearly that level variations generated by the bulging have nose-dived from ±18mm to less than ±1mm. Meanwhile, the magnitude of the stopper position has increased from ±1mm to more than ±2.5mm. Furthermore, it can be noticed that the observer works pretty well because it reproduces the behavior of the disruptive sine wave independently from the compensation actions.

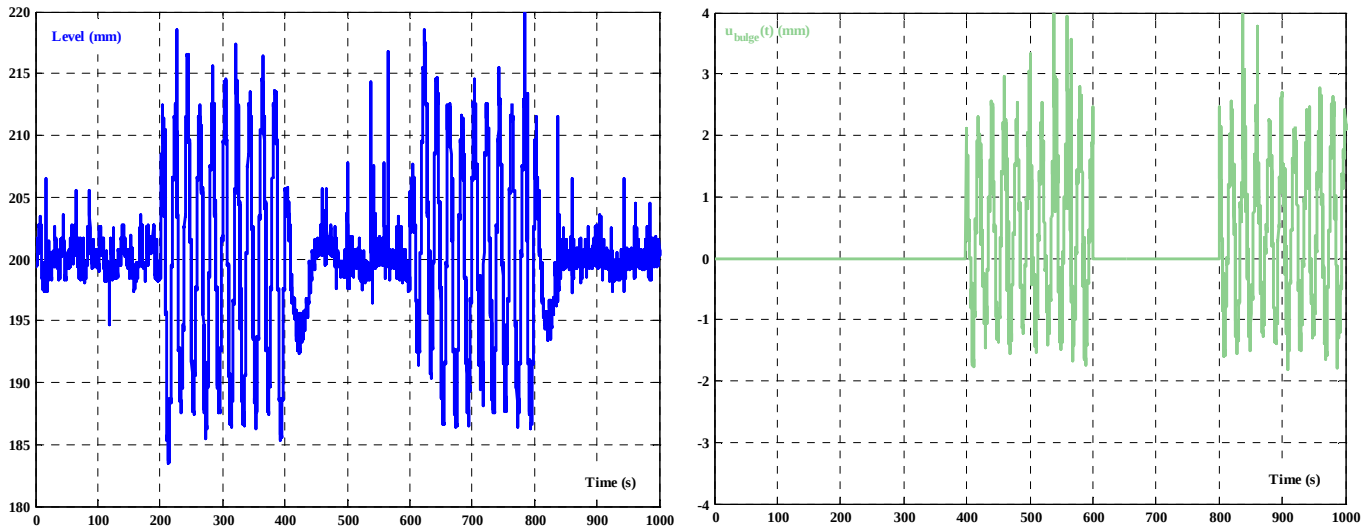

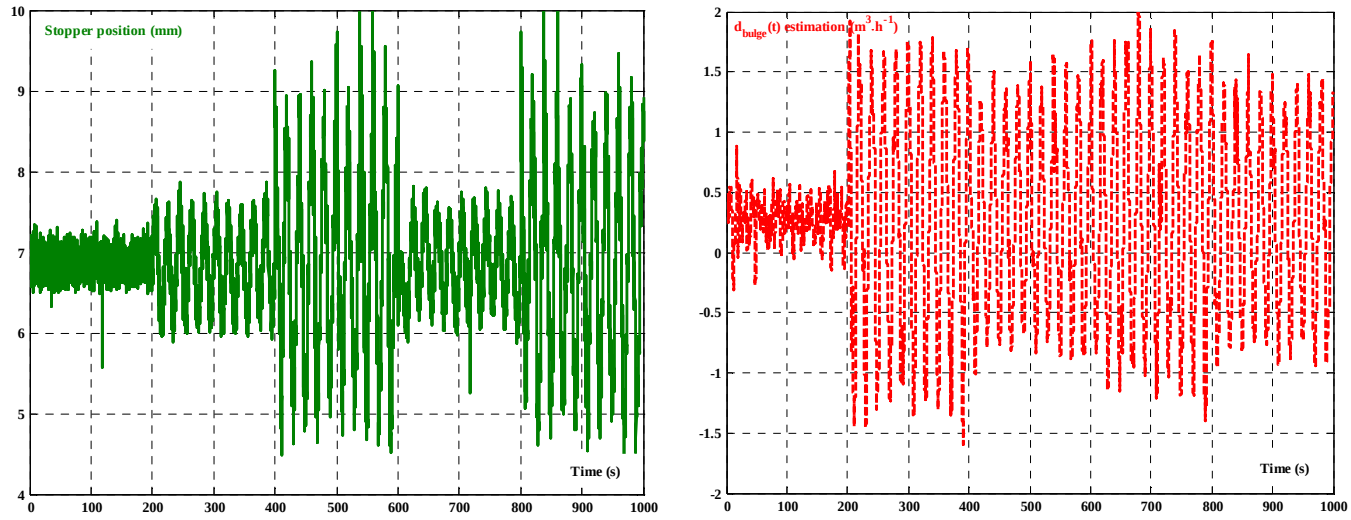

Fig. 3.43. Relevant signals during the experimentation

According to this online test, it can be asserted that the whole control structure is able to compensate the bulging effect on the mould level and to estimate its effect on the flow rate out of the mould. This experimental validation corroborates what was observed in simulation tests.

3.6 Chapter summary and conclusions

In this chapter, we presented, in detail, the guidelines for the plant model identification. In a dedicated section, our objective was to describe the experimental protocol for collecting data that will be used to determine the unknown parameters. Because the excitation signal has significant influence on identification results, several factors are taken into account to select such signal. Popular excitations include step, sinusoidal functions and Pseudo-Random Binary Sequence (PRBS) whose rich frequency content has motivated its use in this work.
Next, we introduced two offline identification algorithms. The first one is based on Least Squares method and is designed to identify the actuator transfer function. The second is based on Prediction Error Estimation method and is intended to identify the two key parameters i.e. the gain and the delay. To accomplish this, a rational approximation describing the time-delay system should be used to derive a linear model. Many equivalent frequency domain transfer functions have been proposed and many of them have been implemented, in particular, the Laguerre second order approximation which yields better results. In fact, numerous simulations, not presented in this dissertation, prove that the identification results are more accurate using the Laguerre functions.

The second part of this chapter was devoted to the estimation and rejection of disturbances. Our objective was to provide an estimation strategy that can help improve casting inspection. Thus, we proposed a global observer that addresses simultaneously both the clogging/unclogging cycle and the bulging but could be applied also to the standing waves. More precisely, an online estimator has been developed to track the behaviors of two exogenous signals modeling the disturbances effects on the mould level control loop using only three measurements, which include the level, the stopper position and the flow rate out of the mould. Furthermore, the estimate of the bulging effect has been integrated in a compensation structure which would allow a much more stable level by reducing drastically the fluctuations generated by the bulging. Intensive simulations and water model experiments have been used to illustrate the usefulness of this technique.

The last part was concerned with validating the bulging effect cancellation structure experimentally and determining the variation ranges of the gain and the delay depending on the water model configuration in the absence or presence of clogging. In both cases, the study findings reveal that the gain is independent of sensor position, nozzle submergence depth and air flow rate but increases with increasing water flow rate and with tundish level. Concerning the delay, it can be stated that its value decreases with increasing flow rates of water or air. However, small changes have been observed when changing the level tundish or the nozzle submergence depth.

Further improvements may consider robustness to model uncertainties and changes in bulging frequencies due to casting speed variations. This can be achieved by exploring robust observer theory based on Linear Matrix Inequalities (LMI) optimization [42] [43].
On the other hand, other estimation methods are suggested in literature and should be mentioned here. The most notable examples are the bulging estimate from the average current of the drive motors [11] and the clogging percentage used to prevent nozzle clogging as well as to optimize argon flow rate [44].

In the next chapter, we shall examine the performances of numerous control laws for continuous casting mould level. Namely, we shall consider two predictive strategies PFC and GPC, the Smith predictor and its modified version proposed by Aström and the Internal Model Control IMC. Each of these will be compared to the PID control law, introduced in this chapter, according to several performance criteria including robustness margins and disturbances rejection performances.

CHAPTER 4
Comparative analysis of non-adaptive control laws

4.1 Introduction (specifications)

Within the thesis general objective trying to develop robust control techniques for continuous casting mould level, this chapter presents a detailed study of classical control laws currently implemented in real plants or which should be reasonably considered for such process. Thus, we shall focus on the PID control law, the two predictive strategies PFC and GPC, the Smith predictor and its modified version proposed by Aström and finally the Internal Model Control IMC. Each of these is discussed in turn below. In particular, its performances are compared with those of the PID control law introduced in chapter 3 and considered here as a reference. This comparison is conducted according to several performance criteria including the gain margin, the delay margin, the modulus margin, the maximum gain of the bulging rejection transfer function over the bulging frequency range, the maximum level amplitude generated by the unclogging and many other factors.
By means of this comparative analysis, one should be able to describe the advantages, limitations and potential of various control systems. Given the crucial importance of disturbances rejection and robustness stability in the mould level control problem, we will examine notably:

- Stability of the closed loop,
- Bode diagram of the open loop TF_{BO},
- Direct sensitivity function σ_d given by $(1+TF_{BO})^{-1}$. It represents the transfer between the level error ε and the level setpoint N^*.
- Complementary sensitivity function σ_c given by $TF_{BO}\cdot(1+TF_{BO})^{-1}$. It represents the closed loop transfer between the measured level N_m and the level setpoint N^*.
- Level and stopper position for a step variation of setpoint,
- Bulging rejection through the transfer function between the flow rate out of the mould and the level,
- Clogging rejection through the level behavior when the flow into the mould is disturbed by a succession of ramps d_{clog}.

First of all, let us recall the plant model used to design control laws in Fig. 4.1 where the actuator has been modeled by a first order function and the level sensor dynamics has been overlooked.

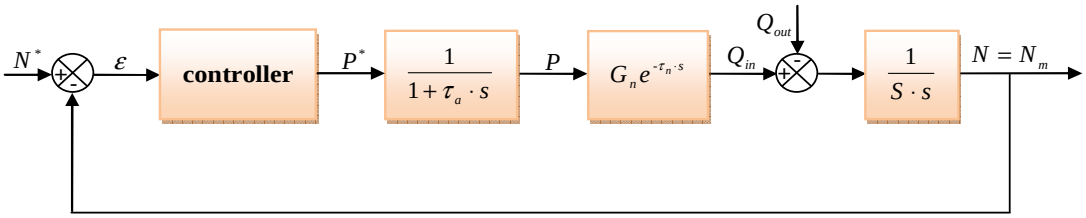

Fig. 4.1. General structure for control law design

From this figure, we can derive the following transfer function of the plant model:

$$\begin{cases} TF_{model}(s) = \dfrac{N}{P^*} = \dfrac{G_n e^{-\tau_n \cdot s}}{S \cdot s \cdot (1+\tau_a \cdot s)} = \dfrac{K_{model} e^{-\tau_n \cdot s}}{s \cdot (1+\tau_a \cdot s)} \\ K_{model} = \dfrac{G_n}{S} \end{cases} \tag{4.1}$$

or by using the Z-transform:

$$TF_{model}(z^{-1}) = (1-z^{-1}) \cdot \mathrm{Z}\left(\frac{TF_{model}(s)}{s}\right) = (1-z^{-1}) \cdot \mathrm{Z}\left(\frac{K_{model} e^{-\tau_n \cdot s}}{s^2 \cdot (1+\tau_a \cdot s)}\right) = z^{-r} \cdot (1-z^{-1}) \cdot \mathrm{Z}\left(\frac{K_{model}}{s^2 \cdot (1+\tau_a \cdot s)}\right)$$

$$\begin{cases} TF_{model}(z^{-1}) = K_{model} \cdot z^{-(r+1)} \cdot \dfrac{T_s - \tau_a(1-a_1) + (\tau_a(1-a_1) - T_s a_1) z^{-1}}{(1-z^{-1}) \cdot (1-a_1 z^{-1})} \\ a_1 = e^{-\frac{T_s}{\tau_a}} \\ r = \left\lfloor \dfrac{\tau_n}{T_s} \right\rfloor \end{cases} \tag{4.2}$$

where T_s is the sampling time.
To get the transfer function of the open loop, one should multiply TF_{model} by the transfer function of the controller as shown in Fig. 4.2 where ADC is an Analog-to-Digital Converter which converts continuous signals to discrete ones and DAC is a Digital-to-Analog Converter which performs the reverse operation.

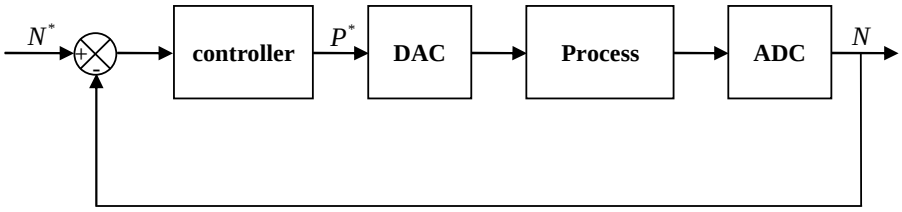

Fig. 4.2. Generic structure for digital control

4.2 State of the art (PID controller)

4.2.1 Transfer function

The control law considered as a reference for this comparative study is the Proportional Integral Derivative (PID) controller already presented in the previous chapter. It is the most common controller implemented by engineers in particular in the iron and steel industry and the standard tool widely used to build the automation systems.
As indicated by its name, the PID control law involves three separate parameters: the proportional gain K_{PID}, the integral time T_i and the derivative time T_d leading to the following transfer function expressed using Laplace transform:

$$TF_{PID}(s) = K_{PID}\left(1 + \frac{1}{T_i s} + \frac{T_d s}{1 + \frac{T_d}{\beta} s}\right) \tag{4.3}$$

By considering the Z-transform, it becomes:

$$TF_{PID}(z^{-1}) = (1-z^{-1}) \cdot Z\left(\frac{TF_{PID}(s)}{s}\right) = K_{PID} \cdot (1-z^{-1}) \cdot \left(\frac{1}{1-z^{-1}} + \frac{T_s}{T_i} \cdot \frac{z^{-1}}{(1-z^{-1})^2} + \frac{\beta}{1 - e^{-\beta\frac{T_s}{T_d}} z^{-1}}\right)$$

and

$$TF_{PID}(z^{-1}) = K_{PID}\left(1 + \frac{T_s}{T_i} \cdot \frac{z^{-1}}{1-z^{-1}} + \beta \frac{1-z^{-1}}{1 - e^{-\beta\frac{T_s}{T_d}} z^{-1}}\right) \tag{4.4}$$

The third term in (4.3) is called the “approximate derivative” and is used to limit the derivative action which is always sensitive to measurement noise. Sometimes, it is merely removed leading to the PI controller.
The discretization method used here preserves the step response.

Summarizing the key features of the PID controller, it can be said that the proportional term has a major impact on the closed loop response time. In other words, increasing the proportional gain tends to increase the bandwidth and to reduce the phase margin. To eliminate the steady-state error at least for step variations, it is both necessary and sufficient to include the integral part. Finally, the derivative action is used to reduce the overshoot magnitude and therefore to improve the overall stability. Specifically, damping increases with increasing derivation time until a certain limit is reached.
For comparison purposes with other control laws, the Z-transform of the PID control law is converted into RST form which is a generic structure for digital control as illustrated in Fig. 4.3 where ADC is an Analog-to-Digital Converter which converts continuous signals to discrete ones and DAC is a Digital-to-Analog Converter which performs the reverse operation.

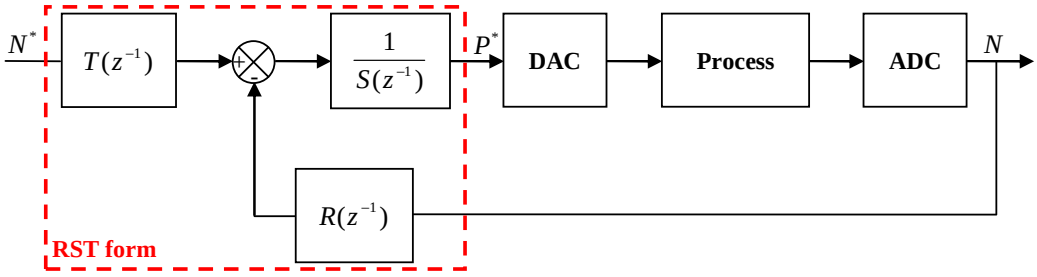

Fig. 4.3. RST form

The control signal P^* is thus expressed using three polynomials R_{PID}, S_{PID} and T_{PID} as follows:

$$S_{PID}(z^{-1}) \cdot P^*(z) = T_{PID}(z^{-1}) \cdot N^*(z) - R_{PID}(z^{-1}) \cdot N(z) \tag{4.5}$$

Equation (4.4) can now be rewritten as:

$$\left[T_i \cdot (1-z^{-1}) \left(1 - e^{-\beta \frac{T_s}{T_d}} z^{-1} \right) \right] P^*(z) = K_{PID} \left[T_i \cdot (1-z^{-1}) \left(1 - e^{-\beta \frac{T_s}{T_d}} z^{-1} \right) + T_s \cdot z^{-1} \cdot \left(1 - e^{-\beta \frac{T_s}{T_d}} z^{-1} \right) + \beta \cdot T_i \cdot (1-z^{-1})^2 \right] (N^*(z) - N(z))$$

Therefore, R_{PID}, S_{PID} and T_{PID} are given by:

$$\begin{cases} R_{PID}(z^{-1}) = T_{PID}(z^{-1}) = K_{PID} \left[T_i \cdot (1-z^{-1}) \left(1 - e^{-\beta \frac{T_s}{T_d}} z^{-1} \right) + T_s \cdot z^{-1} \cdot \left(1 - e^{-\beta \frac{T_s}{T_d}} z^{-1} \right) + \beta \cdot T_i \cdot (1-z^{-1})^2 \right] \\ S_{PID}(z^{-1}) = T_i \cdot (1-z^{-1}) \left(1 - e^{-\beta \frac{T_s}{T_d}} z^{-1} \right) \end{cases} \tag{4.6}$$

Several tuning methods are reported in literature. The most known examples are the Ziegler-Nichols ultimate sensitivity method and the Ziegler-Nichols step response method [80].
In case of mould level control, one should retune the PID parameters whenever the casting operations change. This change having the effect of modifying the plant model parameters according to the conclusions of chapter 3.

4.2.2 Performances

Given the transfer function of the plant model (4.2) and the RST form of the PID controller (4.6), the open loop transfer function is:

$$TF_{BO}(z^{-1}) = \frac{R_{PID}(z^{-1})}{S_{PID}(z^{-1})} \cdot TF_{model}(z^{-1})$$

By using the numerical values of Table 2.1 and Table 3.3, we get:

$$TF_{BO}(z^{-1}) = z^{-51} \frac{0.011 - 0.011z^{-1} - 0.00937z^{-2} + 0.00968z^{-3}}{1 - 3.42z^{-1} + 4.35z^{-2} - 2.42z^{-3} + 0.5z^{-4}} \tag{4.7}$$

where the sampling time T_s is chosen equal to 0.01s.

The stability and the robustness of the mould level system controlled by the PID can be assessed using the diagrams of Fig. 4.4. In particular, the stability is ensured with a gain margin of 8.7dB and a delay margin of 1.1s.

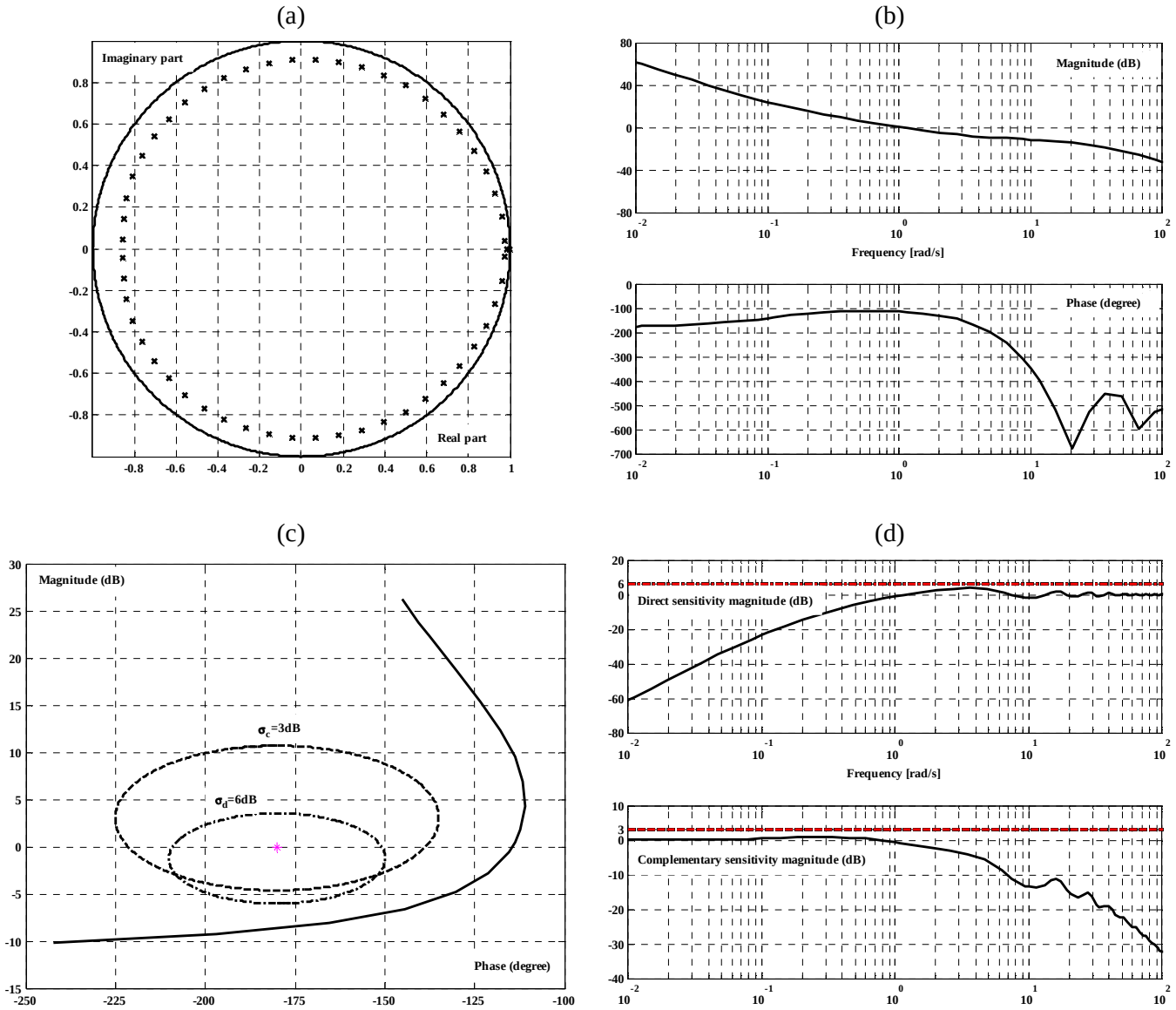

Fig. 4.4. (a) Poles of the closed loop
(b) Open loop Bode frequency response
(c) Open loop Black diagram
(d) Direct and complementary sensitivities magnitudes

Fig. 4.5 shows the level and the stopper position for a step setpoint variation of 10mm. We can notice that the overshoot is about 1mm and the response time is almost equal to 25s.

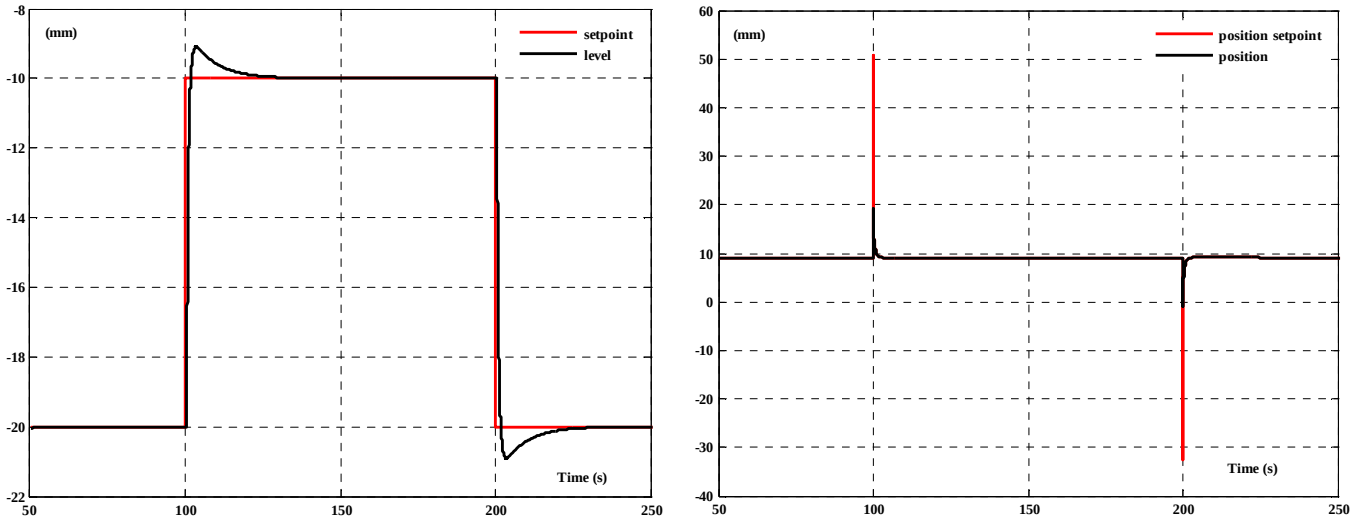

Fig. 4.5. Setpoint response for a step level variation of 10mm

In order to evaluate the PID action against the bulging, the bulging rejection function i.e. the transfer function between the level and the flow rate out of the mould is drawn in Fig. 4.6. Regarding its high magnitude over the bulging frequency band, we can mitigate the PID performances in terms of bulging rejection. This conclusion is even more obvious in the following time-domain simulation where the flow rate out of the mould has been disturbed by an exogenous signal having a frequency of 0.1Hz and peak to peak amplitude of $4L \cdot s^{-1}$. This causes the mould level to vary periodically from about −26 to −14mm.

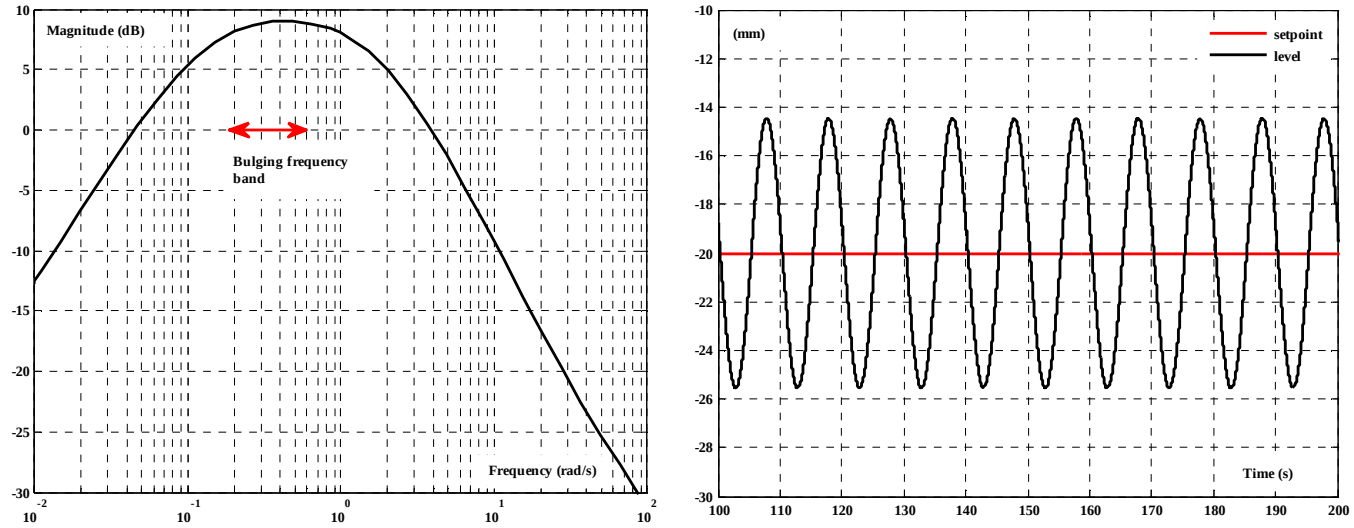

Fig. 4.6. Bulging rejection performances

Furthermore, the flow rate into the mould has been disturbed by an exogenous signal in the form of a succession of ramps in order to model the clogging/unclogging cycle as depicted in Fig. 4.7. Once more, the PID is not able to reject efficiently this disturbance. The highest fluctuations occur at 100, 300 and 700s i.e. at the unclogging instants.

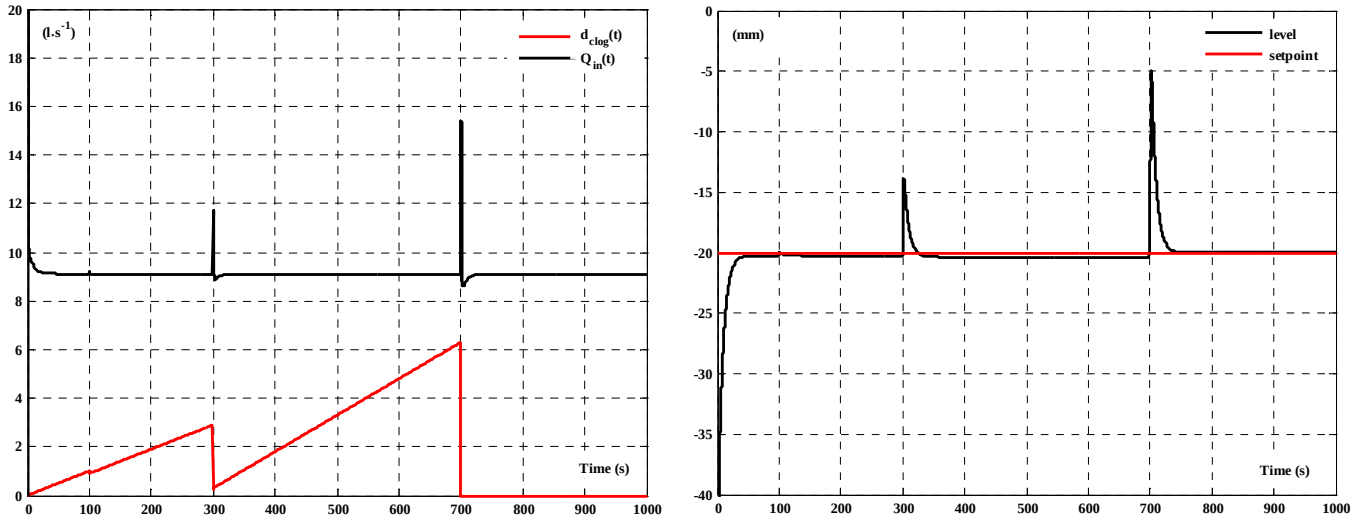

Fig. 4.7. Clogging rejection performances

As a partial conclusion, this study reveals that the previous PID controller is not able to guarantee satisfactory results in a number of situations with disturbances. We believe that these poor performances are not ascribed to the tuning method but to the controller structure.

The performances of the PID controller are summarized and compared with the specifications in Table 4.1.

Table 4.1. PID performances

	Criterion	PID	Specifications
Cutoff frequency ($rad \cdot s^{-1}$)		1.06	
Stability		OK	YES
Steady-state error	Step setpoint variation (mm)	0	0
	Step outflow variation (mm)	0	0
	Clogging occurring between 300 and 700s (mm)	**0.36**	0
Robustness margins	Gain margin (dB)	8.7	≥ 6
	Phase margin (degree)	66	≥ 45
	Delay margin (s)	$110T_s$	$\geq T_s$
	Modulus margin	0.63	≥ 0.5
Sensitivities	$\max\lvert\sigma_d\rvert$ (dB)	4	$\lvert\sigma_d\rvert \leq 6$
	$\max\lvert\sigma_c\rvert$ (dB)	0.79	$\lvert\sigma_c\rvert \leq 3$
Bulging rejection	Maximum gain (dB)	9	As low as possible
	Minimum gain (dB)	8	As low as possible
Unclogging at 700s	Maximum level amplitude (mm)	15	As low as possible
	Time to reach 95% of the steady-state value (s)	23	As fast as possible

4.3 Predictive control laws

In this section, another control strategy, belonging to the family of predictive control techniques, is investigated. It aims at creating an anticipative effect using the explicit knowledge of the trajectory in the future. It can be summarized as follows:

- Definition of a process model able to predict the future system behavior,
- Minimization of a quadratic cost function over a finite prediction horizon using the future predicted errors,
- Elaboration of a sequence of future control values, however, only the first value is applied both on the system and on the model.
- Repetition of the whole procedure at the next sampling period according to the receding horizon principle.

Especially the Predictive Functional Control PFC and the Generalized Predictive Control GPC are in the focus of interest.

4.3.1 Predictive Functional Control PFC

4.3.1.1 Principle

This subsection is dedicated to the Predictive Functional Control technique. Originally developed by J. Richalet, it has had great success in the process industries such as chemical plants and oil refineries. As illustrated in Fig. 4.8, the control variable is calculated to cause the prediction of the process output to reach the final objective (i.e. the setpoint) by following a pre-defined path so-called the reference trajectory. In the sequel, we shall present briefly the procedure but complete details may be found in [82].

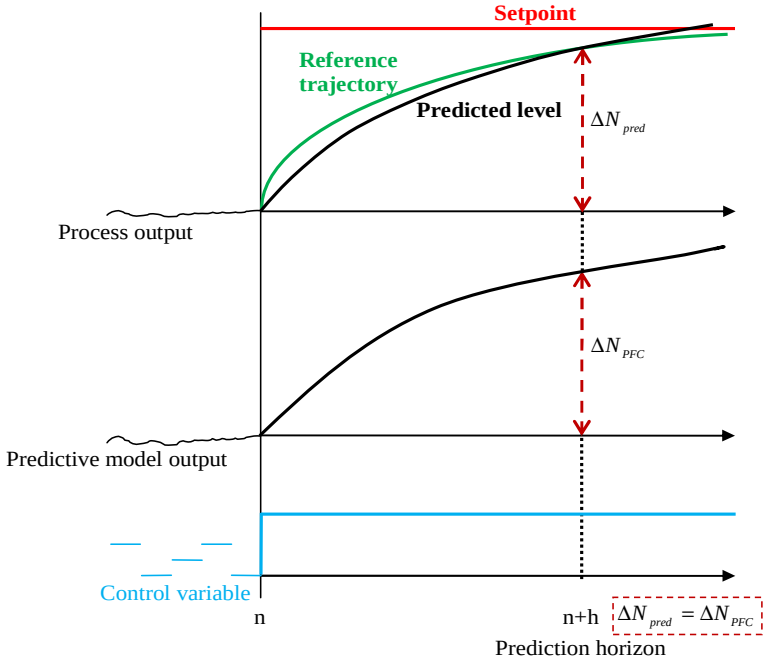

Fig. 4.8. Predictive Functional Control principle

4.3.1.1.1 Prediction model

This model, also called the internal model, is intended to calculate a prediction of the process output. The PFC algorithm is then implemented using this prediction as shown in Fig. 4.9.

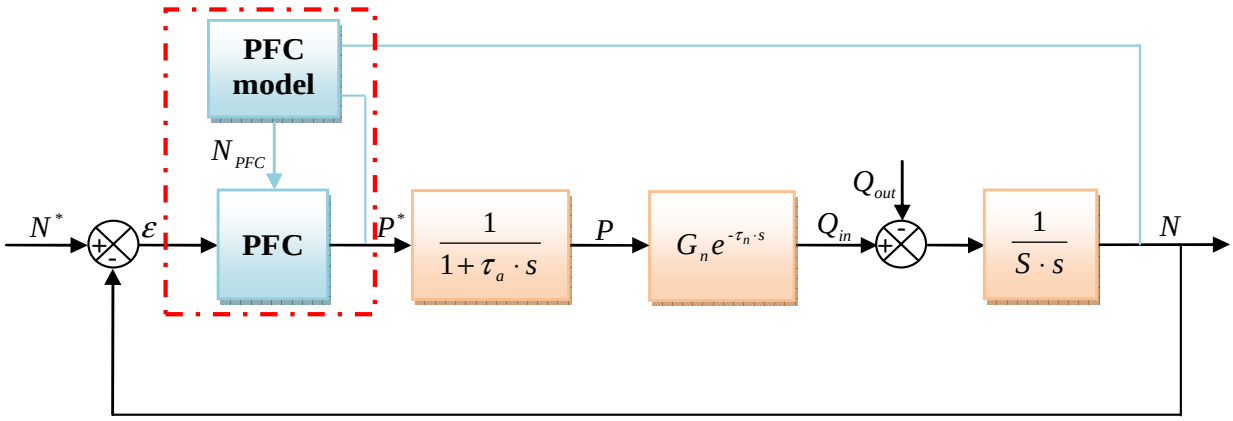

Fig. 4.9. Predictive Functional Control scheme

The model of the process is represented, in the Laplace domain, by:

$$TF_{model}(s) = \frac{K_{model} e^{-\tau_n \cdot s}}{s \cdot (1+\tau_a \cdot s)} = H_0 e^{-\tau_n \cdot s}$$

$$\begin{cases} H_0 = \dfrac{N_a}{P^*} = \dfrac{K_{model}}{s \cdot (1+\tau_a \cdot s)} \\ N_a(t) = N(t+\tau_n) \end{cases} \tag{4.8}$$

where H_0 is the delay free part of the plant model.

For reasons of implementation and initialization, we should develop a stable predictive model. Because the process is an integrator system, one solution would be to decompose it into three stable processes M_1, M_2 and M_3 as illustrated in Fig. 4.10 where τ is an auxiliary time constant chosen arbitrary. They are subject to the inputs P^* and N_a.

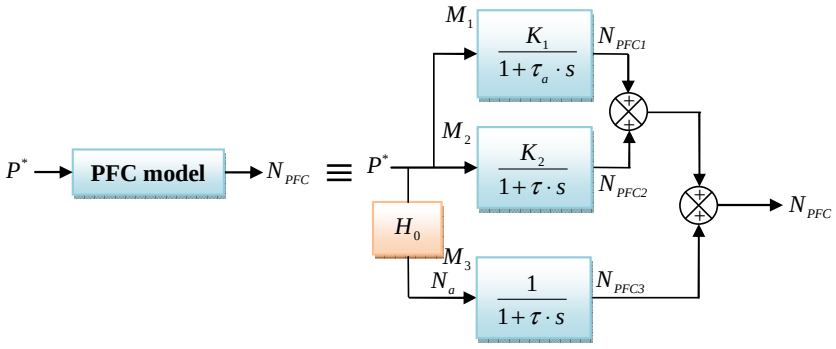

Fig. 4.10. Partial fraction decomposition of H_0

The gains K_1 and K_2 are chosen so that the two models of Fig. 4.10 are equivalent i.e.:

$$\begin{cases} N_{PFC} = N_{PFC1} + N_{PFC2} + N_{PFC3} = (M_1 + M_2) \cdot P^* + M_3 \cdot N_a = (M_1 + M_2 + M_3 \cdot H_0) \cdot P^* \\ N_{PFC} = H_0 \cdot P^* \end{cases} \tag{4.9}$$

$$H_0 = M_1 + M_2 + M_3 \cdot H_0$$

Specifically,

$$\begin{cases} K_2 = \dfrac{\tau^2}{\tau - \tau_a} K_{model} \\ K_1 = \tau \cdot K_{model} - K_2 \end{cases} \tag{4.10}$$

Finally, the transfer functions of the processes M_1, M_2 and M_3 give rise to a model of the form:

$$N_{PFC} = N_{PFC1} + N_{PFC2} + N_{PFC3}$$

$$\begin{cases} N_{PFC1}(n) = a_1 \cdot N_{PFC1}(n-1) + (1-a_1) \cdot K_1 \cdot P^*(n-1) \\ N_{PFC2}(n) = a_2 \cdot N_{PFC2}(n-1) + (1-a_2) \cdot K_2 \cdot P^*(n-1) \\ N_{PFC3}(n) = a_2 \cdot N_{PFC3}(n-1) + (1-a_2) \cdot N_a(n-1) \\ \\ N_a(n) = N(n+r) \end{cases} \quad \text{with:} \quad \begin{cases} a_1 = e^{-\frac{T_s}{\tau_a}} \\ a_2 = e^{-\frac{T_s}{\tau}} \\ r = \left\lfloor \frac{\tau_n}{T_s} \right\rfloor \end{cases} \tag{4.11}$$

4.3.1.1.2 Reference trajectory

This trajectory is considered as the desired behavior of the process output. Theoretically, the level is predicted to reach the setpoint value over a receding horizon [0 h] following this reference trajectory (Fig. 4.11).

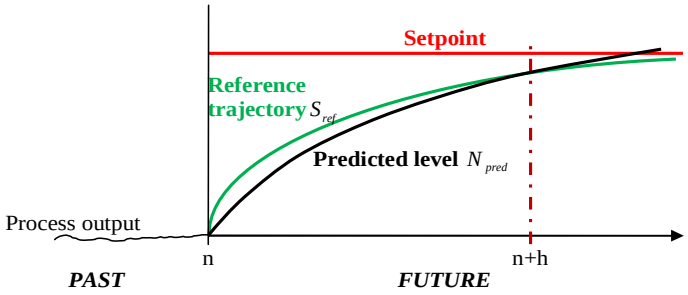

Fig. 4.11. Reference trajectory

In the PFC design, the reference trajectory S_{ref} is usually given for time-delay systems in the following exponential form:

$$\begin{cases} N^* - S_{ref}(n+h) = (N^* - N_a(n)) \cdot \mu^h \\ \mu = e^{\frac{-3T_s}{CLRT}} \end{cases} \tag{4.12}$$

where $CLRT$ is the Closed Loop Response Time in the case of a constant setpoint (which should be the case in the mould level control problem).

4.3.1.1.3 Cost function

The PFC strategy minimizes a quadratic sum of errors between the predicted level N_{pred} and the reference trajectory S_{ref} calculated at certain coincidence points:

$$J_{PFC}(n) = \sum_{i=1}^{n_{CP}} (N_{pred}(n+h_i) - S_{ref}(n+h_i))^2 \tag{4.13}$$

with:

- n_{CP} : the number of coincidence points,
- h_i : the coincidence points over what is called the prediction horizon.

At times, a second term is added to the cost function in order to restrict the magnitude of the control signal.

4.3.1.1.4 Base functions

One of the distinguishing features of the PFC design is the structure of the control law. It is assumed indeed that the control sequence is composed of a set of base functions u_{BK} chosen according to the process feature (with or without an integral term) and the target setpoint nature:

$$P^*(n+j) = \sum_{i=1}^{n_{BK}} \gamma_i(n) \cdot u_{BK}(j) \qquad 0 \le j \le h \tag{4.14}$$

with:

- n_{BK} : the number of base functions,
- γ_i : the coefficients of the linear combination.

u_{BK} are chosen among the following functions: step, ramp or parabola. For example, in the mould level control problem, by considering a step setpoint, only one step base function is required to cancel the steady-state error. In this case, only one coincidence point is taken into account to determine the control law.
According to the receding horizon principle, only the first value of the control sequence is effectively applied, that is:

$$P^*(n) = \sum_{i=1}^{n_{BK}} \gamma_i(n) \cdot u_{BK}(0) \tag{4.15}$$

4.3.1.1.5 Control algorithm

The control law is computed to cause the predicted level to coincide with the reference trajectory at the coincidence point h:

$$N_{pred}(n+h) = S_{ref}(n+h) \tag{4.16}$$

There is a need therefore to calculate $N_{pred}(n+h)$. Let us introduce $dom(n)$ which is the error between the predicted level and the prediction model output i.e.:

$$dom(n) = N_{pred}(n) - N_{PFC}(n) \tag{4.17}$$

$dom(n)$ is usually approximated by a polynomial function such as:

$$dom(n+h) = dom(n) + \sum_{i=1}^{d_e} e_i(n) h^i \tag{4.18}$$

where d_e is the degree of the approximation.

The PFC algorithm most often considers that the objective increment is equivalent to the model output increment introducing a flat prediction:

$$\begin{gathered} dom(n+h) = dom(n) \\ N_{pred}(n+h) = N_{PFC}(n+h) + dom(n+h) = N_{PFC}(n+h) + dom(n) = N_{PFC}(n+h) + N(n) - N_{PFC}(n) \end{gathered} \tag{4.19}$$

By making use of (4.12) and (4.19), the computation of the control law reduces to solving:

$$N_{PFC}(n+h) + N(n) - N_{PFC}(n) = N^* - (N^* - N_a(n)) \cdot \mu^h \tag{4.20}$$

Given equations (4.11) and using the unit step as the base function of the control sequence, it follows:

$$\begin{cases} N_{PFC1}(n+h) = a_1^h \cdot N_{PFC1}(n) + (1-a_1^h) \cdot K_1 \cdot P^*(n) \\ N_{PFC2}(n+h) = a_2^h \cdot N_{PFC2}(n) + (1-a_2^h) \cdot K_2 \cdot P^*(n) \\ N_{PFC3}(n+h) = a_2^h \cdot N_{PFC3}(n) + (1-a_2^h) \cdot N_a(n) \\ N_{PFC}(n+h) = N_{PFC1}(n+h) + N_{PFC2}(n+h) + N_{PFC3}(n+h) \end{cases} \tag{4.21}$$

By substituting (4.21) back into (4.20), we obtain the explicit expression of the control law:

$$P^*(n) = \theta_w \cdot N^* - \theta_N \cdot N(n) + \theta_1 \cdot N_{PFC1}(n) + \theta_2 \cdot N_{PFC2}(n) + \theta_2 \cdot N_{PFC3}(n) + \theta_a \cdot N_a(n)$$

$$\begin{cases} \theta_w = \dfrac{1-\mu^h}{\alpha} \qquad \theta_1 = \dfrac{1-a_1^h}{\alpha} \qquad \theta_2 = \dfrac{1-a_2^h}{\alpha} \qquad \theta_N = \dfrac{1}{\alpha} \qquad \theta_a = \dfrac{a_2^h + \mu^h - 1}{\alpha} \\ \alpha = K_1 \cdot (1-a_1^h) + K_2 \cdot (1-a_2^h) \end{cases} \tag{4.22}$$

All the terms appearing in equation (4.22), except N_a, are measured or have been determined previously. In the sequel, we shall present two versions of PFC which differ only in the way they generate N_a.

4.3.1.2 Performances

4.3.1.2.1 First version

In this case, the delay is not taken into account in the model. This means that:

$$N_a(n) = N(n) \tag{4.23}$$

By making use of (4.11) and (4.22), the Z-transform of the control law is given by:

$$P^*(z) = \theta_w \cdot N^* - \theta_N \cdot N(z) + (\theta_2 \cdot H_{PFC3} + \theta_a) \cdot N(z) + (\theta_1 \cdot H_{PFC1} + \theta_2 \cdot H_{PFC2}) \cdot P^*(z)$$

$$\begin{cases} \dfrac{N_{PFC1}(z)}{P^*(z)} = \dfrac{(1-a_1) \cdot K_1 \cdot z^{-1}}{1-a_1 z^{-1}} = H_{PFC1}(z^{-1}) \\ \dfrac{N_{PFC2}(z)}{P^*(z)} = \dfrac{(1-a_2) \cdot K_2 \cdot z^{-1}}{1-a_2 z^{-1}} = H_{PFC2}(z^{-1}) \\ \dfrac{N_{PFC3}(z)}{N_a(z)} = \dfrac{(1-a_2) \cdot z^{-1}}{1-a_2 z^{-1}} = H_{PFC3}(z^{-1}) \end{cases} \tag{4.24}$$

This equation can also be written in the RST form:

$$\begin{aligned} S_{PFC}(z^{-1}) \cdot P^*(z) &= T_{PFC}(z^{-1}) \cdot N^* - R_{PFC}(z^{-1}) \cdot N(z) \\ (1 - \theta_1 \cdot H_{PFC1} - \theta_2 \cdot H_{PFC2}) \cdot P^*(z) &= \theta_w \cdot N^* + (\theta_2 \cdot H_{PFC3} + \theta_a - \theta_N) \cdot N(z) \end{aligned} \tag{4.25}$$

Finally, the RST form of the PFC control law is:

$$\begin{cases} R_{PFC}(z^{-1}) = (1-a_1 z^{-1}) \cdot \left(\theta_N - \theta_a - \left(\theta_2 \cdot (1-a_2) + a_2 \cdot (\theta_N - \theta_a)\right) \cdot z^{-1}\right) \\ S_{PFC}(z^{-1}) = 1 - \left(a_1 + a_2 + \theta_1 \cdot (1-a_1) \cdot K_1 + \theta_2 \cdot (1-a_2) \cdot K_2\right) \cdot z^{-1} + \left(a_1 \cdot a_2 + \theta_1 \cdot a_2 \cdot (1-a_1) \cdot K_1 + \theta_2 \cdot a_1 \cdot (1-a_2) \cdot K_2\right) \cdot z^{-2} \\ T_{PFC}(z^{-1}) = \theta_w \cdot (1-a_1 z^{-1}) \cdot (1-a_2 z^{-1}) \end{cases} \tag{4.26}$$

To make fair and meaningful comparisons with the PID controller, the PFC parameters have been chosen to achieve the same cutoff frequency i.e. $1.06 \text{rad} \cdot \text{s}^{-1}$. This leads to the tuning listed in Table 4.2.

Table 4.2. PFC parameters (first version)

Parameter	Value
T_s	$0.05s$
$CLRT$	5.65s
τ	$CLRT/3 = 1.88$s
h	$5s$

Given these values, it is now possible to calculate the RST form of the PFC controller as follows:

$$\begin{cases} R_{PFC}(z^{-1}) = 0.3882 - 0.5259z^{-1} + 0.1409z^{-2} \\ S_{PFC}(z^{-1}) = 1 - 1.35z^{-1} + 0.3501z^{-2} \\ T_{PFC}(z^{-1}) = 0.1941 - 0.2604z^{-1} + 0.06953z^{-2} \end{cases} \quad (4.27)$$

Using the PFC control law, the open loop transfer function becomes:

$$TF_{BO}(z^{-1}) = z^{-11}\frac{0.0196 - 0.0125z^{-1} - 0.0119z^{-2} + 0.0051z^{-3}}{1 - 2.72z^{-1} + 2.56z^{-2} - 0.975z^{-3} + 0.129z^{-4}} \quad (4.28)$$

The stability and the robustness of the system controlled by the PFC control law can be analyzed through the same diagrams as used previously for the PID control law (Fig. 4.12).

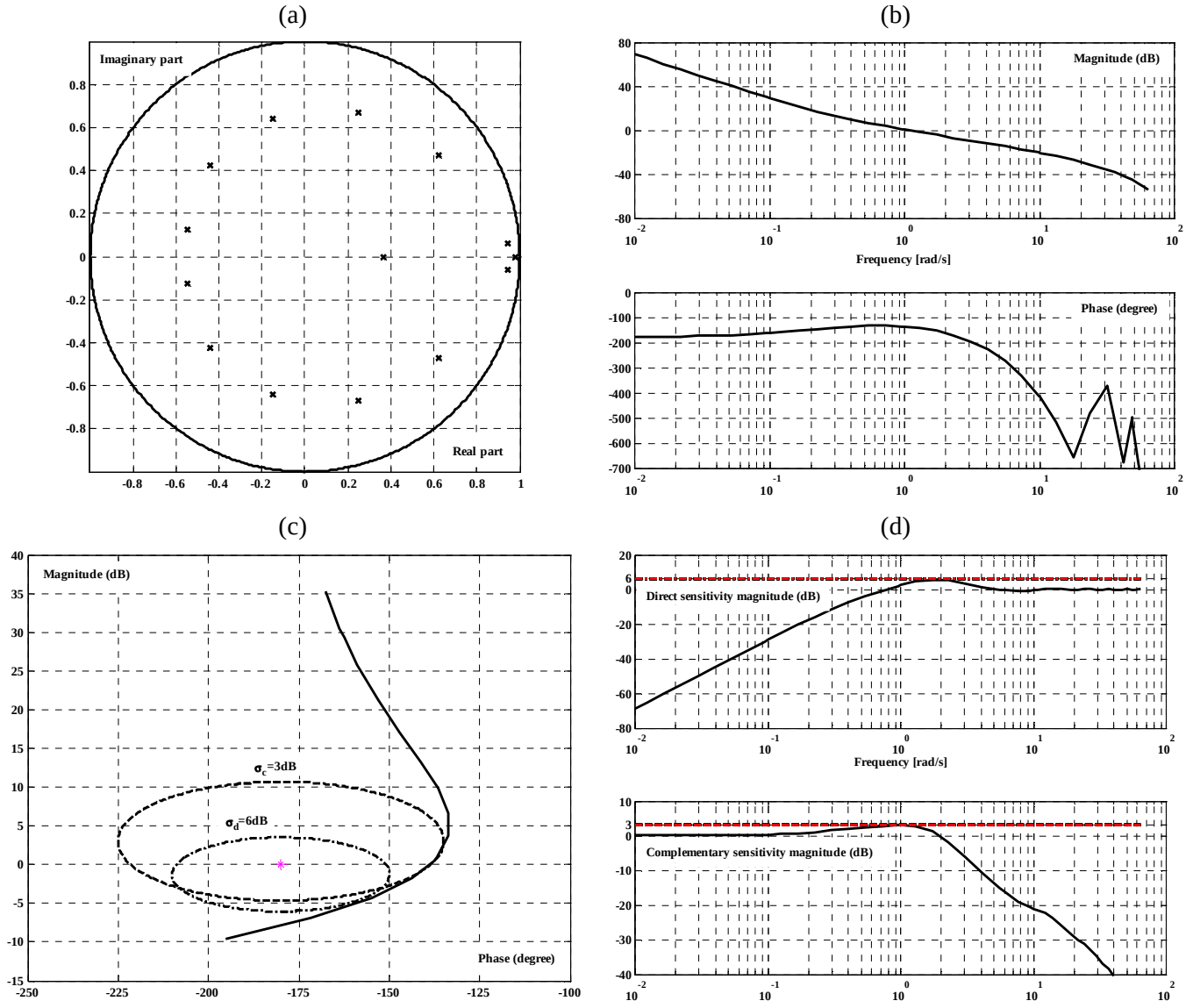

Fig. 4.12. (a) Poles of the closed loop
(b) Open loop Bode frequency response
(c) Open loop Black diagram
(d) Direct and complementary sensitivity functions magnitudes

Fig. 4.13 shows the level and the stopper position for a step level variation of 10mm. We can notice that the setpoint response is faster in case of PFC control law and does not introduce an overshoot contrary to the response

generated by the PID control law. Moreover, the steady-state error is equal to zero and this can be demonstrated rigorously by considering the following equations:

$$\begin{cases} \varepsilon(n) = \varepsilon_N(n) + \varepsilon_Q(n) \\ \varepsilon_N(z^{-1}) = N^*(z^{-1}) - N(z^{-1}) = \dfrac{1 + \dfrac{TF_{model}(z^{-1})}{S_{PFC}(z^{-1})}(R_{PFC}(z^{-1}) - T_{PFC}(z^{-1}))}{1 + TF_{BO}(z^{-1})} N^*(z^{-1}) \underset{z\to 1}{\propto} (R_{PFC}(1) - T_{PFC}(1)) \cdot N^*(z^{-1}) \\ \varepsilon_Q(z^{-1}) = \dfrac{T_s/S}{(1-z^{-1}) \cdot (1 + TF_{BO}(z^{-1}))} Q_{out}(z^{-1}) \underset{z\to 1}{\propto} (1-z^{-1}) Q_{out}(z^{-1}) \end{cases} \quad (4.29)$$

It follows:

$$\lim_{n\to\infty} \varepsilon(n) = \lim_{z\to 1} (z-1) \cdot \varepsilon_N(z) + \lim_{z\to 1} (z-1) \cdot \varepsilon_Q(z) = R_{PFC}(1) - T_{PFC}(1) + 0 = 0$$

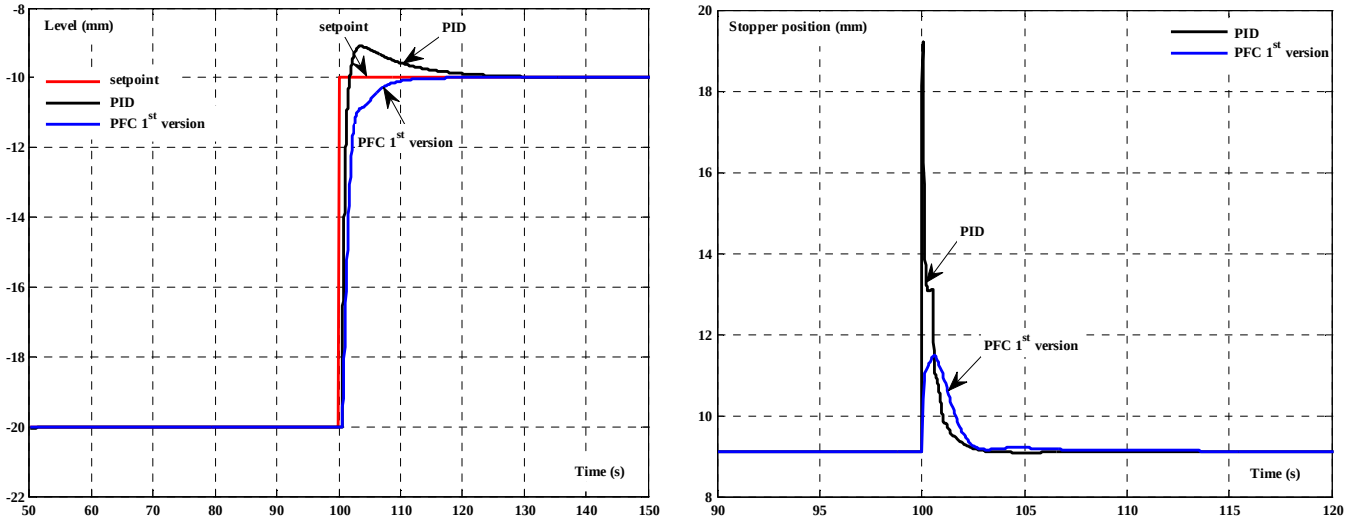

Fig. 4.13. Setpoint response for a step level variation of 10mm

Examining the bulging rejection function, one could make the following observation. The PFC action against the bulging is more effective over the bulging frequency range between 0.2 and 0.4rad$\cdot$s^{-1}. Beyond this value, the PID yields superior bulging rejection. The time-domain simulation confirms this finding. In fact, since the disruptive frequency 0.1Hz lies above 0.4rad$\cdot$s^{-1}, the flow rate variations produced by the bulging will be further amplified in case of PFC controller.

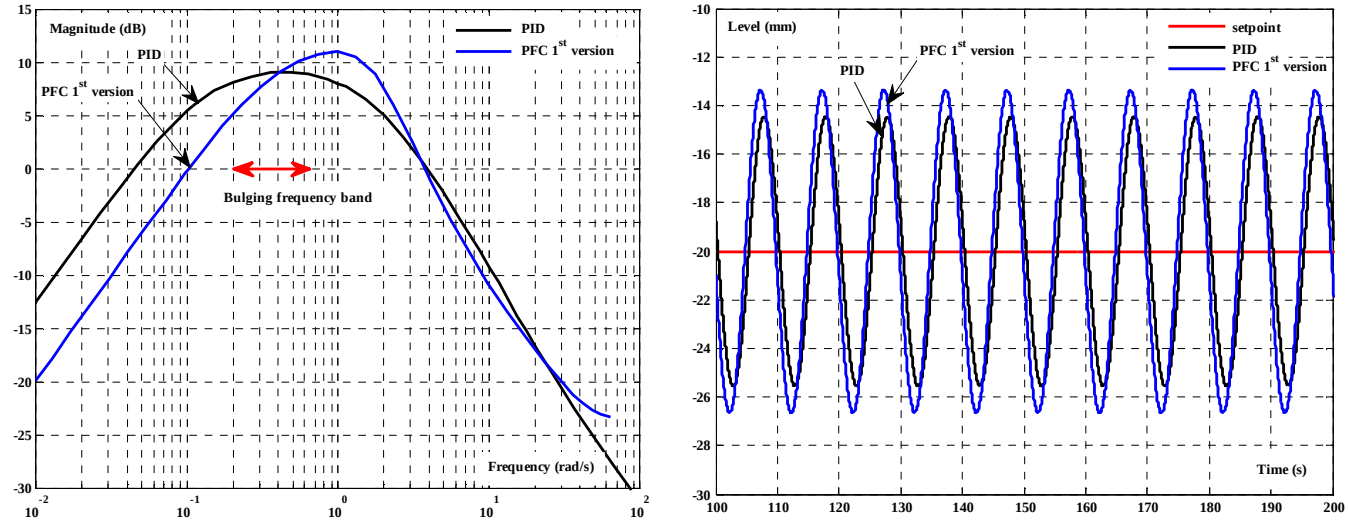

Fig. 4.14. Bulging rejection performances

Concerning the clogging/unclogging disturbance, the same scenario introduced previously to evaluate the PID action, has been tested. As expected, the level moves, one again, with high magnitude at the unclogging instants and reaches a steady-state value after several seconds.

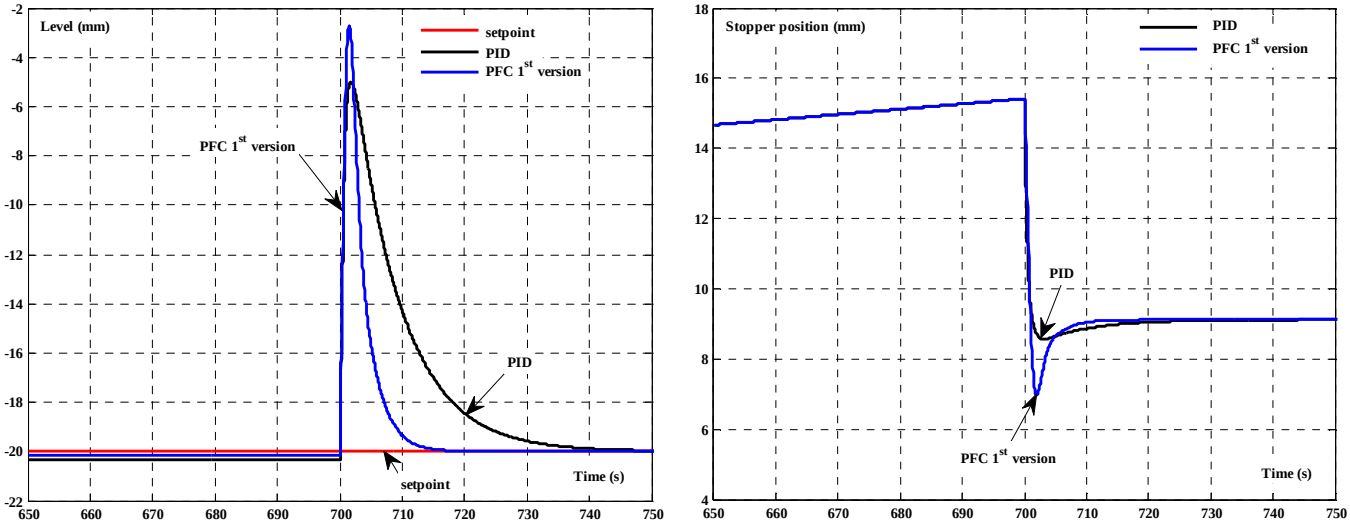

Fig. 4.15. Clogging rejection performances

4.3.1.2.2 Second version

In the second approach, the following hypothesis is proposed, which assumes a flat prediction at $n+r$ of the error between the measured level $N(n)$ and the prediction model output calculated at $n-r$ i.e. $N_{PFC}(n-r)$:

$$N_a(n) = N(n+r) = N(n) + N_{PFC}(n) - N_{PFC}(n-r) \tag{4.30}$$

By using the Z-transform, equation (4.30) becomes:

$$N_a(z) = N(z) + (1-z^{-r}) \cdot N_{PFC}(z) = N(z) + (1-z^{-r}) \cdot \left(H_{PFC1}(z^{-1}) \cdot P^*(z) + H_{PFC2}(z^{-1}) \cdot P^*(z) + H_{PFC3}(z^{-1}) \cdot N_a(z) \right)$$

That is:

$$N_a(z) = \frac{N(z) + (1-z^{-r}) \cdot (H_{PFC1}(z^{-1}) + H_{PFC2}(z^{-1})) \cdot P^*(z)}{1 - (1-z^{-r}) \cdot H_{PFC3}(z^{-1})} \tag{4.31}$$

Calculating the Z-transform of each term in the main control law equation (4.22), we obtain:

$$P^*(z) = \theta_w \cdot N^* - \theta_N \cdot N(z) + (\theta_2 \cdot H_{PFC3} + \theta_a) \cdot N_a(z) + (\theta_1 \cdot H_{PFC1} + \theta_2 \cdot H_{PFC2}) \cdot P^*(z) \tag{4.32}$$

Therefore, the PFC control law can also be written as follows:

$$\left(1 - \theta_1 \cdot H_{PFC1} - \theta_2 \cdot H_{PFC2} + \frac{(\theta_2 \cdot H_{PFC3} + \theta_a) \cdot (1-z^{-r}) \cdot (H_{PFC1} + H_{PFC2})}{(1-z^{-r}) \cdot H_{PFC3} - 1} \right) \cdot P^*(z) = \theta_w \cdot N^* - \left(\theta_N + \frac{\theta_2 \cdot H_{PFC3} + \theta_a}{(1-z^{-r}) \cdot H_{PFC3} - 1} \right) \cdot N(z) \tag{4.33}$$

This form can also lead, after some simplifications, to a standard RST form.
The previous tuning is modified in order to obtain the same cutoff frequency i.e. $1.06 \text{rad} \cdot \text{s}^{-1}$ (Table 4.3).

Table 4.3. PFC parameters (second version)

Parameter	Value
T_s	$0.05s$
$CLRT$	4.9s
τ	$CLRT/3 = 1.88$s
h	$5s$

Following the same methodology, we have examined thus the stability of the closed loop, the Bode diagram of the open loop (Fig. 4.16), the setpoint response for a step level variation of 10mm (Fig. 4.17) and the disturbances rejection performances (Fig. 4.18 and Fig. 4.19). The results point out that the second version of the PFC control law is comparable in terms of performances with the first one. However, the computation of the control law requires more time and resources owing to the presence of the time-delay.

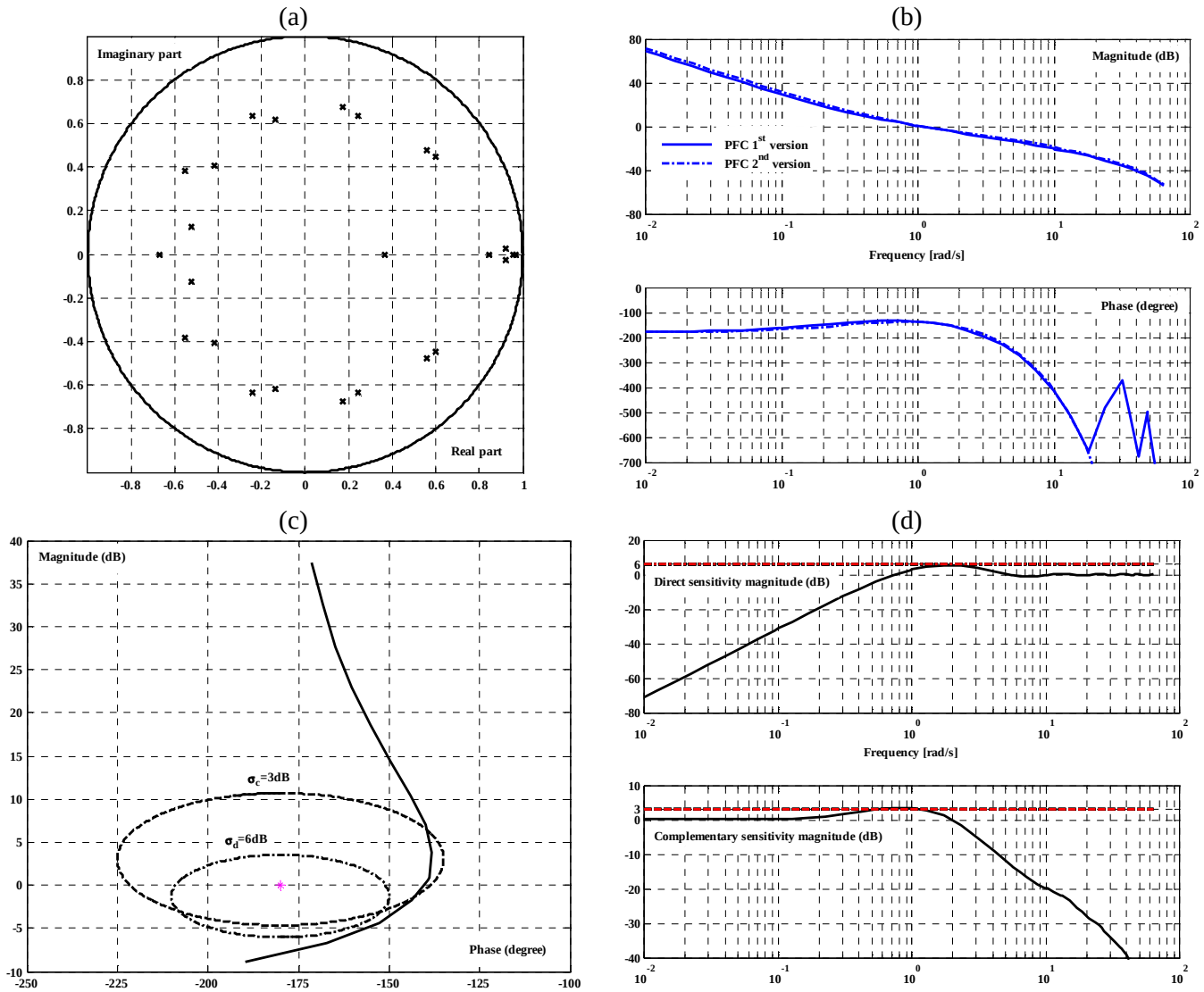

Fig. 4.16. (a) Poles of the closed loop
(b) Open loop Bode frequency response
(c) Open loop Black diagram
(d) Direct and complementary sensitivity functions magnitudes

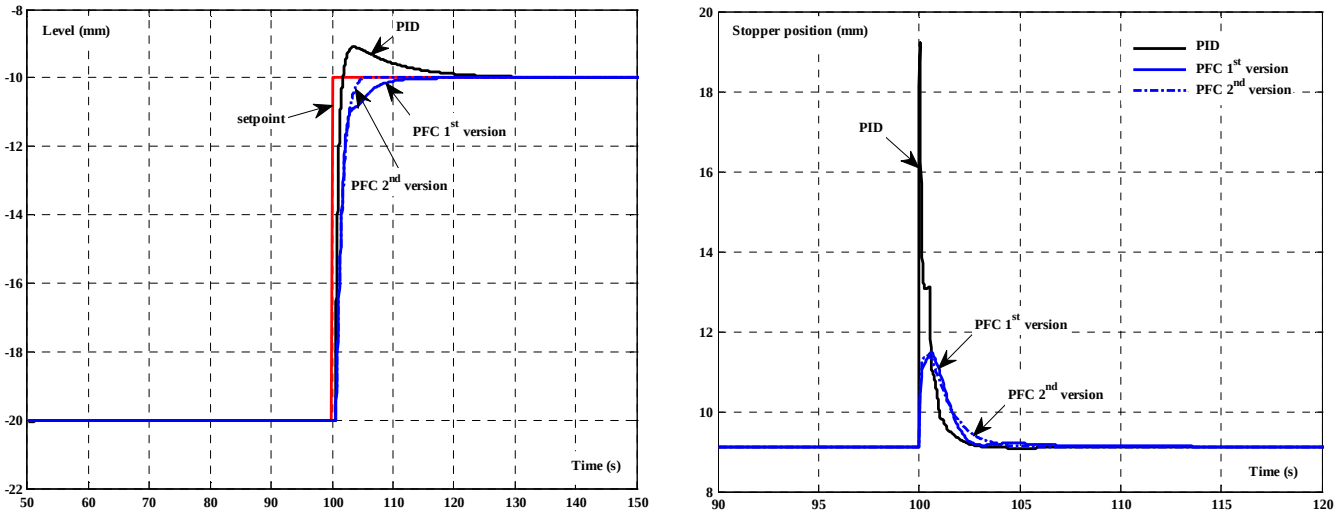

Fig. 4.17. Setpoint response for a step level variation of 10mm

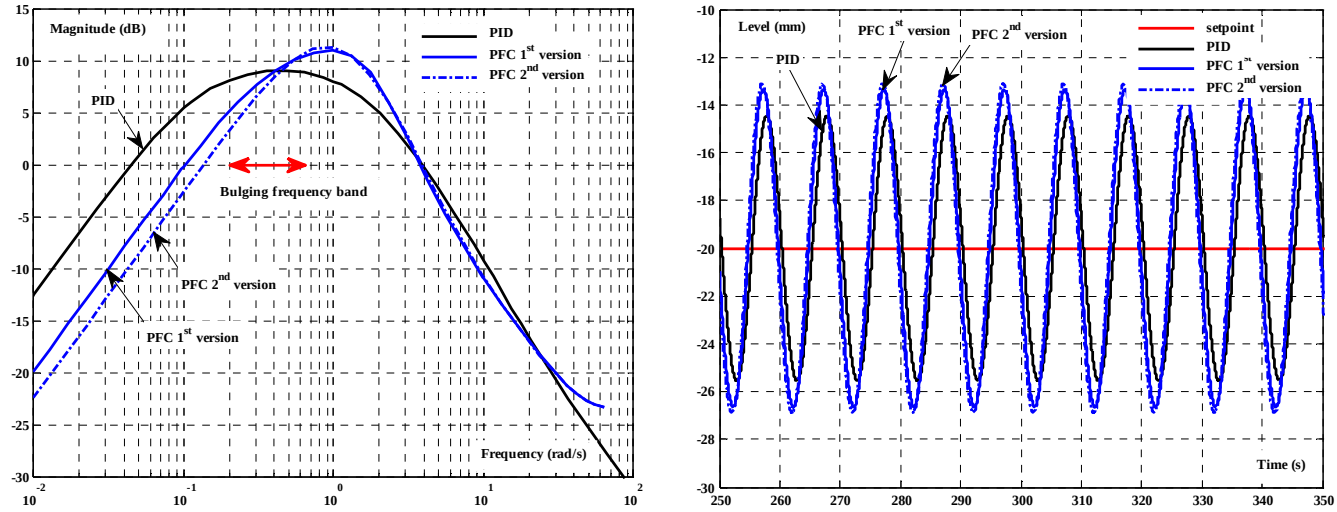

Fig. 4.18. Bulging rejection performances

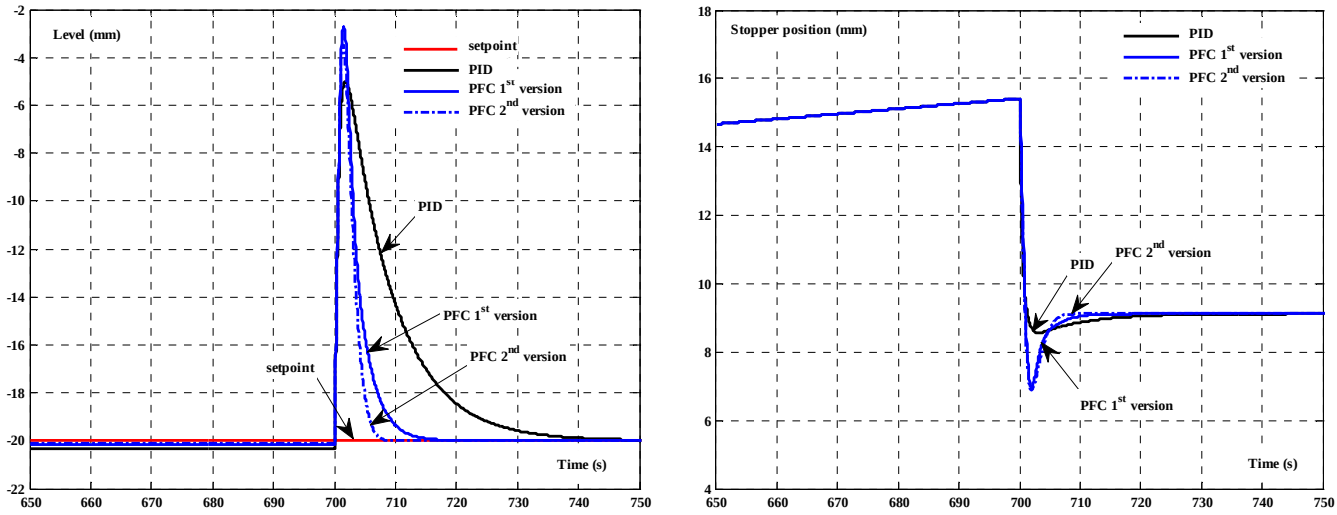

Fig. 4.19. Clogging rejection performances

4.3.1.2.3 Synthesis

In addition to the first and second versions, another idea has been tested. It consists of using a first order approximation of the time-delay and neglecting the actuator dynamics to have the same level of complexity. This third version has been studied following the same methodology.

All the performances of the three versions of the PFC controller are summarized and compared with the specifications in Table 4.4.

Table 4.4. PFC performances

	Criterion	First version	Second version	Third version	Specifications
Cutoff frequency ($rad \cdot s^{-1}$)		1.06	1.06	1.06	
Stability		OK	OK	OK	YES
Steady-state error	Step setpoint variation (mm)	0	0	0	0
	Step outflow variation (mm)	0	0	0	0
	Clogging occurring between 300 and 700s (mm)	**0.15**	**0.11**	**0.13**	0
Robustness margins	Gain margin (dB)	8	8.1	8.5	≥ 6
	Phase margin (degree)	**41**	**40**	45	≥ 45
	Delay margin (s)	$13.6T_s$	$13.2T_s$	$15T_s$	$\geq T_s$
	Modulus margin	0.52	0.54	0.57	≥ 0.5
Sensitivities	$\max\lvert\sigma_d\rvert$ (dB)	5.4	5.4	4.9	$\lvert\sigma_d\rvert \leq 6$
	$\max\lvert\sigma_c\rvert$ (dB)	**3.5**	**3.4**	2.7	$\lvert\sigma_c\rvert \leq 3$
Bulging rejection	Maximum gain (dB)	10	11	10	As low as possible
	Minimum gain (dB)	4.6	2.7	3.7	As low as possible
Unclogging at 700s	Maximum level amplitude (mm)	17	17	16	As low as possible
	Time to reach 95% of the steady-state value (s)	8.9	5.7	7.1	As fast as possible

By means of this work, it is interesting to observe that there are no strong differences between the three versions of the PFC control law. In the sequel, we shall focus our attention on the second version only because it has been used in a real plant.

4.3.2 Generalized Predictive Control GPC

4.3.2.1 Principle

4.3.2.1.1 Prediction model

Fig. 4.20 depicts the conventional version of the Generalized Predictive Control law GPC as initially proposed by D.W. Clarke [45]. Compared to the PFC control law, the GPC is based on the same architecture but differs in a few important computation details. In the next subsection, we shall outline extensively the main differences between the two techniques.

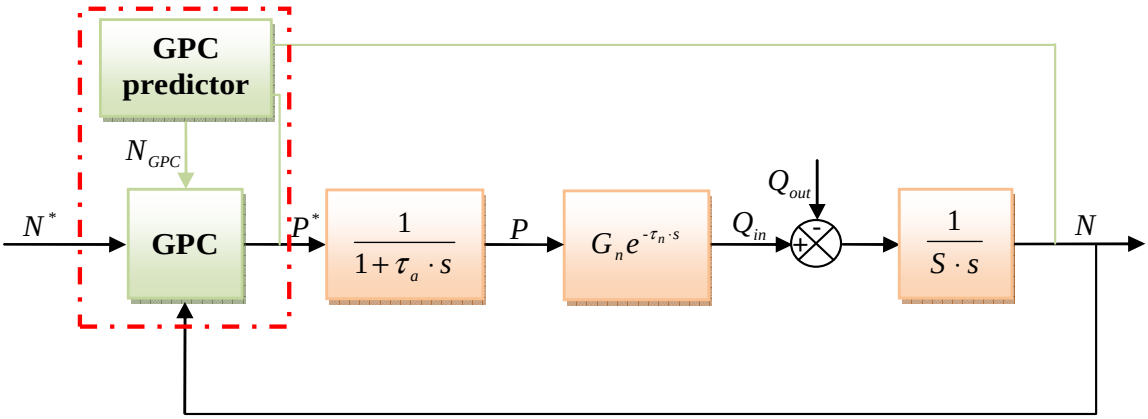

Fig. 4.20. Generalized Functional Control scheme

The GPC control law uses an external input-output representation form so-called CARIMA model [75], given by the following relation where A_{GPC} and B_{GPC} are two polynomials given in the backward shift operator q^{-1}:

$$\begin{cases} A_{GPC}(q^{-1}) \cdot N(t) = B_{GPC}(q^{-1}) \cdot P^*(t-1) + \dfrac{\xi(t)}{\Delta(q^{-1})} \\ \Delta(q^{-1}) = 1 - q^{-1} \end{cases} \tag{4.34}$$

with:

- q^{-1} : the backward shift operator,
- $\Delta(q^{-1})$: the difference operator,
- ξ : a centered white noise.

The GPC predictive strategy requires the definition of an optimal *j*-step ahead predictor which enables to predict the behavior of the process in the future over a finite horizon. The predicted output is most often designed under the classical form:

$$N_{GPC}(n+j) = \underbrace{F_j(q^{-1}) \cdot N(n) + H_j(q^{-1}) \cdot \Delta P^*(n-1)}_{\text{free response}} + \underbrace{G_j(q^{-1}) \cdot \Delta P^*(n+j-1) + J_j(q^{-1}) \cdot \xi(n+j)}_{\text{forced response}} \tag{4.35}$$

The unknown polynomials F_j, G_j, H_j and J_j are the unique solutions of the following Diophantine equations:

$$\begin{cases} \Delta(q^{-1}) \cdot A_{GPC}(q^{-1}) \cdot J_j(q^{-1}) + q^{-j} \cdot F_j(q^{-1}) = 1 \\ G_j(q^{-1}) + q^{-j} \cdot H_j(q^{-1}) = B_{GPC}(q^{-1}) \cdot J_j(q^{-1}) \end{cases} \tag{4.36}$$

The optimal predictor is then calculated considering that the best prediction of the white noise ξ is its average assumed to be equal to zero:

$$N_{GPC}(n+j) = F_j(q^{-1}) \cdot N(n) + H_j(q^{-1}) \cdot \Delta P^*(n-1) + G_j(q^{-1}) \cdot \Delta P^*(n+j-1) \tag{4.37}$$

4.3.2.1.2 Cost function

The GPC strategy minimizes a weighted sum of square prediction errors (between the predicted level and the setpoint) and square control signal increments, defined as follows:

$$\begin{cases} J_{GPC}(n) = \sum_{j=N_1}^{N_2} (N_{GPC}(n+j) - N^*)^2 + \eta \cdot \sum_{j=1}^{N_u} (\Delta P^*(n+j-1))^2 \\ \Delta P^*(n+j) = 0 \quad \text{for} \quad j \geq N_u \end{cases} \tag{4.38}$$

with:

- N_1: the minimum prediction horizon,
- N_2: the maximum prediction horizon,
- N_u: the control horizon,
- η: the weighting factor.

The GPC control law is usually given under its RST form as described in Fig. 4.21. In case of the mould level control system, the setpoint N^* is always set to a constant value. As a result, the polynomial $T(z^{-1})$ can be replaced by the sum of its coefficients.

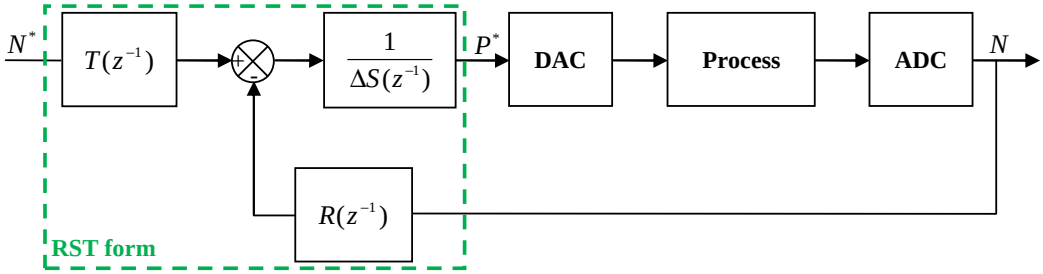

Fig. 4.21. Modified RST form

4.3.2.2 Performances

By using the values of parameters given in Table 2.1, the plant model transfer function can be represented, in the Laplace domain, by:

$$TF_{model}(s) = \frac{N}{P^*} = \frac{K_{model}}{s \cdot (1 + \tau_a \cdot s)} e^{-\tau_n \cdot s} = \frac{2.74}{s + 0.05s^2} e^{-0.5 \cdot s} \tag{4.39}$$

Given this transfer function, the tuning parameters of the GPC control law have been adjusted to obtain a cutoff frequency of the open loop close to the one of the PID controller i.e. $1.06 \text{rad} \cdot \text{s}^{-1}$. Using the values listed in Table 4.5, we were able to achieve a cutoff frequency equal to $1.08 \text{rad} \cdot \text{s}^{-1}$.

Table 4.5. GPC parameters

Parameter	T_s	N_1	N_2	N_u	η
Value	$0.05s$	10	40	1	3200

On the basis of these values, the RST form of the GPC controller can be formulated as follows:

$$\begin{cases} R_{GPC}(q^{-1}) = 0.872 - 1.16q^{-1} + 0.311q^{-2} \\ S_{GPC}(q^{-1}) = 1 + 0.0502q^{-1} + 0.0526q^{-2} + 0.0551q^{-3} + 0.0575q^{-4} + 0.06q^{-5} + 0.0624q^{-6} + 0.0648q^{-7} + 0.0672q^{-8} \\ \qquad + 0.0697q^{-9} + 0.0721q^{-10} + 0.0306q^{-11} \\ T_{GPC}(q^{-1}) = 0.0178 \end{cases} \tag{4.40}$$

$T_{GPC}(q^{-1})$, returned by the GPC algorithm, is a polynomial of degree 40. As explained previously, it is not necessary to consider all the terms of $T_{GPC}(q^{-1})$ fortunately because the level setpoint is always set to a constant value. For this reason, only the sum of its coefficients has been taken onto account.

The lengthy details of the calculations have been omitted but the reader is encouraged to refer to the full development in the reference [83], in particular, the section dealing with the resolution of the Diophantine equations.

Finally, the performances of the GPC control law, in terms of stability robustness and disturbances rejection, have been evaluated and compared to the PID and the PFC second version as illustrated in the following diagrams. The simulations have been performed using the same mould level control simulator.

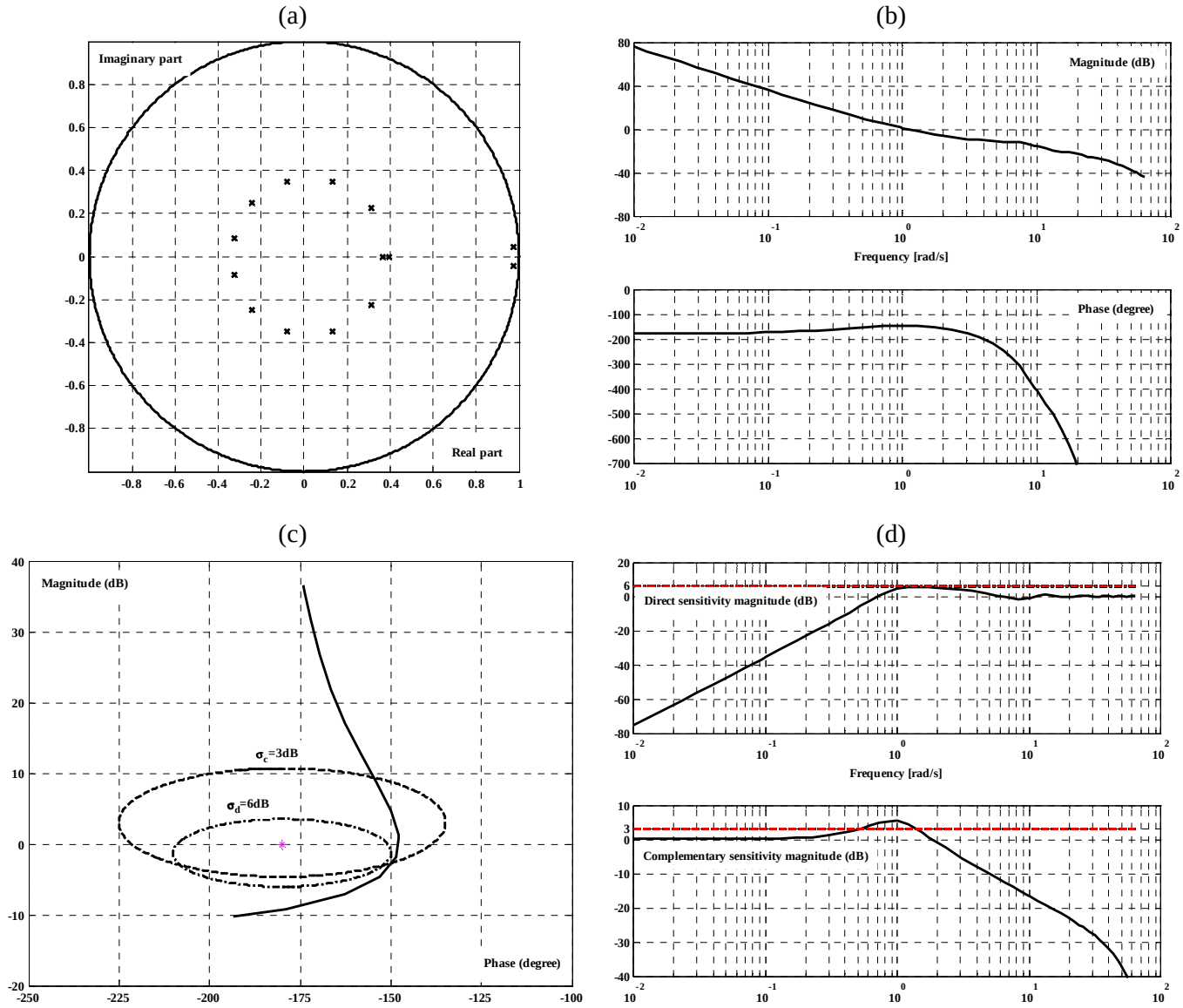

Fig. 4.22. (a) Poles of the closed loop
(b) Open loop Bode frequency response
(c) Open loop Black diagram
(d) Direct and complementary sensitivity functions magnitudes

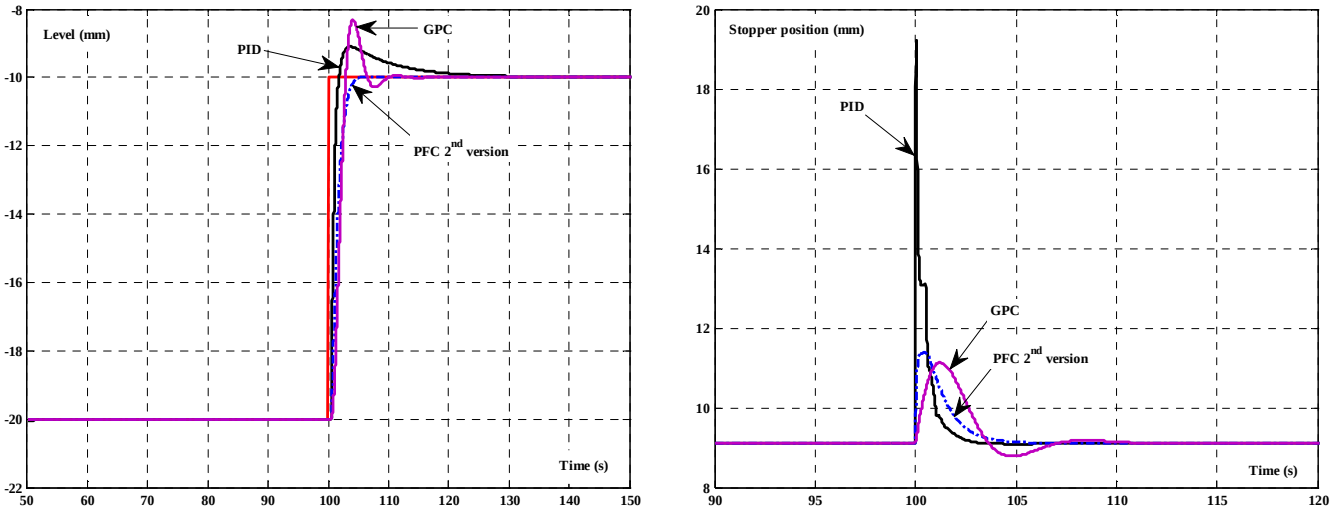

Fig. 4.23. Setpoint response for a step level variation of 10mm

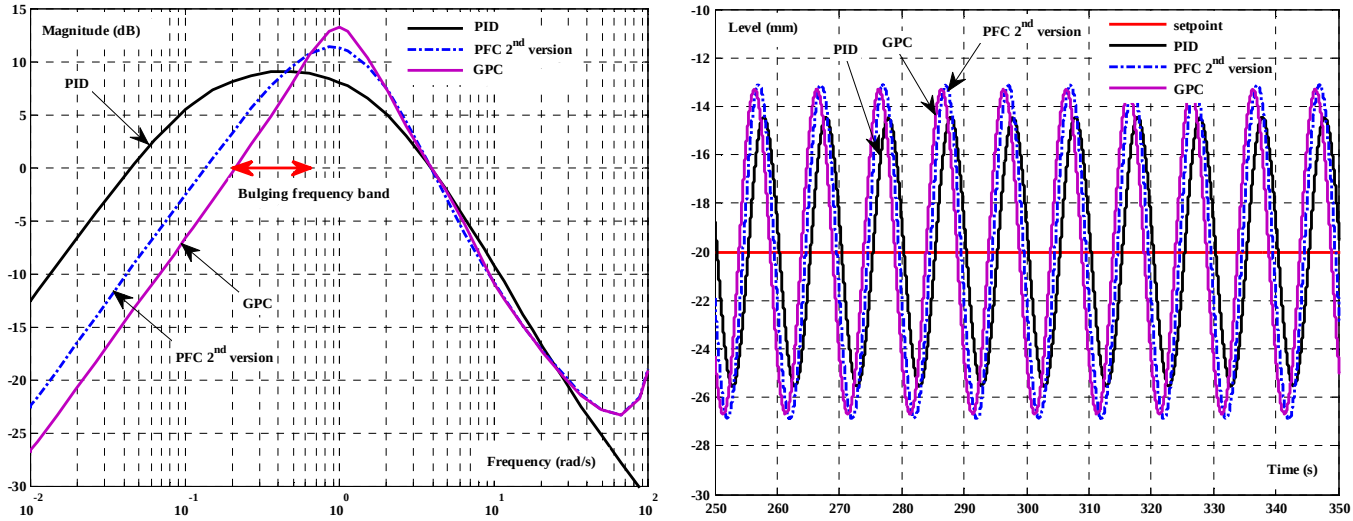

Fig. 4.24. Bulging rejection performances

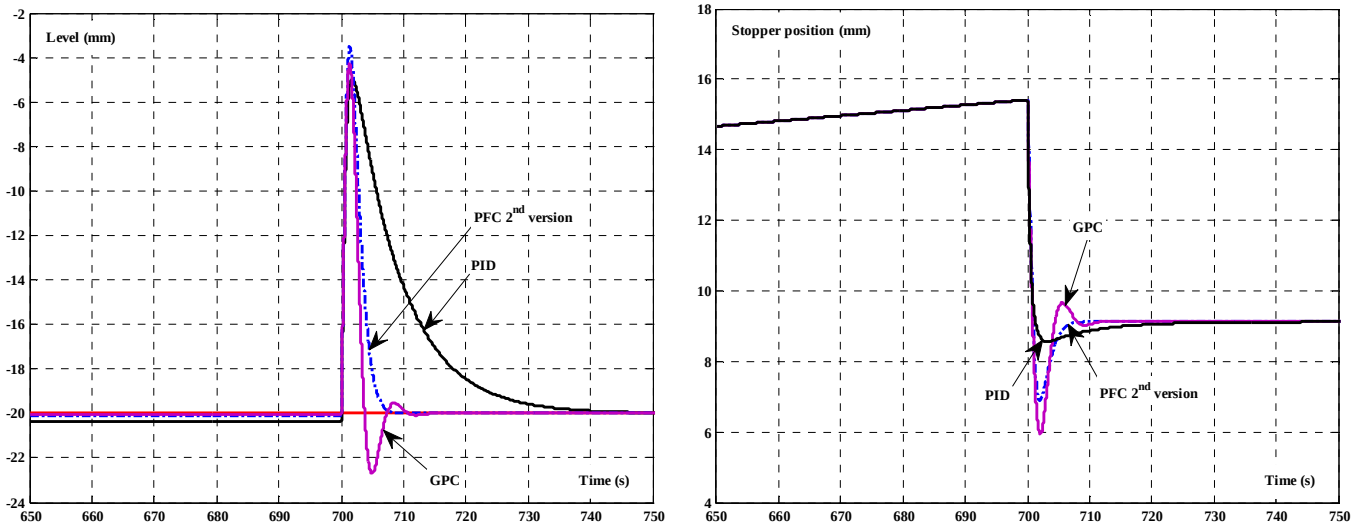

Fig. 4.25. Clogging rejection performances

We can observe that the bulging is noticeably rejected in case of GPC controller especially for low frequencies. As we shall see in Table 4.7, one related consequence is the deterioration of the delay margin. As for the clogging phenomenon rejection, no improvement has been achieved compared to the PFC second version performances.

4.3.3 Key notions

To complete this comparative study between the two predictive strategies, the key notions employed in each design are tabulated below to explain the specificities of each control law.

Table 4.6. Structural comparison between GPC and PFC designs

	GPC	PFC
Error between the process and the prediction model	This notion does not exist in the GPC design. There is no distinction between the outputs of the process and the predictive model. Errors, caused by the modeling, are assumed to be countered thanks to the control law robustness.	In the PFC design, the error between the predicted level and the predictive model output is defined as: $$dom(n) = N_{pred}(n) - N_{PFC}(n)$$ It follows: $$N_{pred}(n+h) = N_{PFC}(n+h) + dom(n+h)$$ $dom(n+h)$ is usually given by: $$dom(n+h) = N_{pred}(n) - N_{PFC}(n) + \sum_{i=1}^{d_e} e_i(n) h^i$$ with d_e the degree of the extrapolation. The adopted approach consists of using, however, a flat prediction that is: $$dom(n+h) = dom(n) = N_{pred}(n) - N_{PFC}(n)$$
Reference trajectory	This notion does not exist in the conventional version of the GPC control law.	The future process output is predicted to reach the setpoint following what is called the reference trajectory, introduced thereby to describe the desired behavior of the process output. In the PFC design and in case of a constant setpoint, the reference trajectory is generally given in the following exponential form: $$\begin{cases} N^* - S_{ref}(n+h) = (N^* - N_a(n)) \cdot \mu^h \\ N_a(n) = N(n+r) \qquad \mu = e^{-\frac{3T_s}{CLRT}} \end{cases}$$ where T_s is the sampling time and $CLRT$ is the Closed Loop Response Time.
Control law structure	There are no constraints imposed to the control law structure.	The control sequence is a linear combination of a set of base functions u_{BK} chosen among the step, ramp and parabola functions according to the process feature (with or without an integral term) and the setpoint nature. $$P^*(n+j) = \sum_{i=1}^{n_{BK}} \gamma_i(n) \cdot u_{BK}(j)$$ γ_i are the unknown coefficients that need to be determined.

<table>
<tr><td rowspan="2">Cost function</td><td>The GPC control law minimizes a weighted sum of square prediction errors (between the predicted level and the setpoint) and square control signal increments:
$\begin{cases} J_{GPC}(n) = \sum_{j=N_1}^{N_2} (N_{GPC}(n+j) - N^*)^2 + \eta \cdot \sum_{j=1}^{N_u} (\Delta P^*(n+j-1))^2 \\ \Delta P^*(n+j) = 0 \text{ for } j \geq N_u \end{cases}$
with:
• N_1: minimum prediction horizon,
• N_2 : maximum prediction horizon,
• N_u : control horizon,
• η : weighting factor.</td><td>The PFC control law is computed by minimizing a weighted sum of square future errors (between the predicted process output and the reference trajectory calculated at certain coincidence points h_i) and square control signal:
$J_{PFC}(n) = \sum_{i=1}^{n_{CP}} (N_{pred}(n+h_i) - S_{ref}(n+h_i))^2 + \eta \cdot (P^*(n))^2$
with:
• h_i : coincidence points,
• n_{CP} : number of coincidence points,
• η : weighting factor.</td></tr>
<tr><td colspan="2">Only the first value of the sequence is really applied according to the receding horizon principle.</td></tr>
<tr><td>Tuning parameters (SISO systems)</td><td>• $CLRT$: Closed Loop Response Time used to adjust the sampling time if necessary.
• N_1: minimum prediction horizon. $N_1 \cdot T_s$ is chosen, most of the time, equal to the time-delay.
• N_2 : maximum prediction horizon. $N_2 \cdot T_s$ is bounded by $CLRT$. Recall that the larger N_2 is, the more the system is stable and slow.
• N_u : control horizon generally set to 1 which simplifies the calculations significantly and does not affect the stability margins.
• η : control law weighting factor. Its optimal value is given by [83]:
$\eta_{opt} = trace(H_{step}^t H_{step})$
where H_{step} is the matrix of the coefficients of the step response.</td><td>• $CLRT$: Closed Loop Response Time used here also to adjust the sampling time. It appears likewise in the reference trajectory equation.
• u_{BK} : base functions used to synthesize the PFC control law.
• n_{BK} : number of base functions.
• h_i : coincidence points over the prediction horizon.
• n_{CP} : number of coincidence points.
• η : control law weighting factor chosen equal to zero in our proposed design.
• τ : auxiliary time constant introduced, when it is necessary, to decompose the process transfer function into stable systems. It could be chosen arbitrary.</td></tr>
<tr><td>Controller form</td><td colspan="2">The two control laws can be expressed using the RST form (Fig. 4.21). In case of time-delay systems, it is noteworthy to mention that GPC design generates polynomials of high degrees contrary to the PFC algorithm.</td></tr>
</table>

4.3.4 Performances comparison

As a conclusion of this section dedicated to the predictive strategies, Table 4.7 summarizes the performances of the PID, the PFC second version and the GPC. It is important to stress at this point that, prior to any comparative study, all the control laws have to be tuned in order to achieve at least one pre-defined performance criterion. Here, we opted for the cutoff frequency to make fair comparisons.

Table 4.7. Performances comparison between PID, PFC second version and GPC

	Criterion	PID	PFC	GPC	Specifications
Cutoff frequency ($rad \cdot s^{-1}$)		1.06	1.06	1.08	
Stability		OK	OK	OK	YES
Steady-state error	Step setpoint variation (mm)	0	0	0	0
	Step outflow variation (mm)	0	0	0	0
	Clogging occurring between 300 and 700s (mm)	**0.36**	**0.11**	**0.07**	0
Robustness margins	Gain margin (dB)	8.7	8.1	9.2	≥ 6
	Phase margin (degree)	66	**40**	**32**	≥ 45
	Delay margin (s)	$110T_s$	$13.2T_s$	$10.4T_s$	$\geq T_s$
	Modulus margin	0.63	0.54	0.53	≥ 0.5
Sensitivities	$\max\lvert\sigma_d\rvert$ (dB)	4	5.4	5.5	$\lvert\sigma_d\rvert \leq 6$
	$\max\lvert\sigma_c\rvert$ (dB)	0.79	**3.4**	**5.4**	$\lvert\sigma_c\rvert \leq 3$
Bulging rejection	Maximum gain (dB)	9	11	10	As low as possible
	Minimum gain (dB)	8	2.7	-1	As low as possible
Unclogging at 700s	Maximum level amplitude (mm)	15	17	16	As low as possible
	Time to reach 95% of the steady-state value (s)	23	5.7	6.5	As fast as possible

From the results given in this table, it can be inferred that the predictive control laws are more effective in terms of bulging rejection especially for low frequencies. The cost of this good performance is a deterioration of the phase and delay margins.

4.4 Smith predictor control

The Smith predictor is widely used to control systems having a time delay. It converts the time-delay control system to a delay free problem provided that the time-delay is well known [46] [84].
In this section, two versions of the Smith predictor are investigated with a view to enhancing the disturbances rejection, in particular, the bulging. Indeed, we shall demonstrate that the classical version of the Smith predictor cannot be used for controlling an integrator process. Since our plant model has an integral term, we will focus our attention on a second version which extends the properties of the conventional scheme with the capability of shaping the frequency characteristics of the disturbance rejection transfer by means of an additional controller.

4.4.1 Initial version

4.4.1.1 Conventional scheme

The problem of designing controllers for processes with time delay has been addressed over the years by several authors with varying degrees of success [47] [48]. The control scheme attributed to Smith so-called Smith predictor, introduces an additional feedback around the controller with the purpose of eliminating the delay effect from the closed loop equation.
Let us recall the plant model transfer function:

$$\begin{cases} TF_{model}(s) = \dfrac{K_{model} e^{-\tau_n \cdot s}}{s \cdot (1 + \tau_a \cdot s)} = H_0(s) \cdot e^{-\tau_n \cdot s} \\ K_{model} = \dfrac{G_n}{S} \end{cases} \tag{4.41}$$

where $H_0(s)$ is the delay free part of the plant model.
Fig. 4.26 depicts the conventional scheme of the Smith predictor. If the plant model is precisely identified, the closed loop transfer function is given by:

$$\frac{N}{N^*} = \frac{C(s) \cdot H_0(s)}{1 + C(s) \cdot H_0(s)} e^{-\tau_n \cdot s} \tag{4.42}$$

where $C(s)$ is the controller transfer function.

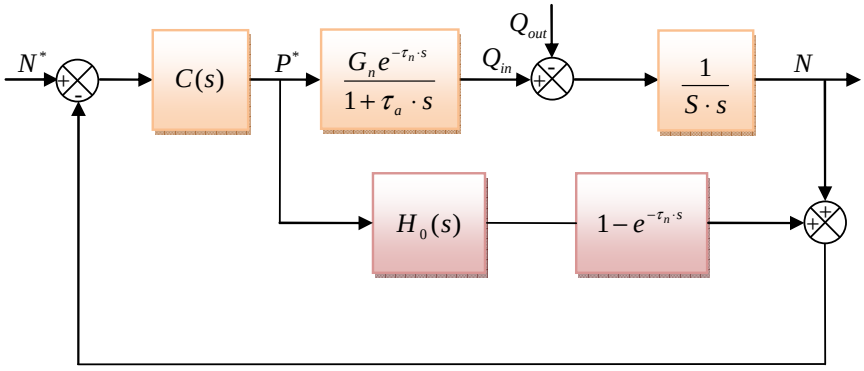

Fig. 4.26. Block diagram of Smith predictor conventional scheme

It can be checked that the Smith predictor equivalent controller is given by:

$$TF_{SP}(s) = \frac{C(s)}{1 + C(s) \cdot H_0(s) \cdot (1 - e^{-\tau_n \cdot s})} \tag{4.43}$$

By removing the delay effect from the dynamics of the closed loop, the tuning of the controller becomes noticeably easier. Furthermore, the closed loop stability can be examined using conventional methods.

On the other hand, the bulging rejection transfer function is given by:

$$\frac{N}{Q_{out}} = \frac{C(s)\cdot H_0(s)\cdot (e^{-\tau_n \cdot s} - 1) - 1}{S\cdot s\cdot (1 + C(s)\cdot H_0(s))} \tag{4.44}$$

The presence of an integral term within the plant model is necessary to cancel the steady-state error in the setpoint response. However, the steady-state error, imposed by a constant flow rate out of the mould, cannot be equal to zero whatever the controller is. This disturbance produces indeed an obvious non-zero offset as shown in the following equation where $\varepsilon_Q(s)$ is the Laplace transform of the level error:

$$\varepsilon_Q(s) = 0 - N(s) = \frac{-C(s)\cdot H_0(s)\cdot (e^{-\tau_n \cdot s} - 1) + 1}{S\cdot s\cdot (1 + C(s)\cdot H_0(s))} Q_{out}(s) \underset{s\to 0}{\propto} \frac{\tau_n}{S} Q_{out}(s) \tag{4.45}$$

This deficiency of the Smith predictor, in regards to disturbances rejection, has been extensively studied and sometimes effectively tackled [51] [52]. Several authors have suggested modifications to the original Smith predictor. In the following, some of them will be discussed.

4.4.1.2 Smith predictor modified version

In [13], the authors propose an extension of the original Smith predictor to cancel the steady-state error. As shown in Fig. 4.27, it is based on the introduction of an additional feedback containing the block $G_n \cdot \tau_n$ and connected in parallel with the inner feedback of the Smith predictor.

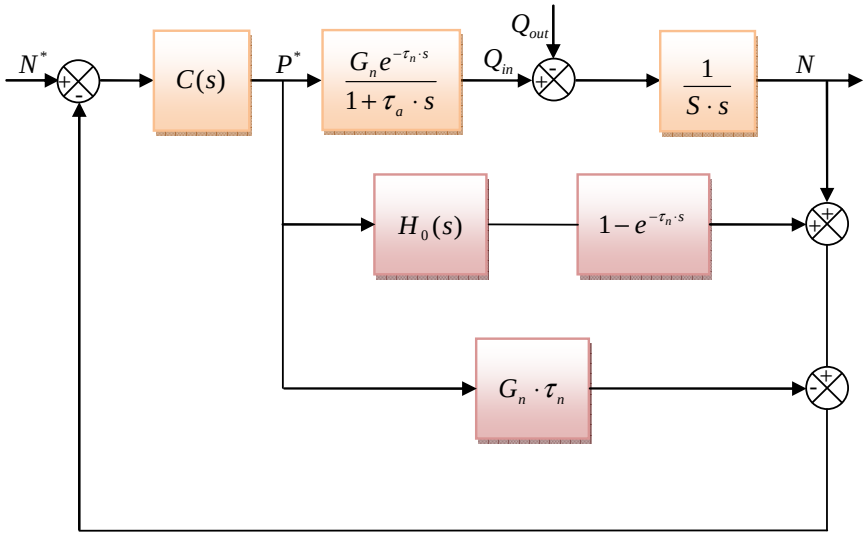

Fig. 4.27. Block diagram of Smith predictor modified version

According to Fig. 4.27, the closed loop transfer function is given by:

$$\frac{N}{N^*} = \frac{C(s)\cdot H_0(s)}{1 + C(s)\cdot H_0(s) - G_n\cdot \tau_n \cdot C(s)} e^{-\tau_n \cdot s} \tag{4.46}$$

and the bulging rejection transfer function is given by:

$$\frac{N}{Q_{out}} = \frac{C(s)\cdot H_0(s)\cdot (e^{-\tau_n \cdot s} - 1) - 1 + G_n\cdot \tau_n \cdot C(s)}{S\cdot s\cdot (1 + C(s)\cdot H_0(s) - G_n\cdot \tau_n \cdot C(s))} \tag{4.47}$$

Although this structure cancels the steady-state error, it does not allow the designer to shape the disturbances rejection transfer function which is a key element of the mould level control problem. The following subsection describes the solution proposed by Aström to overcome this obstacle with the capability of shaping the frequency characteristics of the bulging rejection [49].

4.4.2 Aström's modified version

4.4.2.1 Principle

The Aström's modified Smith predictor is depicted in Fig. 4.28. Compared to the conventional version, an additional feedback from the difference between the system and the model outputs is introduced.
Altogether, there are two controllers for different objectives. The first one C is primarily intended for shaping the setpoint response. The second one M is specifically designed to handle the disturbances. In literature, other complex structures have been proposed where more than two controllers are utilized.

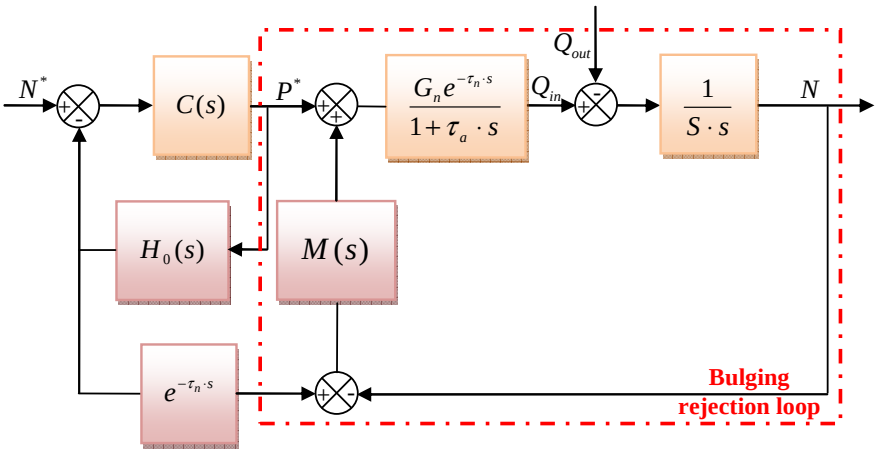

Fig. 4.28. Block diagram of Aström's modified Smith predictor

Therefore, the Aström's modified Smith predictor decouples the setpoint response from the disturbance rejection which can be thereby independently optimized.
By the merit of the Smith predictor scheme, the Aström's modified version removes also the time-delay from the closed loop characteristic equation and the setpoint response is thus always given by equation (4.42). The benefits of the original Smith predictor are thus preserved.
On the other hand, the disturbance rejection transfer becomes:

$$\frac{N}{Q_{out}} = \frac{-1}{S \cdot s \cdot (1 + M \cdot H_0 \cdot e^{-\tau_n \cdot s})} \tag{4.48}$$

This structure provides more freedom in choosing the transfer function M. Namely, in the presence of an integral term in the plant model, the designer should include an integration mode within M in order to cancel the steady-state error aforementioned as can be deduced from equation (4.48).
In this dissertation, the Aström's modified Smith predictor is used to reduce the influence of the bulging on the mould level. The next paragraph proposes a design methodology based on the H_∞ framework for shaping the frequency characteristics of the bulging rejection transfer function.
As for the controller C, the simplest solution is to choose it as a simple gain which is sufficient to tune the closed loop response time.

4.4.2.2 Design procedure

Before starting the design procedure, various forms of $M(s)$ have been tested including the first and second order functions but with varying degrees of success. In [51], it is suggested to use the scheme represented in Fig. 4.29 where $M_0(s)$ is the transfer function that needs to be tuned.

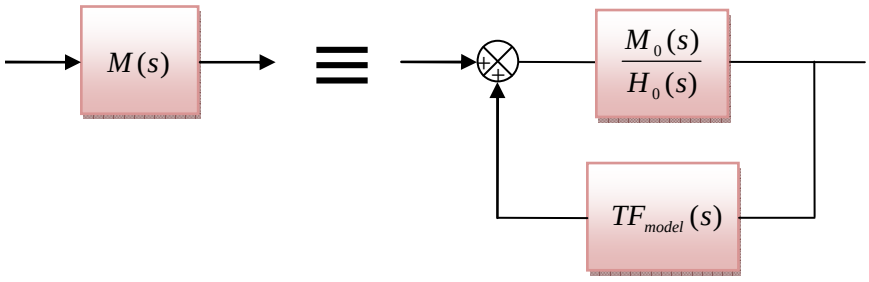

Fig. 4.29. Possible scheme for *M(s)*

Using this scheme, the bulging rejection transfer function becomes:

$$\frac{N(s)}{Q_{out}(s)} = \frac{1}{S \cdot s}\left(M_0(s) \cdot e^{-\tau_n \cdot s} - 1\right) \tag{4.49}$$

Therefore, the bulging rejection response could be directly adjusted from the poles of $M_0(s)$. Some tuning rules are also given with a view to eliminating the steady-state error produced by a step disturbance variation. Unfortunately, this form was not able to improve the bulging rejection. In our view, this issue may be efficiently resolved through the H_∞ framework. This is the focus of the next paragraph.

4.4.2.2.1 *M* design based on H_∞ control theory

For the sake of simplicity, we decided to select only the bulging rejection loop of the Aström's modified Smith predictor as depicted in Fig. 4.30.

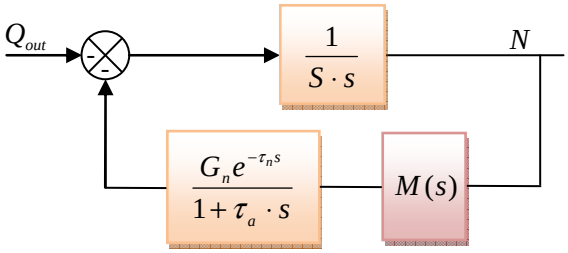

Fig. 4.30. Bulging rejection loop

Our goal is to use the H_∞ control theory as an alternative for shaping the bulging rejection transfer function while ensuring a delay margin fixed in advance.

To do so, a second disturbance W was added to the bulging rejection loop to be able to solve the H_∞ problem which requires several conditions to be met in particular W enables the rank of the transfer between the input of the controller i.e. N and those of the process i.e. $(Q_{out} \quad W)$ to be 1 [85]. More precisely, W is an additional disturbance to the mould level N and may model thereby the standing waves disturbance. Fig. 4.31 shows the augmented plant of the H_∞ control problem where two weighting functions W_1 and W_2 have been introduced in order to reduce the bulging effect on the level and to achieve robust stability under delay uncertainties respectively.

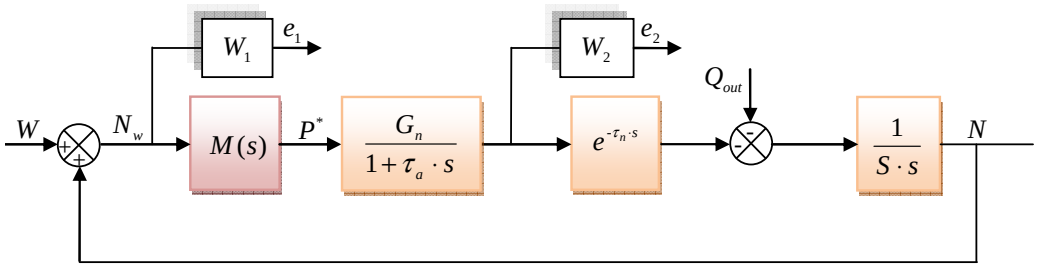

Fig. 4.31. H_∞ control scheme

According to Fig. 4.31, it follows:

$$\begin{cases} e_1(s) = W_1(s)B_{11}(s)\cdot Q_{out}(s) + W_1(s)B_{12}(s)\cdot W(s) \\ e_2(s) = W_2(s)B_{21}(s)\cdot Q_{out}(s) + W_2(s)B_{22}(s)\cdot W(s) \end{cases}$$

with:
$$\begin{cases} B_{11}(s) = \dfrac{-1}{S\cdot s}\dfrac{1}{(1+M(s)\cdot TF_{model}(s))} & B_{12}(s) = \dfrac{1}{1-M(s)\cdot TF_{model}(s)} \\ B_{21}(s) = \dfrac{-M(s)\cdot H_0(s)}{1+M(s)\cdot TF_{model}(s)} & B_{22}(s) = \dfrac{G_n}{(1+\tau_a\cdot s)}\dfrac{M(s)}{(1-M(s)\cdot TF_{model}(s))} \end{cases} \quad (4.50)$$

The general control configuration depicted in Fig. 4.31 is then represented in LFT form as shown in Fig. 4.32 [86].

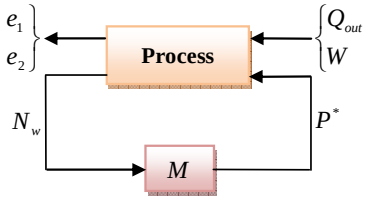

Fig. 4.32. LFT form of H_∞ control scheme

Therefore, the H_∞ algorithm consists of synthesizing a controller which stabilizes the closed loop internally in such a way that the following inequality holds [14]:

$$\left\| \overbrace{\begin{pmatrix} W_1(s)\cdot B_{11}(s) & W_1(s)\cdot B_{12}(s) \\ W_2(s)\cdot B_{21}(s) & W_2(s)\cdot B_{22}(s) \end{pmatrix}}^{Z(s)} \right\|_\infty < 1 \quad (4.51)$$

To improve the bulging rejection, W_1 is chosen so that B_{11} has a small magnitude over the bulging frequencies. Furthermore, W_1 should have a high gain at low frequencies in order to eliminate the steady-state error. A suitable transfer function could be a phase lead filter:

$$W_1^{-1} = K_{w1}\frac{1+T_{w1}\cdot s}{1+a_{w1}T_{w1}\cdot s} \qquad \text{with:} \quad a_{w1} < 1 \quad (4.52)$$

Secondly, W_2 is selected to ensure robust stability under delay changes with the help of the small gain theorem [87]. Indeed, let us consider the interconnection shown in Fig. 5.6 and suppose that both the complementary sensitivity function $\sigma_c(s)$ and the multiplicative uncertainty $\Delta(s)$ are stable. The closed loop is stable if and only if the following robust stability criterion for a multiplicative uncertainty is satisfied:

$$\left\| \sigma_c(s)\cdot\Delta(s) \right\|_\infty < 1 \quad (4.53)$$

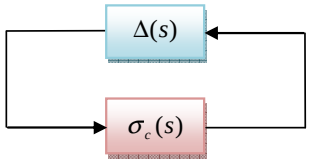

Fig. 4.33. Interconnection of a stable transfer function and an uncertainty block

The complementary sensitivity function $\sigma_c(s)$ has been introduced because the delay uncertainty has been modeled using a multiplicative uncertainty as illustrated in Fig. 4.34.

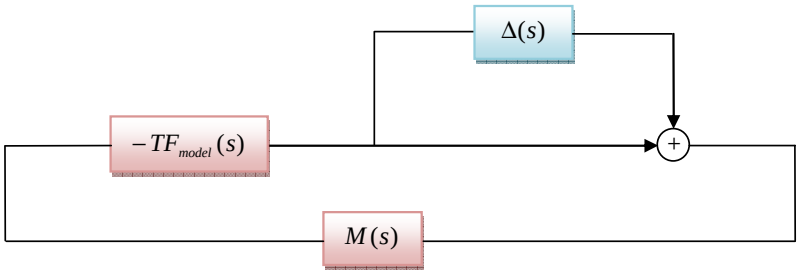

Fig. 4.34. Multiplicative uncertainty representation

We can then verify that the complementary sensitivity function is given by:

$$\sigma_c(s) = \frac{-M(s)\cdot TF_{model}(s)}{1+M(s)\cdot TF_{model}(s)} \tag{4.54}$$

Therefore, the bulging rejection loop is stable if the following relation is satisfied:

$$\left\| \frac{-M(s)\cdot TF_{model}(s)}{1+M(s)\cdot TF_{model}(s)}\Delta(s) \right\|_{\infty} < 1 \tag{4.55}$$

The multiplicative uncertainty $\Delta(s)$ is defined in (4.56) where the time-delay changes are bounded by a value $\Delta\tau_n$ assumed to be known.

$$TF^{\Delta}_{model}(s) = TF_{model}(s)\cdot(1+\Delta(s)) = TF_{model}(s)\cdot e^{\Delta\tau_n\cdot s} \tag{4.56}$$

and so

$$\Delta(s) = e^{\Delta\tau_n\cdot s} - 1 \tag{4.57}$$

We also know that:

$$\left|TF_{model}(s)\right| = \left|H_0(s)\cdot e^{-\tau_n\cdot s}\right| = \left|H_0(s)\right|$$

Therefore,

$$\left\| \frac{-M(s)\cdot TF_{model}(s)}{1+M(s)\cdot TF_{model}(s)}\Delta(s) \right\|_{\infty} = \left\| \frac{-M(s)\cdot H_0(s)}{1+M(s)\cdot TF_{model}(s)}\Delta(s) \right\|_{\infty} = \left\| B_{21}(s)\cdot\Delta(s) \right\|_{\infty}$$

(4.55) is thus equivalent to:

$$\left\| B_{21}(s)\cdot\Delta(s) \right\|_{\infty} < 1 \tag{4.58}$$

By using a rational approximation of the exponential function, we can prove that $\Delta(s)$ satisfies the inequality:

$$\left|\Delta(j\omega)\right| < \left| \frac{2\Delta\tau_n\cdot j\omega}{1+\Delta\tau_n\cdot j\omega} \right| \tag{4.59}$$

W_2 could be chosen such as:

$$\left|W_2(j\omega)\right| > \left| \frac{2\Delta\tau_n\cdot j\omega}{1+\Delta\tau_n\cdot j\omega} \right| \tag{4.60}$$

For example, let us adopt this model:

$$W_2(s) = K_{w2}\frac{2\Delta\tau_n\cdot s}{1+\Delta\tau_n\cdot s} \qquad \text{with:} \quad K_{w2} > 1 \tag{4.61}$$

4.4.2.2.2 Robust tuning based on the Particle Swarm Optimization

The optimization of the weighting functions parameters is crucial to achieve optimal performances. Based on the transfer functions of W_1 and W_2 defined previously, the contribution of this paragraph is to provide a simple design methodology using a sort of randomized algorithms. It is based on the Particle Swarm Optimization (PSO) technique which does not need any gradient or derivative of the objective function. Its algorithm is simple, easy to implement with only a few parameters to adjust. Nevertheless, it is backed only by several simulation examples and it remains difficult to guarantee its effectiveness from a theoretical point of view [15] [16] [53].

The Particle Swarm Optimization is mainly inspired by social behavior patterns of organisms that live and interact within large groups of autonomous individuals moving in random directions as flocks of birds, schools of fishes, swarms of bees and colonies of ants (Fig. 4.35). This intelligent model, initially proposed by Eberhart and Kennedy [17], has shown good performances in a wide range of applications during recent years, especially for non-convex problems.

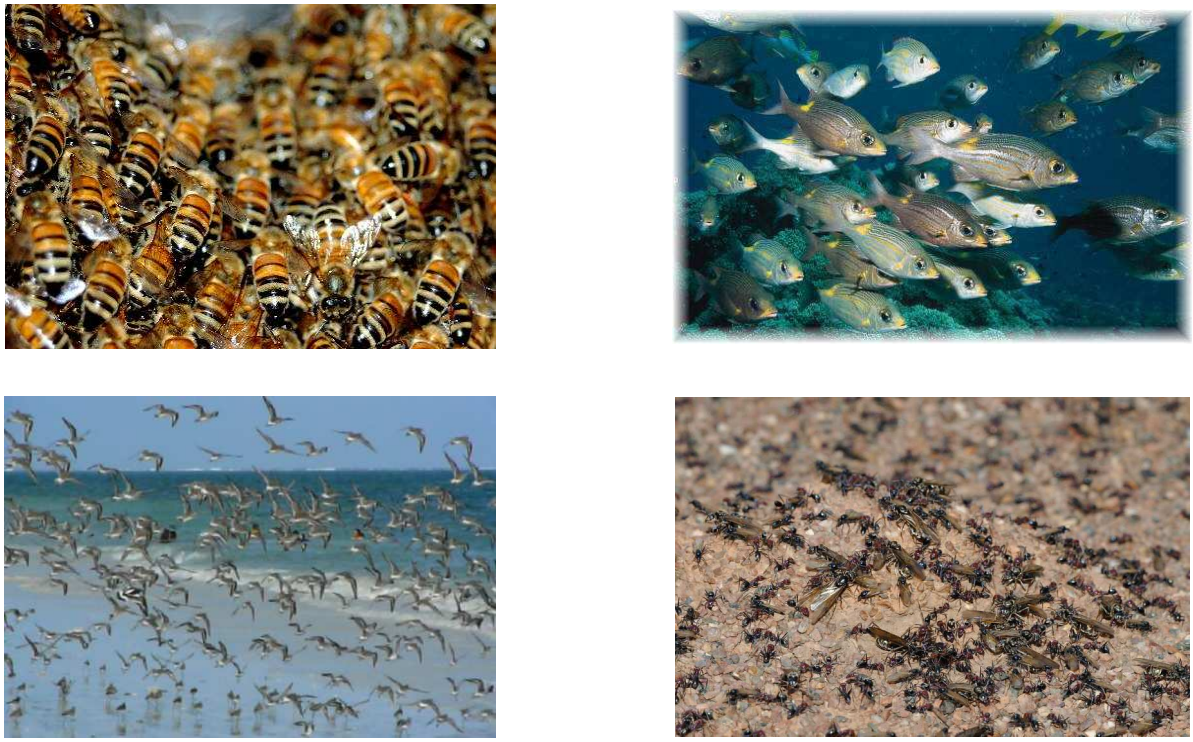

Fig. 4.35. Social behavior of some populations

The general optimization problem is mathematically formulated as follows:

$$\underset{x \in \mathrm{X}}{\text{minimize}} \; f(x) \tag{4.62}$$

The PSO algorithm uses a swarm of p_{swarm} particles in order to find an optimal solution of equation (4.62). Each particle is considered as a point in the search space X. It adjusts its movement according to its own experience as well as those of the other particles both in its neighborhood and in the entire swarm on the basis of the following update law [16], represented graphically in Fig. 4.36:

$$\begin{cases} v_i^{k+1} = c_0 \cdot v_i^k + c_1 \cdot r_{1,i}^k \cdot (x_i^{k,best} - x_i^k) + c_2 \cdot r_{2,i}^k \cdot (x_{i,swarm}^{k,best} - x_i^k) \\ x_i^{k+1} = x_i^k + v_i^{k+1} \end{cases} \tag{4.63}$$

with:

- x_i^k : position of the i^{th} particle at iteration k ,
- v_i^k : velocity of the i^{th} particle at iteration k ,
- c_0 : inertia factor,
- c_1 : cognitive scaling factor,
- c_2 : social scaling factor,
- $r_{1,i}^k$, $r_{2,i}^k$: random numbers uniformly distributed in [0 1],
- $x_i^{k,best}$: best previous position of the i^{th} particle,
- $x_{i,swarm}^{k,best}$: best previous position of particles of the i^{th} particle neighborhood.

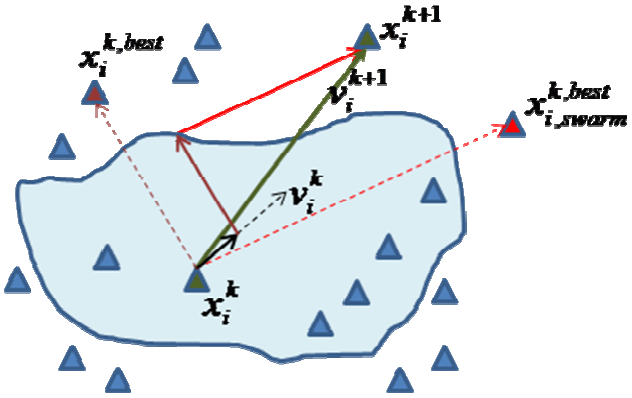

Fig. 4.36. Graphical representation of movements update law

The PSO algorithm consists of the following steps displayed on a chart in Fig. 4.37:

[step 1] Initialize the particles positions and velocities with feasible random values.

[step 2] For each particle, evaluate the objective function at current position $f(x_i^k)$ (fitness value).

[step 3] Update $x_i^{k,best}$ and $x_{i,swarm}^{k,best}$.

[step 4] If the stopping criterion is satisfied, the algorithm terminates with the solution:

$$x^* = \underset{x_i^k}{\text{argmin}}\left\{f(x_i^k), \forall i, j\right\} \tag{4.64}$$

Otherwise, update the positions x_i^k and the velocities v_i^k according to (4.63) and go to [step 2].

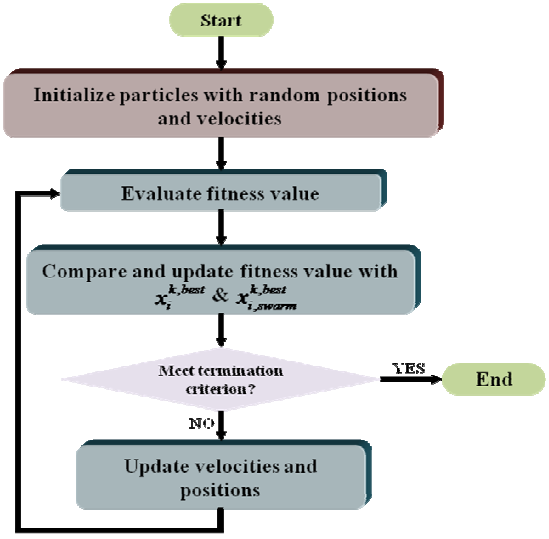

Fig. 4.37. Particle Swarm Optimization algorithm

The number of tuning parameters in the PSO algorithm appears to be limited. Many studies have been published about the tuning rules [54]. This aspect is beyond the scope of this dissertation, aiming only at using this optimization method for control purposes. Amongst all the parameters, the important ones and their typical values, validated by Kennedy [17], are listed in Table 4.8.

Table 4.8. PSO parameters

Parameter	Value
p_{swarm}	$10+\sqrt{\dim(X)}$
c_0	$1/(2\ln(2))$
c_1	$0.5+\ln(2)$
c_2	$0.5+\ln(2)$

where $\dim(X)$ is the dimension of the optimization problem i.e. the number of optimization variables (equal to 5 in our case).
In addition, other options may be set, such as the stopping condition or the maximum number of iterations, the maximum duration of the optimization algorithm and the ranges of particles velocities.

4.4.2.3 Performances

4.4.2.3.1 Simulation results

First of all, the two filters $W_1(s)$ and $W_2(s)$ should be calculated according to equations (4.52) and (4.61). To do this, we propose to use the PSO method in order to optimize the unknown parameters of $W_1(s)$ and $W_2(s)$ i.e. K_{w1}, T_{w1}, a_{w1}, K_{w2} and $\Delta\tau_n$ in such a way that the delay margin $\Delta\tau_n$ is greater than 0.5s and so that $B_{11}^{\max}$ and $B_{11}^{\min}$, respectively the maximum and the minimum gains of the bulging rejection transfer $B_{11}(s)$ over the bulging frequency band between 0.03 and 0.1H, are chosen around 5 and 2dB.
Other criteria as the gain margin or the overshoot of the step response may also be included if desired.
The optimization problem is then mathematically formulated as follows where the matrix $Z(s)$ is defined in (4.51):

$$\underset{K_{w1},T_{w1},a_{w1},K_{w2},\Delta\tau_n}{\text{minimize}} \begin{pmatrix} \|Z(s)\|_\infty \\ +\exp(-1000\cdot(\Delta\tau_n-0.5)) \\ +\exp(-1000\cdot(5-B_{11}^{\max})) \\ +\exp(-1000\cdot(2-B_{11}^{\min})) \end{pmatrix} \tag{4.65}$$

The objective function does not have any analytical expression. It can be computed only through simulations and this is allowed in the particle swarm technique. The H_∞ norm is calculated using the Glover-Doyle algorithm [55]. Finally, this optimization problem was solved using Matlab-Simulink software and takes about ten minutes on a Pentium 4 3.2GHz to return the following weighting functions:

$$W_1(s)=\frac{1+0.84s}{0.31+1.75s} \qquad W_2(s)=\frac{0.82s}{1+0.82s}$$

Based on these weighting functions, the controller $M(s)$ synthesized by the H_∞ algorithm is given by:

$$M_1(s)=\frac{113\cdot(s+20)\cdot(s+4)\cdot(s+1.2)\cdot(s+0.61)}{(s+1282)\cdot(s+13)\cdot(s+1.3)\cdot(s+0.18)} \tag{4.66}$$

Due to the chosen control scheme for H_∞ synthesis (Fig. 4.31), $M(s)$ cannot incorporate an integral term leading to a small steady-state error.

In order to overcome this problem, the least of all the poles in M_1 is replaced by zero. The H_∞ controller becomes:

$$M_2(s) = \frac{113 \cdot (s+20) \cdot (s+4) \cdot (s+1.2) \cdot (s+0.61)}{s \cdot (s+1282) \cdot (s+13) \cdot (s+1.3)} \tag{4.67}$$

Considering M_2, the other controller C was set to 1 to adjust the closed loop response time. Fig. 4.38 presents the step response for a level variation of 10mm. Compared to the other control laws, the Aström predictor enables a faster response without introducing an overshoot but it generates, however, a stopper position setpoint with high magnitude.

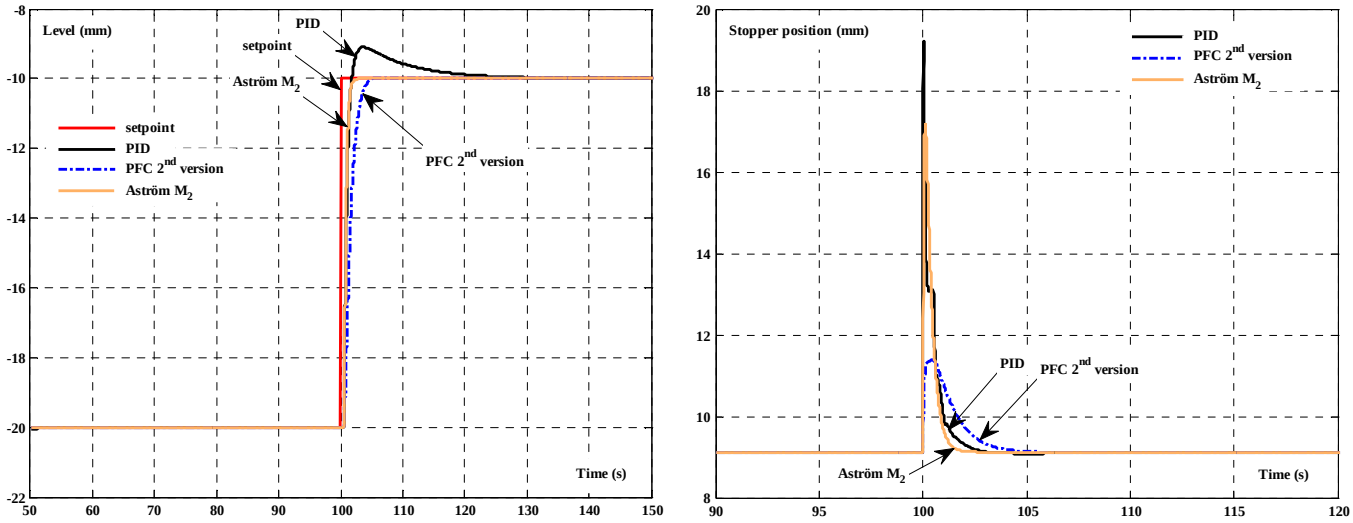

Fig. 4.38. Setpoint response for a step level variation of 10mm

The enhancement of the bulging rejection is clearly exhibited in Fig. 4.39 where the Bode diagrams of the PID, the PFC second version and the Aström predictor M_2 are drawn. The performances have been improved both over the bulging frequency band and at low frequencies. In the right-hand side, we can examine the robustness of the Aström predictor under delay changes in the presence of bulging. Using M_2, the level variations have been reduced by half and the delay value does not appear to have any effect on this performance.

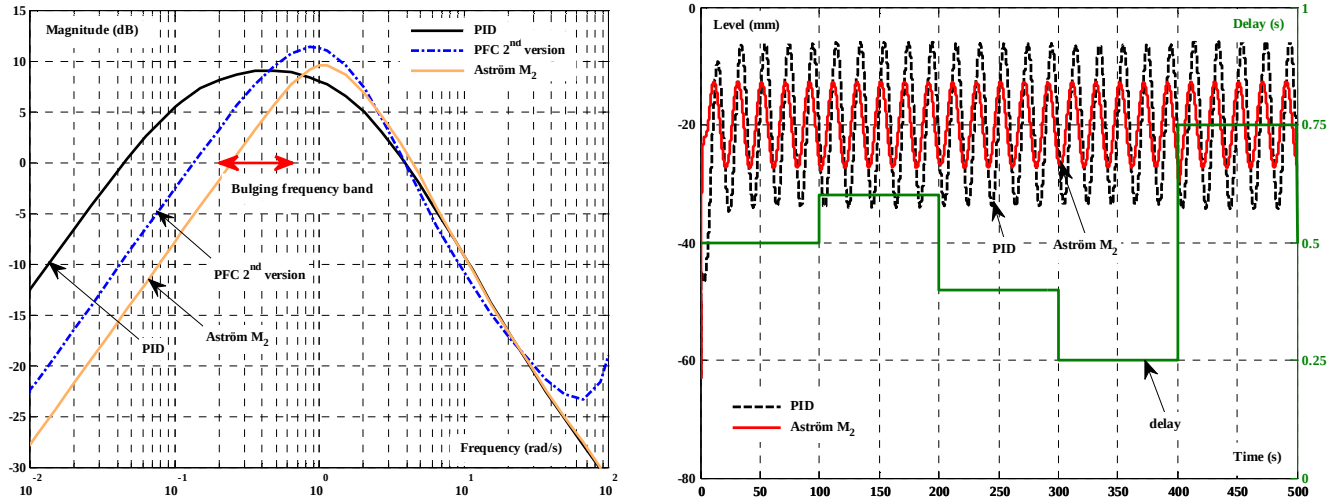

Fig. 4.39. Bulging rejection performances

On the other hand, the clogging rejection has not been taken onto account in the Aström predictor design. Therefore, its performances in this area are comparable to those of the PFC second version as illustrated in Fig. 4.40. One perspective is to include other disturbances in the design process, in particular, the clogging/unclogging phenomenon and the standing waves.

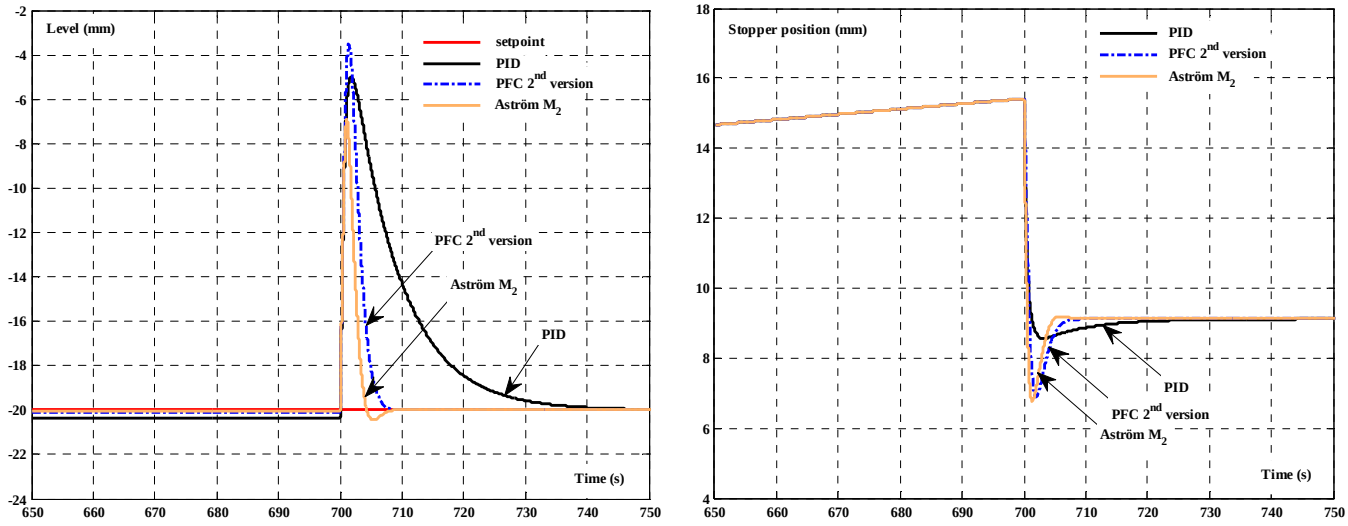

Fig. 4.40. Clogging rejection performances

Finally, the controller M_2 can also be approximated by the following PID control law which would be useful from a practical point of view because the PID form is well known by the operators and already implemented in the industrial PLCs (see Fig. 4.41 for the Bode diagrams of M_1, M_2 and M_3).

$$M_3(s) = 0.8 \cdot \left(0.8 + \frac{0.37}{s} + \frac{0.12s}{1 + 0.0009s} \right) \tag{4.68}$$

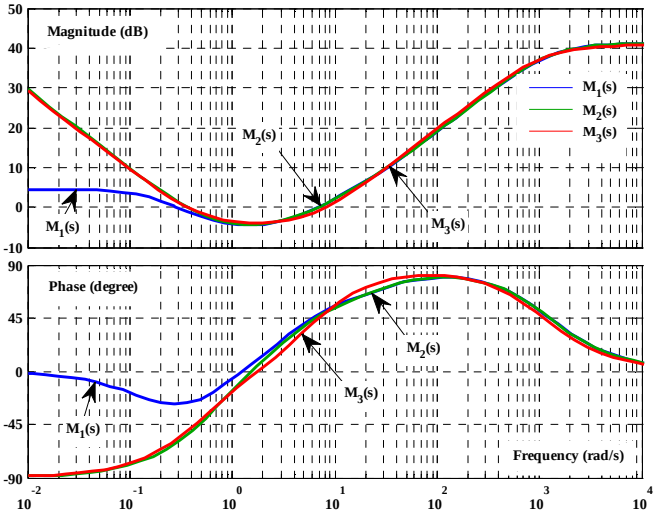

Fig. 4.41. Bode diagrams of the three versions of the Aström predictor M_1, M_2 and M_3

4.4.2.3.2 Global comparison

The performances of the two versions of the Aström predictor M_1 and M_2 are summarized and compared to those of the PID and the predictive strategies in Table 4.9. It can be reasonably deducted that the Aström predictor, designed using the H_∞ framework and the Particle Swarm Optimization method, outperforms the other control laws.

Table 4.9. Performances comparison between PID, PFC second version, GPC and Aström predictor

	Criterion	PID	PFC	GPC	Aström predictor	
					M_1	M_2
Cutoff frequency ($rad \cdot s^{-1}$)		1.06	1.06	1.08	1.33	1.34
Stability		OK	OK	OK	OK	OK
Steady-state error	Step setpoint variation (mm)	0	0	0	0	0
	Step outflow variation (mm)	0	0	0	**6.7**	0
	Clogging occurring between 300 and 700s (mm)	**0.36**	**0.11**	**0.07**	**<11**	**0.06**
Robustness margins	Gain margin (dB)	8.7	8.1	9.2	9.9	9.7
	Phase margin (degree)	66	**40**	**32**	50	**42**
	Delay margin (s)	$110T_s$	$13.2T_s$	$10.4T_s$	0.65	0.55
	Modulus margin	0.63	0.54	0.53	0.92	0.92
Sensitivities	$\max\lvert\sigma_d\rvert$ (dB)	4	5.4	5.5	4.1	4.4
	$\max\lvert\sigma_c\rvert$ (dB)	0.79	**3.4**	**5.4**	2.1	**3.6**
Bulging rejection	Maximum gain (dB)	9	11	10	6.8	7.5
	Minimum gain (dB)	8	2.7	-1	0.38	-2.4
Unclogging at 700s	Maximum level amplitude (mm)	15	17	16	13	13
	Time to reach 95% of the steady-state value (s)	23	5.7	6.5	3.8	3.7

4.5 Internal Model Control IMC

We conclude this study by outlining the Internal Model Control IMC strategy. This section is not intended to give an exhaustive description of this method but only a cursory view of its possibilities. The motivation for considering such technique is that it is already in use in a few plants.

4.5.1 Principle

The Internal Model Control (IMC) strategy relies on the internal model principle [18]. It has the general structure depicted in Fig. 4.42. The process output is compared with the model output, resulting in a signal which will be subtracted from the setpoint. Similarly to the conventional scheme of the Smith predictor, an additional feedback is thus introduced around the controller. They differ only on the block to be included in this feedback. The IMC scheme utilizes the entire model whereas the Smith predictor, dedicated especially to processes with time-delay, incorporates, in addition, another feedback with the delay free part of the plant model $H_0(s)$ (Fig. 4.43).

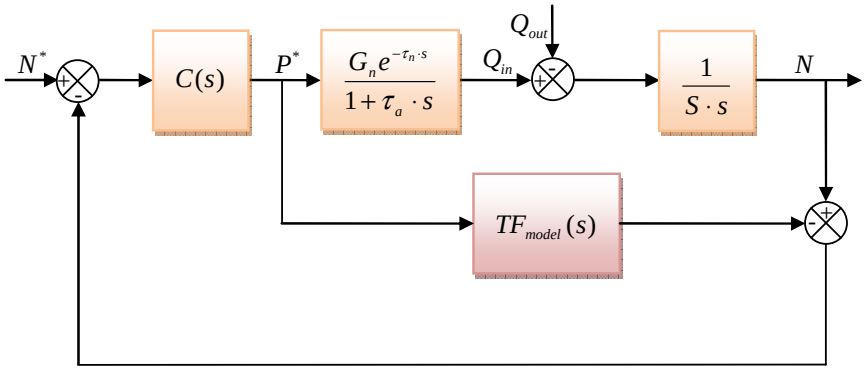

Fig. 4.42. Schematic of the Internal Model Control scheme

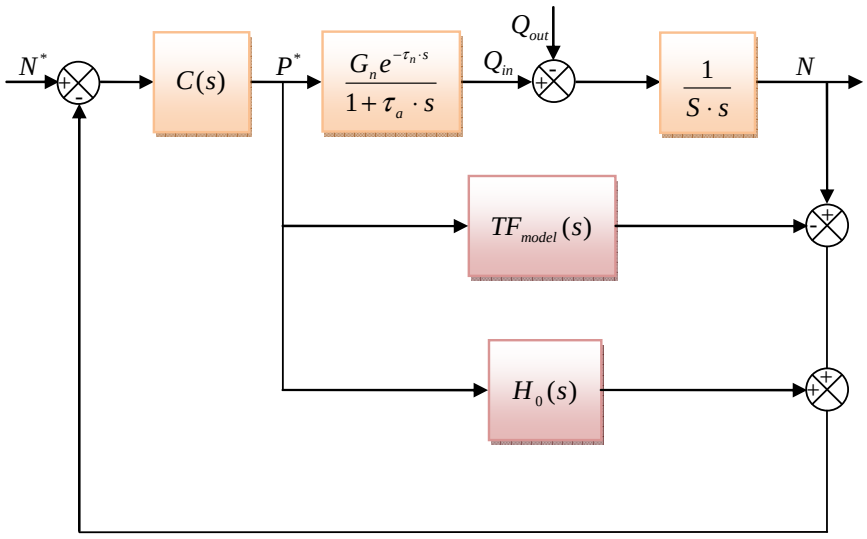

Fig. 4.43. Smith predictor block diagram

We recall that:

$$TF_{model}(s) = H_0(s) \cdot e^{-\tau_n \cdot s} \tag{4.69}$$

From Fig. 4.42, we can see that, if the plant model is exactly identified, the closed loop transfer function is given by:

$$\frac{N}{N^*} = C(s) \cdot TF_{model}(s) \tag{4.70}$$

and the disturbance rejection transfer function for a perfect model is given by:

$$\frac{N}{Q_{out}} = \frac{C(s)\cdot TF_{model}(s) - 1}{S \cdot s} \tag{4.71}$$

In order to improve the robustness of the IMC structure, a low-pass filter is usually added to minimize the discrepancies between process and model behaviors.

4.5.2 Tuning

Considering the process model given in equation (4.41), it is a common practice in the IMC design to do the following factorization into invertible and non-invertible components respectively $TF^{+}_{model}(s)$ and $TF^{-}_{model}(s)$:

$$TF_{model}(s) = \frac{K_{model}}{s\cdot(1+\tau_a \cdot s)} e^{-\tau_n \cdot s} \approx TF^{+}_{model}(s)\cdot TF^{-}_{model}(s)$$

$$\begin{cases} TF^{+}_{model}(s) = \dfrac{K_{model}}{s\cdot(1+\tau_a \cdot s)\cdot\left(1+\dfrac{\tau_n}{2}s\right)} \\ TF^{-}_{model}(s) = 1-\dfrac{\tau_n}{2}s \end{cases} \tag{4.72}$$

where the time-delay term was approximated by a first order Padé function.
The controller $C(s)$ is usually designed as the inverse of the process model in series with a low-pass filter of appropriate order. Here, the order is chosen to be equal to 3 to guarantee a proper transfer function for $C(s)$:

$$H_{filter}(s) = \frac{1}{(1+\tau \cdot s)^3} \tag{4.73}$$

where τ is the filter time constant.
Thus, the controller $C(s)$ is composed of two terms, the inverse of $TF^{+}_{model}(s)$ and the low-pass filter $H_{filter}(s)$:

$$C(s) = (TF^{+}_{model}(s))^{-1} \cdot H_{filter}(s) \tag{4.74}$$

In practice, the IMC scheme of Fig. 4.42 can be rearranged to the following classical form:

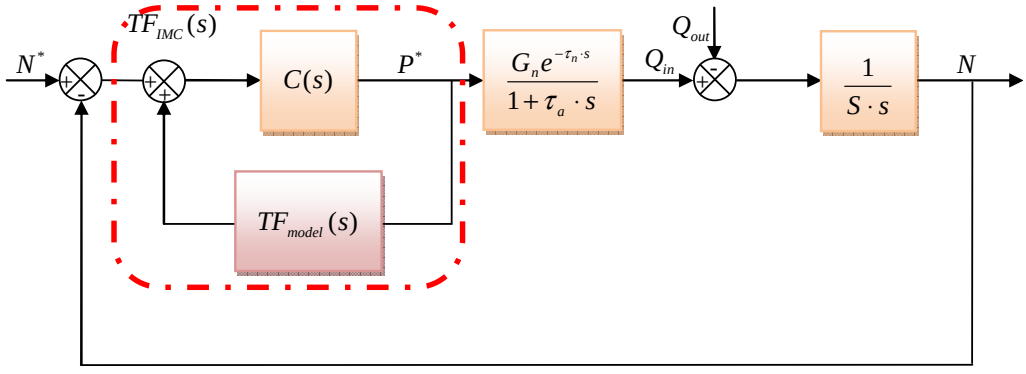

Fig. 4.44. Other form of the IMC Control law

Therefore:

$$TF_{IMC}(s) = \frac{C(s)}{1 - C(s)\cdot TF_{model}(s)} = \frac{(TF^{+}_{model}(s))^{-1}\cdot H_{filter}(s)}{1 - TF^{-}_{model}(s)\cdot H_{filter}(s)} \tag{4.75}$$

In this case:

$$TF_{IMC}(s) = \frac{s \cdot (1 + \tau_a \cdot s) \cdot \left(1 + \frac{\tau_n}{2} s\right)}{K_{model}\left(\left(\frac{\tau_n}{2} + 3\tau^2\right) \cdot s + 3\tau \cdot s^2 + \tau^3 \cdot s^3\right)} \tag{4.76}$$

Note that the IMC controller, designed in this way, does not contain an integral term. As a result, a step disturbance variation will generate a non-zero steady-state error as was proved earlier in case of the initial version of the Smith predictor. To overcome this difficulty, it is convenient for the designer to proceed as follows. The integral term in the plant model should be replaced by a first order system having a large time constant τ^*. The same procedure is then applied on the basis of the two equations (4.73) and (4.74).

$$TF^*_{model}(s) = \frac{K^*_{model}}{(1 + \tau^* \cdot s) \cdot (1 + \tau_a \cdot s)} e^{-\tau_n \cdot s} \approx TF^{*+}_{model}(s) \cdot TF^{*-}_{model}(s)$$

$$\begin{cases} TF^{*+}_{model}(s) = \dfrac{K^*_{model}}{(1 + \tau^* \cdot s) \cdot (1 + \tau_a \cdot s) \cdot \left(1 + \frac{\tau_n}{2} s\right)} \\ TF^{*-}_{model}(s) = 1 - \dfrac{\tau_n}{2} s \end{cases} \tag{4.77}$$

Using equation (4.75), it can be checked easily that this modified model enables the IMC controller to have an integral term, which is needed to cancel the steady-state error aforementioned.
It is important to notice at this point that this modification of the model tends to alter the setpoint response and the disturbance response previously given in (4.70) and (4.71) respectively.
Based on the same philosophy as that of the Aström predictor, other modified versions of the IMC system, giving rise to two-degree of freedom control structures, are reported in literature [88]. One controller is designed to reject the disturbance while the second one is designed to shape the response to setpoint changes. They are, however, outside the scope of this study.
In summary, it can be said that the initial version of the IMC control, which is classically used for stable processes but has serious limitations with the others, tends to perform poorly in case of the mould level control problem.

4.6 Chapter summary

By exploring the mould level control techniques, we can encounter two schools of thought. One is based on disturbance estimation and feed-forward actions such as the strategies developed in chapter 3. This chapter deals with the other techniques focusing on the design of main control law from the error between the measured level and the setpoint. Specifically, a large selection of control laws has been considered, including the PID, the two predictive strategies PFC and GPC, the Smith predictor and its modified version proposed by Aström and finally the Internal Model Control IMC. All the control laws have been examined in terms of closed loop stability, frequency characteristics of the open loop, direct and complementary sensitivities functions, step response, bulging and clogging rejection. Additionally, they have been compared to the PID control law considered here as a reference.

The most striking finding of this comparative study is the functionalities offered by the Aström's modified Smith predictor. Indeed, this structure has the major advantage to decouple the setpoint response from the disturbance rejection by using two controllers. In other words, it avoids degrading the setpoint response in favor of the disturbance response. In this chapter, it was used both to lower the bulging effect on the level and to guarantee appropriate robustness margins. In order to resolve such a design problem and to provide simple directions to non-specialist users, the specifications have been reformulated as a multiple H_∞ constraints problem and optimized using the swarm intelligence technique. The controllers M returned by the H_∞ algorithm are somewhat cumbersome but reduction-order methods may be utilized to reduce the order. At times, they can be approximated by a PID transfer function and can thus be easily implemented in the industrial PLCs.
It is necessary to recall that our approach is completely different from the other ones developed in [19] or [56] where the H_∞ framework has been employed to design the main and unique controller C. In our proposed method, C was set to a constant gain which is sufficient to adjust the closed loop response time.
Compared to the other control laws, it has been demonstrated, through exhaustive simulations, that the Aström predictor yields better performances to a great extent.
Another point to be noted is that it is commonly known that the stability properties of the Smith predictor could be degraded when there is an uncertainty in the delay parameter. Our proposed tuning method provides a solution to this issue because it may satisfy the requirements within a certain delay margin without having to be concerned with the exact identification of the time-delay.
However, it should be implemented if the frequencies of the bulging taking place on the machine are not known precisely or are frequently subject to change. Otherwise, we recommend using the compensation techniques based on the estimation of the bulging effect on the level and its prediction.

In the next chapter, we shall examine another kind of control strategies that is more robust but less obvious than most of the ones presented in this chapter. Indeed, as demonstrated in chapter 3, the gain and the delay of the plant model depend on the water model configuration and probably on the caster configuration in real situation. For example, the delay may vary from 0.1 to 2s. As a consequence, all the studied control laws would not be able to stabilize the mould level over this variation interval. The proposed solution based on the so-called RMMAC architecture would not only make it possible, it also provides the operators with some useful signals in order to pinpoint accurately the gain and the delay variations.

CHAPTER 5
Robust adaptive control – RMMAC architecture

5.1 Introduction

This chapter introduces adaptive methods for designing robust controllers to deal with the uncertain parameters and to counter the effects of disturbances that arise in the continuous casting process. As demonstrated in chapter 3, the gain G_n and the delay τ_n of the plant model change with the machine configuration. The aim of this chapter is to develop an adaptive control law knowing that all the control laws considered in chapter 4 are not able to stabilize the mould level over the entire parameters uncertainties.

In order to place our discussions within a general context of robust control, we are going to remind some of the most useful definitions in the robust control theory. In the first place, the word 'robust' refers to the capability of the controller to meet the posed performance specifications in the presence of process-model mismatch. Indeed, this may happen if the process is not accurately identified or when the process moves to another operating point. The word 'adaptive' refers to the controllers designed in such a way that the control law is modified, whenever necessary, to cope with changing conditions. They do not need, however, a priori information about time-varying parameters.

The first stage of robust control design is to ensure both nominal stability and nominal performance, i.e. that the controller will stabilize the process model and achieve the desired performances. The second stage consists of verifying the robust stability and the robust performance features before applying the controller to the real process. The cost for stability robustness is inevitably poorer performance.

There are several approaches for robust adaptive control. The vast majority of them deal with the case of constant uncertain parameters. In the case of mould level control, the plant model parameters are uncertain and may vary depending on the caster configuration as demonstrated in chapter 3. Such control problem has been addressed efficiently by M. Athans and S. Fekri through a robust adaptive control method so-called Robust Multiple-Model Adaptive Control RMMAC [20] [21] [90].

In this chapter, we shall apply the RMMAC structure to enhance the bulging rejection function. We are interested in this architecture because it deals with slowly varying parameters. More importantly, it answers, in a systematic way, the classical issues related to the need of adaptive control, the number of models, the controllers and the identification part synthesis.

This chapter is organized as follows. Section 2 introduces the multiple-model structures for designing state estimators and feedback controllers. Included is a brief description of the RMMAC architecture.

In section 3, relevant background material about robust stability and robust performance is given. This section also contains the complex-μ synthesis which synthesizes a robust controller via the *D-K* algorithm used when there are no real parameter uncertainties and the mixed-μ synthesis based on the *D,G-K* algorithm dealing with combined real and complex uncertainties.

Since it is central to our control strategy, the design of the RMMAC structure will be fully treated in section 4. We will present also different representative simulation results in order to evaluate the usefulness of the RMMAC compared to the best non-adaptive control law.

Finally, this chapter concludes with several suggestions and some critical issues related to the RMMAC design.

5.2 Multiple-model structures

In this section, we present a literature overview on multiple-model control structures that are at the heart of the main technical results of this doctoral dissertation. In analyzing these structures, it is especially useful to distinguish between two types: the first one is designed to estimate the state of the system while the other is used as the main controller of the process. Therefore, this analysis is carried out in two subsections, each of which is devoted to explaining one of the two types.

5.2.1 Multiple-Model Adaptive Estimation MMAE

From the outset, the MMAE architecture has been introduced to address the state estimation problems characterized by a significant parameter uncertainty [89]. It provides indeed an adaptive estimation of the uncertain parameters by means of a set of n distinct Kalman filters and a Posterior Probability Evaluator PPE.
This subsection explains briefly the fundamental concepts of the MMAE. The reader is referred to [89] for an exhaustive coverage of the literature in this field.
The general block structure is given in Fig. 5.1. Roughly speaking, the Kalman filters generate the state estimates $\hat{x}_k(t)$ for $k=1,2,\ldots,n$, which are combined with the posterior probabilities $P_k(t)$ computed by the Posterior Probability Evaluator PPE in order to calculate an estimate of the overall plant state through the expression:

$$\hat{x}(t)=\sum_{k=1}^{n} P_k(t)\cdot\hat{x}_k(t) \tag{5.1}$$

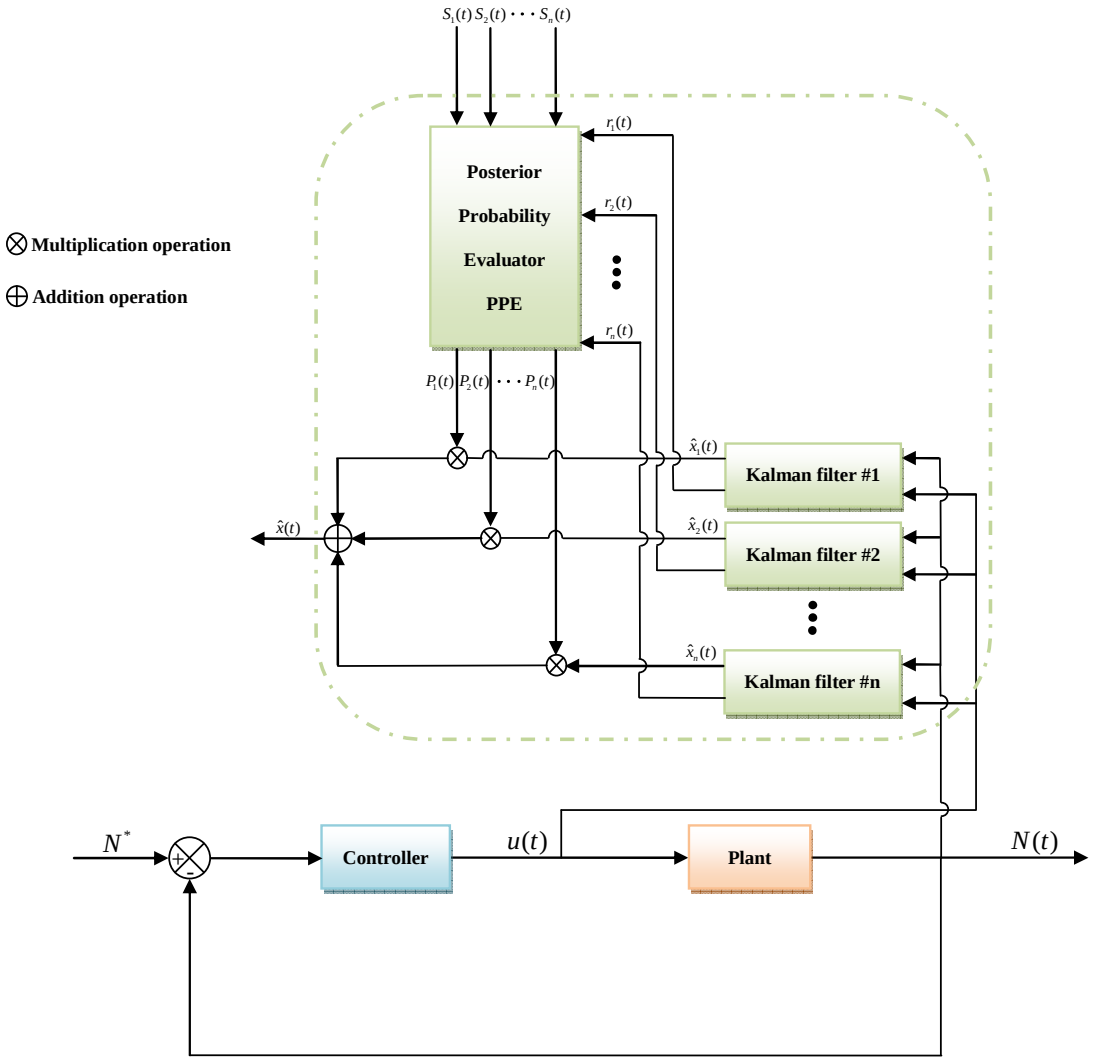

Fig. 5.1. MMAE architecture

The probabilities $P_k(t)$, corresponding to the fact that the model k generates the plant output $N(t)$, are computed from the residuals $r_k(t)$ and the residual covariances $S_k(t)$ (Fig. 5.1). In Kalman filter theory, the residual or the innovation is the discrepancy between the actual and the predicted values of the measurement. $P_k(t)$ are also used to select the right model or the closest one if the true plant does not belong to the model set.
Let us suppose that n discrete-time plant models are known:

$$\begin{cases} x_k(t+1) = A_k x_k(t) + B_k u(t) + F_k w_{WN}(t) \\ y_k(t) = C_k x_k(t) + v_{WN}(t) \end{cases} \tag{5.2}$$

with:

- k : the model index,
- w_{WN} : the Gaussian process white noise,
- v_{WN} : the Gaussian measurement white noise.

$w_{WN}(t)$ and $v_{WN}(t)$, whose covariances are given in (5.3), are assumed to be independent of each other and uncorrelated with $x_k(j)$, $\forall j \le t$.

$$\begin{cases} \mathrm{E}\left(w_{WN}(t) \cdot w_{WN}(t)^T\right) = Q_k \\ \mathrm{E}\left(v_{WN}(t) \cdot v_{WN}(t)^T\right) = R_k \end{cases} \tag{5.3}$$

Additionally, we will make use of the following notation:

$$\begin{cases} \hat{x}_k(t|t) = \mathrm{E}\left(x_k(t) | u(0)\cdots u(t-1), y(1)\cdots y(t)\right) \\ \Phi_k(t|t) = \mathrm{E}\left((x_k(t) - \hat{x}_k(t|t)) \cdot (x_k(t) - \hat{x}_k(t|t))^T | u(0)\cdots u(t-1), y(1)\cdots y(t)\right) \end{cases} \tag{5.4}$$

The problem of synthesizing a steady-state Kalman filter is, most of the time, fully solved through two cycles. The predict cycle estimates the state at time $t+1$, denoted by $\hat{x}_k(t+1|t)$, and the associated covariance matrix Φ_k^p using the measurements collected up to time t and the control inputs available up to time $t-1$.

$$\begin{cases} \hat{x}_k(t+1|t) = A_k \hat{x}_k(t|t) + B_k u(t) \\ \hat{y}_k(t+1|t) = C_k \hat{x}_k(t+1|t) \\ r_k(t+1) = y_k(t+1) - \hat{y}_k(t+1|t) \end{cases} \tag{5.5}$$

$$\begin{cases} \Phi_{k-1}^p = A_k \Phi_k A_k^T + F_k Q_k F_k^T \\ S_k = \mathrm{cov}(r_k(t+1), r_k(t+1)) = C_k \Phi_{k-1}^p C_k^T + R_k \end{cases}$$

During the update cycle, the objective is to compute the Kalman gain, the a posteriori state estimate and the a posteriori error covariance estimate via (5.6).

$$\begin{cases} K_k = \Phi_{k-1}^p C_k^T S_k^{-1} \\ \hat{x}_k(t+1|t+1) = \hat{x}_k(t+1|t) + K_k r_k(t+1) \\ \Phi_k = \Phi_{k-1}^p - \Phi_{k-1}^p C_k^T S_k^{-1} C_k \Phi_{k-1}^p \end{cases} \tag{5.6}$$

Fig. 5.2 illustrates this algorithm.

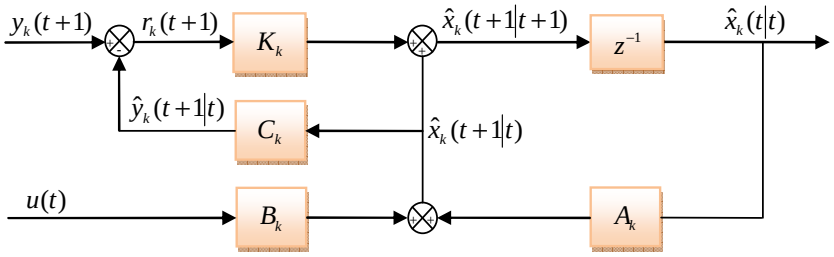

Fig. 5.2. Discrete-time Kalman filter block diagram

Let us now model the fact that the k^{th} model is the one generating the plant output $N(t)$ by a hypothesis random variable H_k :

$$H_k \in \{H_1, H_2, \cdots, H_n\} \tag{5.7}$$

The posterior probabilities $P_k(t)$ are defined in such a way that they satisfy:

$$P_k(t) \geq 0, \quad \sum_{k=1}^{n} P_k(t) = 1$$

$$\begin{cases} P_k(0) = \text{Prob}(H = H_k) \\ P_k(t) = \text{Prob}(H = H_k \,|\, u(0)\cdots u(t-1), y(1)\cdots y(t)) \end{cases} \tag{5.8}$$

Using Bayes rule and assuming that the model set includes the true plant, we obtain the following formula where $p(y(t+1)|u(t),Y(t))$ is a conditional probability density function [89]:

$$P_k(t+1) = \frac{p(y(t+1)|u(t),H_k,Y(t))}{p(y(t+1)|u(t),Y(t))} P_k(t) \tag{5.9}$$

with $Y(t) = (u(0)\cdots u(t-1), y(1)\cdots y(t))$

Using the marginal density and Bayes rule once more, we can prove that:

$$p(y(t+1)|u(t),Y(t)) = \sum_{i=1}^{n} P_i(t) \cdot p(y(t+1)|u(t),H_i,Y(t)) \tag{5.10}$$

By substituting (5.10) back into (5.9), it follows:

$$P_k(t+1) = \frac{p(y(t+1)|u(t),H_k,Y(t))}{\sum_{i=1}^{n} P_i(t) \cdot p(y(t+1)|u(t),H_i,Y(t))} P_k(t) \tag{5.11}$$

There is a need therefore to calculate $p(y(t+1)|u(t),H_k,Y(t))$. It turns out that this density function is Gaussian with mean:

$$\text{E}(y(t+1)|u(t),H_k,Y(t)) = C_k \hat{x}_k(t+1|t) \tag{5.12}$$

and steady-state covariance:

$$\text{cov}(y(t+1),y(t+1)|u(t),H_k,Y(t)) = C_k \Phi_k^p C_k^T + R_k = S_k \tag{5.13}$$

We deduce that [89]:

$$p(y(t+1)/u(t),H_k,Y(t)) = \frac{1}{\sqrt{2\pi \det(S_k)}} e^{-\frac{1}{2} r_k(t+1)\cdot S_k^{-1}\cdot r_k(t+1)} \tag{5.14}$$

In closing, we conclude from the equations (5.11) and (5.14) the general recursive formula of the posterior probabilities, implemented in the Posterior Probability Evaluator PPE:

$$\begin{cases} P_k(t+1) = \dfrac{\dfrac{1}{\sqrt{2\pi \det(S_k)}} e^{-\frac{1}{2} r_k(t+1)\cdot S_k^{-1}\cdot r_k(t+1)}}{\sum_{i=1}^{n} \dfrac{P_i(t)}{\sqrt{2\pi \det(S_i)}} e^{-\frac{1}{2} r_i(t+1)\cdot S_i^{-1}\cdot r_i(t+1)}} P_k(t) \\ P_k(0) = \dfrac{1}{n} \end{cases} \tag{5.15}$$

We stress that the above results are valid only if the true plant belongs to the model set. If it is not the case, the identification subsystem should converge to the closest model of the set in an information metric sense. This can be accomplished using either the Baram Proximity Measure BPM [95] or the Kullback information distance as reported in [20] and [94]. Nevertheless, our perspective is to implement the RMMAC architecture which relies on the first distance to identify the nominal values for each subset.

5.2.2 Multiple-Model Adaptive Control MMAC

This subsection reviews the literature on multiple-model adaptive control. We shall give a brief description of the most common structures including the Robust Multiple-Model Adaptive Control RMMAC which will be extensively described in the fourth section of this chapter.

5.2.2.1 Classical Multiple-Model Adaptive Control CMMAC

The classical MMAC architecture combines process identification and control as shown in Fig. 5.3. It takes advantage of MMAE strategy benefits coupled with the Linear Quadratic Gaussian LQG design. More precisely, it is composed from a set of Kalman filters and LQ controllers.

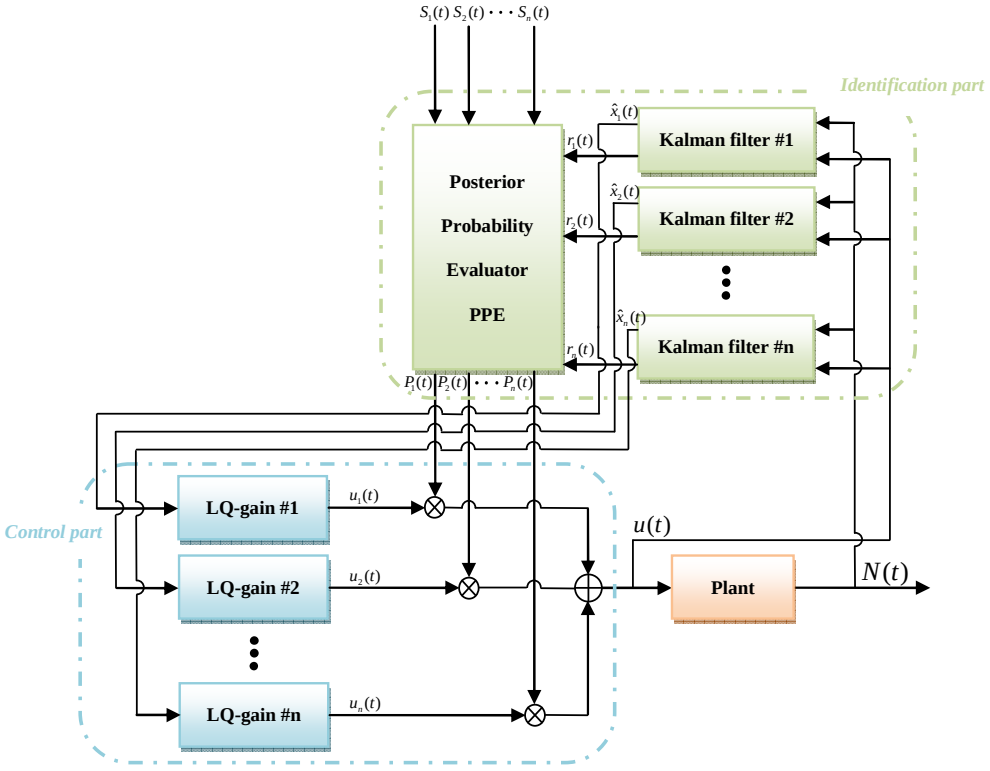

Fig. 5.3. CMMAC architecture

Each local controller generates a local control input $u_k(t)$ by multiplying the state estimate of each Kalman filter by the LQ-gain, i.e.:

$$u_k(t) = -G_{LQ} \cdot \hat{x}_k(t/t) \tag{5.16}$$

The global control input $u(t)$ is then calculated by weighting each local control signal $u_k(t)$ by its associated posterior probability $P_k(t)$ as follows:

$$u(t) = \sum_{k=1}^{n} P_k(t) \cdot u_k(t) \tag{5.17}$$

These equations show that there exists no separation between the identification part and the control part. Indeed, the control input applied to the process strongly depends on the probabilities computed by the identification part. Furthermore, the local control inputs are derived from the state estimates.

Finally, it is important to notice that there exists a switching version of the CMMAC where one unique local controller, corresponding to the largest posterior probability, is selected as the global control input. For a more detailed exposition on this subject see [91] [92].

5.2.2.2 Supervisory Switching Multiple-Model Adaptive Control SMMAC

Unlike the CMMAC architecture, the SMMAC is not an extension of the MMAE architecture even if it is composed of an identification part. In reference to Fig. 5.4, the SMMAC utilizes a set of estimators based on Luenberger observer and a set of controllers of any structure. In addition to these two banks, the SMMAC incorporates a monitoring signal generator and a dwell-time switching block. The first block generates the monitoring signals from the estimation errors $e_k(t)$ while the second provides the signal used to select the appropriate controller. It is worthwhile to note that $e_k(t)$ are the equivalent of the residuals $r_k(t)$ in the MMAE architecture.

Detailed analysis and discussions may be found in [60] [61].

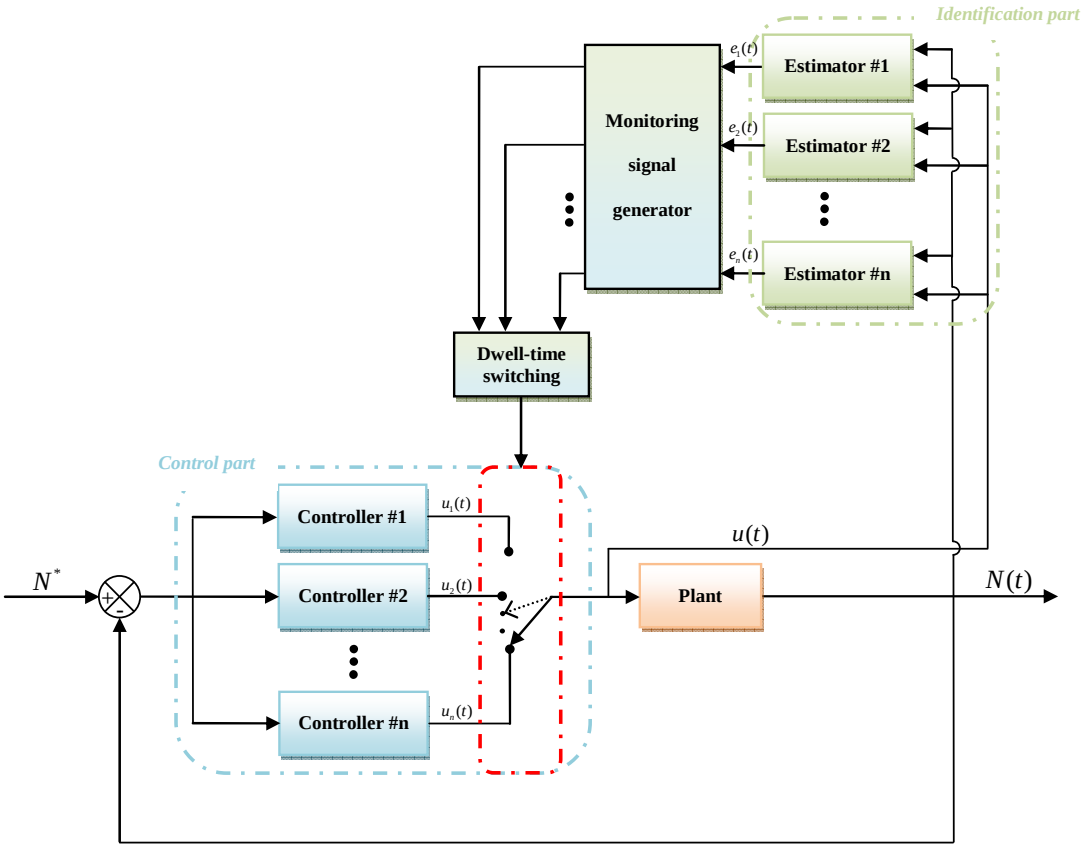

Fig. 5.4. SMMAC architecture

The dwell-time is introduced to avoid rapid switching between the controllers by maintaining a constant output over a period of time.

Because the signal generated by the switching logic is not explicitly taken into account in the global control input, we can assert that the SMMAC architecture performs a separation between the identification part and the control part contrary to CMMAC and RMMAC.

In [62], it is suggested to use the hysteresis switching. It consists of enabling the switch to another controller when the monitoring signal, corresponding to the controller currently in use, exceeds the smallest monitoring signal by a pre-defined factor.

5.2.2.3 Robust Multiple-Model Adaptive Control RMMAC

The third MMAC architecture so-called RMMAC is at the heart of this chapter. It has the same block diagram as the CMMAC but fundamental differences exist between the two structures, in particular with regard to the control part (Fig. 5.5). Indeed, the local control inputs are not computed from the state estimates but using the μ synthesis. This has profound implications for the RMMAC performances. Moreover, with the help of a precise definition of robust performance requirements, the number of models, estimators and controllers are readily derived. More importantly, the RMMAC combines the robust non-adaptive mixed-μ synthesis and the stochastic hypothesis testing concepts.

The notation and the notions we will present along this chapter are essentially taken from [90] where all the material about RMMAC can be found.

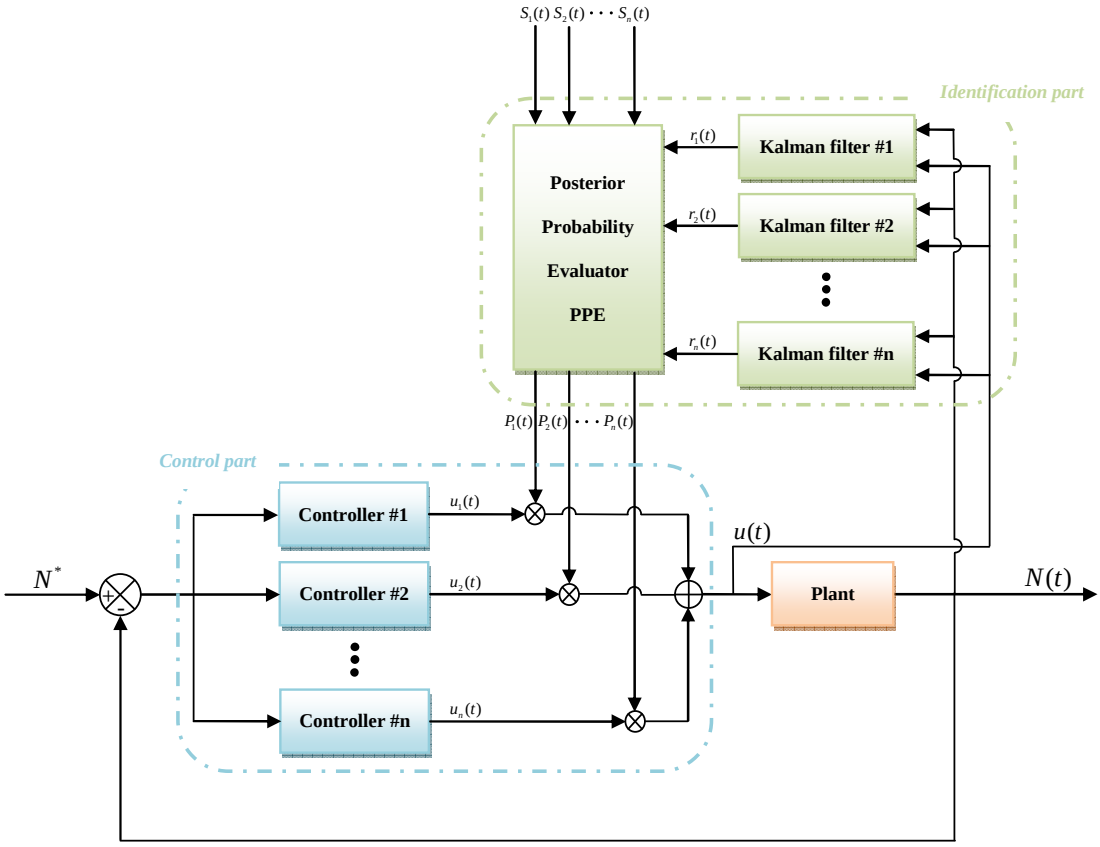

Fig. 5.5. RMMAC architecture

In the RMMAC design, the Kalman filters are only used to generate the residuals $r_k(t)$. The state estimates are not needed contrary to the CMMAC which calculates the local control inputs on the basis of them. Other distinguishing features of the RMMAC lie in its ability to address efficiently the issues about the selection of the number of models and the development of Kalman filters. Namely, the RMMAC designer proceeds as follows:

- The number of models is determined using the Global Non-Adaptive Robust Compensator GNARC and the Fixed Non-Adaptive Robust Compensator FNARC designs and the mixed-μ synthesis as we will see in the third section of this chapter. During this stage, the mixed-μ synthesis generates also the set of controllers so-called the Local Non-Adaptive Robust Compensators LNARCs in RMMAC terminology.
- To implement the Kalman filters, nominal values of the uncertain parameters should be chosen for each model. They are identified using the Baram Proximity Measure BPM to ensure the convergence of the posterior probabilities.

5.3 Structured singular value

As we shall see in the next section, the RMMAC methodology hinges upon the so-called mixed-μ synthesis to determine the size and the boundaries of each parameter subset as well as the associated controller. This section summarizes some important elements of the structured singular value μ currently employed in modern robust control. Included is a description of both the complex-μ synthesis and the mixed-μ synthesis. Because the parameter uncertainties of the mould level control system are real, the complex-μ synthesis can be conservative and therefore the performances of the controllers, designed using this technique, would be inferior. To overcome this shortcoming, one needs to utilize the mixed-μ synthesis, which deals with both real and complex uncertainties, in order to maximize the performances.

5.3.1 Uncertainty representations

This paragraph presents the underlying concepts upon which the μ synthesis methodology is based. First, we need to establish some notations and definitions. In the robust control literature, the uncertainties encountered are represented in two different forms: unstructured and structured uncertainty. In the first form often used to take into account unmodeled dynamics of the system in order to derive simple models, all the uncertainties are merged into a single complex uncertainty matrix $\Delta(s)$ leading to a conservative uncertainty description. With the structured uncertainty however, all the uncertainties are represented separately and merged into a single block diagonal uncertainty matrix as defined in equation (5.18).

$$\underline{\Delta} = \left\{ \begin{array}{l} \Delta = \mathrm{diag}(\Delta_1,\ldots,\Delta_q,\delta_1 I_{r_1},\ldots,\delta_r I_{r_r},\varepsilon_1 I_{c_1},\ldots,\varepsilon_c I_{c_c}) \in \mathrm{C}^{k\times k} \\ \Delta_i \in \mathrm{C}^{k_i\times k_i} \quad ; \quad \delta_i \in \Re \quad ; \quad \varepsilon_i \in \mathrm{C} \end{array} \right\} \tag{5.18}$$

with:

- Δ_i : stable matrix of any structure,
- $\mathrm{C}^{k\times k}$: the field of complex matrices with k rows and k columns,
- $\Re$: the set of real numbers,
- C : the set of complex numbers.

The scalars δ_i and ε_i are repeated r_i and c_i times respectively.
Most of the time, the uncertainties are normalized such as:

$$\|\Delta\|_\infty < 1 \quad \Leftrightarrow \quad \|\Delta_i\|_\infty < 1 \quad ; \quad |\delta_i| < 1 \quad ; \quad |\varepsilon_i| < 1 \tag{5.19}$$

Henceforth, we will restrict our attention only to the structured uncertainty description upon which the structured singular value is based. Indeed, when the structured uncertainties are specified, the structured singular value may be used as a measure of the stability robustness and the performance robustness of a system. More precisely, as we shall see in the next paragraph, to test the stability of a system is equivalent to test a non-conservative condition on the structured singular value of a portion of the transfer function matrix.
The definition of the structured singular value μ depends only upon the block structure of the uncertainties. Namely, the structured singular value of a matrix M with respect to a block structure $\underline{\Delta}$ is given at each frequency by:

$$\left\{ \begin{array}{l} \mu_{\underline{\Delta}}(M) = (\inf_{\Delta\in\underline{\Delta}} (\bar{\sigma}(\Delta) : \det(I - \Delta\cdot M) = 0))^{-1} \\ \mu_{\underline{\Delta}}(M) = 0 \quad \text{if} \quad \forall \Delta \in \underline{\Delta} \quad \det(I - \Delta\cdot M) \neq 0 \end{array} \right. \tag{5.20}$$

with:

- $\bar{\sigma}$: the largest singular value of a matrix,
- M : a square complex matrix,
- det : the determinant of a square matrix,
- I : the identity matrix.

The notation used is fairly standard as may be found in the literature.

The remaining question is how to compute $\mu_{\underline{\Delta}}(M)$. We can note that the formula given in (5.20) is not useful except for low dimensional problems. A practical solution consists of determining an upper and a lower bound. In some cases, they are guaranteed to be quite tight. For a general μ problem, tightness can be severely degraded.

5.3.2 Stability and performance robustness

5.3.2.1 Robust stability

In order to evaluate robust stability using the structured singular value function, the model must be in the LFT form as illustrated in Fig. 5.6 where y is the performance output, w is the model input which includes the setpoint and the disturbances, z_Δ and v_Δ are the input and the output of the uncertainty model Δ respectively.

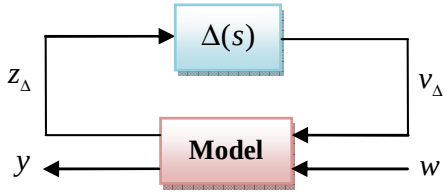

Fig. 5.6. LFT form of the uncertain model

Assuming that the nominal system $M(s)$, which corresponds to an uncertainty Δ equal to zero, is stable, the only source of instability in the LFT form may come from the matrix feedback interconnection depicted in Fig. 5.7.

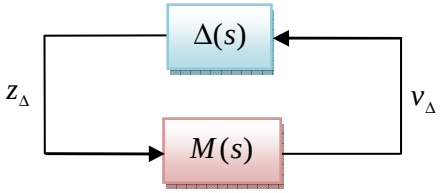

Fig. 5.7. General structure for robust stability analysis

We can then use the following theorem, also known as μ analysis, which provides a necessary and sufficient condition for robust stability [23]. Namely, the system shown in Fig. 5.7 is stable for all Δ with a H_∞ norm bounded by 1 if and only if:

$$\forall \omega \quad \mu_{\underline{\Delta}}(M(j\omega)) < 1 \tag{5.21}$$

This theorem could be interpreted as a generalized small gain theorem, already presented and used in chapter 4, which takes onto account the structure of Δ. Thus, we can evaluate the robustness properties of the system by analyzing the frequency characteristics of μ. The peak value of μ determines the size of uncertainties we can tolerate without destabilizing the system. In other words, the structured singular value can be used to quantify the robustness margins. More precisely, its upper bound guarantees stability for a given range of uncertainties while its lower bound yields a sufficient condition for system instability.

As mentioned above, the computation of the exact structured singular value is not necessary. Only the upper bound is needed.

Efficient software is available for the computation of this bound. The routines developed by G.J. Balas have been found to compute tight upper bounds and have been thereby widely used. They are based on an optimization problem subject to several Linear Matrix Inequality LMI constraints [93].

5.3.2.2 Robust performance

We now wish to consider the problem of robust performance which is another property of the closed loop system. Indeed, after ensuring the stability of the system, the next step is to check the performance objectives for all possible uncertainties.

First, we place the problem in a standard robust performance framework as shown in Fig. 5.8 where W_1 is a scalar transfer function introduced as a weighting function in order to shape the frequency characteristics of the transfer function between the model output y and the input w.

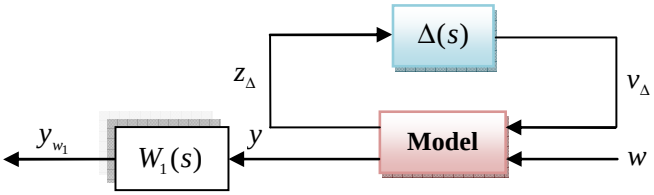

Fig. 5.8. General block diagram for robust performance analysis

Therefore, robust performance is achieved if the following inequality holds for all Δ with a norm bounded by 1:

$$\forall \omega \quad \bar{\sigma}(TF_{yw}(j\omega)) \le \frac{1}{|W_1(j\omega)|} \qquad \Leftrightarrow \qquad \forall \omega \quad \bar{\sigma}\left(W_1(j\omega)\cdot TF_{yw}(j\omega)\right) \le 1 \tag{5.22}$$

According to the small gain theorem, this condition is satisfied if and only if the system depicted in Fig. 5.9 is stable for all Δ_f with a norm bounded by 1 where Δ_f is a full complex matrix of appropriate dimensions.

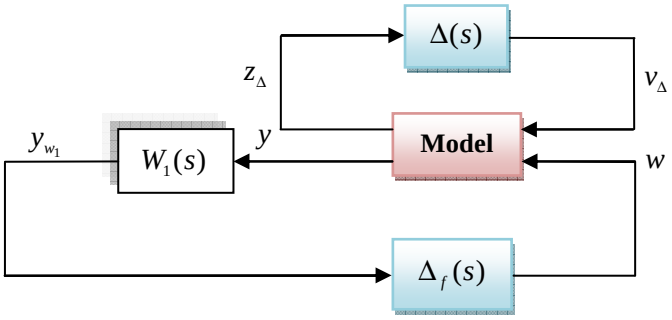

Fig. 5.9. Block diagram for testing robust performance

The structure of the uncertainties is now given by:

$$\underline{\Delta}^{f} = \left\{ \begin{matrix} \Delta^{f} = \mathrm{diag}(\Delta, \Delta_f) \\ \Delta \in \underline{\Delta} \quad ; \quad \Delta_f \in \mathbb{C}^{k_f \times k_f} \end{matrix} \right\} \tag{5.23}$$

The robust performance scheme of Fig. 5.9 can be rearranged into the following block diagram:

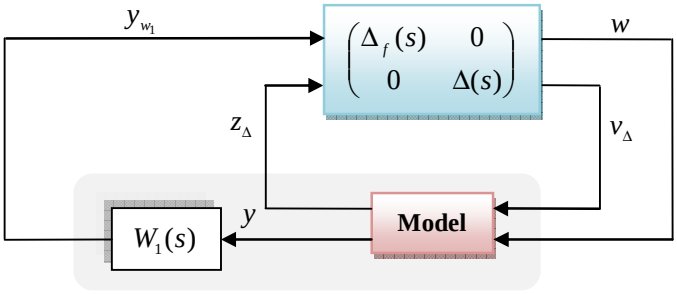

Fig. 5.10. Block diagram for testing robust stability

Therefore, equation (5.22) is equivalent to:

$$\forall \omega \quad \mu_{\underline{\Delta}_f}(M(j\omega)) < 1 \tag{5.24}$$

Thus, through simple rearrangements, we can convert robust performance problem into the standard μ analysis setup of Fig. 5.10.
In control theory, the structured singular value seems to be an adequate tool for evaluating both robust stability and robust performance.

5.3.3 Complex-μ synthesis

Prior to considering the mixed-μ synthesis problem, we begin with a brief review of the problem of synthesizing a controller to meet the posed performance specifications in the presence of uncertain parameters so-called μ synthesis problem. Such controller guarantees thus both stability and performance robustness.
Let us place the problem in a standard setup as shown in Fig. 5.11 where the uncertainty block $\Delta(s)$ contains the uncertain real and complex parameters as well as the unmodeled dynamics. The model is assumed here to contain all the appropriate weights for the problem (e.g. W_1 in Fig. 5.8).

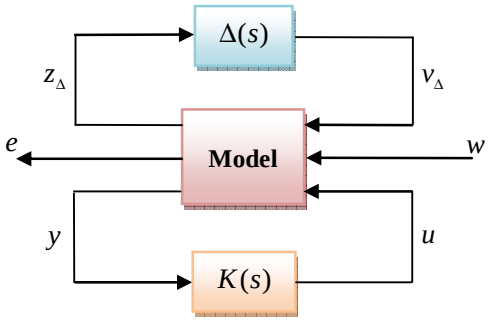

Fig. 5.11. μ synthesis setup

As in the analysis of the robust performance, the problem can be converted into a standard μ analysis problem as shown in Fig. 5.12 where Δ_f is a full complex matrix. This is accomplished by absorbing the controller $K(s)$ into $TF_{model}(s)$ to define the transfer function $F_l(TF_{model}(s), K(s))$.

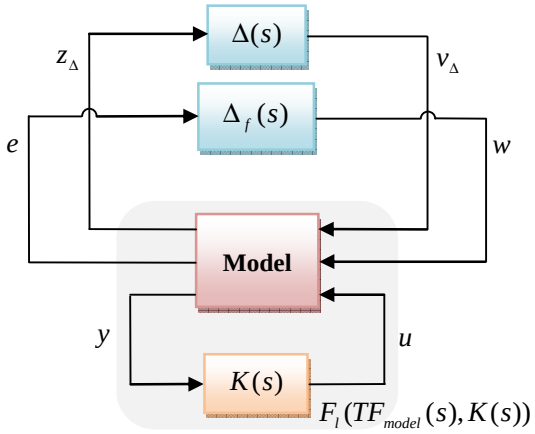

Fig. 5.12. Standard framework for μ analysis

Accordingly, the μ synthesis problem is equivalent to finding a controller $K(s)$ achieving:

$$\forall \omega \quad \mu_{\underline{\Delta}^f}(F_l(TF_{model}(j\omega), K(j\omega))) \le 1 \tag{5.25}$$

Rather than solving the complex-μ synthesis, we consider in practice the problem obtained by replacing μ by its upper bound given in (5.26).

$$\forall \omega \quad \mu_{\underline{\Delta}^f}(F_l(TF_{model}(j\omega), K(j\omega))) \le \overline{\sigma}(D(\omega) \cdot F_l(TF_{model}(j\omega), K(j\omega)) \cdot D^{-1}(\omega)) \tag{5.26}$$

Equation (5.26) holds for any matrix D_ω that commutes with the structure $\underline{\Delta}^f$.
This modified problem is then solved by means of an iterative algorithm so-called *D-K* iteration for which Matlab solvers are available [93]. Such a procedure alternates convex problems and standard H_∞ problems.
In reference to Fig. 5.13, if we fix the transfer matrix $D(\omega)$, finding $K(j\omega)$ is a standard H_∞ problem. On the other hand, if we fix a real rational proper controller $K(j\omega)$, then the problem of finding $D(\omega)$ reduces to calculate the μ upper bound using (5.26) for a set of $D(\omega)$ matrices at certain frequency points and fit a stable transfer matrix to them.

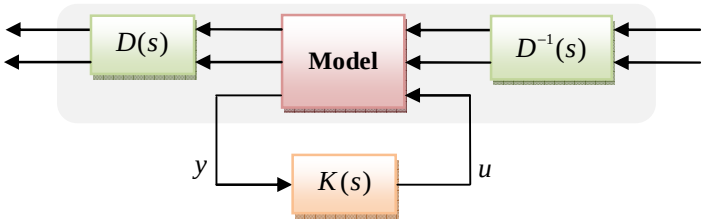

Fig. 5.13. H_∞ standard problem for complex-μ synthesis

We obtain thus the following *D-K* iteration scheme [25] [96]:

[step 1] Find an initial set of the scaling matrices $D(\omega)$ pointwise across frequency. For instance, one can use the identity matrix.

[step 2] Find a stable transfer matrix $D(s)$ fitting the scaling matrices $D(\omega)$, so that $D(j\omega)$ approximates $D(\omega)$ and $D^{-1}(s)$ is stable.

[step 3] Find the optimal feedback controller $K(s)$ solving the H_∞ problem:

$$\left\| D(s) \cdot F_l(TF_{model}(s), K(s)) \cdot D^{-1}(s) \right\|_\infty < 1 \tag{5.27}$$

[step 4] At a set of frequency points, find a matrix $\hat{D}(\omega)$ minimizing the μ upper bound i.e. solving:

$$\inf_{D(\omega)} \overline{\sigma}(D(\omega) \cdot F_l(TF_{model}(j\omega), K(j\omega)) \cdot D^{-1}(\omega)) \tag{5.28}$$

which is a convex problem and can be efficiently solved.

[step 5] Compare $\hat{D}(\omega)$ with those obtained in the previous iteration. If they are close, the algorithm terminates, otherwise return to [step 2].

Note that the *D-K* iteration algorithm is not guaranteed to converge to the global optimum albeit the μ upper bound and the H_∞ control problems are convex. However, it has shown good performances in many design problems [26] [27]. Another point to be noted here is that this methodology does not allow specifying real parameter uncertainties. All the uncertain parameters are considered to be complex, which may lead to conservative conclusions and so inferior performance improvement. This is the reason why we shall focus upon the mixed-μ synthesis which removes this restriction.

5.3.4 Mixed-μ synthesis

In this paragraph, a summary of the key concepts of the mixed-μ synthesis is presented. References [23] [24] [64] contain however extensive theoretical details.

We are interested in this algorithm because our plant model includes three real uncertainties respectively in the gain, the delay and in the actuator time constant. Accordingly, the complex-μ synthesis would provide conservative controllers. The mixed-μ synthesis however offers the designer the possibility to distinguish between real and complex uncertainties and hence to synthesize controllers with enhanced performance.

As we shall see in the next section, the mixed-μ synthesis is central to the RMMAC architecture and will be carried out, whenever necessary, using the advanced software provided to us by G.J. Balas [22].

In the mixed-μ framework, the uncertainty block Δ contains repeated real scalars δ_i^r, repeated complex scalars δ_i^c and full complex blocks Δ_i and this defines the set of allowable uncertainties as follows:

$$\aleph = \left\{ \begin{array}{l} \mathrm{diag}(\delta_1^r I_{k_1}, \ldots, \delta_{n_r}^r I_{k_{n_r}}, \delta_1^c I_{k_{n_r+1}}, \ldots, \delta_{n_c}^c I_{k_{n_r+n_c}}, \Delta_1, \ldots, \Delta_q) \\ \delta_i^r \in \Re \quad ; \quad \delta_i^c \in \mathrm{C} \quad ; \quad \Delta_i \in \mathrm{C}^{k_{n_r+n_c+i} \times k_{n_r+n_c+i}} \end{array} \right\} \tag{5.29}$$

Similarly to the complex-μ synthesis, the mixed-μ procedure exploits the fact that the value of μ, which is difficult to compute, is close to its upper bound.
First, let us recall some fairly standard notations:

$$D_s = \left\{ \begin{matrix} \text{diag}(D_1,\ldots,D_{n_r+n_c},d_1 I_{k_{n_r+n_c+1}},\ldots,d_{n_c} I_{k_{n_r+n_c+q}}) \\ d_i \in \mathrm{C}, d_i \neq 0 \quad ; \quad D_i \in \mathrm{C}^{k_i \times k_i}, \det(D_i) \neq 0 \end{matrix} \right\} \tag{5.30}$$

$$G_s = \left\{ \begin{matrix} \text{diag}(G_1,\ldots,G_{n_r},0 I_{k_{n_r+1}},\ldots,0 I_{k_{n_r+n_c+q}}) \\ G_i \in \mathrm{C}^{k_i \times k_i} \quad ; \quad G_i = G_i^* \end{matrix} \right\} \tag{5.31}$$

where G_i^* is the complex conjugate transpose of G_i.
By introducing G_s, the mixed-μ synthesis takes advantage of the presence of real uncertainties contrary to the complex-μ synthesis which approximates them by complex ones.
Now for any complex matrix M, we have:

$$\mu(M) \leq \inf_{D \in D_s, G \in G_s} \inf_{\beta \in \Re, \beta > 0} \left\{ \beta : \overline{\sigma}\left(\left(\frac{DMD^{-1}}{\beta} - jG \right) \cdot (I + G^2)^{-\frac{1}{2}} \right) \leq 1 \right\} \tag{5.32}$$

Therefore, the mixed-μ problem can be replaced by the following synthesis problem where K_s is the set of real proper controllers which nominally stabilize TF_{model}:

$$\inf_{K \in K_s} \quad \sup_{\omega \in \Re} \quad \inf_{D(\omega) \in D_s, G(\omega) \in G_s} \quad \inf_{\beta(\omega) \in \Re, \beta(\omega) > 0} \{\beta(\omega) : \Gamma \leq 1\}$$

with:

$$\Gamma = \overline{\sigma}\left(\left(\frac{D(\omega) \cdot M(TF_{model}(j\omega), K(j\omega)) \cdot D^{-1}(\omega)}{\beta(\omega)} - jG(\omega) \right) \cdot (I + G^2(\omega))^{-\frac{1}{2}} \right) \tag{5.33}$$

It follows that if we fix $K(j\omega)$, the problem of finding $D(\omega)$, $G(\omega)$ and $\beta(\omega)$ is essentially the μ upper bound convex problem. On the other hand, for fixed D, G and β, finding K is merely a standard H_∞ problem. This leads to the following *D,G-K* iteration scheme [97]:

[step 1] Find initial estimates of the scaling matrices $D(\omega)$, $G(\omega)$ and the scalar $\beta(\omega)$. For instance, one can choose $D(\omega)$ as the identity matrix, $G(\omega)$ to be the zero matrix and β^* equal to unity ($\beta = \beta^*$).

[step 2] Find the transfer matrices $D(s)$ and $G(s)$ fitting respectively the scaling matrices $D(\omega)$ and $G(\omega)$;
Replace $D(s)$ and $G(s)$ with appropriate factors so that D, D^{-1}, G_h and GG_h are all stable satisfying:

$$(I + \tilde{G}G)^{-1} = G_h \tilde{G}_h \qquad \tilde{G}(s) = G^T(-s) \tag{5.34}$$

Augment D and G_h with identity matrices and G with a zero matrix so that D, G and G_h are compatible with TF_{model};
Define the state space system as shown in Fig. 5.14:

$$TF_{model}^{DG} = (D \cdot TF_{model} \cdot D^{-1} - \beta^* \cdot G) \cdot G_h \tag{5.35}$$

[step 3] Find the optimal feedback controller $K(s)$ minimizing the H_∞ problem $\left\| M(TF_{model}^{DG}, K) \right\|_\infty$.

[step 4] Compute β^* such as:

$$\beta^* = \sup_{\omega \in \Re} \inf_{\tilde{D}(\omega) \in D_s, \tilde{G}(\omega) \in G_s} \inf_{\beta(\omega) \in \Re, \beta(\omega) > 0} \{\beta(\omega) : \Gamma \le 1\}$$

with:

$$\Gamma = \overline{\sigma}\left(\left(\frac{\tilde{D}(\omega) \cdot M(TF_{model}(j\omega), K(j\omega)) \cdot \tilde{D}^{-1}(\omega)}{\beta(\omega)} - j\tilde{G}(\omega) \right) \cdot (I + \tilde{G}^2(\omega))^{-\frac{1}{2}} \right) \tag{5.36}$$

[step 5] Solve the minimization problem:

$$\inf_{\hat{D}(\omega) \in D_s, \hat{G}(\omega) \in G_s} \overline{\sigma}\left(\left(\frac{\hat{D}(\omega) \cdot M(TF_{model}(j\omega), K(j\omega)) \cdot \hat{D}^{-1}(\omega)}{\beta^*} - j\hat{G}(\omega) \right) \cdot (I + \hat{G}^2(\omega))^{-\frac{1}{2}} \right) \tag{5.37}$$

pointwise across frequency.

[step 6] Compare $\hat{D}(\omega)$ and $\hat{G}(\omega)$ with those obtained in the previous iteration. The algorithm terminates if they are close, otherwise go to [step 2].

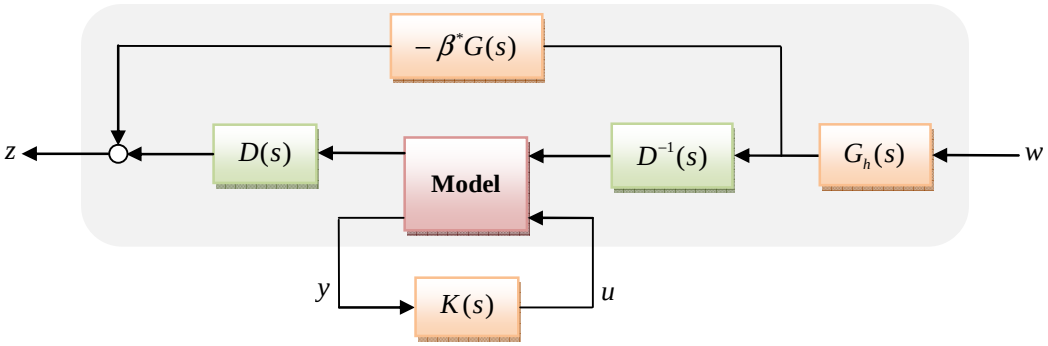

Fig. 5.14. H_∞ problem in the *D,G-K* iteration algorithm

Similarly to what was noted in case of complex-μ synthesis, the *D,G-K* iteration algorithm, as described above, is not convex and so is not guaranteed to converge to the global optimum of the equation (5.33). Further technical discussions can be found in [97].

5.4 RMMAC architecture for a delay uncertainty

In this section, the RMMAC methodology is described and applied in the case of the mould level control. In such control problem, it is highly desirable that the controller stabilizes the system and also meets the posed performance specifications whatever the parameters variations. Our interest in the RMMAC architecture is motivated by its ability to deal with slow changes of the plant parameters. As stated in chapter 3, the gain G_n and the delay τ_n of the plant model change with the machine configuration and it is particularly instructive to examine the RMMAC performances knowing that all the control laws considered in chapter 4 are not able to stabilize the mould level over the entire parameters uncertainties. As a consequence, these controllers do not allow the caster to reach certain operating points such as high casting velocities.

In the sequel, the step-by-step RMMAC algorithm originally presented in [21] and [90] is outlined and applied assuming that the delay τ_n and the time constant of the actuator τ_a are unknown and the gain G_n is fixed and known. τ_a is an uncertain parameter while τ_n and G_n depend on the operating point. G_n is set to a constant value in order to consider only a one-dimensional problem.

Let us recall the transfer function of the plant model in Fig. 5.15.

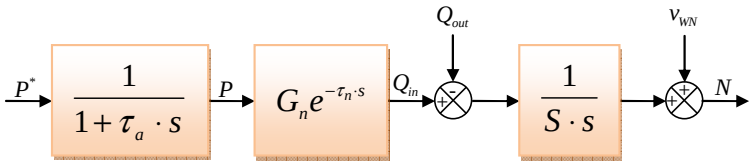

Fig. 5.15. Plant model

Using the first order Padé function as an approximation of the time-delay term, the continuous-time state space equation of the plant model is given by:

$$\begin{cases} \dot{x} = Ax + Bu \\ y = N = Cx + v_{WN} \end{cases}$$

$$x^T = \begin{pmatrix} N & P & q_p \end{pmatrix} \qquad u^T = \begin{pmatrix} Q_{out} & P^* \end{pmatrix} \qquad q_p(t) = G_n P(t-\tau_n) + G_n P(t) \tag{5.38}$$

$$A = \begin{pmatrix} 0 & -G_n/S & 1/S \\ 0 & -1/\tau_a & 0 \\ 0 & 4G_n/\tau_n & -2/\tau_n \end{pmatrix} \qquad B = \begin{pmatrix} -1/S & 0 \\ 0 & 1/\tau_a \\ 0 & 0 \end{pmatrix} \qquad C^T = \begin{pmatrix} 1 \\ 0 \\ 0 \end{pmatrix}$$

It can be seen that the actuator dynamics has now been taken into account in the state space representation.

The level N is corrupted by an additive sensor white noise $v_n(t)$ whose intensity is defined as:

$$\mathrm{E}\left(v_{WN}(t) \cdot v_{WN}(t-\tau)\right) = V_{WN} \cdot \delta(\tau) \tag{5.39}$$

where $\delta(\tau)$ is the Dirac symbol.

The following parameters are fixed and known (see chapter 2):

$$G_n = 1\mathrm{L} \cdot \mathrm{s}^{-1} \cdot \mathrm{mm}^{-1} \qquad S = 0.3648\mathrm{m}^2 \qquad V_{WN} = 0.01\mathrm{mm}^2 \tag{5.40}$$

As for the uncertain parameter τ_n, only the upper and lower bounds can be identified as shown in chapter 3:

$$\tau_n \in [0.1\mathrm{s} \;\; 2\mathrm{s}] \tag{5.41}$$

The upper and lower bounds for the uncertain actuator time constant τ_a are:

$$\tau_a \in [0.001\mathrm{s} \;\; 0.1\mathrm{s}] \tag{5.42}$$

The performance variable is the level N and from now on, we focus our attention on the problem of bulging rejection. As explained in chapter 2, the bulging disturbance has a frequency range between 0.03 and 0.1Hz. The bulging effect on the level can be thus 'measured' using the average magnitude of the transfer function between the flow out the mold Q_{out} and the level N over this range. From a performance point of view, this average magnitude should be as small as possible.

Prior to design the identification and the control parts, we need to examine the potential benefit we will obtain using adaptive control in particular the RMMAC architecture. In addition to performing identification and control functions, the utility of this control structure sterns also from the fact that it provides the designer with necessary framework to understand and predict the performance characteristics. This is accomplished during the first step of the RMMAC methodology.
Next, if it appears that there is a potential improvement in performance by using adaptive control, the RMMAC algorithm continues with the second stage whose purpose is to find the number of models and their boundaries (Fig. 5.5). At the end of this iterative process, the local controllers are also synthesized.
Another question covered in the design part is how to select the nominal values of the uncertain parameters in order to ensure the convergence of the posterior probabilities and the correct model selection. The idea is to use the Baram Proximity Measure method which will be defined later.
Finally, the development step integrates the issues related to the design of Kalman filters, the model order reduction to avoid controllers of high dimensions and the implementation of the Posterior Probability Evaluator.
In short, the RMMAC methodology is carried out in three steps as illustrated in Fig. 5.16.

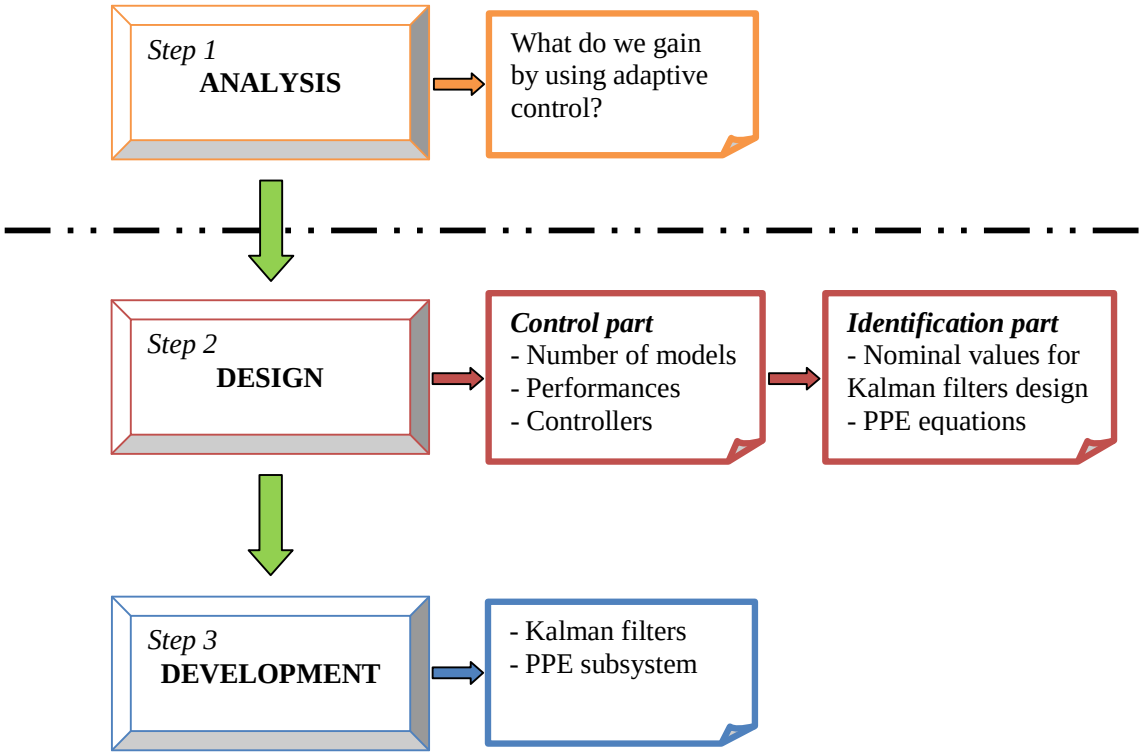

Fig. 5.16. RMMAC methodology

The next subsection defines the performance parameter and analyses the potential benefits of using adaptive control. Next, we describe the proper way of dividing the initial parameter uncertainty range into smaller parameter subsets and designing the local robust controllers. Afterwards, the concept of Baram Proximity Measure is made precise and employed to specify the nominal values of the uncertain parameter in each subset. Finally, the simulation results are presented confirming thus the positive aspects of the RMMAC architecture.

5.4.1 RMMAC benefits

Contrary to the non-adaptive control laws, the RMMAC design always begins with the performances analysis step which provides the designer with the information to decide whether or not to implement adaptive control. The complexity of the RMMAC architecture can be justified only by a performance improvement.
In [20], the idea is to compute the upper and lower bounds of the performance parameter achieved using adaptive and non-adaptive control respectively. Thus, the lower bound so-called Global Non-Adaptive Robust Compensator GNARC represents the highest performance we can obtain for **the entire uncertain parameter set** with a unique controller. Since our plant model uncertainties are real, it is recommended to use the mixed-μ synthesis rather than the complex-μ synthesis which deals only with the complex uncertainties and may provide conservative results if it is used here. The other performance bound so-called Fixed Non-Adaptive Robust Compensator FNARC corresponds to a robust controller that can be used to understand the best possible performance achieved when **the real parameter is exactly identified**. Similarly to the GNARC controller, it is computed using the mixed-μ software.
Afterwards, careful comparison between the upper and the lower bounds should be performed before making a final decision on using adaptive control.
For both GNARC and FNARC designs, the designer should consider the following elements in the plant model:

- Parameters uncertainties and unmodeled dynamics,
- Sensors noises,
- Performance requirements in the frequency domain. In order to achieve superior bulging rejection, we introduce a frequency weight on the level which shapes the magnitude of the bulging rejection over the bulging frequency range. The derived scheme can be completed by frequency weights on the control signal, the level error and other disturbances.

5.4.1.1 GNARC design

The GNARC is designed using the mixed-μ synthesis. We should first extend the plant model configuration to include model uncertainty. Fig. 5.17 depicts the required diagram for the mixed-μ synthesis. The generalized plant includes the nominal plant dynamics. The block $\Delta(s)$ incorporates the normalized real parameters uncertainties and $K(s)$ is the stabilizing controller which guarantees the posed performance specifications for the entire uncertain parameters intervals.

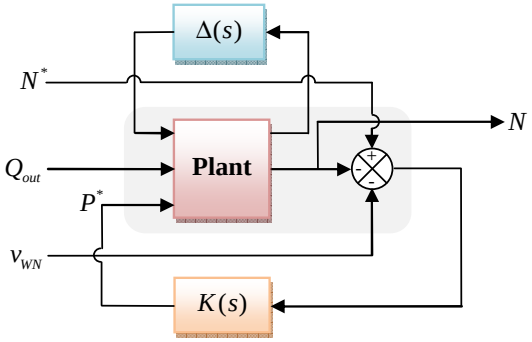

Fig. 5.17. Plant model for the mixed-μ synthesis

The GNARC is designed for the entire uncertain delay set and by taking into account the bulging rejection performance, the actuator time constant uncertainty as well as the sensor noise. The corresponding controller must maximize the performance and guarantee both robust stability and robust performance.
The bulging rejection criterion used here to evaluate the quality of bulging rejection, is defined as follows:

$$C_{perf} = \frac{\left(\max\limits_{\omega \in [0.03\ 0.1\text{Hz}]} \left| TF_{bulge}(j\omega) \right| + \min\limits_{\omega \in [0.03\ 0.1\text{Hz}]} \left| TF_{bulge}(j\omega) \right| \right)}{2} \tag{5.43}$$

where $TF_{bulge}(s)$ is the transfer function between the flow rate out of the mould and the level ($TF_{bulge}(s) = \frac{N(s)}{Q_{out}(s)}$).

The basic idea is to find an initial weighting function so that the mixed-μ software generates a controller with an upper bound $\mu_{ub}(\omega)$ such as:

$$\forall \omega \quad \mu_{ub}(\omega) < 1 \tag{5.44}$$

Therefore, the control loop is guaranteed to be stable for all the parameters uncertainties. Moreover, the posed performance requirements are met.
GNARC is then determined by minimizing the bulging rejection criterion C_{perf} until the $\mu(\omega)$ upper bound is just below the unity. More formally,

$$\forall \omega \quad 0 < 1 - \mu_{ub}(\omega) < 0.01 \tag{5.45}$$

GNARC is thereby the best possible robust performance we can expect in the absence of adaptation.
To carry out the mixed-μ synthesis, two weighting functions $W_b(s)$ and $W_n(s)$ have been included as shown in Fig. 5.18:

$$\begin{cases} W_b(s) = \dfrac{10.4 \cdot (s + 0.314) \cdot (s + 3.14)}{(s + 0.0209) \cdot (s + 314)} \\ W_n(s) = 0.01 \end{cases} \tag{5.46}$$

$W_b(s)$ is intended to determine the potential performance benefit in the bulging frequency region while $W_n(s)$ is introduced to produce a sensor white noise with intensity of 0.01.

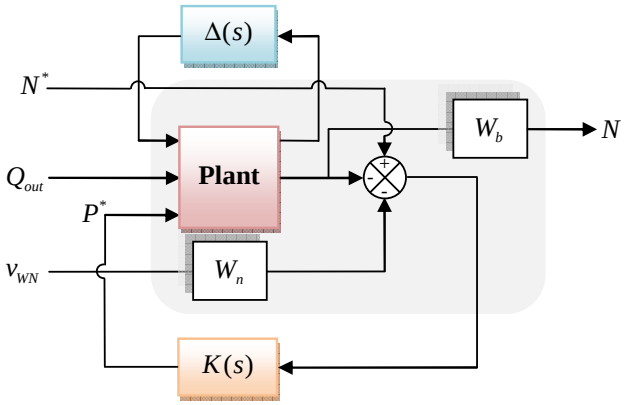

Fig. 5.18. Plant model with weighting functions for the mixed-μ synthesis

In order to agree with the notations already introduced in [90], the performance parameter is formulated as follows:

$$A_p = \frac{1}{10^{C_{perf}/20}} \tag{5.47}$$

Based on this definition, A_p should be as large as possible for superior bulging rejection. It is maximized until the $\mu(\omega)$ upper bound satisfies the inequality (5.45). The largest value of the performance parameter A_p was to be:

$$\begin{cases} A_p = 0.212 \\ C_{perf} = 13.5\text{dB} \\ \mu_{ub}(\omega) \approx 0.993 \end{cases} \tag{5.48}$$

5.4.1.2 FNARC design

Prior to making any decision on using adaptive control, one needs to compute the other performance bound so-called the Fixed Non-Adaptive Robust Compensator FNARC assuming that the uncertain parameter, here the delay τ_n, takes a known value in the range uncertainty. If it is implemented in a multiple-model adaptive architecture, the FNARC performance supposes an infinite number of models. Therefore, the FNARC is the upper bound while the GNARC is the lower bound on robust performance.

From a practical point of view, we use the same scheme as the one previously employed for the GNARC design (Fig. 5.18). We begin by defining a dense grid of the delay denoted by $\tau_n(i)$. For each fixed value $\tau_n(i)$, the bulging rejection criterion C_{perf} is minimized and so the performance parameter A_p is maximized until the inequality (5.45) is satisfied in order to attain as large a bulging rejection as possible. The FNARC is thus determined as the best possible performance that we may expect if the uncertain parameter is exactly identified. Since we still must consider the real actuator time constant uncertainty, the FNARC design is carried out using the mixed-μ software. To make fair comparisons, one should apply the same weighting functions $W_b(s)$ and $W_n(s)$ as previously used for the GNARC i.e.:

$$\begin{cases} W_b(s) = \dfrac{K_{W_b} \cdot (s+0.314)\cdot(s+3.14)}{(s+0.0209)\cdot(s+314)} \\ W_n(s) = 0.01 \end{cases} \tag{5.49}$$

where the gain K_{W_b} has to be adjusted in function of the delay value $\tau_n(i)$.

Each of the resulting FNARC designs and their optimized $\mu(\omega)$ upper bounds are summarized in Table 5.1.

Table 5.1. Best FNARC performance

$\tau_n(i)$ (s)	K_{W_b}	C_{perf} (dB)	A_p	$\mu_{ub}(\omega)$
0.1	77.8	–1.55	1.19	0.994
0.2	65.6	–0.0657	1.01	0.993
0.3	58.3	–0.984	0.893	0.995
0.4	51.2	2.12	0.784	0.994
0.5	46.3	3.14	0.696	0.993
0.6	41.8	3.82	0.644	0.99
0.7	38.2	4.64	0.586	0.994
0.8	35	5.4	0.537	0.993
0.9	32.9	6	0.501	0.999
1	30.1	6.66	0.465	0.989
1.1	27.9	7.33	0.43	0.986
1.2	26	7.96	0.4	0.986
1.3	24.3	8.78	0.364	0.993
1.4	22.8	9.33	0.342	0.993
1.5	21.5	9.84	0.322	0.993
1.6	20.3	10.3	0.304	0.985
1.7	19.2	10.8	0.287	0.985
1.8	18.2	11.2	0.274	0.991
1.9	17.2	11.8	0.257	0.991
2	16.4	12.1	0.248	0.998

5.4.1.3 Performances analysis

This step is vital before deciding to implement adaptive control which could lead most often to complex structures.

The bulging rejection criterion C_{perf} of the GNARC and FNARC as functions of the delay are plotted in Fig. 5.19. Clearly, if we know the delay exactly, we can improve significantly the bulging rejection performance from 13.5dB to a range between −1.55 and 12.1dB. This agrees with the engineering intuition.

Furthermore, the performance improvement seems to be higher if the delay is near to its lower bound 0.1s. The benefit of using adaptive control is obvious in this region. However, it decreases when the delay is increased where the best expected performance is 12.1dB which is closer to the GNARC value.

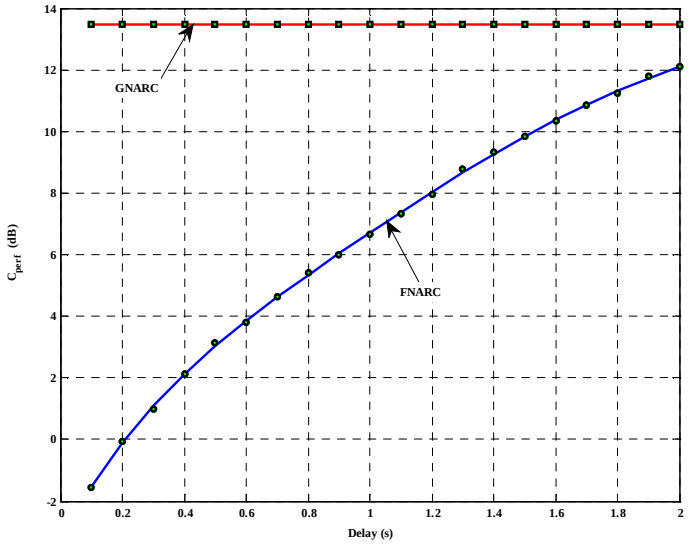

Fig. 5.19. Comparison of the bulging rejection criterion C_{perf} for the GNARC and FNARC in case of uncertain delay

By considering the performance parameter A_p, the GNARC becomes the performance lower bound while the FNARC provides the expected upper bound. Fig. 5.20 shows that the performance may be improved about $1.2/0.21 = 5.7$ times by using adaptive control in the low delay region.

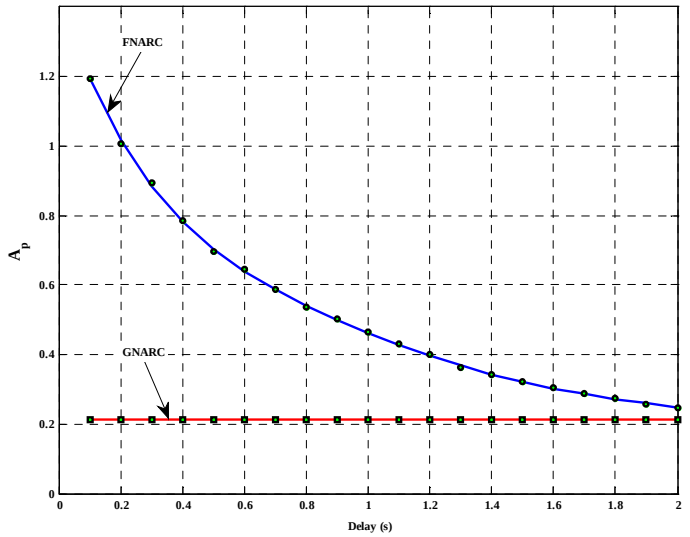

Fig. 5.20. Best GNARC and FNARC performance for delay uncertainty

To summarize the underlying results, the analysis above reveals that there is a meaningful benefit in using adaptive control in particular the multiple-model architecture. It is noteworthy to mention that the GNARC and FNARC curves are to be used as the performance comparison basis as well as a helpful tool to obtain the RMMAC models which cover the whole initial uncertainty set.

5.4.2 Control part design

The previous subsection indicates that the mould level control system will benefit from adaptive control strategies. By decreasing the lack of knowledge on the delay value, it is indeed possible to improve the bulging rejection. Our choice, in this thesis work, is to implement the RMMAC architecture which utilizes a systematic approach to determining the number of models and designing the local controllers and the Kalman filters. In reference to Fig. 5.16, this subsection deals with the control part design which initiates the second step in the RMMAC methodology. As reported in [90], the number of models can be obtained using the Brute-Force approach or the % FNARC method. In the sequel, the two methods are presented but only the second one is utilized for models selection.

5.4.2.1 The Brute-Force approach

In the Brute-Force approach, the designer fixes the number of models in advance in opposition to the % FNARC method where it cannot be known precisely until the end of the optimization process.

Fig. 5.21 illustrates a Brute-Force selection of five models. The performance in each subset A_p^k, $k=1,2,3,4,5$ is thus maximized using the mixed-μ synthesis applied on the same scheme as the one previously used for GNARC and FNARC designs. A_p^k should be as large as possible to allow optimal rejection of the bulging. The mixed-μ software also generates the Local Non-Adaptive Robust Compensators LNARCs which represent the local controllers associated to the models. At the end of this iterative process, if the performances A_p^k are not satisfactory, one should adjust the number of models and the boundaries of each model.

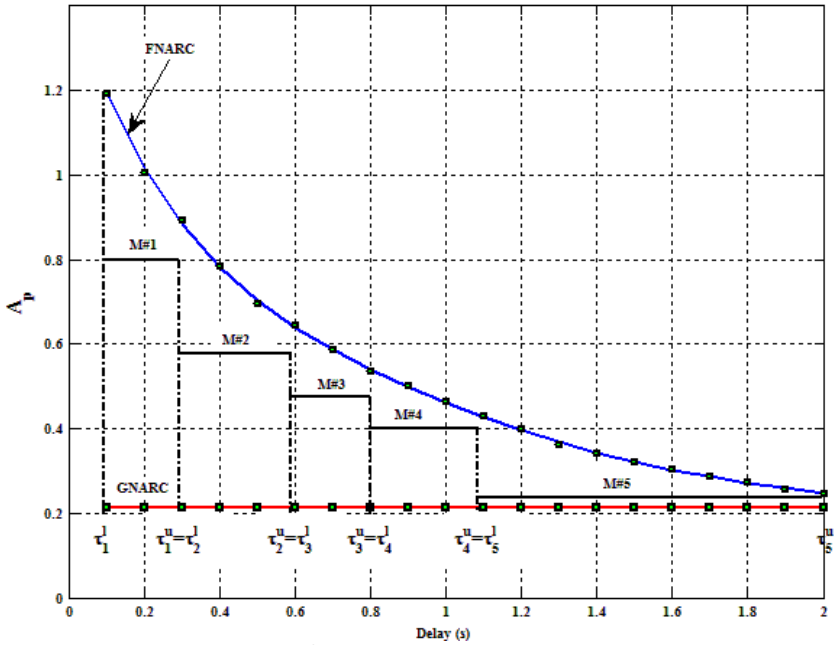

Fig. 5.21. Determination of RMMAC models using the Brute-Force approach

In closing, we stress that this approach defines the boundaries of the models, the associated performances and the local controllers as shown in Table 5.2. The complexity of the RMMAC architecture related to the number of models is however decided by the designer.

Table 5.2. Illustration of the definition of five models using the Brute-Force approach

Model	*Lower bound*	*Upper bound*	A_p^k
1	τ_1^l	τ_1^u	A_p^1
2	τ_2^l	τ_2^u	A_p^2
3	τ_3^l	τ_3^u	A_p^3
4	τ_4^l	τ_4^u	A_p^4
5	τ_5^l	τ_5^u	A_p^5

5.4.2.2 The % FNARC approach

Instead of fixing in advance the number of models required by the RMMAC architecture, the % FNARC method provides an alternative way to determine it with the help of the FNARC and GNARC curves as well as a third one which represents the lower bound of the RMMAC performance. More precisely, the designer imposes a limit on the RMMAC performance. The number of models is then computed in such a way that the achieved performance in each model is equal or exceeds this limit. Since the FNARC is the performance upper bound of any adaptive control law, the limit is most often specified to be X% of FNARC. Thereafter, we wish the level of performance to be:

$$X\% = 60\% \tag{5.50}$$

Following the algorithm described in [90], we start from the lower bound of the delay 0.1s where the FNARC is maximum. We increase then slowly the uncertainty set of the first model and we calculate the maximum performance parameter A_p in this interval using the mixed-μ synthesis. This leads to the dashed curve in Fig. 5.22. We iterate this process as long as the performance parameter is greater than the maximum of the 60% FNARC curve. As a result, the upper bound of the first subset lies at the intersection of the dashed curve with the maximum of the 60% FNARC curve. The first model is thus defined as follows:

$$M\#1 = [0.1 \;\; 0.24] \qquad \mathrm{A}_p^1 = 0.718 \tag{5.51}$$

Needless to say that this procedure yields both the first subset (M#1) and the associated controller (LNARC#1).
Next, the same process is repeated starting from the upper bound of the first subset. The second uncertainty set is thus increased until the performance parameter, calculated using the mixed-μ software, is equal to the maximum of the 60% FNARC curve over this new uncertainty set. This leads to the second model:

$$M\#2 = [0.24 \;\; 0.45] \qquad \mathrm{A}_p^2 = 0.577 \tag{5.52}$$

Then, three other iterations have been performed before reaching the upper boundary of the delay uncertainty interval 2s.
At the end of this iterative process, five subsets have been identified as necessary to achieve a performance greater than 60% of FNARC over the whole initial uncertainty set (Fig. 5.22).

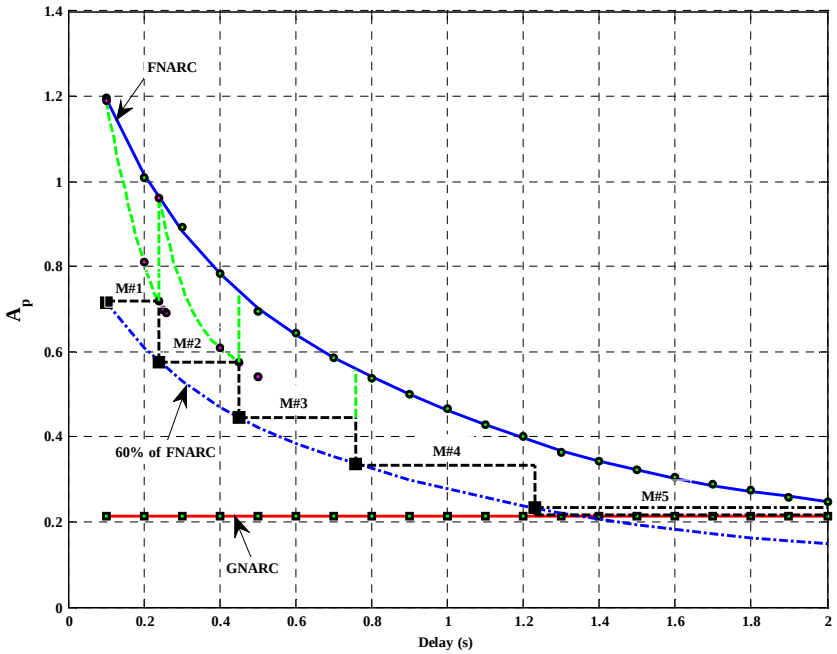

Fig. 5.22. Determination of RMMAC models using the % FNARC approach

It is tempting to impose a higher performance, say 80%. This will require undoubtedly more models. One should recall that the FNARC requires an infinite number of models while the GNARC requires only one model.

Accordingly, the larger is the performance parameter A_p, the more the RMMAC architecture is complex and this, of course, agrees with the intuition.
In our design, the whole delay uncertainty is covered by five models $M\#k$, $k=1,2,3,4,5$. Table 5.3 compares the expected performance in each model with that of the best non-adaptive GNARC design. Clearly, we can expect better bulging rejection especially for low values of the delay.

Table 5.3. Comparison between LNARCs and GNARC performances

Controller	*Subset*	A_p	$\mu_{ub}(\omega)$
1	[0.1 0.24]	0.718	0.994
2	[0.24 0.45]	0.577	0.995
3	[0.45 0.76]	0.444	0.991
4	[0.76 1.23]	0.333	0.988
5	[1.23 2]	0.215	0.988
GNARC	[0.1 2]	0.212	0.993

Fig. 5.23 depicts the five-model RMMAC architecture. The control part has been completely designed in this paragraph. All that remains to do is to design the Kalman filters of the identification subsystem. This is the issue of the next subsection.

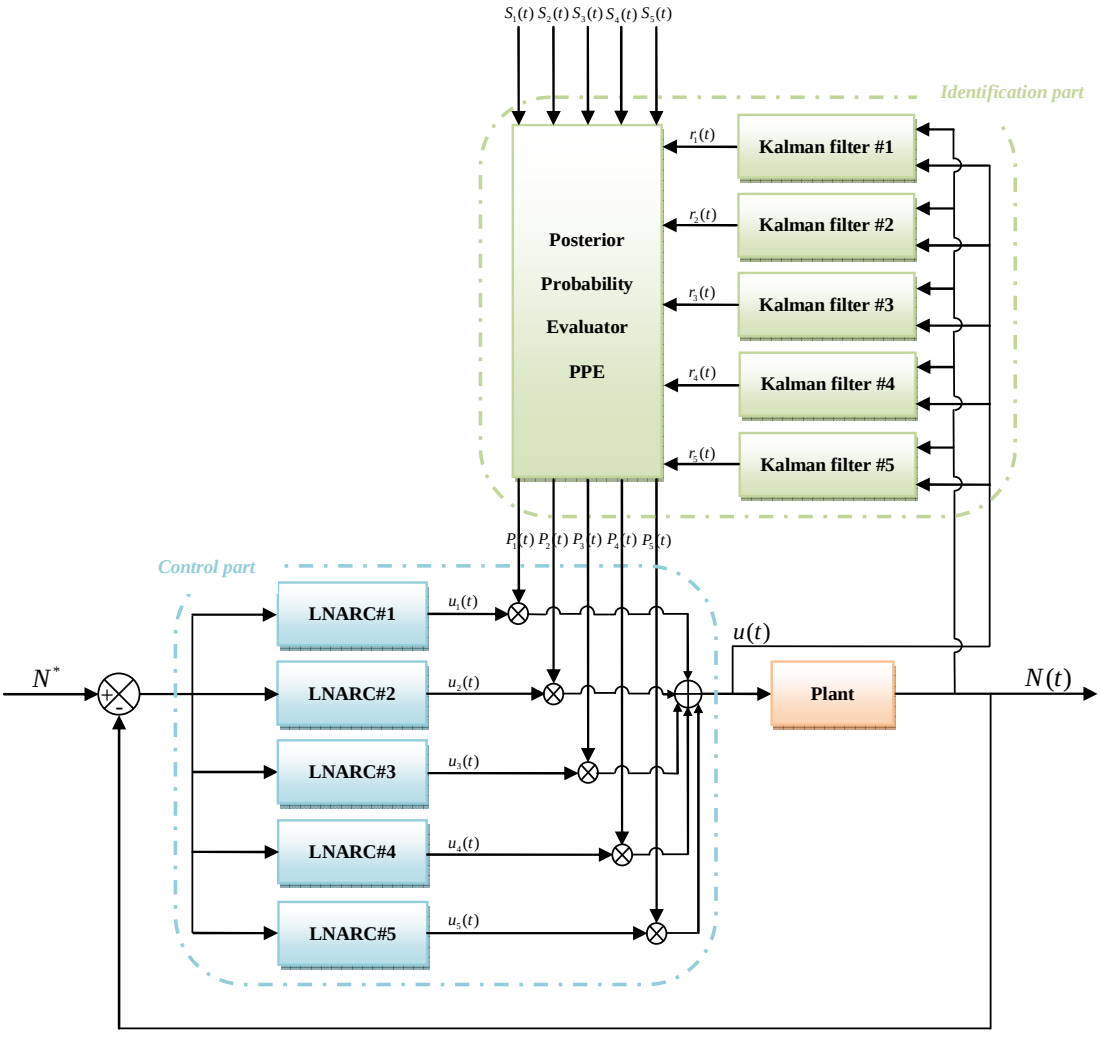

Fig. 5.23. RMMAC architecture for mould level control

5.4.3 Identification part design

The second important issue in the RMMAC design concerns the identification part including the Posterior Probability Evaluator PPE. Since the RMMAC can be considered as an extension of the MMAE architecture, all the development related to the Kalman filters and the posterior probabilities as presented in the second section of this chapter still applies. In this paragraph, we discuss the proper way of determining the nominal values of the delay τ_n^k that are needed to design the Kalman filters. A great deal of care must be taken to satisfy some theoretical assumptions in order to enable the RMMAC architecture to converge to the closest model of the set if the true plant delay does not belong to the nominal values set. At this stage, it is necessary to mention that the strategy consisting of choosing τ_n^k at the centers of the subsets leads to unpredictable behaviors of the posterior probabilities. In [89] and [90], it is suggested to use the Baram Proximity Measure BPM in order to select τ_n^k. This real function measures the stochastic distance between the residuals $r(t)$ and $r_k(t)$. The BPM theory is too dense for a review in the framework of this dissertation. In the sequel, we shall provide only a summary of the main conclusions and the key equations for calculating this distance. Full details can be found however in [95].
We stress that the design of the identification part must be carried out after that of the control part which establishes the number of models and their boundaries.
Recall that our process is governed by the linear equation:

$$\begin{cases} x_k(t+1) = A_k x_k(t) + B_k u(t) + F_k w_{WN}(t) \\ y_k(t) = C_k x_k(t) + v_{WN}(t) \end{cases} \qquad \begin{cases} \mathrm{E}\left(w_{WN}(t)\cdot w_{WN}(t)^T\right) = Q_k \\ \mathrm{E}\left(v_{WN}(t)\cdot v_{WN}(t)^T\right) = R_k \end{cases} \tag{5.53}$$

and the posterior probabilities $P_k(t)$ are given by:

$$\begin{cases} P_k(0) = \mathrm{Prob}(H = H_k) \\ P_k(t) = \mathrm{Prob}(H = H_k \,|\, u(0)\cdots u(t-1), y(1)\cdots y(t)) \end{cases} \tag{5.54}$$

where H_k is a random variable modeling the fact that the k^{th} model is the one generating the plant output.
Let M^* denotes the whole model set which includes the nominal values τ_n^k and the true plant delay denoted by $*$. The convergence of the posterior probabilities is made more precise by the following fundamental theorem [95].

Theorem Under the following assumptions:
$[x(t)]$ is stationary i.e. for every F belonging to the σ-algebra of Borel sets of $\Re^3 \times \Re^3 \times \cdots$, we have:

$$P[x(1), x(2), \ldots, x(t) \in F] = P[x(l+1), x(l+2), \ldots, x(l+t) \in F] \tag{5.55}$$

$[x(t)]$ is ergodic i.e.

$$\lim_{t\to\infty} \frac{1}{t+1} \sum_{l=0}^{t} \left|\mathrm{E}(x(t)\cdot x(t+l)^T)\right|^2 = 0 \tag{5.56}$$

For $i \in M^*$, the residual covariance S_i exists and has a finite positive definite value,
For $i \in M^*$, the residual sequence $[y(t) - \hat{y}_i(t)]$ is ergodic.
If the BPMs $L(\tau_n, \cdot)$ satisfy the inequality:

$$\forall k \neq i \quad L(\tau_n, \tau_n^i) < L(\tau_n, \tau_n^k) \tag{5.57}$$

then the posterior probabilities converge almost surely to the correct model i.e.

$$\lim_{t\to\infty} P_i(t) \to 1 \qquad \lim_{t\to\infty} P_{k\neq i}(t) \to 0 \tag{5.58}$$

As an illustration, two BPMs are plotted in Fig. 5.24. The delay of the true plant τ_n^* has been arbitrary chosen so that $L(\tau_n^*, \tau_n^2) < L(\tau_n^*, \tau_n^1)$. As a result, the theorem will guarantee that:

$$\lim_{t\to\infty} P_2(t) \to 1 \qquad \lim_{t\to\infty} P_1(t) \to 0 \tag{5.59}$$

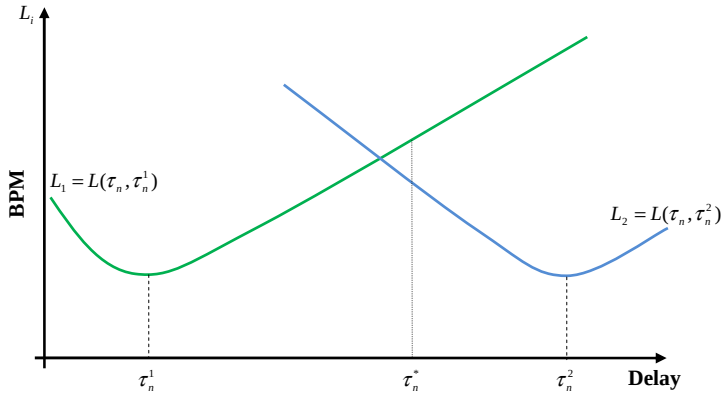

Fig. 5.24. Baram Proximity Measure BPM

All the stationarity and ergodicity conditions are important and must be satisfied [98] [99]. If it is not the case, one can use a fake white noise to robustify the Kalman filters [78] [100].

In the rest of this subsection, we shall provide all necessary equations to compute the BPM distance. Let us first establish some notation. For $i, j \in M^*$, define:

$$\Gamma_j^i = E\left\{(y(t) - \hat{y}_j(t))(y(t) - \hat{y}_j(t))^T / H_i \neq H_j\right\} \qquad \Psi_j^i(t) = E\left\{\begin{pmatrix} x_i(t) \\ \hat{x}_j(t) \end{pmatrix}\begin{pmatrix} x_i(t) \\ \hat{x}_j(t) \end{pmatrix}^T\right\}$$

$$A_j^i = \begin{pmatrix} A_i & 0 \\ A_j K_j C_i & A_j(I - K_j C_j) \end{pmatrix} \qquad F_j^i = \begin{pmatrix} F_i & 0 \\ 0 & A_j K_j \end{pmatrix} \qquad Q^i = \begin{pmatrix} Q_i & 0 \\ 0 & R_i \end{pmatrix} \qquad C_j^i = (H_i \quad -H_j) \tag{5.60}$$

It can be shown that $\Psi_j^i(t)$ is generated by:

$$\Psi_j^i(t+1) = A_j^i \Psi_j^i(t) A_j^{iT} + L_j^i Q^i L_j^{iT} \tag{5.61}$$

Its steady-state Ψ_j^i is finite if and only if the matrix A_j^i has all its eigenvalues inside the unit circle. It can be readily calculated by solving the Lyapunov equation:

$$\Psi_j^i = A_j^i \Psi_j^i A_j^{iT} + L_j^i Q^i L_j^{iT} \tag{5.62}$$

Ψ_j^i permits then to calculate Γ_j^i through the expression:

$$\Gamma_j^i = C_j^i \Psi_j^i C_j^{iT} + R_i \tag{5.63}$$

For $k, j \in M^*$, we denote the mean information in $y(t)$ favoring model k against model j by:

$$I_n(k, j) = \mathrm{E}\left\{\log \frac{p(y(t)/H_k, Y(t-1))}{p(y(t)/H_j, Y(t-1))}\right\} \tag{5.64}$$

with: $Y(t) = (u(0)\cdots u(t-1), y(1)\cdots y(t))$

By making use of (5.14), we see that:

$$\mathrm{E}\{\log p(y(t)/H_k, Y(t-1))\} = -\frac{1}{2}\log 2\pi - \frac{1}{2}\log|S_k| - \frac{1}{2}\mathrm{trace}(S_k^{-1}\Gamma_k^*) \tag{5.65}$$

It follows:

$$I_n(k, j) = \frac{1}{2}\log|S_j| + \frac{1}{2}\mathrm{trace}(S_j^{-1}\Gamma_j^*) - \frac{1}{2}\log|S_k| - \frac{1}{2}\mathrm{trace}(S_k^{-1}\Gamma_k^*) \tag{5.66}$$

This equation gives rise to the Baram Proximity Measure BPM of the j[th] subset denoted by L_j^i :

$$\forall i \in M^* \quad L_j^i = \log\left|S_j\right| + \mathrm{trace}(S_j^{-1}\Gamma_j^i) \tag{5.67}$$

The BPM measures the distance between one model and each of the other ones forming the identification part. By substituting (5.67) back into (5.66), we have:

$$I_n(k, j) = \frac{1}{2}(L_j^* - L_k^*) \tag{5.68}$$

Therefore, the following equations are equivalent:

$$I_n(k, j) \geq 0 \qquad L_j^* \geq L_k^* \tag{5.69}$$

If such model k exists, this means that the true plant is closer to the k[th] model. Hence, the associated posterior probability should converge to 1. Since the condition (5.57) is satisfied, this convergence is ensured fortunately thanks to the theorem aforementioned.
Finally, the Kalman filters nominal points are determined through an iterative optimization routine so that the BPMs agree at the boundaries of adjacent models as shown in Fig. 5.25.

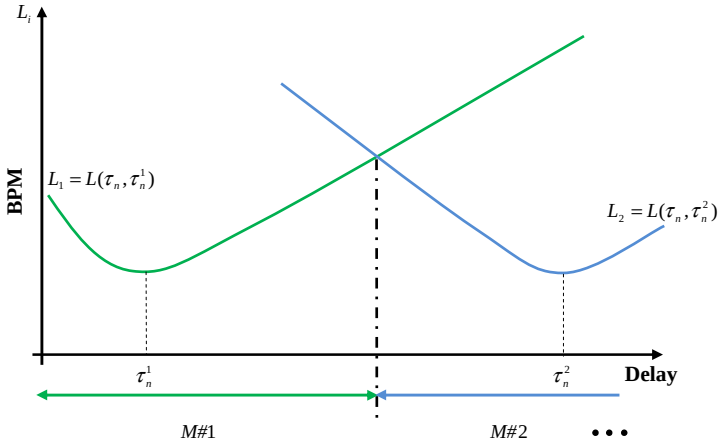

Fig. 5.25. Determination of Kalman filters nominal points using the BPMs

From this figure, it follows:

$$\tau_n \in M\#i \quad \Rightarrow \quad \lim_{t\to\infty} \mathrm{P}_i(t) \to 1 \tag{5.70}$$

Thus, the posterior probability of the closest model to the true plant (i.e. having the smallest BPM) will converge almost surely to 1.
The nominal values of the delay calculated in this manner are summarized in Table 5.4.

Table 5.4. Nominal values of the delay for designing the Kalman filters

Model	*Subset*	τ_n^k
M#1	[0.1 0.24]	0.15
M#2	[0.24 0.45]	0.3
M#3	[0.45 0.76]	0.65
M#4	[0.76 1.23]	1
M#5	[1.23 2]	1.5

5.4.4 Performance evaluation

Because of its advanced structure, many aspects of the RMMAC architecture should be investigated. This subsection presents some representative simulations which evaluate the benefits of using RMMAC in the presence of delay uncertainties. Several scenarios have been tested to examine the behaviors of the posterior probabilities as well as the bulging rejection performance of the RMMAC compared to that of the best non-adaptive GNARC design. We stress that the other controllers studied in chapter 4 or currently implemented in real plants are not stable over the whole delay uncertainty and cannot be compared thus to the RMMAC.

Based on the same simulator used on several occasions throughout this dissertation, the bulging is modeled by a sine wave whose frequency is 0.03 or 0.05Hz. In Fig. 5.26, the true delay is equal to 0.15s and so its nearest model is the first one. As expected, the corresponding probability converges to 1 in a few seconds.

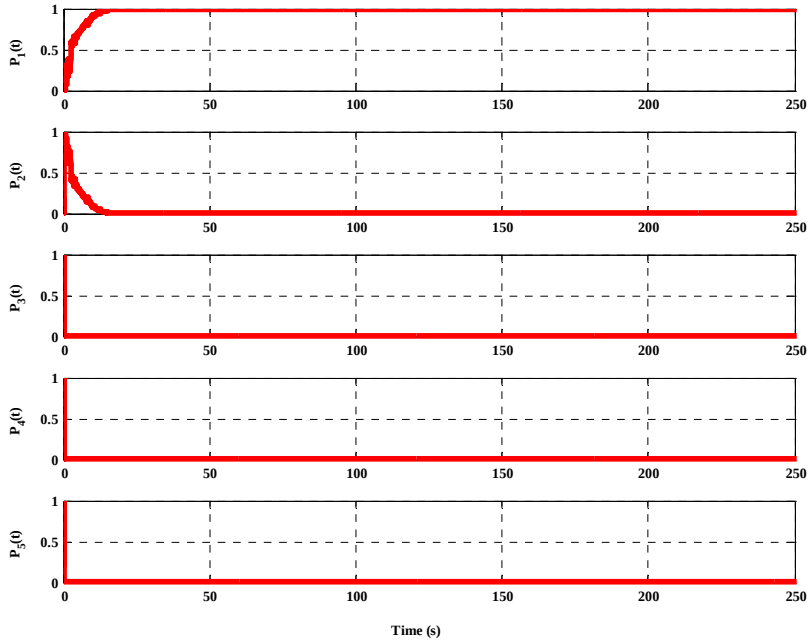

Fig. 5.26. Posterior probabilities when the true plant delay belongs to the nominal values set

In Fig. 5.27, we assess the performance of the RMMAC obtained with the first local controller against that of the GNARC control law. The improvement in bulging rejection is obvious and is in a good agreement with our expectations highlighted in Table 5.3.

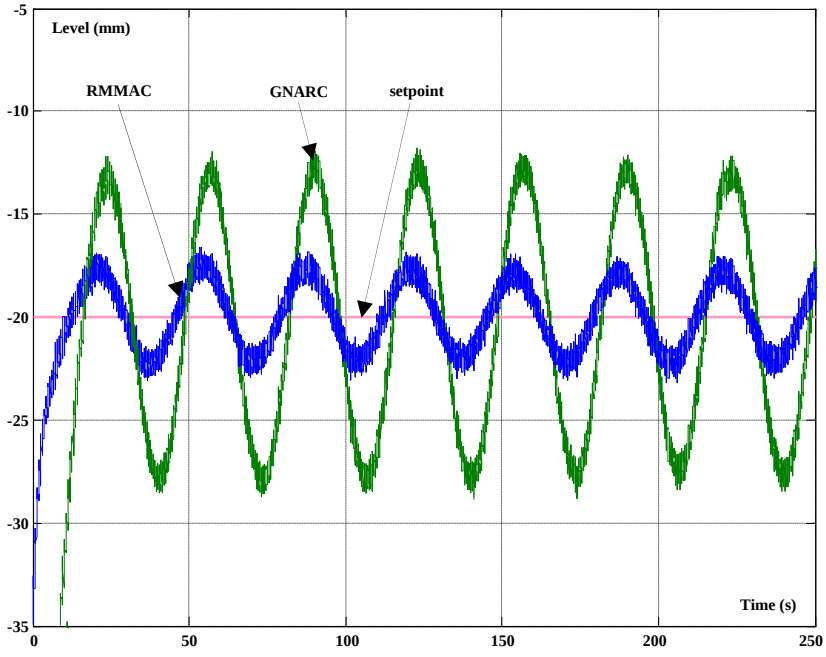

Fig. 5.27. Bulging rejection performance when the true plant delay belongs to the nominal values set

We next evaluate the RMMAC performance when the true plant delay is equal to an arbitrary constant value, say 0.8s which does not belong to the nominal values set. It belongs however to the fourth model values set. Fig. 5.28 confirms that we have convergence to model 4 albeit the Euclidean distances indicate the opposite. Indeed, it is easy to check that:

$$\left|\tau_n^* - \tau_n^3\right| < \left|\tau_n^* - \tau_n^4\right| \tag{5.71}$$

This is because the convergence of the posterior probabilities is based upon the BPM measure. In this case, the convergence to subset 4 occurs because the calculations show that:

$$L(\tau_n^*, \tau_n^4) < L(\tau_n^*, \tau_n^3) \tag{5.72}$$

Fig. 5.29 illustrates that the RMMAC yields, once more, superior bulging rejection. It is also of interest to notice that the performance improvement is much better for low values of the delay and this agrees with the conclusions of the subsection dealing with the RMMAC benefits.

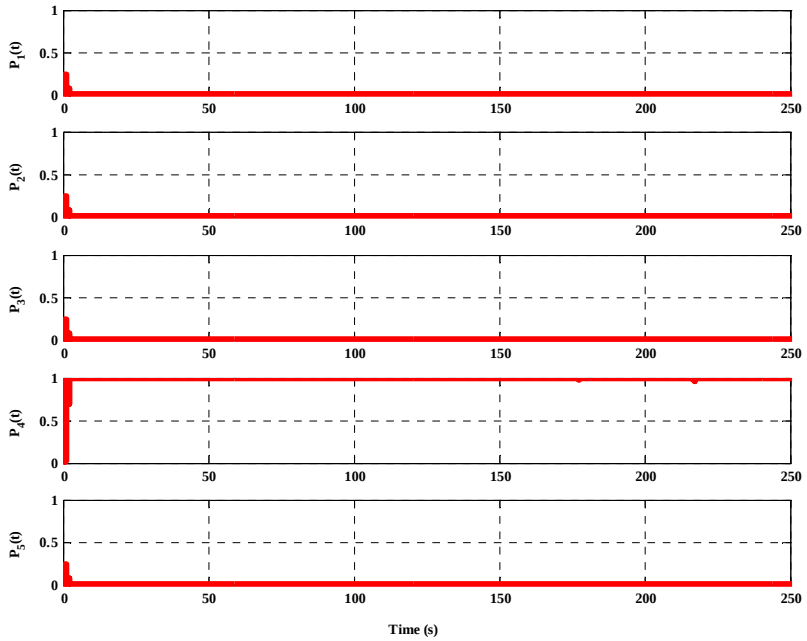

Fig. 5.28. Posterior probabilities when the true plant delay has an arbitrary constant value

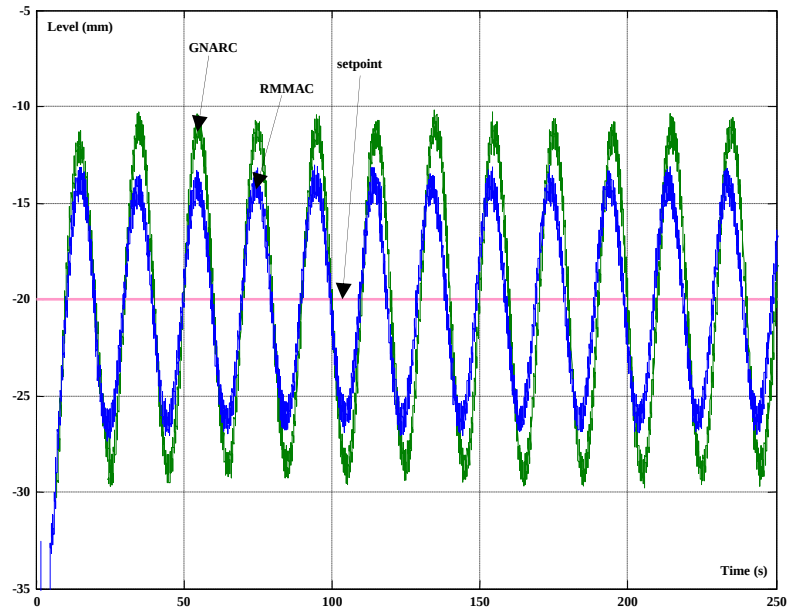

Fig. 5.29. Bulging rejection performance when the true plant delay has an arbitrary constant value

In a real plant, the delay changes with time according to the operating point. Fig. 5.30 shows a representative simulation result where the delay is assumed to vary according to a sequence stair chosen arbitrary in the uncertainty set. In this case, the true plant takes values in $\{0.6s, 1.5s, 1s, 0.2s\}$ with a period of 250s. This set contains two nominal values, namely 1s and 1.5s.
During each period, the appropriate model is identified without any serious problems. The convergence of the posterior probabilities is achieved in about 5s. For other values of the uncertain delay especially those close to the models boundaries, one could expect a long period of time for the probabilities to converge.

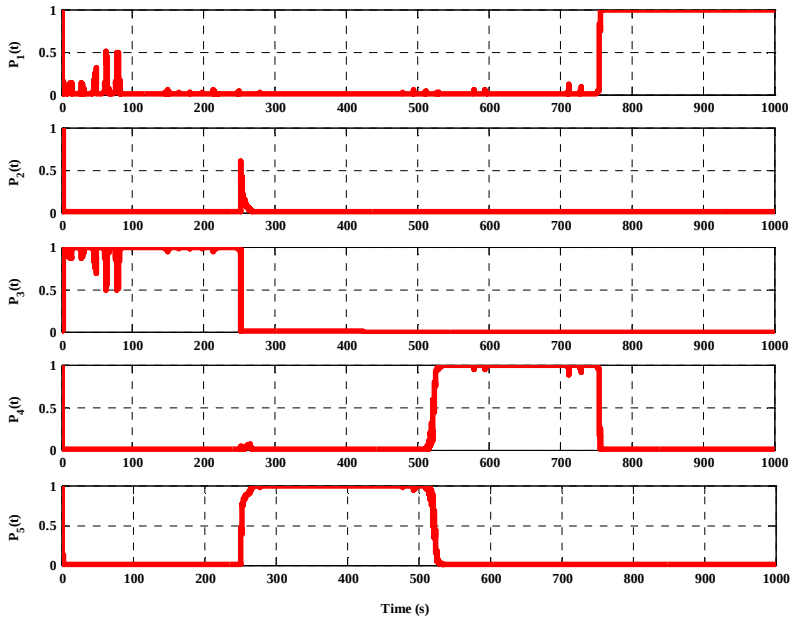

Fig. 5.30. Posterior probabilities when the true plant delay varies according to a specified sequence stair

Fig. 5.31 shows the RMMAC response to the level variations generated by the bulging superimposed with that of the GNARC control law. We see that the RMMAC outperforms truly the best non-adaptive robust strategy. Other simulations have revealed similar conclusions.

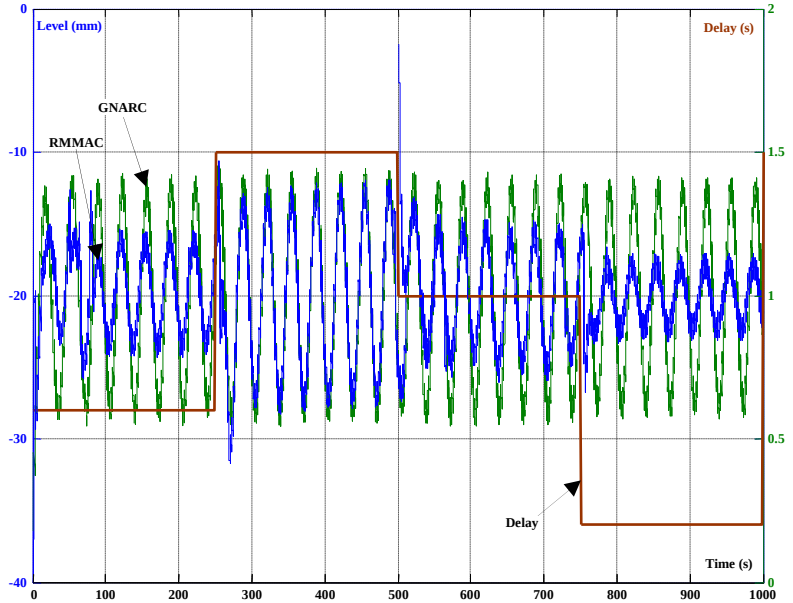

Fig. 5.31. Bulging rejection performance when the true plant delay varies according to a specified sequence stair

5.5 Chapter summary

In this chapter, we examined a robust solution to the mould level control problem, which hinges upon the most recent progress on adaptive control. Contrary to other multiple-model strategies, this methodology so-called Robust Multiple-Model Adaptive Control RMMAC, uses the mixed-μ synthesis to design multiple controllers for smaller parameter uncertainties so that the adaptive performance is equal or greater than a certain limit fixed in advance. We are interested in this architecture also because it may provide the operators with valuable insights about the flow phenomena in the mould region thanks to the Posterior Probability Evaluator PPE of its identification part which pinpoints the locations of the process parameters.
Furthermore, the RMMAC architecture enables the prediction of the potential performance benefits in each subset. More precisely, the designer should determine first the upper and the lower bounds achieved using adaptive control. In the RMMAC terminology, we refer to these bounds as the Fixed Non-Adaptive Robust Compensator FNARC and the Global Non-Adaptive Robust Compensator GNARC respectively. Then, we impose a limit on the RMMAC performance as a function of the FNARC performance. The models are derived in such a way that the performance obtained in each subset is guaranteed to meet or exceed the posed limit.
In our approach, we have considered two uncertain parameters which are the delay and the actuator time constant. Since the RMMAC methodology is well documented only for a unique scalar parameter, the models have been determined by decreasing only the delay uncertainty. To guarantee 60% of the FNARC performance, the initial delay uncertainty ([0.1s 2s]) yields five models and five local controllers so called Local Non-Adaptive Robust Compensator LNARCs. Needless to say that five models is the smallest number to achieve this desired adaptive performance. If one is willing to have superior performance, the optimization process will calculate more models with better performance and greater complexity.
We have presented some representative simulations to demonstrate the RMMAC performance improvement compared to the best non-adaptive control law GNARC in case of a constant uncertain delay or in presence of delay variations. Similar conclusions were arrived at from other simulations where the uncertain delay is located inside the subintervals or close to the models boundaries.

Future directions for this research should include:

- Performance comparison with other adaptive control laws. Indeed, the RMMAC architecture performance has been compared only to that of the best non-adaptive robust strategy GNARC. Because the RMMAC is an adaptive control law, we should consider other multiple-model adaptive structures to make meaningful comparisons.
- Integration of the gain uncertainties in the RMMAC design. In such multiple uncertain parameters cases, the GNARC and the FNARC performances as well as the BPMs distances become surfaces. Although the calculations are somewhat burdensome, the same philosophy still applies to determine the minimum number of models and in the definition of the nominal values for designing the Kalman filters. This integration may imply numerous subtleties which we will not go into here. The reader is referred to [90] for more exhaustive details.
  The ability to include the gain uncertainties in the design process would provide a more complete and global solution to the mould level control problem.

Summary and Future Directions

Conclusions

Steel casting process is of vital importance in the steel manufacturing chain to mass-produce semi-finished products with consistent quality in a variety of sizes and shapes. Although it has higher capital costs, the operating costs are lower. As a consequence, the entire production of the steel plants is continuously cast today enabling large volumes of steel to solidify. The essence of continuous casting is that the solidification should take place on a continuous basis with minimal disruptions. Unfortunately, several factors influence the performance of this process and have a significant effect on both surface quality and internal quality. This thesis focuses on the level variations in the mould region. Due to their magnitude and frequency, current mould level control systems are not always able to compensate the mould level fluctuations. In a number of situations with disturbances, the operators are forced to change the casting conditions (e.g. casting speed changes, increase of secondary cooling, etc.) or to interrupt the casting sequence. These actions are not desirable since they slow down the production. Therefore, new control design methods must be developed to account for process disturbances and casting conditions changes. Specifically, when the unclogging of the nozzle occurs, the control system should react as quickly as possible to compensate the mould level fluctuation generated. In situations where periodic disturbances arise such as the unsteady bulging or the standing waves, the mould level control system should bring a solution capable to weaken the effect of the disturbance on the mould level and in no case to strengthen it. On the other hand, the control system should improve its response when the process moves to another operating point.

In the context of this thesis, a great deal of care has been given to different kinds of process disturbances. Increased disturbance activity causes important mould level variations and it is particularly helpful for the operators to monitor the disturbances evolution. Chapter 3 was devoted to the estimation of the clogging/unclogging cycle and the bulging. We developed a global observer that addresses simultaneously these two disturbances by tracking the behaviors of two exogenous signals modeling the disturbances effects on the mould level control loop. This online monitoring strategy could improve casting inspection. Furthermore, the estimate of the bulging effect has been used in a compensation structure which cancels the bulging effect on the mould level. The proposed structure was found to be highly effective to reduce drastically the mould level variations generated by the bulging in the water model.
In chapter 3, we examined also techniques for offline identification of the gain and the delay of the process. These two key parameters vary with time due to many factors and in such situations the feedback control is less effective leading sometimes to instability. The water model has been used to investigate the links between the values of the model parameters and the casting conditions in the absence or presence of clogging. Intensive water model experiments were carried out to determine the variation ranges of the gain and the delay in function of the casting conditions. Thus, the study findings reveal that the gain decreases with increasing water flow rate and with tundish level. Concerning the delay, it has been found that its value decreases with increasing flow rates of water or air. Therefore, these variations should be taken onto account in the controller design, which would lead to improved control.

In chapter 4, a large selection of control laws has been considered, including the PID, the Predictive Functional Control PFC, the Generalized Predictive Control GPC, the Smith predictor and its modified versions and finally the Internal Model Control IMC. Tests of such control systems indicate generally good control in normal casting situations. However, they are not able to reject efficiently the bulging disturbance or the clogging/unclogging phenomenon. This comparative analysis shows the need of incorporating the specifications in terms of disturbances rejection and robustness margins into the control problem formulation. Fortunately, this is made possible in the H_∞ framework. Based on the modified version of the Smith predictor proposed by Aström, which has the major advantage to decouple the setpoint response from the disturbance rejection with the help of two controllers, the specifications have been reformulated as a multiple H_∞ constraints problem and optimized using the Particle Swarm Optimization technique. The Aström predictor, designed in this way, yields better bulging rejection within a certain delay margin. Simulations have been used to show that changing the delay parameter, as a result of many factors, has no influence on the Aström predictor performances. Therefore, we do

not have to be concerned with the exact identification of the time-delay which is a serious issue when dealing with the Smith predictor. Finally, the Aström predictor scheme can be easily implemented in the industrial PLCs since its controllers can be expressed using the PID form.
The results, presented in this chapter, will aid and guide steelmakers in the selection of the appropriate control law.

Finally, our attention was turned to the use of an adaptive control law. Chapter 5 examines, in a systematic way, the application of the Robust Multiple-Model Adaptive Control architecture RMMAC to the mould level system in order to enhance the bulging rejection. Our primary interest in this control and estimation structure is because it deals with large parameter uncertainty. Indeed, our successful water model tests have revealed that the gain and the delay may vary depending on the chosen configuration, which would render a vast majority of control techniques unsuitable for mould level control. Additionally, the RMMAC architecture integrates both the stochastic hypothesis-testing concepts and the robust non-adaptive mixed-μ synthesis. More importantly, it answers all the classical issues related to the number of models, the local controllers and the Kalman filters design. Nevertheless, this approach is constrained by an increasing complexity in terms of the number of elements necessary for the implementation.
In our design, the models have been determined by taking into account only the delay uncertainty in order to consider a one-dimensional problem.
We concluded this chapter by presenting some simulations where the delay was varied in a predefined way, while the flow rate out of the mould was disturbed by a sine wave modeling the bulging. The RMMAC performances have been assessed compared to the best non-adaptive robust controller. As expected, the improvement in bulging rejection was obvious and in a good agreement with the predictions.
From an operating point of view, the feature consisting of tracking the parameters variations made the RMMAC architecture so attractive to operators.

Extensions and Suggestions for Future Research

Continuous casting represents one of the major areas of technological development within the steel industry. New technologies are under rapid development and are driven by many factors including low capital and operating costs, strict environmental regulations and customer satisfaction. Future developments will be directed largely towards process control which presents many opportunities for casting improvement. Given the high cost associated with surface defects, continued advances especially in the area of mould level control will contribute to remove such defects, improve the quality, reduce costs and ensure compliance with markets requirements. Indeed, our work on mould level control has raised a huge number of issues that merit further research. Most of the time, operators do not have an online information about the disruptive phenomena when operating a caster. The ability to monitor the fluid flow in order to be able to take the corrective actions if necessary is essential for a successful casting operation. Other needs include the implementation of an efficient diagnosis system in order to improve the defects detection and to establish links with the mould level fluctuations.
On the other hand, the ability to develop a robust control system, taking into account the most significant uncertainties of model parameters, will diminish the interventions of operators. Such issue is becoming increasingly critical and current research should focus on the use of robust control tools such as the mixed-μ synthesis.
Finally, more training on the engineering principles involved in the mould level control, is needed for operators in order to enable them to solve any problems that occur and consequently to expand the use of such advanced control schemes. Other area that should be looked at is the extraction of a set of rules from the operator's knowledge and experience to be considered in the control design.

In this thesis, we provided innovative solutions to the difficulties aforementioned but other challenges remain. Future directions for this research should include:

- Use of advanced fluid flow models, which include the liquid free surface inside the mould, in the control scheme design could be beneficial to help understand the causes of mould level variations.

- The identification methods, developed in this dissertation, are able to identify the process model with a good accuracy and do not require any information about the controller. A major disadvantage, however, is that the stopper position setpoint needs to be excited leading to large mould level variations. Furthermore, if we apply smaller setpoint variations in order to avoid this unwanted behavior, there will be less information available for identification purposes. Therefore, it is convenient to perform an identification of the process parameters without external perturbation in order to avoid the production of surface defects during casting.
- Apart from the gain and the delay of the process, there may also be other process parameters that vary with time such as the mould section. Advances in mould level control should evolve in response to such variations.
- Sophisticated control strategies require the inclusion of multiple parameters, not yet fully explored, such as the steel level in the tundish, the argon flow rate, the nozzle submergence depth, the level sensor position, the average current of the drive motors, the secondary cooling flow rate, the mould displacement, etc.
- The water model has been used to highlight the relationships between the process parameters and the casting conditions. It turns out that the delay tends to decrease with increasing flow rates of water or air. We believe that further research is needed to give a physical interpretation to such behaviors. In this thesis, we performed several PIV (Particle Image Velocimetry) measurements in order to track the water flow pattern inside the mould but no obvious correlation, between the process parameters and the flow regime, has been established.
- Further improvements of the disturbances estimation techniques and feed-forward actions should consider robustness to model uncertainties and changes in bulging frequencies. Indeed, this may occur particularly as a result of casting speed changes. One solution would be to explore robust observer theory based on Linear Matrix Inequalities (LMI) optimization that is well documented in recent literature.
- Inclusion of other disturbances in the design methodology of the Aström's modified Smith predictor, in particular, the clogging/unclogging phenomenon and the standing waves. The derived control scheme will likely improve the disturbances rejection and bring a global solution to the mould level control problem. To the best of our knowledge, the state of the art control methods never take them simultaneously into account.
- Inclusion of the gain uncertainties in the RMMAC design. The methodology becomes more complicated since the GNARC and the FNARC bounds as well as the BPMs distances become surfaces but the same philosophy still applies.
- RMMAC performances comparison with other robust multiple-model structures or adaptive control laws. Indeed, the RMMAC has been compared here only to the GNARC controller using extensive simulations essentially because the other control laws are not able to stabilize the mould level over the entire parameters uncertainties. It is of interest to note that significant work has already been undertaken to compare the SMMAC and RMMAC architectures applied to an example that comes from the aerospace industry.
- Full controlled automatic start and restart of the mould level control system is desired to facilitate the casting operations.

The above suggestions will probably enhance the performances of the mould level control system to a great extent and can be applied to other iron and steel processes as well. Hopefully, this will have profound implications for the performance of the entire steel production chain.

APPENDICES

I. Key figures

The aim of this appendix is to provide some key figures about the steel industry. Table A.1 and Table A.2 detail the production of crude steel by region over a half century and in the last decade respectively. It should be noted that China is currently a significant contributor to the world steel production. Its economic expansion and demand growth will reinforce further its position in the global market.

Table A.1. World steel production by region in a half century (million tonnes)

	1950	1970	1990	2008
NAFTA	91.107	134.47	110.88	123.69
CIS	25.785	115.43	154.77	114.38
EU27	62.075	192.78	191.73	198.17
Japan	4.775	93.415	110.11	118.37
China	0.573	17.85	66.99	502.74
Others	6.685	41.055	135.52	272.65
Total	**191**	**595**	**770**	**1330**

Table A.2. World steel production by region in last decade (million tonnes)

	2000	2001	2002	2003	2004	2005	2006	2007	2008
NAFTA	134	118.7	121.6	124.8	132.7	126.4	130.2	130.1	124.2
CIS	98.5	99.7	101.2	106.5	113.4	113.2	119.7	124	114.1
EU27	193.3	187.5	188.3	192.5	202.3	195.5	206.9	210.3	198.6
Japan	106.4	102.9	107.7	110.5	112.7	112.5	116.2	120.2	118.7
China	127.2	150.9	182.2	222.4	282.8	352.4	423	489.2	502.74
Others	188.3	190.8	203.1	213.3	225	242	243.5	269.2	272
Total	**848**	**851**	**904**	**970**	**1069**	**1142**	**1240**	**1343**	**1330**

The steel industry is dominated by a few multinational companies created through acquisitions and mergers. The largest are ArcelorMittal, Nippon Steel, POSCO, JFE Steel, Tata Steel and ThyssenKrupp as shown in Table A.3.

Table A.3. List of biggest steel companies

Company	Production (million t)	Turnover (billion €)
ArcelorMittal	103.3	80.9
Nippon Steel	36.9	27.3
POSCO	34.7	23.9
JFE Steel	33.8	23.1
Tata Steel	24.4	22.4
ThyssenKrupp	16	21.8
Baosteel	35.4	16.2
U.S. Steel	23.3	16.1
Nucor	18.2	15.7
Gerdau	19.6	15.6
Severstal	19.2	15.2
Evraz Group	17.7	12.2
Sumitomo Metals	13.9	11.8
Voestalpine	7.7	11.4
Riva Group	16.9	11.3

Table A.4 shows global consumption in 2008 by region. China is the largest steel consuming region and accounts for 36% of the world consumption, followed by the EU27 and the NAFTA region.
The steel industry primarily supplies the construction sector, the automotive sector and the mechanical engineering sector as shown in Table A.5.

Table A.4. World finished steel consumption in 2008 by region (%)

	2008
NAFTA	11
CIS	4
EU27	15
Japan	6
China	36
Others	28

Table A.5. World finished steel consumption in 2008 by sector (%)

	2008
Construction	27
Mechanical engineering	14
Tubes	12
Automotive	16
Shipyard	1
Structural steelwork	11
Domestic equipments	4
Metalware	12
Others	3

II. PIV measurements

Several PIV (Particle Image Velocimetry) measurements of water flow pattern inside the mould have been carried out. In Table A.6 and Table A.7, horizontal velocity, vertical velocity and velocity amplitude are given as a function of the distance from the narrow face of the mould when the flow rate out of the mould is $3.5 m^3 \cdot h^{-1}$ and $6 m^3 \cdot h^{-1}$ respectively. The results are plotted in Fig. A.1.

Table A.6. Liquid velocity as a function of the distance from the narrow face of the mould (Q_{out}=3.5$m^3 \cdot h^{-1}$)

Distance (mm)	Horizontal component of velocity (m/s)		Vertical component of velocity (m/s)		Velocity amplitude (m/s)	
	1st record	2nd record	1st record	2nd record	1st record	2nd record
4.34	0.003	-0.002	0.017	0.011	0.017	0.011
9.51	0.159	0.136	0.017	0.001	0.160	0.136
14.95	0.162	0.124	0.015	-0.008	0.162	0.124
20.44	0.136	0.115	0.007	-0.005	0.136	0.115
25.96	0.167	0.141	0.005	-0.002	0.167	0.141
31.48	0.155	0.134	0.002	-0.001	0.155	0.134
37.01	0.164	0.138	0.003	-0.002	0.164	0.138
42.54	0.156	0.137	0.000	-0.003	0.156	0.137
48.08	0.163	0.162	0.001	-0.008	0.163	0.163
53.61	0.168	0.137	0.005	-0.018	0.168	0.138
59.15	0.182	0.151	0.005	-0.013	0.182	0.151
64.69	0.166	0.137	0.003	-0.004	0.166	0.137
70.22	0.135	0.131	0.008	-0.005	0.135	0.131
75.76	0.136	0.102	0.003	-0.007	0.136	0.102
81.30	0.149	0.134	-0.005	-0.011	0.149	0.134
86.84	0.153	0.154	0.004	-0.021	0.153	0.155
92.38	0.159	0.156	0.005	-0.024	0.159	0.157
97.92	0.155	0.154	0.002	-0.022	0.155	0.156
103.46	0.144	0.147	0.003	-0.025	0.144	0.150
109.00	0.140	0.141	0.006	-0.020	0.140	0.142
114.54	0.136	0.133	0.000	-0.021	0.136	0.134
120.08	0.143	0.124	-0.006	-0.024	0.143	0.127
125.62	0.114	0.096	-0.004	-0.011	0.114	0.097
131.16	0.095	0.068	-0.007	-0.014	0.095	0.070
136.70	0.116	0.115	-0.010	-0.021	0.116	0.117
142.24	0.114	0.128	-0.019	-0.028	0.116	0.131
147.78	0.102	0.131	-0.007	-0.033	0.103	0.135
153.32	0.107	0.118	-0.011	-0.027	0.108	0.121
158.86	0.097	0.123	-0.014	-0.034	0.098	0.128
164.40	0.092	0.111	-0.012	-0.034	0.093	0.116
169.94	0.091	0.103	-0.015	-0.035	0.092	0.109
175.48	0.087	0.081	-0.015	-0.032	0.088	0.087
181.02	0.087	0.076	-0.017	-0.028	0.089	0.081
186.56	0.083	0.081	-0.013	-0.033	0.084	0.088
192.11	0.079	0.082	-0.013	-0.040	0.080	0.091
197.65	0.073	0.061	-0.007	-0.041	0.073	0.073
203.19	0.053	0.040	-0.008	-0.042	0.054	0.058

Table A.7. Liquid velocity as a function of the distance from the narrow face of the mould (Q_{out}=6m^3·h^{-1})

Distance (mm)	Horizontal component of velocity (m/s)		Vertical component of velocity (m/s)		Velocity amplitude (m/s)	
	1st record	2nd record	1st record	2nd record	1st record	2nd record
4.34	-0.003	0.007	0.000	0.039	0.003	0.039
9.51	0.214	0.248	-0.002	0.002	0.214	0.248
14.95	0.206	0.247	-0.011	0.000	0.207	0.247
20.44	0.232	0.209	0.002	0.001	0.232	0.209
25.96	0.226	0.238	-0.011	-0.004	0.227	0.238
31.48	0.202	0.311	-0.013	0.003	0.203	0.311
37.01	0.188	0.318	-0.011	-0.002	0.188	0.318
42.54	0.182	0.283	-0.015	0.011	0.183	0.283
48.08	0.223	0.309	-0.011	-0.023	0.223	0.309
53.61	0.239	0.318	-0.023	-0.004	0.240	0.318
59.15	0.221	0.295	-0.038	-0.002	0.224	0.295
64.69	0.224	0.308	-0.023	-0.003	0.225	0.308
70.22	0.198	0.199	-0.006	-0.007	0.198	0.200
75.76	0.151	0.142	-0.017	-0.010	0.152	0.142
81.30	0.208	0.263	-0.006	-0.010	0.208	0.263
86.84	0.242	0.281	-0.019	-0.017	0.242	0.281
92.38	0.203	0.302	-0.010	-0.024	0.203	0.303
97.92	0.204	0.282	-0.016	-0.035	0.204	0.284
103.46	0.206	0.281	-0.027	-0.047	0.208	0.285
109.00	0.181	0.243	-0.011	-0.033	0.182	0.246
114.54	0.189	0.230	-0.020	-0.025	0.190	0.231
120.08	0.175	0.208	-0.014	-0.036	0.176	0.211
125.62	0.133	0.181	-0.011	-0.035	0.133	0.184
131.16	0.102	0.141	-0.009	-0.037	0.102	0.145
136.70	0.174	0.160	-0.029	-0.059	0.176	0.170
142.24	0.180	0.196	-0.033	-0.080	0.183	0.212
147.78	0.190	0.186	-0.025	-0.080	0.192	0.202
153.32	0.167	0.178	-0.046	-0.062	0.174	0.189
158.86	0.168	0.178	-0.054	-0.077	0.176	0.194
164.40	0.149	0.163	-0.057	-0.061	0.159	0.174
169.94	0.142	0.152	-0.054	-0.058	0.152	0.162
175.48	0.095	0.102	-0.048	-0.043	0.106	0.111
181.02	0.104	0.090	-0.055	-0.045	0.118	0.100
186.56	0.116	0.100	-0.078	-0.043	0.139	0.109
192.11	0.104	0.101	-0.064	-0.039	0.122	0.108
197.65	0.078	0.079	-0.070	-0.037	0.105	0.087
203.19	0.063	0.056	-0.066	-0.025	0.091	0.062

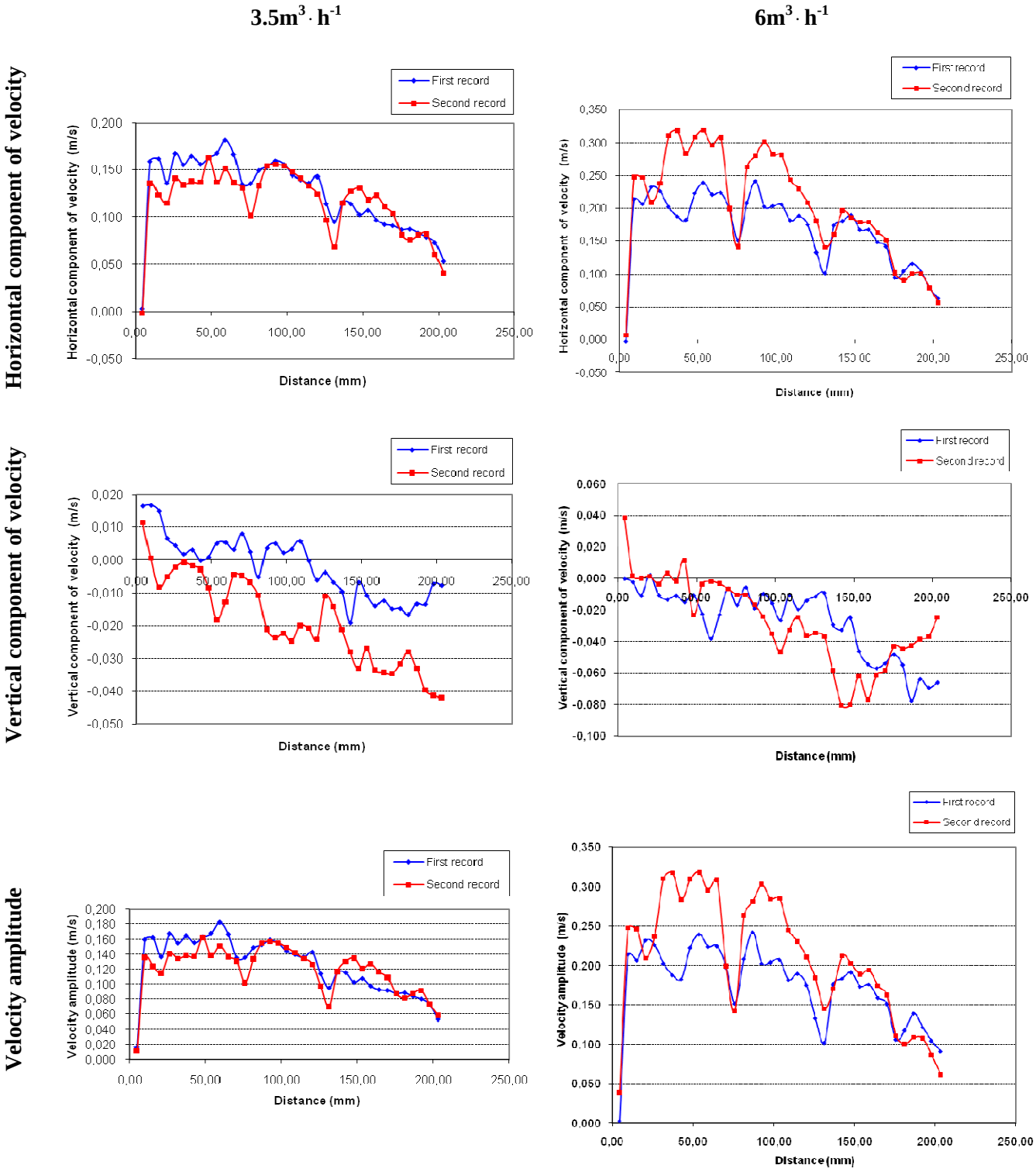

Fig. A.1. Distribution of velocity at two different flow rates

The distributions of water velocity at $3.5 m^3 \cdot h^{-1}$ and $6 m^3 \cdot h^{-1}$ are compared in Table A.8 and Fig. A.2.

Table A.8. Comparison between both velocity distributions

Distance (mm)	Horizontal component of velocity (m/s)		Vertical component of velocity (m/s)		Velocity amplitude (m/s)	
	$6 m^3 \cdot h^{-1}$	$3.5 m^3 \cdot h^{-1}$	$6 m^3 \cdot h^{-1}$	$3.5 m^3 \cdot h^{-1}$	$6 m^3 \cdot h^{-1}$	$3.5 m^3 \cdot h^{-1}$
4.34	0.002	0.001	0.019	0.014	0.021	0.014
9.51	0.231	0.147	0.000	0.009	0.231	0.148
14.95	0.227	0.143	-0.005	0.003	0.227	0.143
20.44	0.221	0.126	0.002	0.001	0.221	0.126
25.96	0.232	0.154	-0.007	0.001	0.232	0.154
31.48	0.257	0.145	-0.005	0.001	0.257	0.145
37.01	0.253	0.151	-0.006	0.001	0.253	0.151
42.54	0.233	0.147	-0.002	-0.001	0.233	0.147
48.08	0.266	0.163	-0.017	-0.004	0.266	0.163
53.61	0.279	0.152	-0.013	-0.006	0.279	0.153
59.15	0.258	0.166	-0.020	-0.004	0.260	0.166
64.69	0.266	0.151	-0.013	-0.001	0.267	0.152
70.22	0.199	0.133	-0.006	0.002	0.199	0.133
75.76	0.146	0.119	-0.014	-0.002	0.147	0.119
81.30	0.236	0.141	-0.008	-0.008	0.236	0.142
86.84	0.261	0.153	-0.018	-0.009	0.262	0.154
92.38	0.252	0.158	-0.017	-0.009	0.253	0.158
97.92	0.243	0.155	-0.025	-0.010	0.244	0.155
103.46	0.243	0.146	-0.037	-0.011	0.246	0.147
109.00	0.212	0.140	-0.022	-0.007	0.214	0.141
114.54	0.209	0.135	-0.022	-0.010	0.210	0.135
120.08	0.191	0.134	-0.025	-0.015	0.193	0.135
125.62	0.157	0.105	-0.023	-0.007	0.159	0.106
131.16	0.121	0.082	-0.023	-0.010	0.124	0.082
136.70	0.167	0.115	-0.044	-0.015	0.173	0.116
142.24	0.188	0.121	-0.056	-0.024	0.198	0.123
147.78	0.188	0.117	-0.052	-0.020	0.197	0.119
153.32	0.173	0.113	-0.054	-0.019	0.181	0.115
158.86	0.173	0.110	-0.066	-0.024	0.185	0.113
164.40	0.156	0.101	-0.059	-0.023	0.167	0.104
169.94	0.147	0.097	-0.056	-0.025	0.157	0.100
175.48	0.098	0.084	-0.046	-0.023	0.109	0.087
181.02	0.097	0.082	-0.050	-0.022	0.109	0.085
186.56	0.108	0.082	-0.060	-0.023	0.124	0.086
192.11	0.102	0.081	-0.051	-0.027	0.115	0.086
197.65	0.078	0.067	-0.053	-0.024	0.096	0.073
203.19	0.060	0.047	-0.045	-0.025	0.076	0.056

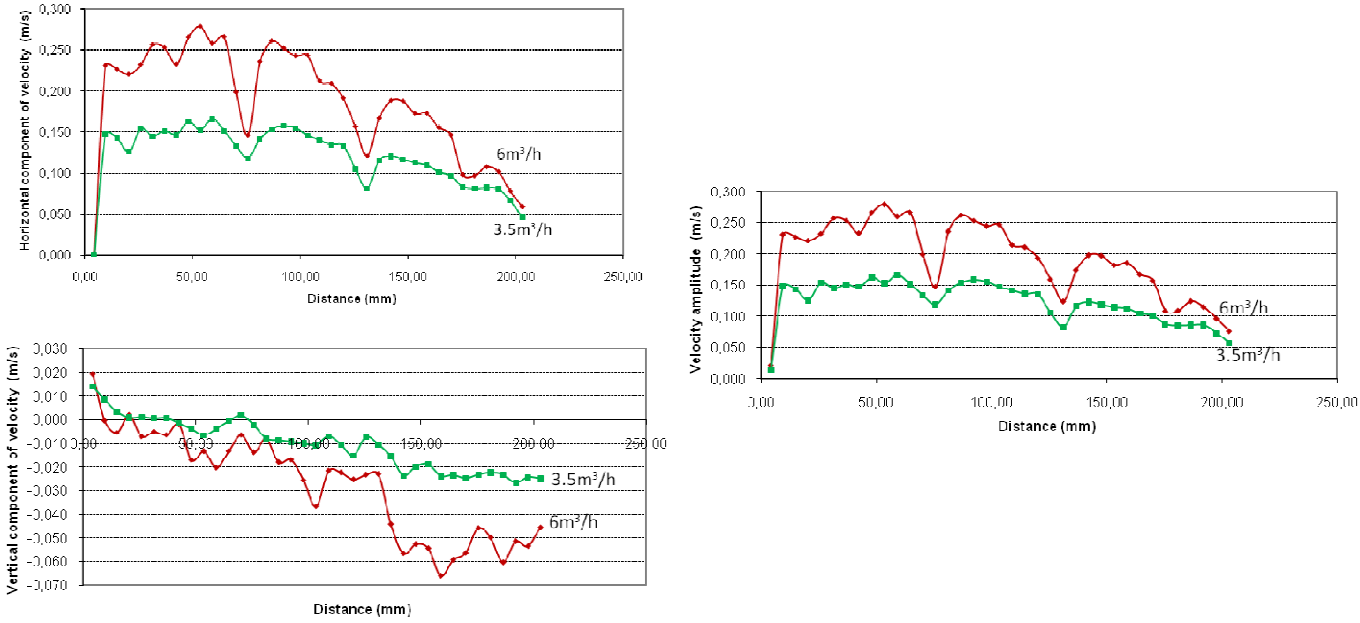

Fig. A.2. Comparison between both velocity distributions

Fig. A.3 shows the flow patterns obtained using PIV measurements in the middle plane of the mould at $3.5m^3 \cdot h^{-1}$ and $6m^3 \cdot h^{-1}$.

$3.5m^3 \cdot h^{-1}$ **$6m^3 \cdot h^{-1}$**

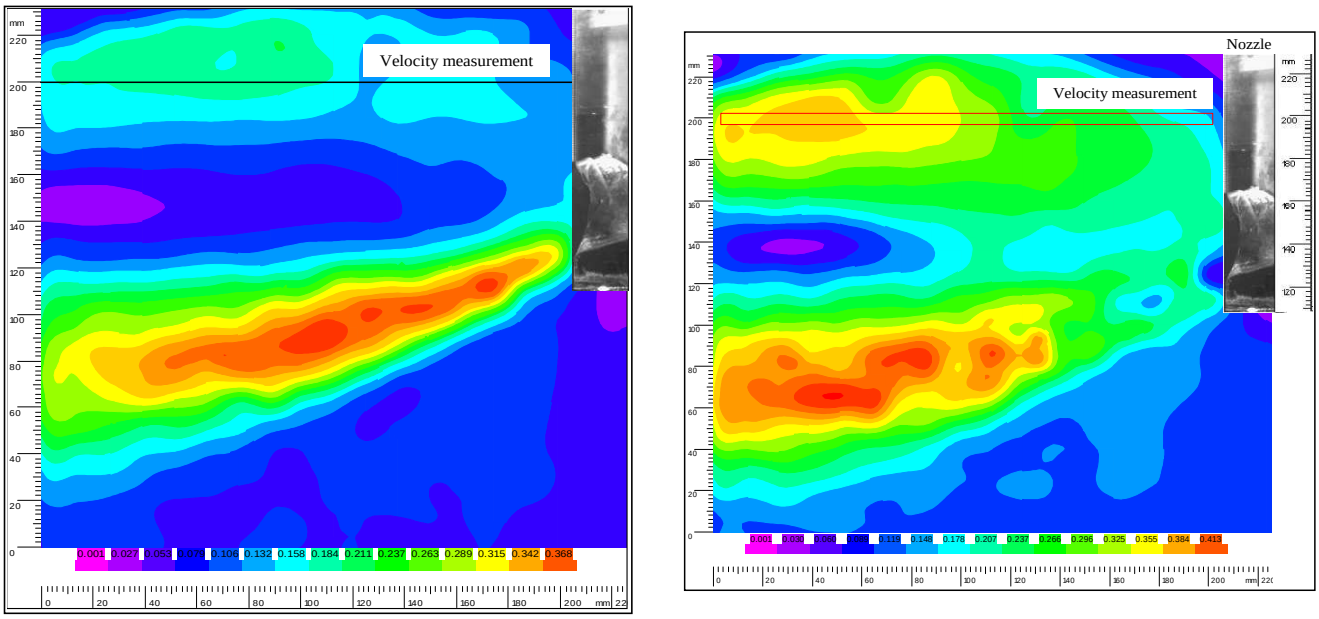

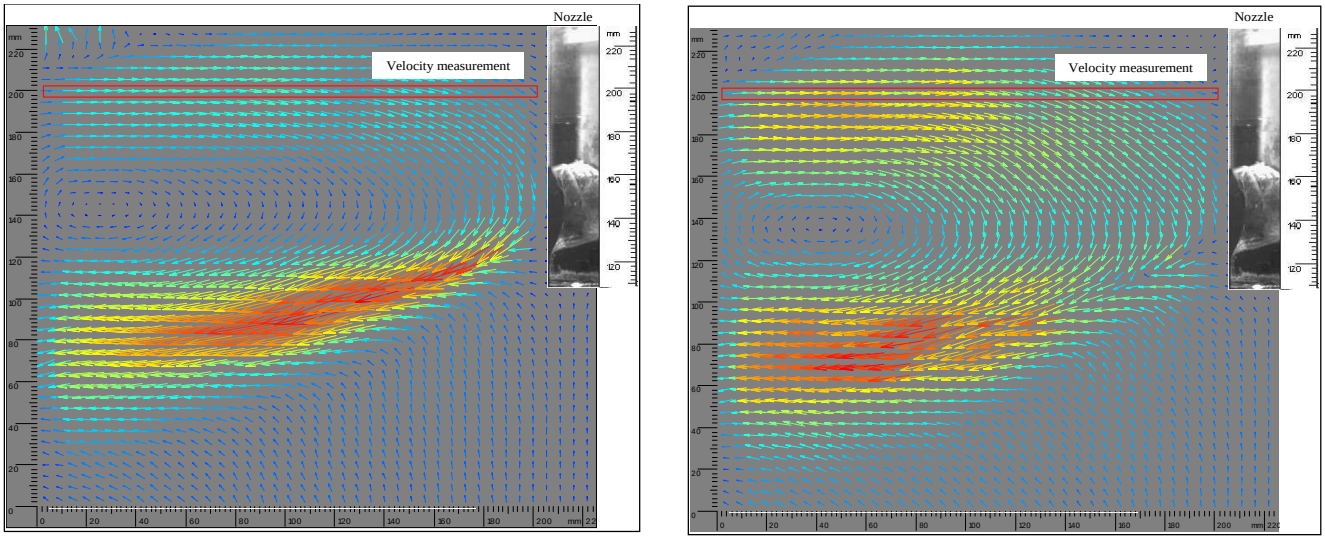

Fig. A.3. Velocity vectors in the middle plane at two different flow rates

REFERENCES

i. Conference articles

[1] M.M. Wolf, "History of continuous casting", in 75th steelmaking conference proceedings, pp. 83-137.

[2] B.G. Thomas, H. Bai, "Tundish nozzle clogging – Application of computational models", in 18rd Process Technology Division Conference proceedings, vol. 18, pp. 895-912, Warrendale, 2001.

[3] C. Furtmueller, E. Gruenbacher, "Suppression of periodic disturbances in continuous casting using an internal model predictor", in Proc. IEEE Intl. Conf. on Control Applications, Munich, Germany, 2006.

[4] D. Suzuki et al., "Level control model by numerical fluid dynamics method", in Proc. of the 4th International Conference on Intelligent Processing and Manufacturing of Materials IPMM, 2003.

[5] M. Javurek, M. Thumfart, K. Rieger, J. Kepler, M. Hirschmanner, "Mathematical mould level model based on numerical simulations and water model experiments", in 6th European Conference on Continuous Casting, Italy, 2008.

[6] S.F. Graebe, G.C. Goodwin, M.R. West, P. Stepien, "An application of advanced control to steel casting", in Proc. of the 3th Conference on Control Applications, vol. 3, pp. 1533-1538, Glasgow, 2002.

[7] A. Vaterlaus, "Steel flow control in continuous casting tundishes by a new precision control valve", in proceedings of the 6th International Iron and Steel Congress, vol. 3, pp. 454-461, 1990.

[8] S.H. Al-Amer, F.M. Al-Sunni, "Approximation of time-delay systems", in Proc. of the American Control Conference, vol. 1, pp. 2491-2495, Chicago, USA, 2000.

[9] A. Radke, Z. Gao, "A survey of state and disturbance observers for practitioners", in Proc. of the American Control Conference, pp. 5183-5188, Minnesota, USA, 2006.

[10] W. Wang, Z. Gao, "A comparison study of advanced state observer design techniques", in Proc. of the American Control Conference, vol. 6, pp. 4754-4759, Denver, USA, 2003.

[11] C. Furtmueller, L. Del Re, H. Bramerdorfer, K. Moerwald, "Periodic disturbance suppression in a steel plant with unstable internal feedback and delay", in Proc. of the 5th International Conference on Technology and Automation ICTA, Greece, 2005.

[12] C. Furtmueller, L. Del Re, "Disturbance suppression for an industrial level control system with uncertain input delay and uncertain gain", in Proc. of the International Conference on Control Applications, pp. 3206-3211, Munich, Germany, 2006.

[13] D.J. Lim, H.S. Jeong, D.H. Hong, "A study on the mold level control of continuous casting system", 1990.

[14] F. Zhang, S. Hosoe, M. Kouno, "Synthesis of robust output regulators via H_∞ control", in Proc. of the 13th Symposium Dynamical Systems Theory, pp. 5-10, 1991.

[15] G. Sandou, G. Duc, D. Beauvois, "Optimisation par essaim particulaire du réglage d'un correcteur H_∞", in Proc. of the International French-Speaking Conference on Automatic Control CIFA, Romania, 2009.

[16] I. Maruta, T.H. Kim, T. Sugie, "Fixed structure H_∞ controller synthesis: A meta-heuristic approach using simple constrained particle swarm optimization", in Proc. of the 17th IFAC World Congress, Korea, 2008.

[17] R.C. Eberhart, J. Kennedy, "A new optimizer using particle swarm theory", in Proc. of the 6th International Symposium on Micromachine and Human Science, Nagoya, Japan, 1995.

[18] M. Morari, S. Skogestad, D.E. Rivera, "Implications of internal model control for PID controllers", in Proc. of the American Control Conference, pp. 661-666, 1984.

[19] T. Kurokawa, T. Kondo, T. Mita, K. Liu, M. Sapei, "Development of mold level control in continuous casting by H_∞ control theory", in Proc of the 2nd IEEE Conference on Control Applications, pp. 865-871, 1993.

[20] M. Athans, S. Fekri, A. Pascoal, "Issues on robust adaptive feedback control", invited plenary paper, in Preprints of the 16th IFAC World Congress, pp. 9-39, 2005.

[21] S. Fekri, M. Athans, A. Pascoal, "RMMAC: a novel robust adaptive control scheme – Part 1: Architecture", in Proc. of the IEEE Conference on Decision and Control, pp. 1134-1139, Bahamas, 2004.

[22] G.J. Balas, Private communication re mixed-μ software, 2009.

[23] P.M. Young, M.P. Newlin, J.C. Doyle, "μ analysis with real parametric uncertainty", in Proc. of the IEEE Conference on Decision and Control, pp. 1251-1256, 1991.

[24] P.M. Young, "Controller design with mixed uncertainties", in Proc. of the American Control Conference, pp. 2333-2337, Baltimore, 1994.

[25] J.C. Doyle, "Structured uncertainty in control systems design", in Proc. of the 24th Conference on Decision and Control, pp. 260-265, Floride, 1985.

[26] G.J. Balas, C. Chu, J.C. Doyle, "Vibration damping and robust control of the JPL/AFAL experiment using μ-synthesis", in Proc. of the 28th Conference on Decision and Control, pp. 2689-2694, 1989.

[27] G.J. Balas, J.C. Doyle, "Robustness and performance tradeoffs in control design for flexible structures", in Proc. of the 29th Conference on Decision and Control, pp. 2999-3010, 1990.

ii. Journal articles

[28] D. Suzuki, "Formulation of a mold level control by molten steel flow analysis method", Shinnittetsu Giho, no. 379, pp. 39-42, 2003.

[29] P. Moin, "Advances in large eddy simulation methodology of complex flows", International Journal of Heat Fluid Flow, vol. 23, no. 5, pp. 710-720, 2002.

[30] C.W. Hirt, B.D. Nichols, "Volume of fluid (VOF) method for the dynamics of free boundaries", Journal of Computational Physics, vol. 39, pp. 201-225, 1981.

[31] U.S. Yoon, I.W. Bang, J.H. Rhee, S.Y. Kim, J.D. Lee, K.H. Oh, "Analysis of mold level hunching by unsteady bulging during thin slab casting", ISIJ international, vol. 42, no. 10, pp. 1103-1111, 2002.

[32] J.D. Lee, C.H. Yim, "The mechanism of unsteady bulging and its analysis with the finite element method for continuously cast steel", ISIJ international, vol. 40, no. 8, pp. 765-770, 2000.

[33] S.Y. Kim, C.J. Ko, Y.S. Park, “The control of mold level fluctuation in TSMP Kwangyang Works”, SEAISI Quarterly, vol. 26, no. 4, pp. 64-75, 1997.

[34] J.S. Ha, J.R. Cho, B.Y. Lee, M.Y. Ha, “Numerical analysis of secondary cooling and bulging in the continuous casting of slabs”, Journal of Materials Processing Technology, no. 113, pp. 257-261, 2001.

[35] S.F. Graebe, G.C. Goodwin, G. Elsley, “Control design and implementation in continuous steel casting”, Control Systems Magazine, vol. 15, pp. 64-71, 2002.

[36] J. Rohac, V. Pisoft, “The use of emission and electromagnetic bath level measurements in the continuous casting mould”, Stahl und Eisen, no. 112, 1992.

[37] L. Ljung, “On the estimation of transfer functions”, Automatica, vol. 21, no. 6, pp. 677-696, 1985.

[38] R. Pintelon, L.V. Biesen, “Identification of transfer functions with time delay and its application to cable fault location”, IEEE Transactions of Instruments and Measures, vol. 39, vol. 3, pp. 479-484, 1990.

[39] B. Ninness, “Integral constraints on the accuracy of least squares estimation”, Automatica, vol. 32, no. 3, pp. 391-197, 1996.

[40] J. Lam, “Convergence of a class of Padé approximations for delay systems”, International Journal of Control, vol. 52, no. 4, pp. 989-1008, 1990.

[41] J. Lam, “Analysis on the Laguerre formula for approximating delay systems”, IEEE Transactions on Automatic Control, vol. 39, pp. 1517-1521, 1994.

[42] C.H. Lien, K.W. Yu, “LMI optimization approach on robustness and H_∞ control analysis for observer based control of uncertain systems”, Chaos, Solitons & Fractals, vol. 36, no. 3, pp. 617-627, 2006.

[43] C.H. Lien, “An efficient method to design robust observer based control of uncertain linear systems”, Applied Mathematics and Computation, vol. 158, no. 1, pp. 29-44, 2004.

[44] D.S. Kumar, T. Rajendra, A. Sarkar, A.K. Karande, U.S. Yadav, “Slab quality improvement by controlling mould fluid flow”, Ironmaking & steelmaking, vol. 34, no. 2, pp. 185-191, 2007.

[45] D.W. Clarke, C. Mohtadi, P.S. Tuffs, “Generalized predictive control – part 1, the basic algorithm”, Automatica, vol. 23, no. 2, pp. 137-148, 1987.

[46] O.J. Smith, “A controller to overcome dead time”, ISA Journal, vol. 6, no. 2, pp. 28-33, 1949.

[47] Z.J. Palmor, D.V. Powers, “Improved dead-time compensator controllers”, AIChE Journal, vol. 31, no. 2, pp. 215-221, 1985.

[48] A. Bhaya, C.A. Desoer, “Controlling plants with delay”, International Journal of Control, vol. 41, no. 3, pp. 813-830, 1985.

[49] K.J. Aström, C.C. Hang, B.C. Lim, “A new Smith predictor for controlling a process with an integrator and lond dead-time”, IEEE Transactions on Automatic Control, vol. 39, no. 2, pp. 343-345, 1994.

[50] Y.D. Chen, P.C. Tung, C.C. Fuh, “Modified Smith predictor scheme for periodic disturbance reduction in linear delay systems”, Journal of Process Control, vol. 17, pp. 799-804, 2007.

[51] Z. Guanghui, Q. Feng, S. Huihe, "Robust tuning method for modified Smith predictor", Journal of Systems Engineering and Electronics, vol. 18, no. 1, pp. 89-94, 2007.

[52] H.Q. Zhou, Q.G. Wang, L. Min, "Modified Smith predictor design for periodic disturbance rejection", ISA Transactions, vol. 46, no. 4, pp. 493-503, 2007.

[53] T.H. Kim, I. Maruta, T. Sugie, "Robust PID controller tuning based on the constrained particle swarm optimization", Automatica, vol. 44, no. 4, pp. 1104-1110, 2008.

[54] I.C. Trelea, "The particle swarm optimization algorithm: convergence analysis and parameter selection", Information Processing Letters, vol. 85, no. 6, pp. 317-325, 2003.

[55] K. Glover, J.C. Doyle, "State-space formulae for all stabilizing controllers that satisfy an H_∞-norm bound and relations to risk sensitivity", Systems and Control Letters, vol. 11, pp. 167-188, 1988.

[56] H. Kitada, O. Kondo, H. Kusachi, K. Sasame, "H_∞ control of molten steel level in continuous caster", IEEE Transactions on Control Systems Technology, vol. 6, no. 2, pp. 200-207, 1998.

[57] D. Lainiotis, "Optimal adaptive estimation: Structure and parameter adaptation", IEEE Transactions on Automatic Control, vol. 16, no. 2, pp. 160-170, 1971.

[58] D. Magill, "Optimal adaptive estimation of sampled stochastic processes", IEEE Transactions on Automatic Control, vol. 10, no. 4, pp. 434-439, 1965.

[59] X. Li, Y. Bar-Shalom, "Multiple-model estimation with variable structure", IEEE Transactions an Automatic Control, vol. 41, no. 4, pp. 478-493, 1996.

[60] B. Anderson *et al.*, "Multiple-model adaptive control. part 1: Finite controller coverings", International Journal of Robust and Nonlinear Control, vol. 10, no. 11-12, pp. 909-929, 2000.

[61] B. Anderson *et al.*, "Multiple-model adaptive control with safe switching", International Journal of Adaptive Control and Signal Processing, vol. 15, no. 5, pp. 445-470, 2001.

[62] A. Morse *et al.*, "Applications of hysteresis switching in parameter adaptive control", IEEE Transactions on Automatic Control, vol. 37, pp. 1343-1354, 1992.

[63] A. Morse, "Supervisory control of families of linear set-point controllers – part 1: Exact matching", IEEE Transactions on Automatic Control, vol. 41, no. 10, pp. 1413-1431, 1996.

[64] M. Fan *et al.*, "Robustness in the presence of mixed parametric uncertainty and unmodeled dynamics", IEEE Transactions on Automatic Control, vol. 36, no. 1, pp. 25-38, 1991.

iii. Books

[65] G.R. Irwin, *Fracture mechanics – Structural mechanics*, Pergamon Press, New York, 1960.

[66] A.S. Tetelman, A.J. Evily, *Fracture of structural materials*, Wiley, New York, 1967.

[67] A. Jackson, *Oxygen steelmaking for steelmakers*, Newnes-Butterworths, London, 1964.

[68] G. Beranger, G. Henry, G. Sanz, *The book of steel*, Lavoisier publishing, 1996.

[69] T. Nagaoka, *History of continuous casting of steel*, 1991.

[70] G. Carlsson, *Process control in the steel industry*, MEFOS, Sweden, 1986.

[71] Berthold Technologies, *Mould level gauge LB 352*, Technical report, 1997.

[72] T. Soderstrom, P.G. Stoica, *System identification*, Prentice-Hall, 1989.

[73] H. Beker, F. Piper, *Cipher systems: the protection of communications*, van Nostrand Reinhold, 1982.

[74] I.D. Landau, A. Besançon-Voda, *Identification des systèmes*, Hermes, 2001.

[75] L. Ljung, *System identification – Theory for the user*, Prentice-Hall, Upper Saddle River, N.J., 2nd edition, 1999.

[76] J. Chiasson, J.J. Loiseau, *Applications of time delay systems*, Springer, 2007.

[77] S.I. Niculescu, K. Gu, *Advances in time-delay systems*, Springer, 2004.

[78] M. Grewal, A. Andrews, *Kalman filtering*, Prentice-Hall, 1993.

[79] E. Sontag, *Mathematical control theory: Deterministic finite dimensional systems*, Springer, 1998.

[80] F.M. White, *Fluid mechanics*, McGraw-Hill, 1999.

[81] G.F. Franklin, J.D. Powell, A. Emami-Naeini, *Feedback control of dynamic systems*, Addison-Wesley, 1991.

[82] J. Richalet, G. Lavielle, J. Mallet, *La commande prédictive*, Eyrolles, 2004.

[83] D. Dumur, P. Boucher, *La commande prédictive*, Technip, 1996.

[84] R.J. Bibbero, *Microprocessors in instruments and control*, John Wiley and Sons, 1981.

[85] M. Green, D. Limebeer, *Linear robust control*, Prentice-Hall, 1995.

[86] J.F. Magni, S. Bennani, J.P. Dijkgraaf, *An overview of system modelling in LFT form*, Springer, 2002.

[87] Z.P. Jiang, A.R. Teel, L. Praly, *Small-gain theorem for ISS systems and applications*, Springer, 1994.

[88] C. Brosilow, B. Joseph, *Techniques of model-based control*, Prentice-Hall, 2002.

[89] M. Athans, C. Chang, *Adaptive estimation and parameter identification using multiple-model estimation algorithms*, Technical report 28, MIT, Lexington, MA, USA, 1976.

[90] S. Fekri, *Robust adaptive MIMO control using multiple-model hypothesis testing and mixed-μ synthesis*, Ph.D. dissertation, Instituto Superior Técnico, Portugal, 2005.

[91] C. Greene, *An analysis of the multiple model adaptive control algorithm*, Ph.D. dissertation, MIT, Cambridge, MA, USA, 1978.

[92] H. Shomber, *An extended analysis of the multiple model adaptive control algorithm*, Ph.D. dissertation, MIT, Cambridge, MA, USA, 1980.

[93] G.J. Balas, J.C. Doyle, K. Glover, A. Packard, R. Smith, *μ analysis and synthesis toolbox*, MathWorks, MA, 1995.

[94] B. Anderson, J. Moore, *Optimal filtering*, Prentice-Hall, 1979.

[95] Y. Baram, *Information, consistent estimation and dynamic system identification*, Ph.D. dissertation, MIT, Cambridge, USA, 1976.

[96] K. Zhou, J.C. Doyle, K. Glover, *Robust and optimal control*, Prentice-Hall, 1996.

[97] P.M. Young, "Robustness with parametric and dynamic uncertainty", Ph.D. dissertation, California Institute of Technology, Pasadena, California, USA, 1993.

[98] J. Doob, *Stochastic processes*, John Wiley & Sons, 1953.

[99] P. Halmos, *Lectures on ergodic theory*, Chelsea Publ. Co, 1956.

[100] M. Grewal *et al.*, *Global positioning systems, inertial navigation, and integration*, John Wiley & Sons, 2001.

Résumé

La coulée continue est une étape importante dans la chaîne de fabrication de l'acier. Ce procédé agit comme un échangeur thermique qui permet de solidifier l'acier en fusion. De nombreuses études ont révélé qu'une partie importante des défauts de surface du produit solidifié est provoquée par les perturbations du niveau d'acier liquide en lingotière. Chaque ligne de production dispose d'un système de régulation de niveau dont l'objectif est de maintenir un niveau stable d'acier liquide. En présence de certaines perturbations ou lors des phases transitoires, les performances de ces systèmes de régulation se dégradent fortement.

L'objectif principal de la thèse est de développer des solutions de contrôle robuste de niveau afin de rejeter les perturbations internes et externes à la boucle de régulation quelles que soient les conditions de coulée. Un outil d'estimation a été développé pour diagnostiquer et rejeter certaines perturbations. L'activité de recherche a porté également sur le recensement et l'évaluation des lois de commande utilisées actuellement dans les usines ou proposées par les fournisseurs dans le but d'établir un référentiel de performances que nous avons ensuite amélioré en mettant en œuvre de nouvelles stratégies de régulation. Enfin, une commande adaptative multi-modèles combinant à la fois les fonctions de régulation robuste de niveau et d'identification des paramètres a été implantée. Une maquette hydraulique a été utilisée à plusieurs reprises pour reproduire le fonctionnement de la coulée continue sur site afin d'évaluer le gain en performance de la solution retenue. Les solutions proposées présentent un caractère générique et peuvent s'appliquer à d'autres procédés sidérurgiques avec seulement quelques ajustements.

Mots clés : Sidérurgie, Coulée continue, Régulation de niveau, Bouchage, Gonflement, Ondes stationnaires, Maquette hydraulique, Modélisation, Identification, Observateur, Commande prédictive, Prédicteur de Smith, Synthèse H_∞, μ synthèse mixte, Commande multi-modèles, RMMAC.

Abstract

During the continuous casting of steel, several disturbances occur and affect all the parts of the caster, including the mould where the molten steel has to be stable for good quality of the final product. Especially at high casting velocities, it is difficult to achieve, using the conventional control schemes, both stability and performance robustness because of different classes of disturbances and parameters uncertainties in the process. Therefore, improved process control techniques are needed to cope with such obstacles.

This thesis focuses on developing methods for designing controllers to force the level to respond in a desired manner to a setpoint change and to counter the effects of disturbances. An online monitoring of some of the most disruptive phenomena is also developed because more information is needed to improve casting inspection. In addition, particular attention is paid to reject some disturbances with the help of an estimator module. Since the process is prone to important variability, other needed developments include robust control design methods that incorporate other casting parameters such as mould section, tundish weight and argon flow rate. The water model is used to validate the theoretical developments and to investigate several important issues related to mould level control.

The combination of these techniques is used as a sophisticated control tool for the continuous casting machine as well as for other iron and steel processes.

Keywords: Iron and steel processes, Continuous casting, Level control, Clogging, Bulging, Standing waves, Water model, Process modeling, Identification, Observer, Predictive control, Smith predictor, H_∞ synthesis, mixed-μ synthesis, Multiple-model control, RMMAC.